Entangled Photon Interferometry: Development of Photonic Systems Towards Quantum Spectroscopy

Thesis by
Szilard Szoke

In Partial Fulfillment of the Requirements for the
Degree of
Doctor of Philosophy

CALIFORNIA INSTITUTE OF TECHNOLOGY
Pasadena, California

2022
Defended (January 21, 2022)

© 2022

Szilard Szoke
ORCID: 0000-0001-7860-4638

All rights reserved

ACKNOWLEDGEMENTS

First and foremost, I would like to extend my deepest thanks to my advisor, Scott Cushing. Scott's very enthusiastic love of science made the day-to-day research work a genuine joy (even during a global pandemic). His constant encouragement to think about new scientific research avenues that could be interesting to explore is something that I think every young scientist would highly cherish. It has certainly allowed me to venture outside of my comfort zone and investigate a lot of new areas during my graduate studies, which ended up teaching me more than I can possibly relay. Beyond his comprehensive scientific knowledge and insights on how to connect seemingly unrelated fields by just focusing on the fundamentals, I really appreciated Scott's mentorship over the years. Thanks to Scott, the lab atmosphere was always upbeat and the encouragement to try new things made work fun and enjoyable even when things weren't working as they were supposed to. Thank you for all the fun science discussions, the group meetings, the laser alignments (or disassembly when they became a headache), the intellectual freedom to get on with research, and obviously all the time spent in the lab/on Zoom teaching or helping out. Future students are lucky to have you as their advisor and mentor.

I also wish to say a sincere thank you to my committee, Ryan Hadt, Alireza Marandi, and Austin Minnich. Thank you for all the feedback on my research and for the stimulating scientific discussions when our work overlapped.

Special thank you to Oskar Painter and Jeff Kimble, who brought me to Caltech to begin with. I am extremely grateful for having been given the opportunity by you to come to such a special place. Thank you for your trust in my abilities and for all the time you invested in teaching me.

Thank you also to all the faculty I've either taken classes from or had the chance to work with during my time at Caltech, whose help, scientific insights, and mentorship were essential to my scientific development and PhD journey. I would also like to thank Jeroen Elzerman, Paul Warburton, Mark Buitelaar, Florian Mintert, and Ortwin Hess, who have all guided me in my research during my times at UCL and Imperial. They were all exceptional mentors and left a lasting impression on me. I could not have reached this point in my career without their help and guidance.

To all past and present members of the Cushing Lab: - Manni He, Bryce Hickam, Isabel Klein, Jonathan Michelsen, Hanzhe Liu, Alex Krotz, Danika Nimlos, Kim

Pham, Hamilton Evans, Nathan Harper, Emily Hwang, Wonseok Lee, Levi Palmer, William Denman. You have all played an instrumental role in my graduate school experience, and I want to thank all of you for the time I got to spend working together with you, and to have learned from you along the way. Also an exceptionally big thank you to Elisha Okawa for organizing everything and keeping the group from falling into disarray.

Thank you for the mentorship and friendship of Su-Peng Yu, Andrew McClung, Greg MacCabe, Jared Ren, and Roger Luo. I'm really grateful for everything you taught me and for the good times either in the office or in the cleanroom working together. Roger, I still can't believe our round-the-clock ALD/XRD effort...

To everyone at KNI who are essential to keeping it running like the well-oiled machine that it is, and who have always lent a helping hand when I needed it - Barry Baker; thanks for all the good laughs and for having my back. I really enjoyed working with you whenever I got the chance and still cherish the memories of fixing stuff in the lab together. Guy DeRose, thank you for all your help and advice with the EBPGs and lithorgraphy in general, as well as all the fun chats whenever our paths crossed in the lab. Bert Mendoza, cheers for all your assistance and advice around the cleanroom and for making sure everything is safe and tidy.

To Carmen Luna, Josh Moreira, and Laura Madrigal at the Caltech gym. It was always such a pleasure to come chat with you after a long day in the lab and have a good laugh about everything. Thank you for always listening and offering your advice. I am not sure I could have kept my sanity without you.

Thank you to everyone in APhMS, in particular Christy Jenstad, Jennifer Blankenship, and Connie Rodriguez for making the department such a lovely place and for always being on top of things.

To Michelle Rodriguez. Thank you for always being around to chat, for listening to me when I needed it, and for always offering your support and help. I really appreciate your friendship and for making me feel so welcome when I first arrived at Caltech.

Luke Frankiw, Constantine Sideris, Bill Ling, Joe Ruan, Nikolay Dedushenko, you guys deserve a plaque on campus. Caltech wouldn't be half as fun without you, and I'm really grateful to have had my time here overlap with yours.

To Joanne Whalley. Thank you for your kindness, for all the fun evenings, for the home away from home, and for always being cool with me constantly digging up half of your garden. At least the quantum sprinklers were worth it. (I hope this work satisfies your high standards.)

I am not sure I can put into words how thankful I am to have had the support and love of my girlfriend, Eileen. Throughout my PhD, you made the difficult days easier and always made sure that I had you to look forward to. You have always been the best part of my day and I can't thank you enough for looking out for me and making sure I knew you were there for me. I don't think you realize what a difference you make, and I will do my utmost best to do the same for you going forward.

And of course, last but not least, to my family. To my parents, Szabolcs and Valeria, and my sister, Alexandra (a.k.a Sasha). This thesis is as much yours as it is mine. Without you, none of this would have been possible, and I will never be able to properly thank you for the amount of effort and sacrifice you had to make for me to go through this journey. You always provided me with the opportunities in life to freely pursue my interests and passions, and for that I will forever be grateful. Thank you for the constant support, the words of encouragement, and the guidance whenever I needed it the most. I couldn't have asked for two better people to raise me.

ABSTRACT

Entangled photon spectroscopy is an emergent field offering the potential to perform nonlinear and non-classical measurements at low photon fluxes. The entangled photon pairs which are generated using a continuous-wave laser pumped spontaneous parametric downconversion (SPDC) process simultaneously display strong correlations in time and anti-correlations in frequency space. Measuring changes in these correlations provides classical and non-classical information about the underlying dynamics and fluctuations of the sample-system. Further, because these two variables are not Fourier conjugates, entangled photon spectroscopy makes it possible to exploit the spectral resolution of continuous-wave lasers, while leveraging the temporal relationship of the near-simultaneously generated photon pairs which effectively mimicks an ultrafast pulsed laser experiment. Nonlinear and ultrafast measurements can therefore be performed with low-power sources while also achieving superior signal-to-noise ratios due to the underlying quantum statistics. As photons in a pair can be separately manipulated, spectroscopic setups using these quantum states of light have marked benefits in contrast to measurements performed using traditional single photon states.

Here, we describe our efforts towards implementing quantum interferometers to test the abilities of entangled photon pairs in nonlinear spectroscopic studies. Specifically, we present work on the development of free-space, fiber-optic, and nanophotonic systems that leverage nonlinear materials to generate narrow to broadband entangled photon pairs via SPDC. The numerical methods used for designing and tailoring these entangled photon sources are outlined together with associated experimental limitations. The spectral-temporal correlations of the two-photon states are characterized using fourth-order interferometry, demonstrating Hong-Ou-Mandel interference with picoseconds to femtoseconds coherence times, and wavelengths ranging from the IR to the UV. A monolithic nanophotonics architecture is proposed for completely on-chip, entangled, ultrafast, and nonlinear spectroscopy.

PUBLISHED CONTENT AND CONTRIBUTIONS

[1] S. Szoke et al. "Designing high-power, octave spanning entangled photon sources for quantum spectroscopy". In: *The Journal of Chemical Physics* 154.24 (2021), p. 244201. DOI: 10.1063/5.0053688. URL: https://doi.org/10.1063/5.0053688.
S.S. participated in the design of the experiment, implementation of the simulations, preparation of the data, and writing of the manuscript.

[2] Scott K. Cushing et al. "Layer-resolved ultrafast extreme ultraviolet measurement of hole transport in a $Ni - TiO_2 - Si$ photoanode". In: *Science Advances* 6.14 (2020), eaay6650. DOI: 10.1126/sciadv.aay6650. URL: https://www.science.org/doi/abs/10.1126/sciadv.aay6650.
S.S. performed the sample characterization.

[3] Szilard Szoke et al. "Entangled light–matter interactions and spectroscopy". In: *J. Mater. Chem. C* 8 (31 2020), pp. 10732–10741. DOI: 10.1039/D0TC02300K. URL: http://dx.doi.org/10.1039/D0TC02300K.
S.S. participated in the implementation of numerical calculations, preparation of the data, and writing of the manuscript.

[4] Jacob P. Covey et al. "Telecom-Band Quantum Optics with Ytterbium Atoms and Silicon Nanophotonics". In: *Phys. Rev. Applied* 11 (3 Mar. 2019), p. 034044. DOI: 10.1103/PhysRevApplied.11.034044. URL: https://link.aps.org/doi/10.1103/PhysRevApplied.11.034044.
S.S. participated in the conception of the project, design of the system, implementation of the simulations, preparation of the data, and writing of the manuscript.

TABLE OF CONTENTS

LIST OF ILLUSTRATIONS

LIST OF TABLES

LIST OF ABBREVIATIONS

ALD. Atomic-Layer Deposition.

AMO. Atomic, Molecular, and Optical (physics).

BPM. Birefringent Phase-Matching.

emCCD. electron multiplying Charge-Coupled Device.

EPS. Entangled Photon Spectroscopy.

ETPA. Entangled Two-Photon Absorption.

FDTD. Finite-Difference Time-Domain.

FEM. Finite-Element Method.

FP. Fabry-Pérot.

HF. Hydrofluoric acid.

HOMI. Hong-Ou-Mandel Interference.

ICP-RIE. Inductively-Coupled Plasma - Reactive-Ion Etch.

IR. Infra-red.

KTP. Potassium titanyl phosphate.

LBGO. $LaBGeO_5$.

LN. Lithium niobate.

LT. Lithium tantalate.

OPA. One-Photon Absorption.

PhC. Photonic Crystal.

QPM. Quasi Phase-Matching.

SEM. Scanning-Electron Microscope.

SPAD. Single-Photon Avalanche Detector.

SPDC. Spontaneous Parametric Downconversion.

TPA. Two-Photon Absorption.

UV. Ultraviolet.

Chapter 1

INTRODUCTION

Entanglement is arguably one of the most interesting (or mundane, depending on whom you ask) phenomena in the realm of quantum theory. The idea that distinct particles can exhibit correlations between them that are classically impossible has led to decade-spanning research efforts trying to understand, exploit, and utilize this concept. More specifically, quantum entanglement refers to many-body quantum states that cannot be decomposed into a product of each individual particle's state in the system [1]. This can be understood if one considers that, provided a past/present shared location in spacetime, the vector spaces, more specifically Hilbert spaces, associated with each particle must be treated as a new, unified space that encompasses linear (nonlocal) superpositions. It is precisely this extension to regular tensor product states that gives rise to new physics. The inherent non-locality associated with such entangled states oftentimes leads to paradoxical outcomes and is fundamentally incompatible with postulations rooted in classical physics. While the argument could be made that this should come as no surprise, our reality *is* indeed founded in quantum mechanics after all, there can be no denying that the way in which we utilize these resources and the new information we gain from doing so is of fundamental scientific importance. To substantiate the difference between classical and quantum correlations and why indeed the experiments proposed fundamentally rely on quantum entanglement, we can highlight several pieces of work over the past decades that underline the advantages gained [2, 3, 4]. In essence, beyond the fact that quantum correlations have been shown to be stronger than their classical counterparts, the primary distinguishing factor is that quantum mechanical entanglement can be entirely basis independent, in contrast to classical correlations which are very much restricted to a singular basis.

Entangled states can be generated in a variety of different systems, ranging from fundamental particles such as photons and electrons, to macroscopic objects composed of millions of atoms like mechanical resonators [5, 6, 7, 8, 9]. Regardless of the underlying approach, the shared notion of decoherence through interaction with the environment persists. The negative association with decoherence ultimately stems from the fact that it is taken to be somewhat synonymous with "*loss of information*," though it must not necessarily be so. Obviously within the context of

specific quantum technologies (e.g. computation/communication) decoherence is indeed the black sheep, leading to the conception of elaborate techniques for mitigating any coupling to the black hole that is the environment. In stark contrast, if one is specifically interested in studying what surrounds us, one can take a more '*how I learned to stop worrying and love the...*' approach. This is precisely the role that quantum metrology/spectroscopy is aiming to exploit. Thus, instead of forcing lavish quantum states to lead a solitary life, the goal is to figure out how the interactions can be made strong enough such that the observed changes in the probe state provide us with new information about the system we want to study. At the end of the day, if there exists some method to extract the global evolution of a quantum state, it becomes possible to not only investigate system-intrinsic structures, but also the potential decoherence pathways that are accessible to the system itself.

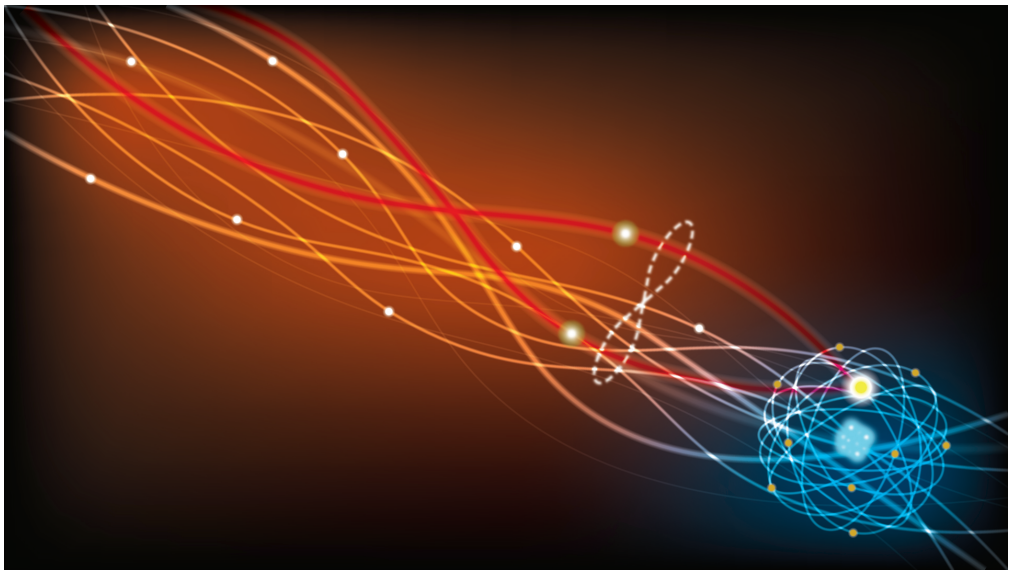

Figure 1.1: Artistic interpretation of an atomic, two-photon absorption event.

Owing to their underlying simplicity and ubiquity, photons have been the workhorse of scientific measurements ranging from the macroscopic scales all the way down to the nanoscale. Serving as an idealized probe, using which information can be extracted from a system of interest, the study of how to increase the interaction strength between light and matter has been long at the forefront of research in optics/photonics. In particular, nanophotonic approaches have provided a major step forward on this front, whereby the confinement of light to wavelength-scale dimensions together with the use of novel device geometries has propelled us to the point of being on the verge of building medium-to-large-scale quantum computers/simulators [10, 11, 12, 13, 14].

Techniques based on utilizing single photons are also what stimulated progress in quantum optics and spectroscopy over the years. Enabling the interaction and coherent control of quantum systems with individual particles of light where the quantum nature of the field must be taken into account holds great importance in many scientific disciplines, notably the field of nonlinear spectroscopy where the experimentally measured signatures are a result of convolutions of the electric field, and matter time-correlation functions. This inherent connection to the foundational framework set out by quantum optics [15, 16, 17, 18] is what ultimately distinguishes quantum spectroscopy, and the associated new information which can be extracted from complex systems, from the familiar classical spectroscopy techniques as we know them. In particular, the use of entangled photons serves to provide a novel area of research in spectroscopy, as time-energy entanglement can be manipulated so as to enable non-Fourier-conjugate limited temporal and spectral measurement resolutions. This offers a remarkably new tool that has potential advantages ranging from low-photon, high-resolution microscopy [19, 20, 21, 22, 23], the fine control of excited-state distributions [24, 25, 26], superior signal-to-noise ratios in measurements which can surpass the standard quantum limit [27, 28, 29], and efficient two-photon absorption in samples for the systematic study of virtual states and exotic decoherence pathways [30, 31, 32, 33]. Recent progress has also demonstrated that quantum states can be topologically protected and that special topological phases in materials could be accessed through two-photon techniques [34, 35, 36, 37, 38].

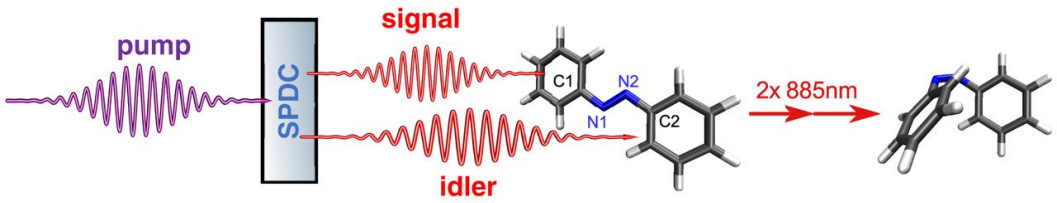

Figure 1.2: Example of an Azobenzene trans → cis isomerization process being initiated by entangled two-photon absorption. [39]

These emerging trends in spectroscopy to explore how entangled light-matter interactions differ from their classical counterparts, and what new practical applications could be derived from the insights gained, is what the research presented in this work is hoping to make progress towards. To test many of the previously described potential new avenues that take advantage of entangled photon states, such as two-photon absorption and sum-frequency processes that scale linearly, requires the instruments that allow for such photonic states to be created, manipulated, interfered, and finally measured. While theoretical research in this field has been very

active in recent years, experimental measurements to verify many of the predictions is still underway. The limited number of experimental results in this exciting field can be partially attributed to the fact that the spectroscopic instruments capable of testing these phenomena are still being actively developed. There are quite significant entrance barriers to making fast progress as a result of the almost exceedingly large parameter space available for exploration. More precisely, what we mean is that in contrast to measurements relying on coherent fields or single photon states to probe systems, entangled photon spectroscopy offers a rich set of variables that can be tweaked. These include considerations pertaining to the linewidths of both the entangled photons as well as the field generating them, the degrees-of-freedom in which entanglement can manifest itself, or the quality of the entanglement itself just to name a few. How each of these variables ultimately affects the entangled light-matter interaction is a question we hope to get closer to answering.

Towards this goal, initial work in our lab has centered around the development of spectroscopy setups which utilize periodically-poled nonlinear materials that generate entangled photons via spontaneous parametric downconversion (SPDC). These instruments are designed to exploit the simultaneous ps-fs scale temporal resolutions and kHz-MHz spectral resolutions at sub-μW level fluxes that are needed to replace classical spectroscopy techniques. With the secondary objective of scaling these systems down and improving their experimental robustness, we have focused on two closely related, yet distinct implementations in parallel. The first of which is a fiber-optic system that is suited for narrowband SPDC, and thus ~ps scale temporal measurements, while at the same time acting as a stop-gap solution between full miniaturization onto an on-chip platform. In contrast, the second setup was built with the intended specification of generating and taking advantage of as broadband of an SPDC spectrum as possible. Given that this requirement is exceedingly challenging to meet in geometries utilizing optical confinement due to the additional difficulty of needing components capable of working over the entire bandwidth, the setup is based on free-space optical elements. However, these free-space gratings suffer from several issues, ranging from unwieldy experimental footprints and stringent optical alignment demands, to difficult-to-control output mode profiles as will be described in this body of work. These problems are compounded as the downconverted output flux and bandwidth are increased. Ultimately, implementations residing in the nanophotonic domain offer a particularly attractive solution and were therefore pinpointed as the "north-star" of this experimental endeavour. Waveguided entangled photon sources eliminate the issues of severe spatial mode

distributions, while also facilitating on-chip form factors and single-molecule type experiments. The strong spatial confinement of the propagating fields allows single-mode operation (a requisite for high quality interference), vastly smaller footprints, long-term alignment-free operation, and superior down-conversion efficiencies. Not to mention the trivial and unrivaled scalability of photonic circuits. The associated trade-off is that waveguided on-chip approaches carry a significantly higher initial design and fabrication barrier.

This thesis serves to describe progress towards building these optical and photonic setups, ranging from free-space to nanophotonic implementations, that aim to exploit new paradigms in spectroscopy through the use of quantum states of light. In addition, it aims to provide an extensive discussion of theoretical and experimental considerations that are deemed to be crucial from a systems-level perspective. Thus, each chapter is geared to cover a number of topics both in breadth and depth, ranging from fundamentally mathematical elements, to computational simulations, design and modeling, (nano)fabrication, and experimental implementations. Chapter 2 contains an introduction and perspective about entangled light-matter interactions, and specifically entangled photon spectroscopy. We discuss the merits and proposed scientific benefits, as well as how advances in metrology have lead to the requirement of experimental techniques such as this. Chapter 3 outlines some of the more significant theoretical elements set out by quantum spectroscopic measurements, which this thesis heavily leans upon. Chapter 4 describes the design and implementation of a fiber-optic entangled photon interferometer based on a narrowband SPDC source, in conjunction with detailed discussions of experimental methodology and ultimate limitations of the system. Potential solutions for resolving these are outlined here, as well as at the very end of this thesis. Chapter 5 describes the design of broadband SPDC sources and their experimental characterization through the use of free-space entangled photon interferometers, as well as their experimental benefits and drawbacks. Chapter 6 provides a novel method (based on analogous techniques used in previous chapters) of extending the accessible wavelength range in which entangled photons can be generated, through the design and implementation of cavity-enhanced generation of deep-UV continuous-wave radiation. The purpose of this work is to open up the possibility of UV-quantum spectroscopy experiments through the generation of entangled photon pairs using these sources. Chapter 7 is dedicated to the design of entirely nanophotonic implementations of entangled photon interferometers and spectroscopy, containing details about numerical photonic device design and simulation, proposed photonic integrated circuit

architectures, as well as fabrication procedures for novel nanophotonic devices that aim to pave the way towards integration into single-atom/molecule spectroscopy experiments. Chapter 8 discusses a silicon nanophotonics platform for the extension of atomic quantum optics into the telecom-band by utilizing appropriate transitions in ytterbium as the host system. Finally, the conclusion and outlook are dedicated to discussions of near-term improvements and goals as well as future directions.

References

[1] Ryszard Horodecki et al. “Quantum entanglement”. In: *Reviews of modern physics* 81.2 (2009), p. 865.

[2] Adán Cabello. “How much larger quantum correlations are than classical ones”. In: *Physical Review A* 72.1 (2005), p. 012113.

[3] Jin-Shi Xu et al. “Experimental investigation of classical and quantum correlations under decoherence”. In: *Nature communications* 1.1 (2010), pp. 1–6.

[4] J Maziero et al. “Classical and quantum correlations under decoherence”. In: *Physical Review A* 80.4 (2009), p. 044102.

[5] J Robert Johansson et al. “Entangled-state generation and Bell inequality violations in nanomechanical resonators”. In: *Physical Review B* 90.17 (2014), p. 174307.

[6] Jie Song, Yan Xia, and He-Shan Song. “Entangled state generation via adiabatic passage in two distant cavities”. In: *Journal of Physics B: Atomic, Molecular and Optical Physics* 40.23 (2007), p. 4503.

[7] Matthew Neeley et al. “Generation of three-qubit entangled states using superconducting phase qubits”. In: *Nature* 467.7315 (2010), pp. 570–573.

[8] Robert Stockill et al. “Phase-tuned entangled state generation between distant spin qubits”. In: *Physical review letters* 119.1 (2017), p. 010503.

[9] Jun Chen, Xiaoying Li, and Prem Kumar. “Two-photon-state generation via four-wave mixing in optical fibers”. In: *Physical Review A* 72.3 (2005), p. 033801.

[10] Tim Schröder et al. “Quantum nanophotonics in diamond”. In: *JOSA B* 33.4 (2016), B65–B83.

[11] May E Kim et al. “Trapping single atoms on a nanophotonic circuit with configurable tweezer lattices”. In: *Nature communications* 10.1 (2019), pp. 1–8.

[12] Mercedes Gimeno-Segovia et al. “From three-photon Greenberger-Horne-Zeilinger states to ballistic universal quantum computation”. In: *Physical review letters* 115.2 (2015), p. 020502.

[13] Sara Bartolucci et al. “Fusion-based quantum computation”. In: *arXiv preprint arXiv:2101.09310* (2021).

[14] Sara Bartolucci et al. “Creation of entangled photonic states using linear optics”. In: *arXiv preprint arXiv:2106.13825* (2021).

[15] Daniel F Walls and Gerard J Milburn. *Quantum optics*. Springer Science & Business Media, 2007.

[16] Leonard Mandel and Emil Wolf. *Optical coherence and quantum optics*. Cambridge university press, 1995.

[17] Werner Vogel and Dirk-Gunnar Welsch. *Quantum optics*. John Wiley & Sons, 2006.

[18] Igor B Mekhov and Helmut Ritsch. "Quantum optics with ultracold quantum gases: towards the full quantum regime of the light–matter interaction". In: *Journal of Physics B: Atomic, Molecular and Optical Physics* 45.10 (2012), p. 102001.

[19] Malvin C Teich and Bahaa EA Saleh. "Entangled-photon microscopy". In: *Cesk. Cas. Fyz* 47 (1997), pp. 3–8.

[20] Takafumi Ono, Ryo Okamoto, and Shigeki Takeuchi. "An entanglement-enhanced microscope". In: *Nature communications* 4.1 (2013), pp. 1–7.

[21] Oleg Varnavski and Theodore Goodson III. "Two-photon fluorescence microscopy at extremely low excitation intensity: The power of quantum correlations". In: *Journal of the American Chemical Society* 142.30 (2020), pp. 12966–12975.

[22] Ernst Niggli and Marcel Egger. "Applications of multi-photon microscopy in cell physiology". In: *Front Biosci* 9 (2004), pp. 1598–1610.

[23] Sanjit Karmakar, Ronald E Meyers, and Yanhua Shih. "Noninvasive high resolving power entangled photon quantum microscope". In: *Journal of biomedical optics* 20.1 (2015), p. 016008.

[24] Frank Schlawin et al. "Suppression of population transport and control of exciton distributions by entangled photons". In: *Nature communications* 4.1 (2013), pp. 1–7.

[25] Frank Schlawin, Konstantin E Dorfman, and Shaul Mukamel. "Entangled two-photon absorption spectroscopy". In: *Accounts of chemical research* 51.9 (2018), pp. 2207–2214.

[26] Akihito Ishizaki. "Probing excited-state dynamics with quantum entangled photons: Correspondence to coherent multidimensional spectroscopy". In: *The Journal of Chemical Physics* 153.5 (2020), p. 051102.

[27] Tomohisa Nagata et al. "Beating the standard quantum limit with four-entangled photons". In: *Science* 316.5825 (2007), pp. 726–729.

[28] Vittorio Giovannetti, Seth Lloyd, and Lorenzo Maccone. "Quantum-enhanced measurements: beating the standard quantum limit". In: *Science* 306.5700 (2004), pp. 1330–1336.

[29] Michael A Taylor et al. "Biological measurement beyond the quantum limit". In: *Nature Photonics* 7.3 (2013), pp. 229–233.

[30] Bahaa EA Saleh et al. "Entangled-photon virtual-state spectroscopy". In: *Physical review letters* 80.16 (1998), p. 3483.

[31] Jan Peřina, Bahaa EA Saleh, Malvin C Teich, et al. "Multiphoton absorption cross section and virtual-state spectroscopy for the entangled n-photon state". In: *Physical Review A* 57.5 (1998), p. 3972.

[32] Jun Kojima and Quang-Viet Nguyen. "Entangled biphoton virtual-state spectroscopy of the A2Σ+–X2Π system of OH". In: *Chemical physics letters* 396.4-6 (2004), pp. 323–328.

[33] Hisaki Oka. "Two-photon absorption by spectrally shaped entangled photons". In: *Physical Review A* 97.3 (2018), p. 033814.

[34] Netanel H Lindner et al. "Topological Floquet spectrum in three dimensions via a two-photon resonance". In: *Physical Review B* 87.23 (2013), p. 235131.

[35] Junpeng Qiao et al. "Two-photon absorption within layered Bi 2 Te 3 topological insulators and the role of nonlinear transmittance therein". In: *Journal of Materials Chemistry C* 7.23 (2019), pp. 7027–7034.

[36] Nikita A Olekhno et al. "Topological edge states of interacting photon pairs emulated in a topolectrical circuit". In: *Nature communications* 11.1 (2020), pp. 1–8.

[37] Andrea Blanco-Redondo et al. "Topological protection of biphoton states". In: *Science* 362.6414 (2018), pp. 568–571.

[38] Yao Wang et al. "Topological protection of two-photon quantum correlation on a photonic chip". In: *Optica* 6.8 (2019), pp. 955–960.

[39] Bing Gu et al. "Photoisomerization transition state manipulation by entangled two-photon absorption". In: *Proceedings of the National Academy of Sciences* 118.47 (2021).

Chapter 2

ENTANGLED LIGHT-MATTER INTERACTIONS AND SPECTROSCOPY

Adapted from: Szilard Szoke et al. "Entangled light–matter interactions and spectroscopy". In: *Journal of Materials Chemistry C* 8.31 (2020), pp. 10732–10741.

2.1 Hong-Ou-Mandel Interference and Biphotons

To better understand entangled photon light-matter interactions, it is insightful to first look at the fundamentals of Hong-Ou-Mandel (HOM) interference [1]. The HOM effect serves as the basis for most entangled spectroscopy methods. In general, one pump photon is down-converted to create two lower energy daughter photons through spontaneous parametric down-conversion (SPDC). The daughter photons are collectively termed a *biphoton*. After temporal and polarization compensation in one arm, the two photons are made to meet and interfere at a 50:50 beamsplitter. Two single photon avalanche detectors (SPADs) then measure whether the photons leave opposite or same sides of the beamsplitter. Classically, there are four possible outcomes of transmission (**T**) and reflection (**R**) for the two photons, as depicted in Fig.2.1(a): **RR**, **TT**, **RT**, **TR**. The indistinguishable character of the biphoton leads to the amplitudes of **TT** and **RR** destructively interfering in the entangled case [1], leaving the only measurable outcome of both photons leaving the same side of the beamsplitter. If the time delay or relative polarization between the photons is changed, or any other modification occurs to the biphoton pair, the interference will decrease. The width and amplitude of the interference dip therefore carries a signature of the light-matter interaction that the entangled photons have witnessed [2]. Measuring these variations in the interference dip enable the possibility for spectroscopy. As an example, Fig.2.1(b) & 2.1(c) show the modulation of the interference dip when absorption is introduced in one arm of the HOM interferometer [3].

For a full mathematical derivation of the HOM dip, please refer to Ch. 3 or Ref. [4]. Briefly, the interference dip is explained mathematically as follows. Beamsplitter operators are first defined which give a unitary transformation of an input state in

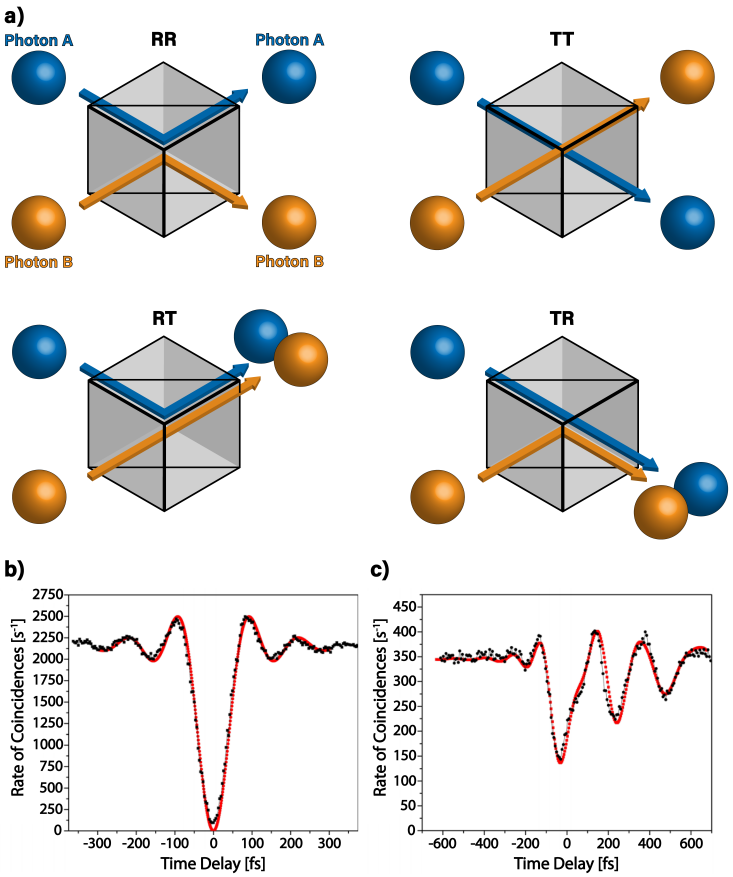

Figure 2.1: Hong-Ou-Mandel interference with photons. (a) Depiction of the four possible outcomes when two photons interact at a beamsplitter. When two entangled photons are present, the TT and RR outcomes cancel, and both photons leave the same side of the beam splitter. (b) This nonclassical interference leads to a dip in the coincidence counts. (c) HOM dip modulation due to a Nd:YAG crystal being placed in one arm of the HOM interferometer causing an entangled photon to interact with a sample with resonant states before the beam splitter. The excited state polarization is imprinted on the interference. Experimental results adapted from Ref. [1].

ports a/b to the output in ports c/d.

$$\hat{a}^\dagger \xrightarrow{\hat{B}_a} \frac{1}{\sqrt{2}}\left(\hat{c}^\dagger + i\hat{d}^\dagger\right) \tag{2.1}$$

$$\hat{b}^\dagger \xrightarrow{\hat{B}_b} \frac{1}{\sqrt{2}}\left(i\hat{c}^\dagger + \hat{d}^\dagger\right) \tag{2.2}$$

$$\hat{B}_a \left|1\right\rangle_a = \hat{B}_a\hat{a}^\dagger \left|0\right\rangle_a = \frac{1}{\sqrt{2}}\left(\left|1\right\rangle_c \left|0\right\rangle_d + i\left|0\right\rangle_c \left|1\right\rangle_d\right) \tag{2.3}$$

$$\hat{B}_b \left|1\right\rangle_b = \hat{B}_b\hat{b}^\dagger \left|0\right\rangle_b = \frac{1}{\sqrt{2}}\left(i\left|1\right\rangle_c \left|0\right\rangle_d + \left|0\right\rangle_c \left|1\right\rangle_d\right) \tag{2.4}$$

with $a^\dagger$, $b^\dagger$, $c^\dagger$, and $d^\dagger$ being the creation operators for the photons in ports a, b, c, and d, respectively, acting on the vacuum state $|0\rangle$. It is important to note that the beamsplitter operator for reflection introduces a $\pi/2$ phase shift in the photon's output state. Next, assume a pair of entangled photons, each of which is described as a Fock state, is introduced into both input ports a and b:

$$\begin{aligned}\hat{B}_a\hat{B}_b\,|1\rangle_a\,|1\rangle_b &= \frac{1}{2}\left(\hat{c}^\dagger + i\hat{d}^\dagger\right)\left(i\hat{c}^\dagger + \hat{d}^\dagger\right)\\ &= \frac{1}{2}\left(i\hat{c}^{\dagger 2} + \hat{c}^\dagger\hat{d}^\dagger - \hat{d}^\dagger\hat{c}^\dagger + i\hat{d}^{\dagger 2}\right).\end{aligned} \tag{2.5}$$

The phase shift leads to the commutator between the two photons in Eq.2.5. Given that the photons are indistinguishable, the commutation relation for the creation operators equals zero,

$$\left[\hat{c}^\dagger, \hat{d}^\dagger\right] = \left[\hat{c}^\dagger\hat{d}^\dagger - \hat{d}^\dagger\hat{c}^\dagger\right] = 0 \tag{2.6}$$

and the only terms left are the **RT** and **TR** terms such that both photons must leave the same side resulting in a $N00N$ state as the output:

$$\frac{1}{2}\left(i\hat{c}^{\dagger 2} + i\hat{d}^{\dagger 2}\right)|0\rangle_c\,|0\rangle_d = \frac{i}{\sqrt{2}}\left(|2\rangle_c\,|0\rangle_d + |0\rangle_c\,|2\rangle_d\right). \tag{2.7}$$

Consequently, only one of the two photon counting detectors will register a detection event. This results in the characteristic interference dip in the coincidence counting scheme (Fig.2.1(b)). Entangled photon spectroscopy can therefore be thought of as a measure of how light-matter interactions modify the commutator in Eq.2.5.

Before discussing the practical applications of SPDC, a few technical points should be clarified. First, HOM interference should be more correctly viewed as 'biphoton interference' since it relies on the indistinguishability of the two bosons as well as the underlying entanglement between them. Second, an HOM interference for a two-photon entangled state is only possible if the entangled biphoton wavepacket has a symmetric spectrum about the frequency degenerate diagonal, irrespective of whether the two photons are frequency degenerate or non-degenerate. Without this condition being met, the interference vanishes, and the beamsplitter becomes transparent with respect to the two input photons. In the case of two independent single-photon wavepackets, the condition for HOM interference indeed becomes that the two single-photon wavepackets must be identical. In practice, this means that care must be taken how the two-photon states to be used are generated and how the two independent beam paths are optically treated [2].

2.2 Generation and Detection of Entangled Photons

The two down-converted photons from SPDC display strong correlations in time, energy, and momentum due to the parametric mixing process. The time and energy correlations originate from the individual photons being generated simultaneously with energies that must sum to that of the pump photon. The momentum correlation is dictated by the phase matching condition. Energy-time entangled states can be viewed as the most general type of entangled states. Hyper-entangled photon states, e.g. entangled both in energy-time and in polarization, can lead to significant improvements in the experimental measurement statistics and the robustness of the spectroscopic setup [5, 6].

The simplest experimental approach to SPDC is using birefringent phase matching (BPM) in a χ^2 nonlinear crystal such as β-barium borate or lithium triborate [7, 8]. Generation rates of $\sim 10^3 - 10^4$ counts/s/mW are achieved with pump powers of a few tens of mW. Given that SPADs generally saturate at around $10^6 - 10^7$ counts/s, this generation rate is sufficient for coincidence counting experiments with most pulsed laser systems. However, due to the strict phase matching condition, the generated entangled photons have a narrow bandwidth. Other issues include cross-polarized pump/daughter photon combinations in Type-I and Type-II down-conversion, beam walk-off issues due to birefringence, a limited wavelength mixing range, and reliance on weaker nonlinear tensor elements.

Quasi-phase matching (QPM) can generate broadband entangled photons more efficiently for spectroscopic applications. In this approach, a spatially periodic modulation of a ferroelectric nonlinear material is used to rectify the phase-mismatch of the three-wave mixing process, as illustrated in Fig.2.2(a). This is achieved by using the additional momentum contribution from the crystal periodicity in the overall phase matching [9, 10]. The QPM approach makes it possible to take advantage of stronger elements of the nonlinear tensor, as well as to implement Type-0 phase-matching whereby all three waves are co-polarized [11]. The down-converted photon flux can be as high as 10^9 pairs/s/mW of the pump power by spatially confining the pump in chip-integrated photonic waveguides [12]. A particularly salient feature of QPM is that, since the crystal period can be arbitrarily chosen, it can be used to phase-match any desirable wavelength combinations. Further, by utilizing a longitudinally varying period, a collection of phase matching conditions can be used to create broadband SPDC fluxes [13, 14, 15, 16]. Temperature controlled lithium niobate, lithium tantalate, and potassium titanyl phosphate are generally used given that they

are transparent from the UV to mid-infrared wavelengths [17, 18].

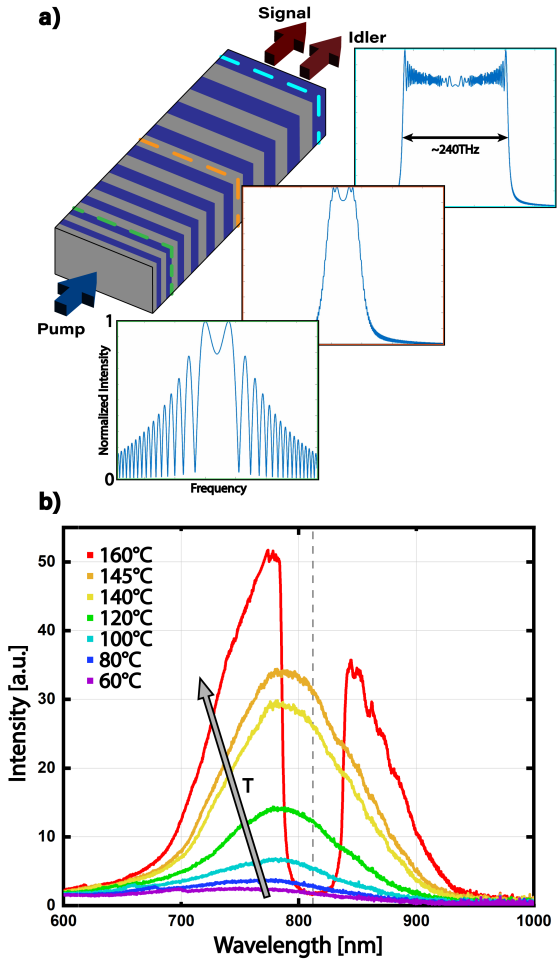

Figure 2.2: (a) Cartoon of a periodically poled waveguide with linear chirp, where purple and gray represent domains of opposing poling. Insets show the simulated downconversion spectrum at three points along the lithium tantalate waveguide; (green)-start, (orange)-center, (cyan)-end. The effect of the chirp is to broaden the output to a bandwidth of ~240THz (~510nm). (b) Experimental spectra of a periodically poled lithium tantalate grating where the working temperature of the crystal is tuned.

Quasi-phase matching allows for two important advantages in spectroscopy. First, a sufficiently broadband flux of entangled photons can be used to increase average power levels without saturating the single photon per mode limit. As measured in our lab and others, almost μW fluxes of entangled photons spanning more than 500 nm can be created using QPM gratings [19]. The broad bandwidth allows for pulse-shaping and few-femtosecond resolutions. Second, the enhanced power levels allow spectrally and temporally resolved detection in reasonable time frames. In practice, this means that even microwatts of pump power would be enough to saturate a SPAD,

suggesting that ultrafast entangled photon spectroscopy can be driven by a diode laser instead of expensive femtosecond laser amplifiers. Chip-integrated entangled photons are also easily fiber coupled. This provides alignment-free daily operations and an easy way to control and maintain the properties of entangled photons, such as spatial profile, over a broad bandwidth.

Multiplexed photon counting schemes are another area that is allowing growth in entangled spectroscopy. Both em-CCDs and SPAD arrays are coming to maturity, allowing spectral multiplexing of the photon counting process [20, 21, 22, 23]. With a broadband, higher flux source, even a simple USB spectrometer can be used to measure spectral changes. Higher fluxes also allow phase-sensitive HOM techniques to be used which measure both 2^{nd} and 3^{rd} order correlations [24]. The difference between an HOM interferometer and a phase-unlocked HOM interferometer is similar to the difference between an autocorrelator and a frequency resolved optical gating (FROG) setup in ultrafast optics – the former only measures the intensity autocorrelation while the latter contains additional phase information.

2.3 Spectroscopy with One Entangled Photon

One class of entangled photon spectroscopy utilizes the non-local nature of the entanglement. The general idea is that the interaction between the sample and one photon in the entangled pair can be revealed by measuring its entangled partner, even when it does not interact with the sample directly. Experimentally, one-photon interaction can be introduced by placing a sample in one arm of the HOM interferometer shown in Fig.2.3. The sample imparts phase and amplitude changes on the entangled photon it interacts with, which affects the biphoton indistinguishability and modulates the HOM dip [3].

While it seems trivial to measure absorption profiles with entangled photon interference, the technique allows spectroscopy and microscopy at one wavelength using vastly different wavelengths [25, 26, 27]. Spectroscopic signatures, such as absorption spectra are reconstructed by monitoring the changes to the coincidence counts when a sample is inserted into the signal arm of the HOM interferometer and resolving the wavelength of the idler arm [28, 29, 30]. For example, if the SPDC process creates an entangled IR and visible photon pair, the absorption of the photon at the IR wavelength can be inferred by measuring its visible partner [31]. This particular case has been demonstrated in CO_2 as shown in Fig.2.3 [25]. This effect is predicted to work for any range of experiments, such as X-Ray [32, 33], THz, and

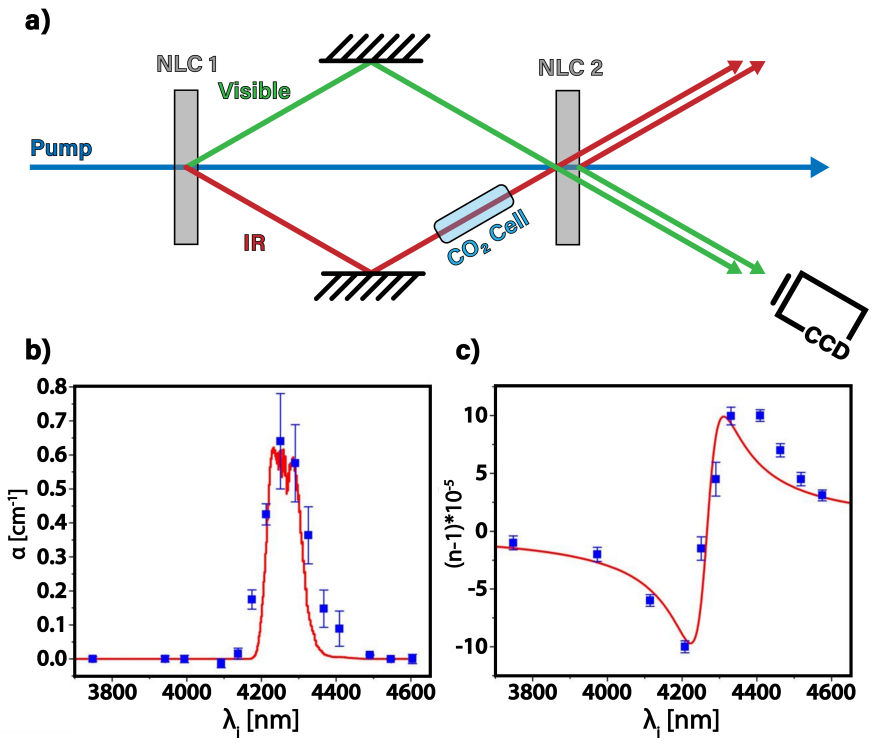

Figure 2.3: Measuring infrared absorption with visible photons. (a), Experimental layout. Entangled infrared (IR) and visible photons are generated through SPDC on the first nonlinear crystal (NLC1). A CO_2 cell is placed in the IR path to introduced absorption. The IR and visible photons cross at the second nonlinear crystal (NLC2) and interfere with the SPDC photons from NLC2. The interference pattern for the visible photons, which do not interact with the CO_2 are recorded. (b), IR absorption spectrum extracted from visible interference measurement. (c) refractive index near the CO_2 resonance. Adapted from Ref. [22].

electron spectroscopies, although practical limitations arise from generating such ultra-broadband SPDC sources.

Entangled one photon spectroscopy has been applied to applications ranging from remote sensing to ghost imaging. For example, quantum ghost imaging relies on the coherence between the down-converted beams to record the image of an object with photons that do not interact with it directly [27, 34, 35, 36, 37, 38, 39, 40]. Quantum optical coherence tomography (QOCT) offers improved resolution and sensitivity by exploiting the dispersion cancelling properties of the entangled wavepacket, as well as the anticorrelation between entangled pairs, to construct quantum interference patterns corresponding to sample depth [41, 42, 43]. Entangled photons can also increase measurement sensitivities as compared with classical photons. The standard quantum limit for noise scales as $1/\sqrt{N}$, where N is the number of measurements.

Using entangled photons, this improves to $1/N$ [44]. A prototypical example is using $N00N$ states to enhance the measurement precision of the phase shift in an interferometer [45, 46]. Sub-shot-noise imaging of weak absorbing objects has also been achieved [47].

2.4 Spectroscopy with Two or More Entangled Photons

Multiphoton entangled experiments are performed by replacing the beamsplitter in an HOM interferometer so that both entangled photons interact with a sample. Whereas many one-photon entangled interactions can be reproduced with shaped classical light, the interactions of two or more entangled photons with a sample lead to non-classical processes [48, 49, 50]. These interactions arise directly from the two-photon indistinguishability. Overly generalized, when the sample interacts with the biphoton pair, its response is as if only one photon is incident with the sum of their energy. Before being spatially and temporally overlapped, the two entangled photons propagate in the material as if separate photons.

The two-photon interaction can therefore be modulated by time-delaying or shaping one side of the HOM interferometer. This allows for the measurement of excited state polarizations as well as populations. For example, multidimensional spectroscopy can be recreated by using three or more entangled photons or pulse shaping the entangled photons [48, 51, 52]. Compared to conventional multidimensional spectroscopy, entangled multidimensional spectroscopy is predicted to suppress the uncorrelated background levels and enhance the sensitivity to electronic couplings, manifested as off-diagonal cross-peaks in the 2D spectra, Fig.2.4.

There are other distinct differences between nonlinear entangled and classical spectroscopy. First, the two entangled photons are predicted to act as one only if their coherence/entanglement time, represented by the width of the HOM dip, is shorter than the decoherence of the excited state being measured. The coherence/entanglement time can therefore be used to alter and control the nonlinear process, allowing another route to multidimensional spectroscopy [53]. The measured spectrum is again more sensitive to electronic coupling than in the classical case. Second, temporal dynamics in entangled photon experiments are measured via the correlations between the two entangled photons. Unlike pump-probe spectroscopy, the temporal dynamics are not inferred from the sample's impulse response to a multiphoton pump pulse. Third, the entangled photons can measure whether an excited state superposition they excite in a qubit preserves their entanglement. Entangled photon

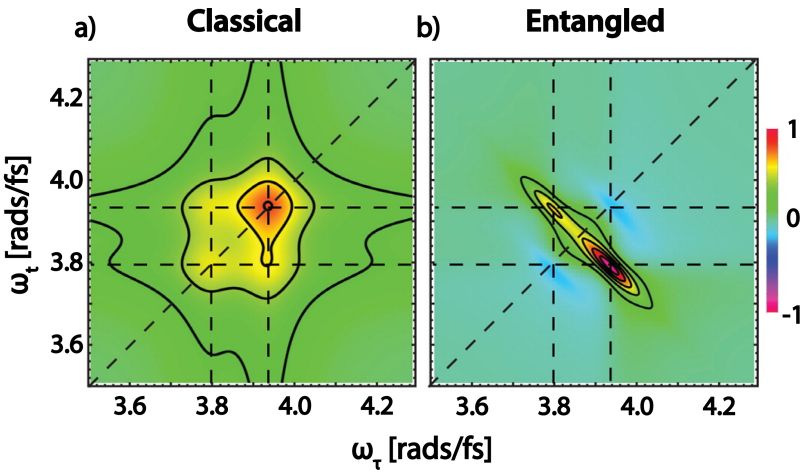

Figure 2.4: Simulated two-dimensional fluorescence spectra for electronically coupled molecular dimer with (a), classical light sources, and (b), entangled photon pairs. Multidimensional spectroscopy with entangled photons has improved sensitivity to the dimer conformation. Adapted from Ref. [45].

interactions are therefore predicted to be sensitive probes for many-body dynamics and collective states [54, 55, 56].

Entangled photon spectroscopy also has the potential to measure ultrafast dynamics with higher spectral resolution than a classical approach. For entangled photon spectroscopy, the energy resolution is given by the down-converted pump source's linewidth. This is because the frequency-frequency photon distribution created by SPDC is correlated to the down-converted center frequency as shown in Fig.2.5 [57]. This is compared with the Gaussian distribution commonly associated with a laser, in which any two photons can interact (Fig.2.5(a) compared to Fig.2.5(b)). In an entangled interaction, only the frequency symmetric pair will interact, post-selecting the photons along the frequency diagonal. All entangled photon interactions therefore add up to within the pump linewidth of the original pump laser source for the SPDC, and the frequency resolution is decoupled from the temporal resolution (Fig.2.5(c) compared to Fig.2.5(d)). Broadband entangled two-photon absorption in rubidium has already demonstrated a 3 to 5 orders of magnitude improvement on

spectral and temporal resolution.86 It has also been suggested that the creation of only conjugate electric fields optimizes the otherwise nonlinear interaction.

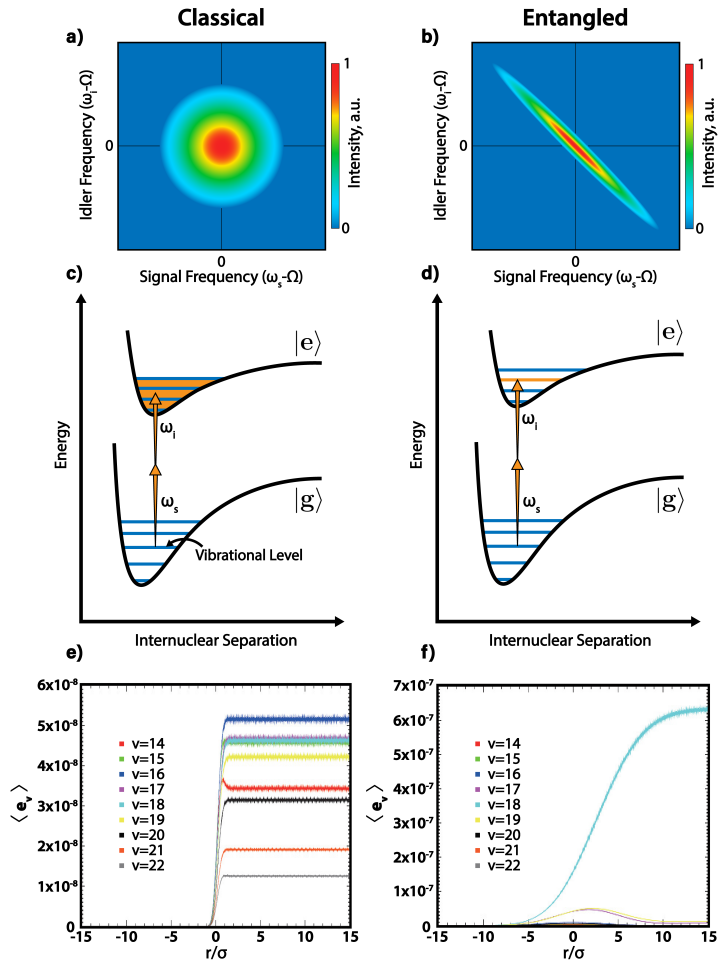

Figure 2.5: Spectral resolution in entangled two-photon spectroscopy. (a), Gaussian frequency distribution for uncorrelated photons as common from a classical laser. (b), frequency anti-correlation for entangled photon pairs from SPDC. (c), The classical frequency distribution means that any combination of photons can excite the sample. A pulsed laser therefore excites an ensemble of vibrational states as predicted in (e). (d), The entangled photon frequency distribution means that transitions only occur that add up to the pump source's linewidth. Selective excitation of a single vibronic level therefore is predicted to occur independent of the SPDC bandwidth and temporal resolution (f). (e), excited states population with pulsed laser excitation, where multiple vibronic levels are populated. Theoretical data (e) and (f) adapted from Ref. [57].

The temporal resolution of the entangled experiment is still proportional to the spectral width the bandwidth of the down-converted photons. The width of the HOM dip can therefore be changed by modulating the relative time delay of the

different frequencies using a pulse shaper [58]. Combining pulse-shaping and entangled photons is predicted to allow non-classical population distribution and novel photochemistry processes [58, 59, 60, 61]. The decoupled temporal and spectral resolution has been predicted to create narrow bandwidth excited state populations from femtosecond bandwidths as shown in Fig.2.5(e) compared to Fig.2.5(f). Simulation also suggests that under entangled two-photon excitation, the intermediate single-exciton transport in the bacterial reaction center of Blastocholoris viridis can be suppressed and non-classical control of two-exciton states can be achieved [59].

2.5 Current Directions in Entangled Light-Matter Interactions

Several intriguing directions exist in exploring entangled light-matter interactions. One entangled photon interactions suggest that material and molecular interactions can modulate the probability of measuring a second, non-interacting photon. The role this could have in transmuting material and chemical changes, as well as in processes like energy transfer, leave many open questions. Perhaps most intriguing are interactions with two or more entangled photon interactions. Oversimplified, when two entangled photons are incident on a sample, they can appear as one photon with their summed energy. Nonlinear, multiphoton interactions up to N photons are therefore predicted to scale linearly [62]. The linearity of two photon entangled process was previously measured in sodium and cesium [63, 64] and has now been repeated in some molecular and solid-state systems (Fig.2.6) [65, 66, 63, 67, 68, 69]. Similar to the beamsplitter in the HOM interferometer, the strong amplitude and phase correlation [70] within the entangled photon pair of SPDC suppresses higher order interaction terms [58]. While the entangled two-photon intensity scaling can be understood, the cross section of the process raises many questions. The entangled photon cross sections measured to date in molecular systems fall within the $10^{-17}-10^{-18} cm^2$ range [66]. This cross section is closer to that of a single photon absorption event, $10^{-16} cm^2$, and orders of magnitude larger than that of a classical two-photon absorption event, $10^{-47} cm^4 s$. Why the entangled two photon absorption cross section does not match the classical one photon cross section, despite both processes being linear, is an open question. The entangled two-photon absorption cross section also does not appear to follow classical two-photon absorption rules in organic porphyrin dendrimers [66].

In practice, the entangled two photon absorption will compete with the semiclassical two photon absorption. Their relative contribution is quantified by the ratio between the entangled absorption rate αI and the uncorrelated two photon absorption rate

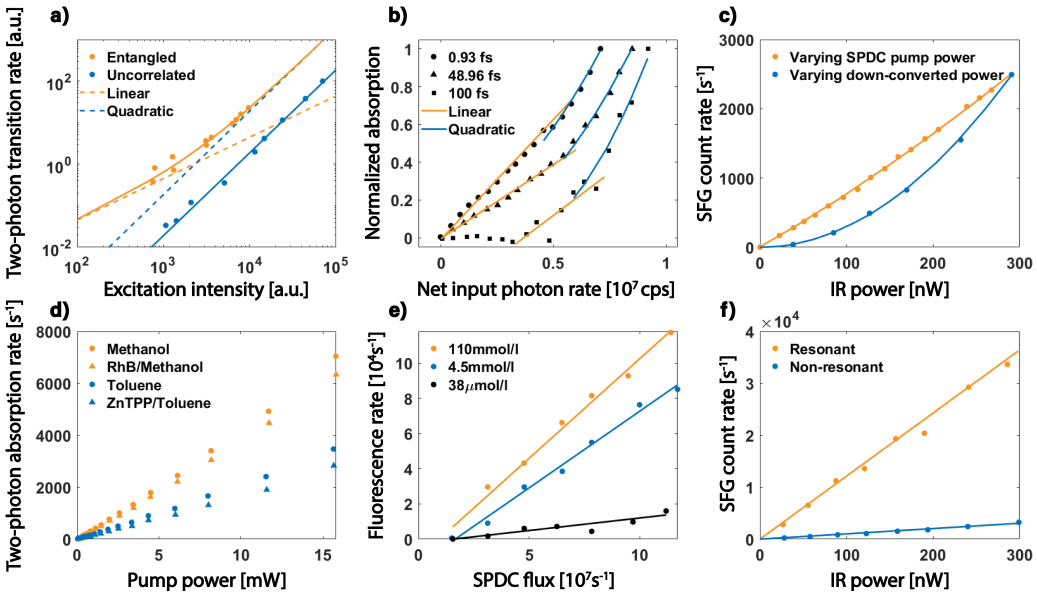

Figure 2.6: The linearity of various entangled two-photon processes as a function of power. (a), two-photon transition rate in trapped cesium with entangled and coherent light. Transition rate for uncorrelated coherent excitation is reduced by a factor of 10 for comparison. (b), power dependence of ETPA rate in porphyrin dendrimer under 3 different entanglement times. (c), power dependence of sum-frequency generation with entangled photons. (d), ETPA rate for RhB and ZnTPP in solvent. (e), ETPA-induced fluorescence rate for Rh6G in ethanol under different concentration. (f), resonantly enhanced sum-frequency generation with entangled photons. Data presented are adapted from Ref. [65, 66, 63, 67, 71, 72].

βI^2, where α and β are associated cross sections. An entangled process is more efficient ($I < \alpha/\beta$) for fluxes lower than a GW for currently measured cross sections. The ratio can also be used to see that, for example, a one μW entangled photon flux has the same excitation rate as a million times more powerful classical laser. When calculating these ratios, it is important to include the conversion from W to photons/s through the ratio of 1 J = 6.242×10^{18} eV for βI^2. This must be done to cancel the $cm^4 s$ units when going to photons/s.

To study ultrafast material dynamics, an important factor in entangled two photon absorption is the coherence (entanglement time) relative to the decoherence of the excited state. Studies on several diatomic molecules and organic porphyrin den-

drimers have suggested that transitions involving virtual states respond to entangled two-photon excitations at a different timescale than transitions involving other mechanisms, such as excited state charge transfer [66, 73]. The entangled two-photon absorption cross section may therefore vary drastically between different transitions, exhibiting nonmonotonic dependence on the entanglement time, even if two systems classical cross sections are similar.

However, few experimental systems have been measured to date to confirm these rules. Measurements have yet to be repeated in condensed matter, low dimensional, or other common molecules – leaving many open questions as to how two or more photon entangled interactions can be optimized. The primary questions can be summarized as: 1) How do intermediate states control the entangled photon interaction, 2) what structural motifs can increase or decrease the strength of the entangled photon interaction, and 3), how does excited state coupling with spins, vibrations, and electrons preserve or decrease the entangled light-matter interactions? Other open questions, such as how selection rules are modified by polarization entangled photons and how photonic enhancement techniques will modify the interactions [74, 75, 76, 77, 78, 79, 80, 81, 82], promise for intriguing expansions to existing fields.

Controlling the entangled multiphoton interactions has practical as well as fundamental motivation. Entangled two-photon processes can occur at the same rate as a pulsed-laser-induced two-photon excitations but at over a million times lower fluxes, accounting for the intensity scaling between quadratic and linear processes. If the material and molecular design parameters can be optimized, optoelectronic and biomedical applications using two photon processes could be driven by a CW laser diode instead of a pulsed laser. Theory has also shown that due to the linear scaling, the spectrally overlapped simulated Raman scattering and two-photon absorption can be separated and selectively excited by tuning the entanglement properties of the pump [83]. For imaging applications, entangled two-photon fluorescence is suitable for in-depth imaging of photosensitive tissues at low flux. The linear scaling and enhanced cross section are predicted to occur for N-photon interactions, potentially bringing linearization to a family of nonlinear optical techniques [62]. Entangled multiphoton interactions have also been predicted to increase resonance energy transfer by several orders of magnitude [84] – and it can be extrapolated that the entangled effects will extend to most applications of multiphoton processes.

2.6 New Opportunities in Materials Science

The key distinction of entangled photon excitation, aside from the linearization of nonlinear processes, is that the entangled photons can be made to show quantum correlations in multiple variables (polarization, energy, OAM, etc) [85]. By interfering these entangled states of light with the quantum correlated excitations of a material, new properties and applications are to be expected [86]. Or, it may be possible to dynamically form correlations between two independent excitations that are not regularly present [87, 88, 89, 90, 91]. This key difference may lead to new insights in spectroscopy, but perhaps more excitingly, new degrees of control in quantum materials. In this section, we outline a few potential directions that entangled-light matter interactions could have an immediate benefit in.

First and foremost, the study and understanding of entangled light matter interactions could become critical in the age of quantum computing and information systems [92, 93]. How the entangled photon correlations are modified, favorably or not, by material elements is key for coupling qubit systems together as well as for investigating the types of control schemes that could be applicable to complex quantum systems [94]. Perhaps even more fundamentally, entanglement is suggested to be at the heart of quantum materials, which display strong electronic and nucleon correlations [95]. The inclusion of correlations in any Hamiltonian is the key to describing complex phenomena and for accurate calculations [96]. Many such Hamiltonians are also proposed to include entanglement, such as singlet-triplet scattering [97]. While the Fermi liquid theory and the Hubbard model have been used with great success, the direct experimental measurement of these strong interactions remains a difficult challenge [98, 99, 100]. The change in entangled photon correlations interacting with such systems may prove key, complementing approaches like ultracold atoms in optical lattices [101] and second quanta scans in multidimensional spectroscopy [102].

The ability of entangled photons to perform nonlinear optics with low power CW lasers should also prove transformative for photonics and electro-optical devices. Common components such as frequency mixers, saturable absorbers, or phase shifters can operate without a pulsed laser input, while wide band gap materials can be interacted with via photons at half the band gap energy. Additional functionality can be implemented in such devices relying on the preservation or change of the entangled photon correlations. An experiment that demonstrates this concept is to create polarization entangled biphoton states and couple one of the photons

into a plasmonic metamaterial [103]. The coupled polarization state is determined and modulated by detecting the polarization of its partner. By altering the coupled polarization non-locally, the plasmonic device could in principle operate from perfect absorption to full transmission. The general idea of manipulating the material's functions non-locally via entanglement could lead to multifunctional integrated devices such as quantum logic gates, but also has fundamental advantages in processes like resonant energy transfer [84, 104].

An important goal in materials science is the on-demand manipulation of electrons in solids via the application of external stimuli [105]. The coupling of the entangled photon pair's quantum correlations to strongly correlated materials could result in novel, exotic responses. One example would be in the field of valleytronics [106, 107]. In two-dimensional semiconductors such as MoS_2, distinct valleys can be populated under a resonant excitation by circularly polarized light [106]. The circularly polarized excitation photon can be replaced by an entangled photon pair. More precisely, a cross-polarized pair could be generated via type-II down-conversion, after which the biphoton is split into its orthogonal polarization modes via a polarizing beamsplitter. A subsequent change in basis to circular polarization can be achieved by a pair of quarter-waveplates in both arms of the HOM type setup. The entangled photon energies could be set to select one or both valley excitations. The superposition between the spin state and the entangled photons would allow measurements of spin decoherence and coupling between the valleys. A similar idea could be used to test the ability of topological insulators to maintain spin correlations relative to photonic correlations.

Entangled photons could also find applications in material fabrication and lithography. Proposed techniques such as quantum photolithography aim to utilize entangled photons prepared in a $N00N$ state to overcome the diffraction limit by a factor of $1/N$, alleviating the need to go to shorter UV wavelengths [108]. The enhanced cross-section for entangled multiphoton absorption could allow simplified photolithography and growth schemes, techniques that use below band gap light for patterning, or even additional degrees of freedom by using two or more entangled states. The microscopic chemical processes that govern photopolymerization or photocatalytic growth processes might similarly be tuned by entanglement.

2.7 Conclusion and Outlook

While much work has gone into exploring entangled photons for quantum information and computational applications, the basics of entangled light-matter interactions and the potential applications in chemistry and material science are largely unexplored. In general, the field is advancing rapidly on the theoretical front, but most experimental questions remain open. How materials and molecular design can control entangled two-photon interactions remains unknown, let alone how these interactions can be used in novel applications. Given the relative ease in high-flux entangled photon generation, simplicity in the optical schemes, and the various potential advantages of using non-classical light, we foresee entangled light-matter interactions being a rapidly growing field in the near future.

References

[1] Chong-Ki Hong, Zhe-Yu Ou, and Leonard Mandel. “Measurement of subpicosecond time intervals between two photons by interference”. In: *Physical review letters* 59.18 (1987), p. 2044.

[2] Ilaria Gianani. “Robust spectral phase reconstruction of time-frequency entangled bi-photon states”. In: *Physical Review Research* 1.3 (2019), p. 033165.

[3] Dmitry A Kalashnikov et al. “Time-resolved spectroscopy with entangled photons”. In: *arXiv preprint arXiv:1611.02415* (2016).

[4] Marlan O Scully and M Suhail Zubairy. *Quantum optics*. 1999.

[5] Julio T Barreiro et al. “Generation of hyperentangled photon pairs”. In: *Physical review letters* 95.26 (2005), p. 260501.

[6] Paul G Kwiat. “Hyper-entangled states”. In: *Journal of modern optics* 44.11-12 (1997), pp. 2173–2184.

[7] Pavel Trojek et al. “Compact source of polarization-entangled photon pairs”. In: *Optics express* 12.2 (2004), pp. 276–281.

[8] Jürgen Volz, Christian Kurtsiefer, and Harald Weinfurter. “Compact all-solid-state source of polarization-entangled photon pairs”. In: *Applied Physics Letters* 79.6 (2001), pp. 869–871.

[9] Raymond Reinisch and DB Ostrowsky. *Guided Wave Nonlinear Optics*. Kluwer Academic Publishers, 1992.

[10] JA Armstrong et al. “Interactions between light waves in a nonlinear dielectric”. In: *Physical review* 127.6 (1962), p. 1918.

[11] Robert L Byer. “Quasi-phasematched nonlinear interactions and devices”. In: *Journal of Nonlinear Optical Physics & Materials* 6.04 (1997), pp. 549–592.

[12] Andreas Jechow, Axel Heuer, and Ralf Menzel. “High brightness, tunable biphoton source at 976 nm for quantum spectroscopy”. In: *Optics express* 16.17 (2008), pp. 13439–13449.

[13] S Sensarn, GY Yin, and SE Harris. “Generation and compression of chirped biphotons”. In: *Physical review letters* 104.25 (2010), p. 253602.

[14] Stephen E Harris and Steven Sensarn. “Toward single-cycle biphotons”. In: *Conference on Coherence and Quantum Optics*. Optical Society of America. 2007, p. CMD1.

[15] SE Harris. “Chirp and compress: toward single-cycle biphotons”. In: *Physical review letters* 98.6 (2007), p. 063602.

[16] S Carrasco, JP Torres, and L Torner. "A. Sergienko, BEA Saleh, and MC Teich "Enhancing the axial resolution of quantum optical coherence tomography by aperiodic quasi-phase-matching"". In: *Optics Letters* 29 (2004), pp. 2429–2431.

[17] David S Hum and Martin M Fejer. "Quasi-phasematching". In: *Comptes Rendus Physique* 8.2 (2007), pp. 180–198.

[18] Roberto de J León-Montiel et al. "Temperature-controlled entangled-photon absorption spectroscopy". In: *Physical review letters* 123.2 (2019), p. 023601.

[19] Magued B Nasr et al. "Ultrabroadband biphotons generated via chirped quasi-phase-matched optical parametric down-conversion". In: *Physical review letters* 100.18 (2008), p. 183601.

[20] Gur Lubin et al. "Quantum correlation measurement with single photon avalanche diode arrays". In: *Optics express* 27.23 (2019), pp. 32863–32882.

[21] Matthew Reichert, Hugo Defienne, and Jason W Fleischer. "Massively parallel coincidence counting of high-dimensional entangled states". In: *Scientific reports* 8.1 (2018), pp. 1–7.

[22] Paul-Antoine Moreau et al. "Realization of the purely spatial Einstein-Podolsky-Rosen paradox in full-field images of spontaneous parametric down-conversion". In: *Physical Review A* 86.1 (2012), p. 010101.

[23] Matthew P Edgar et al. "Imaging high-dimensional spatial entanglement with a camera". In: *Nature communications* 3.1 (2012), pp. 1–6.

[24] Ayman F Abouraddy, Timothy M Yarnall, and Giovanni Di Giuseppe. "Phase-unlocked Hong-Ou-Mandel interferometry". In: *Physical Review A* 87.6 (2013), p. 062106.

[25] Dmitry A Kalashnikov et al. "Infrared spectroscopy with visible light". In: *Nature Photonics* 10.2 (2016), pp. 98–101.

[26] Chiara Lindner et al. "Fourier transform infrared spectroscopy with visible light". In: *Optics express* 28.4 (2020), pp. 4426–4432.

[27] Inna Kviatkovsky et al. "Microscopy with undetected photons in the mid-infrared". In: *Science Advances* 6.42 (2020), eabd0264.

[28] AA Kalachev et al. "Biphoton spectroscopy of YAG: Er3+ crystal". In: *Laser Physics Letters* 4.10 (2007), p. 722.

[29] AA Kalachev et al. "Biphoton spectroscopy in a strongly nondegenerate regime of SPDC". In: *Laser Physics Letters* 5.8 (2008), pp. 600–602.

[30] Atsushi Yabushita and Takayoshi Kobayashi. "Spectroscopy by frequency-entangled photon pairs". In: *Physical Review A* 69.1 (2004), p. 013806.

[31] Anna Paterova et al. "Measurement of infrared optical constants with visible photons". In: *New Journal of Physics* 20.4 (2018), p. 043015.

[32] Bernhard W Adams et al. “X-ray quantum optics”. In: *Journal of modern optics* 60.1 (2013), pp. 2–21.

[33] S Shwartz and SE Harris. “Polarization entangled photons at x-ray energies”. In: *Physical review letters* 106.8 (2011), p. 080501.

[34] Miles J Padgett and Robert W Boyd. “An introduction to ghost imaging: quantum and classical”. In: *Philosophical Transactions of the Royal Society A: Mathematical, Physical and Engineering Sciences* 375.2099 (2017), p. 20160233.

[35] Ayman F Abouraddy et al. “Entangled-photon imaging of a pure phase object”. In: *Physical review letters* 93.21 (2004), p. 213903.

[36] Nicholas Bornman et al. “Ghost imaging with engineered quantum states by Hong–Ou–Mandel interference”. In: *New Journal of Physics* 21.7 (2019), p. 073044.

[37] Todd B Pittman et al. “Optical imaging by means of two-photon quantum entanglement”. In: *Physical Review A* 52.5 (1995), R3429.

[38] DV Strekalov et al. “Observation of two-photon “ghost” interference and diffraction”. In: *Physical review letters* 74.18 (1995), p. 3600.

[39] Reuben S Aspden et al. “EPR-based ghost imaging using a single-photon-sensitive camera”. In: *New Journal of Physics* 15.7 (2013), p. 073032.

[40] Thomas J Lane and Daniel Ratner. “What are the advantages of ghost imaging? Multiplexing for x-ray and electron imaging”. In: *Optics express* 28.5 (2020), pp. 5898–5918.

[41] Malvin Carl Teich et al. “Variations on the theme of quantum optical coherence tomography: a review”. In: *Quantum Information Processing* 11.4 (2012), pp. 903–923.

[42] MD Mazurek et al. “Dispersion-cancelled biological imaging with quantum-inspired interferometry”. In: *Scientific reports* 3.1 (2013), pp. 1–5.

[43] Masayuki Okano et al. “0.54 μm resolution two-photon interference with dispersion cancellation for quantum optical coherence tomography”. In: *Scientific reports* 5.1 (2015), pp. 1–8.

[44] Vittorio Giovannetti, Seth Lloyd, and Lorenzo Maccone. “Advances in quantum metrology”. In: *Nature photonics* 5.4 (2011), pp. 222–229.

[45] Guo-Yong Xiang et al. “Entanglement-enhanced measurement of a completely unknown optical phase”. In: *Nature Photonics* 5.1 (2011), pp. 43–47.

[46] HF Okamoto and T Nagata Hofmann. “K. Sasaki, and S. Takeuchi”. In: *New J. Phys* 10 (2008), p. 073033.

[47] Giorgio Brida, Marco Genovese, and I Ruo Berchera. "Experimental realization of sub-shot-noise quantum imaging". In: *Nature Photonics* 4.4 (2010), pp. 227–230.

[48] Konstantin E Dorfman, Frank Schlawin, and Shaul Mukamel. "Nonlinear optical signals and spectroscopy with quantum light". In: *Reviews of Modern Physics* 88.4 (2016), p. 045008.

[49] Frank Schlawin, Konstantin E Dorfman, and Shaul Mukamel. "Entangled two-photon absorption spectroscopy". In: *Accounts of chemical research* 51.9 (2018), pp. 2207–2214.

[50] André Stefanov. "On the role of entanglement in two-photon metrology". In: *Quantum science and technology* 2.2 (2017), p. 025004.

[51] Michael G Raymer et al. "Entangled photon-pair two-dimensional fluorescence spectroscopy (EPP-2DFS)". In: *The Journal of Physical Chemistry B* 117.49 (2013), pp. 15559–15575.

[52] Matthew Otten et al. "Coherent photon coincidence spectroscopy of single quantum systems". In: *Physical Review A* 102.4 (2020), p. 043118.

[53] Oleksiy Roslyak and Shaul Mukamel. "Multidimensional pump-probe spectroscopy with entangled twin-photon states". In: *Physical Review A* 79.6 (2009), p. 063409.

[54] Eric R Bittner et al. "Probing exciton/exciton interactions with entangled photons: Theory". In: *The Journal of chemical physics* 152.7 (2020), p. 071101.

[55] Hao Li et al. "Photon entanglement entropy as a probe of many-body correlations and fluctuations". In: *The Journal of chemical physics* 150.18 (2019), p. 184106.

[56] Dany Lachance-Quirion et al. "Entanglement-based single-shot detection of a single magnon with a superconducting qubit". In: *Science* 367.6476 (2020), pp. 425–428.

[57] Hisaki Oka. "Selective two-photon excitation of a vibronic state by correlated photons". In: *The Journal of chemical physics* 134.12 (2011), p. 124313.

[58] Barak Dayan et al. "Two photon absorption and coherent control with broadband down-converted light". In: *Physical review letters* 93.2 (2004), p. 023005.

[59] Frank Schlawin et al. "Suppression of population transport and control of exciton distributions by entangled photons". In: *Nature communications* 4.1 (2013), pp. 1–7.

[60] Fabiano Lever, Sven Ramelow, and Markus Gühr. "Effects of time-energy correlation strength in molecular entangled photon spectroscopy". In: *Physical Review A* 100.5 (2019), p. 053844.

[61] Hisaki Oka. “Entangled two-photon absorption spectroscopy for optically forbidden transition detection”. In: *The Journal of chemical physics* 152.4 (2020), p. 044106.

[62] Jan Peřina, Bahaa EA Saleh, Malvin C Teich, et al. “Multiphoton absorption cross section and virtual-state spectroscopy for the entangled n-photon state”. In: *Physical Review A* 57.5 (1998), p. 3972.

[63] N Ph Georgiades et al. “Nonclassical excitation for atoms in a squeezed vacuum”. In: *Physical review letters* 75.19 (1995), p. 3426.

[64] MC Teich, JM Schroeer, and GJ Wolga. “Double-quantum photoelectric emission from sodium metal”. In: *Physical Review Letters* 13.21 (1964), p. 611.

[65] Barak Dayan et al. “Nonlinear interactions with an ultrahigh flux of broadband entangled photons”. In: *Physical review letters* 94.4 (2005), p. 043602.

[66] Dong-Ik Lee and Theodore Goodson. “Entangled photon absorption in an organic porphyrin dendrimer”. In: *The Journal of Physical Chemistry B* 110.51 (2006), pp. 25582–25585.

[67] S Sensarn et al. “Resonant sum frequency generation with time-energy entangled photons”. In: *Physical review letters* 102.5 (2009), p. 053602.

[68] Dmitry Tabakaev et al. “Energy-time-entangled two-photon molecular absorption”. In: *Physical Review A* 103.3 (2021), p. 033701.

[69] Juan P Villabona-Monsalve et al. “Entangled two photon absorption cross section on the 808 nm region for the common dyes zinc tetraphenylporphyrin and rhodamine b”. In: *The Journal of Physical Chemistry A* 121.41 (2017), pp. 7869–7875.

[70] Joakim Bergli et al. “Frequency and phase relations of entangled photons observed by a two-photon interference experiment”. In: *Physical Review A* 100.2 (2019), p. 023850.

[71] Michael R Harpham et al. “Thiophene dendrimers as entangled photon sensor materials”. In: *Journal of the American Chemical Society* 131.3 (2009), pp. 973–979.

[72] Oleg Varnavski, Brian Pinsky, and Theodore Goodson III. “Entangled photon excited fluorescence in organic materials: an ultrafast coincidence detector”. In: *The journal of physical chemistry letters* 8.2 (2017), pp. 388–393.

[73] Ryan K Burdick et al. “Predicting and controlling entangled two-photon absorption in diatomic molecules”. In: *The Journal of Physical Chemistry A* 122.41 (2018), pp. 8198–8212.

[74] Stefano Pirandola et al. “Advances in photonic quantum sensing”. In: *Nature Photonics* 12.12 (2018), pp. 724–733.

[75] Wenjiang Fan, Benjamin J Lawrie, and Raphael C Pooser. "Quantum plasmonic sensing". In: *Physical Review A* 92.5 (2015), p. 053812.

[76] Raphael C Pooser and Benjamin Lawrie. "Plasmonic trace sensing below the photon shot noise limit". In: *ACS Photonics* 3.1 (2016), pp. 8–13.

[77] Joong-Sung Lee et al. "Quantum noise reduction in intensity-sensitive surface-plasmon-resonance sensors". In: *Physical Review A* 96.3 (2017), p. 033833.

[78] Hisaki Oka. "Highly-efficient entangled two-photon absorption with the assistance of plasmon nanoantenna". In: *Journal of Physics B: Atomic, Molecular and Optical Physics* 48.11 (2015), p. 115503.

[79] Yoshiki Osaka et al. "Enhanced up-conversion of entangled photons and quantum interference under a localized field in nanostructures". In: *Physical review letters* 112.13 (2014), p. 133601.

[80] Sahar Basiri-Esfahani et al. "Integrated quantum photonic sensor based on Hong-Ou-Mandel interference". In: *Optics express* 23.12 (2015), pp. 16008–16023.

[81] Changhyoup Lee et al. "Quantum plasmonic sensing: beyond the shot-noise and diffraction limit". In: *ACS Photonics* 3.6 (2016), pp. 992–999.

[82] Dmitry A Kalashnikov et al. "Quantum spectroscopy of plasmonic nanostructures". In: *Physical Review X* 4.1 (2014), p. 011049.

[83] Oleksiy Roslyak, Christoph A Marx, and Shaul Mukamel. "Nonlinear spectroscopy with entangled photons: Manipulating quantum pathways of matter". In: *Physical Review A* 79.3 (2009), p. 033832.

[84] K Nasiri Avanaki and George C Schatz. "Entangled photon resonance energy transfer in arbitrary media". In: *The journal of physical chemistry letters* 10.11 (2019), pp. 3181–3188.

[85] Jian-Wei Pan et al. "Multiphoton entanglement and interferometry". In: *Reviews of Modern Physics* 84.2 (2012), p. 777.

[86] Shaul Mukamel et al. "Roadmap on quantum light spectroscopy". In: *Journal of Physics B: Atomic, Molecular and Optical Physics* 53.7 (2020), p. 072002.

[87] WB Gao et al. "Observation of entanglement between a quantum dot spin and a single photon". In: *Nature* 491.7424 (2012), pp. 426–430.

[88] M Bayer et al. "Coupling and entangling of quantum states in quantum dot molecules". In: *Science* 291.5503 (2001), pp. 451–453.

[89] Ka Chung Lee et al. "Entangling macroscopic diamonds at room temperature". In: *Science* 334.6060 (2011), pp. 1253–1256.

[90] Ashok Muthukrishnan, Girish S Agarwal, and Marlan O Scully. "Inducing disallowed two-atom transitions with temporally entangled photons". In: *Physical review letters* 93.9 (2004), p. 093002.

[91] Lukas Prochaska et al. "Singular charge fluctuations at a magnetic quantum critical point". In: *Science* 367.6475 (2020), pp. 285–288.

[92] Dirk Bouwmeester and Anton Zeilinger. "The physics of quantum information: basic concepts". In: *The physics of quantum information*. Springer, 2000, pp. 1–14.

[93] H Jeff Kimble. "The quantum internet". In: *Nature* 453.7198 (2008), pp. 1023–1030.

[94] DE Chang et al. "Colloquium: Quantum matter built from nanoscopic lattices of atoms and photons". In: *Reviews of Modern Physics* 90.3 (2018), p. 031002.

[95] B Keimer and JE Moore. "The physics of quantum materials". In: *Nature Physics* 13.11 (2017), pp. 1045–1055.

[96] Robert O Jones. "Density functional theory: Its origins, rise to prominence, and future". In: *Reviews of modern physics* 87.3 (2015), p. 897.

[97] Fabrizio Buscemi, Paolo Bordone, and Andrea Bertoni. "Entanglement dynamics of electron-electron scattering in low-dimensional semiconductor systems". In: *Physical Review A* 73.5 (2006), p. 052312.

[98] Douglas J Scalapino. "A common thread: The pairing interaction for unconventional superconductors". In: *Reviews of Modern Physics* 84.4 (2012), p. 1383.

[99] Hilbert v Löhneysen et al. "Fermi-liquid instabilities at magnetic quantum phase transitions". In: *Reviews of Modern Physics* 79.3 (2007), p. 1015.

[100] Dimitri N Basov et al. "Electrodynamics of correlated electron materials". In: *Reviews of Modern Physics* 83.2 (2011), p. 471.

[101] Immanuel Bloch, Jean Dalibard, and Sylvain Nascimbene. "Quantum simulations with ultracold quantum gases". In: *Nature Physics* 8.4 (2012), pp. 267–276.

[102] Konstantin E Dorfman, Frank Schlawin, and Shaul Mukamel. "Stimulated Raman spectroscopy with entangled light: enhanced resolution and pathway selection". In: *The journal of physical chemistry letters* 5.16 (2014), pp. 2843–2849.

[103] Charles Altuzarra et al. "Coherent perfect absorption in metamaterials with entangled photons". In: *ACS photonics* 4.9 (2017), pp. 2124–2128.

[104] Ying Li, Andrei Nemilentsau, and Christos Argyropoulos. “Resonance energy transfer and quantum entanglement mediated by epsilon-near-zero and other plasmonic waveguide systems”. In: *Nanoscale* 11.31 (2019), pp. 14635–14647.

[105] DN Basov, RD Averitt, and D Hsieh. “Towards properties on demand in quantum materials”. In: *Nature materials* 16.11 (2017), pp. 1077–1088.

[106] Kin Fai Mak et al. “Control of valley polarization in monolayer MoS 2 by optical helicity”. In: *Nature nanotechnology* 7.8 (2012), pp. 494–498.

[107] Xiaodong Xu et al. “Spin and pseudospins in layered transition metal dichalcogenides”. In: *Nature Physics* 10.5 (2014), pp. 343–350.

[108] Agedi N Boto et al. “Quantum interferometric optical lithography: exploiting entanglement to beat the diffraction limit”. In: *Physical Review Letters* 85.13 (2000), p. 2733.

Chapter 3

THEORY OF ENTANGLED PHOTON GENERATION AND HONG-OU-MANDEL INTERFERENCE

This chapter serves to cover a broad range of theoretical considerations which have formed an important part of the design and analysis of the presented experiments around quantum interferometry. Of particular importance are the interactions at a beamsplitter in the single-photon input case, the generated quantum states via the process of spontaneous parametric downconversion, the phase-matching conditions in periodically poled nonlinear materials for the generation of narrow and broadband entangled photon fluxes, as well as the estimation of entangled photon fluxes as a function of the downconversion source's parameters.

These few distinct components fully encompass the overall interferometer operation principle. In particular, the insights gained from these derivations have been found to aid in the quick analysis of experimental results so as to qualitatively better understand certain measured features.

3.1 Quantum Entanglement

Bipartite Entangled States

A quantum-mechanical state $|\Psi\rangle_{A,B} \in \mathcal{H}_A \otimes \mathcal{H}_B$ representing a two-particle system constituent of two Hilbert spaces A and B is defined as entangled if there exists no basis in which the state can be decomposed into a product state of the form $|\chi\rangle_1 \otimes |\phi\rangle_1$ with $|\chi\rangle_A \in \mathcal{H}_A$ and $|\phi\rangle_B \in \mathcal{H}_B$.

The simplest example of an entangled state based on the spin of a particle has the form:

$$|\Psi\rangle_{A,B} = \frac{1}{\sqrt{2}} \left(|\uparrow_A, \downarrow_B\rangle - |\downarrow_A, \uparrow_B\rangle \right). \tag{3.1}$$

The state shows strong correlations between the spins of each particle, despite the spin of each individual particle not being well-defined. These correlations lead to the outcome where measurement of one particle's state completely determines that of the other. The arising nonlocality which is a fundamental part of quantum mechanics underpins the Bell-CHSH inequality which shows that a certain correlation measure cannot exceed the value of 2 if one assumes that physics respects the constraints of a local "hidden variable" theory [1]. However certain systems permitted in quantum

mechanics can attain values as high as $2\sqrt{2}$ and hence violate the inequality and the concept of hidden variables [2].

The EPR wavefunction [3] is defined as:

$$|\Psi\rangle = \sum_{a,b} \delta(a + b - c_0) \, |a\rangle \, |b\rangle \tag{3.2}$$

where a and b represent some DOF of photons 1 and 2. c_0 is a constant. The delta function is what ensures that the total wavefunction is not separable (i.e. entangled). Note however that this is not necessarily a maximally entangled state.

In comparison, the four maximally entangled EPR-Bohm-Bell states are defined as follows:

$$\left|\Phi^{(}\pm)_{12}\right\rangle = \frac{1}{\sqrt{2}} \{|0_1 0_2\rangle \pm |1_1 1_2\rangle\} \tag{3.3}$$

$$\left|\Psi^{(}\pm)_{12}\right\rangle = \frac{1}{\sqrt{2}} \{|0_1 1_2\rangle \pm |1_1 0_2\rangle\} \, . \tag{3.4}$$

These four states are completely orthogonal to each other and hence form a complete orthogonal basis. The states are also maximally entangled, meaning that when we trace over the state B, the reduced density operator ρ_A of the system will be a multiple of the identity operator I. Hence, if we measure system A in any basis, the result will be completely random (0 or 1 with equal probability 1/2).

Discrete and Continuous Variable Entanglement

SPDC being a popular system which is capable of generating photonic quantum entanglement in a rather straightforward way, there is indeed some subtlety to the nature of the underlying entanglement characteristic.

Photon pairs generated via type-II SPDC can be entangled in their polarization states without additional optical elements, which, of course, can be taken to be a discrete variable (or degree of freedom) by considering only the orthonormal basis that is experimentally accessible through the downconversion process. While polarization entanglement has been widely utilized due to its comparatively simple quantum description, entanglement in a continuous variable such as frequency is perhaps even more interesting given its potential advantages. Such high-dimensional Hilbert spaces that are a result of some continuous variable entanglement in a two-particle quantum system allow for markedly large photon fluxes which still retain non-classical characteristics. Photon pairs sourced from SPDC are particularly interesting as they exhibit both low-dimensional discrete (polarization), as well as high-dimensional continuous (momentum/energy) entanglement.

Characterization of the degree of entanglement is possible via a Schmidt decomposition [4]. Here, the Schmidt number K quantifies the number of mode pairs which can be occupied independently, or in other words is a quantifier for the effective dimensionality of the Hilbert space being populated. As such, entangled states must possess a K value strictly greater than 1. By this definition, polarization entangled states are fundamentally limited to K=2. In a continuous variable entangled system, K values of arbitrarily high number can be attained, given that the correlation between photons of an entangled pair exist in the continuous frequency degree of freedom. Hence the limitation is set via the downconverted bandwidth. Via this perspective, it is easy to understand that singular occupation of a particularly large number of Schmidt modes (i.e. frequency pairs) is possible while still making sure that photons pairs can be treated as distinct pairs without any cross-correlation effects arising. (This could be experimentally shown via a linear power dependence that has no quadratic transition.) Worth pointing out is also that the degree of entanglement provides a good measure for the mutual information content.

For a narrowband pump and under an approximation where the joint spectrum is described in terms of Gaussian functions, the Schmidt number can be expressed as:

$$K = \frac{\sigma_-}{\sqrt{2}\sigma_+} \tag{3.5}$$

where $\sigma_\pm$ represents the spectral width along the $\omega_\pm = \omega_s \pm \omega_i$ direction. Note that σ_- is related to SPDC emission bandwidth, while σ_+ follows the pump bandwidth.

From this it is trivial to see that minimizing the pump bandwidth (i.e. attaining a very narrow cw linewidth) and maximizing the SPDC emission bandwidth, such as through chirped periodic poling as will be shown later, is the method for generating highly entangled photon pairs.

A particularly interesting consequence of a large SPDC bandwidth is that it implies a short correlation time between the signal and idler photons. This is defined as the width of the time of emission difference probability distribution. This short correlation time, of course, implies a high resolution in related applications like quantum optical coherence tomography which rely on detecting differences in arrival times.

The number of Schmidt modes that is realistically accessible is limited by a number of experimental parameters such as the nonlinear media used, the properties of the pump beam, and so forth. The most applicable strategy to determine the

number of Schmidt modes is through the so-called joint-spectral-amplitude/intensity (JSA/JSI). This two-dimensional function is representative of the allowed frequency combinations in an SPDC process, and is fully characterized by the pump beam and the phase-matching curve of the nonlinear medium. The details of this are discussed in Ch. 5.

3.2 Lossless Beamsplitter Interaction

Although the derivations for beamsplitter interactions have been presented in numerous sources, some of which generalize the approaches to multi-mode considerations as well as the inclusion of realistic loss factors, here we shall introduce the most basic formalism in its completeness based on the foundations and treatment presented in [5]. By doing so, we aim to elucidate on certain steps taken so as to make the derivation clearer from an introductory perspective. This will hopefully serve as a solid basis for the extension of this formalism to include specific considerations and degrees-of-freedom that are specific to the type of interferometric setup used in future experiments.

We begin by defining that the input and output boson-annihilation operators are related via the unitary BS operator U_{BS} in the Schrödinger picture:

$$|\Psi\rangle_{out} = \hat{U}_{BS}\,|\Psi\rangle_{in} \tag{3.6}$$

$$\begin{bmatrix} \hat{b}_1 \\ \hat{b}_2 \end{bmatrix} = \begin{bmatrix} B_{11} & B_{12} \\ B_{21} & B_{22} \end{bmatrix} \begin{bmatrix} \hat{a}_1 \\ \hat{a}_2 \end{bmatrix} \tag{3.7}$$

where the boson creation-annihilation operators at the input and output are represented by $\hat{a}$ and $\hat{b}$, respectively. For simplicity, let the elements $B_{11} = t$, $B_{21} = t'$, $B_{12} = r$, and $B_{22} = r'$, hence giving in the Heisenberg picture:

$$\begin{cases} \hat{b}_1 = t\hat{a}_1 + r\hat{a}_2 \\ \hat{b}_2 = t'\hat{a}_2 + r'\hat{a}_1. \end{cases} \tag{3.8}$$

The commutator

$$\left[\hat{b}_k, \hat{b}_l^\dagger\right] = \delta_{kl}, (k, l = 1, 2) \tag{3.9}$$

leads to the following simultaneous equations:

$$\begin{cases} |t|^2 + |r|^2 = 1 \\ |t'|^2 + |r'|^2 = 1 \\ \quad |t| = |t'| \\ \quad |r| = |r'| \\ t^*r' + r^*t' = 0. \end{cases} \tag{3.10}$$

These yield the following phase relation.

$$\psi_t + \psi_r - \psi_{t'} - \psi_{r'} = \pi. \tag{3.11}$$

This phase relation is universal and independent of the specifics of the beamsplitter. Simply relies on the fact that reflections introduce a π phase shift in the photon phase. Given the arbitrary choice of ψ_t,ψ_r,$\psi_{t'}$, and $\psi_{r'}$, we can set ψ_t,ψ_r,$\psi_{t'}$ to be zero and $\psi_{r'} = -\pi$ from which follows that:

$$\begin{cases} \hat{b}_1 = t\hat{a}_1 + r\hat{a}_2 \\ \hat{b}_2 = t\hat{a}_2 - r\hat{a}_1. \end{cases} \tag{3.12}$$

For differing polarization states being incident on the beamsplitter, one has to decompose them into parallel and perpendicular components which gives 4 equations instead of 2. For Fock or coherent states, no explicit form of $\hat{U}_{BS}$ is needed. As an example, a single photon state input at port 1:

$$|\Psi\rangle_{in} = |1\rangle_1 \otimes |0\rangle_2 = (\hat{a}_1^\dagger |0\rangle_1) \otimes |0\rangle_2 \tag{3.13}$$

becomes:

$$|\Psi\rangle_{out} = \hat{U}\hat{a}_1^\dagger |0\rangle_1 \otimes |0\rangle_2 = \hat{U}\hat{a}_1^\dagger \hat{U}^\dagger \hat{U} |0\rangle_1 \otimes |0\rangle_2 . \tag{3.14}$$

Trivially, since a vacuum input gives a vacuum output, all that is left is to evaluate $\hat{U}\hat{a}_1^\dagger\hat{U}^\dagger$.

Inverting the simultaneous equations in the Heisenberg picture above to solve for $\hat{a}$:

$$\begin{cases} \hat{a}_1 = \hat{U}\hat{b}_1\hat{U}^\dagger = t\hat{b}_1 - r\hat{b}_2 \\ \hat{a}_2 = \hat{U}\hat{b}_2\hat{U}^\dagger = t\hat{b}_2 + r\hat{b}_1 \end{cases} \tag{3.15}$$

and therefore, by the principle of reversibility

$$\begin{cases} \hat{U}\hat{a}_1\hat{U}^\dagger = t\hat{a}_1 - r\hat{a}_2 \\ \hat{U}\hat{a}_2\hat{U}^\dagger = t\hat{a}_2 + r\hat{a}_1. \end{cases} \tag{3.16}$$

Hence for the output state, we get

$$|\Psi\rangle_{out} = (t\hat{b}_1^\dagger - r\hat{b}_2^\dagger) |0\rangle_1 \otimes |0\rangle_2 = t |1,0\rangle - r |0,1\rangle . \tag{3.17}$$

In the case of an input state $|1,1\rangle$ such as in an HOM interferometer:

$$\begin{aligned} |\Psi\rangle_{out} &= \hat{U} |1\rangle_1 |1\rangle_2 = \hat{U}\hat{a}_1^\dagger |0\rangle_1 \hat{a}_2^\dagger |0\rangle_2 = \hat{U}\hat{a}_1^\dagger\hat{a}_2^\dagger |0\rangle \\ &= \hat{U}\hat{a}_1^\dagger\hat{U}^\dagger\hat{U}\hat{a}_2^\dagger\hat{U}^\dagger\hat{U} |0\rangle \\ &= (\hat{U}\hat{a}_1^\dagger\hat{U}^\dagger)(\hat{U}\hat{a}_2^\dagger\hat{U}^\dagger) |0\rangle \\ &= (t\hat{a}_1^\dagger - r\hat{a}_2^\dagger)(t\hat{a}_2^\dagger + r\hat{a}_1^\dagger) |0\rangle \\ &= (t^2 - r^2)\hat{a}_1^\dagger\hat{a}_2^\dagger |0\rangle + tr(\hat{a}_1^{\dagger 2} - \hat{a}_2^{\dagger 2}) |0\rangle \\ &= (t^2 - r^2)\hat{a}_1^\dagger\hat{a}_2^\dagger |1,1\rangle + \sqrt{2}tr(|2,0\rangle - |0,2\rangle) \end{aligned} \tag{3.18}$$

which for a 50:50 beamsplitter results in the two-photon entangled $N00N$ state:

$$|\Psi\rangle_{out} = \frac{|2,0\rangle - |0,2\rangle}{\sqrt{2}}. \tag{3.19}$$

3.3 Phase Matching

By taking the response of a material to an applied electric field, one can recognize that the material polarization behaves differently for varying field intensities. At the low-intensity limit, the response is completely dominated by a first order linear term, whereas for higher intensities, the second order non-linearity becomes appreciable (obviously as long as the material has a non-zero second order susceptibility). Solving the wave equation in a nonlinear medium, one then arrives at the result that this second order response is a function of the product of two electric fields, leading to a variety of frequency mixing processes inside the nonlinear material.

One must however also take into account the spatial dependence of the electric fields inside the medium, as constructive/destructive interference of the propagating waves cannot be ignored. As such, introducing the spatial modulation via the wave vector $\vec{k}_j$, the three-wave mixing process takes on the form:

$$\frac{dE_{1i}}{dz} \propto K d_{ijk} E_{3j} E^*_{2k} e^{-i(\vec{k}_3 - \vec{k}_2 - \vec{k}_1)z} \tag{3.20}$$

where d_{ijk} is the second order ($n = 2$) susceptibility tensor of rank $n + 1$. The argument of the complex exponential term is defined as the "phase-mismatch" $\Delta\vec{k} = \vec{k}_3 - \vec{k}_2 - \vec{k}_1$ and has a clear effect on the strength of the second order process. This vectorial relationship is depicted in Fig.3.1 for the specific case of spontaneous parametric downconversion, whereby a pump photon with wave vector $\vec{k}_{pump}$ splits into two lower energy photons (signal and idler) with wave vectors $\vec{k}_{signal}$ & $\vec{k}_{idler}$, respectively. To somewhat simplify the problem, it is convenient

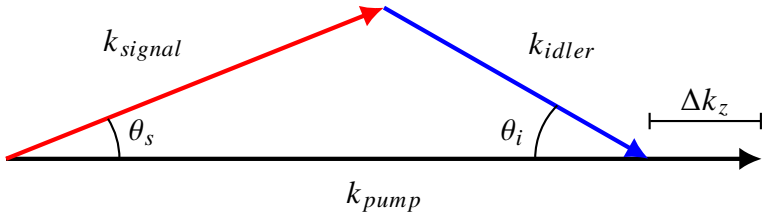

Figure 3.1: Phase-matching diagram for a two-photon downconversion process. To note is that this is a fully three-dimensional problem, and thus requires the independent treatment of the transverse and longitudinal components if no geometric constraints are imposed.

to define the transverse momenta $\vec{\boldsymbol{q}}_p$, $\vec{\boldsymbol{q}}_s$, and $\vec{\boldsymbol{q}}_i$ as the projections of the pump wave vector $\vec{\boldsymbol{k}}_p$, the signal wave vector $\vec{\boldsymbol{k}}_s$, and the idler wave vector $\vec{\boldsymbol{k}}_i$, onto the plane transverse to the optic axis. Let us also define k_{pz}, k_{sz}, and k_{iz}, as the longitudinal components of the corresponding wave vectors.

Since most experiments are performed in the paraxial regime (essentially a more or less purely collinear emission characteristic), it is well suited to only focus on the longitudinal components of the phase-mismatch Δk and re-write it as $\Delta k = k_{pz} - k_{sz} - k_{iz}$. Hence Eq.1 can be re-formulated into a one dimensional form that is only dependent on the z-components of the interacting waves:

$$\frac{dE_{1i}}{dz} \propto K d_{ijk} E_{3j} E^*_{2k} e^{-i(k_{pz}-k_{sz}-k_{iz})z}. \tag{3.21}$$

To obtain a solution for the field E_{3j} one simply needs to integrate the equation w.r.t. the spatial variable z between the beginning and end of the nonlinear medium $\left[\frac{-L}{2}, \frac{L}{2}\right]$ or $[0, L]$ depending on convention. While, of course, this is not difficult to carry out via a complex integral:

$$\int_0^L e^{i\Delta k z} dz = \frac{e^{i\Delta k L} - 1}{i\Delta k} = \frac{sin(\Delta k L/2)}{\Delta k}. \tag{3.22}$$

,a somewhat more elegant approach is to recognize that the integral can be extended to $[-\infty, \infty]$ via the introduction of a rectangular function $\Pi(z)$ which is equal to unity across the physical extent of the medium. This results in a Fourier transform being defined for the rectangular function which is by definition:

$$\int_{-\infty}^{\infty} \Pi(z) e^{-i2\pi k z} dz = sinc(k) \tag{3.23}$$

This transform dual is shown below in Fig.3.2 where the rectangular function $\Pi(z)$ is representative of the medium's spatial "selectivity" in real-space, and the *sinc* function is its corresponding representation in k-space, depicting the effect a mismatch in the phases has on the nonlinear interaction efficiency. Intuitively, this relationship between the two spaces can be understood by assuming that the amplitude for a downconversion event to occur (i.e. for a pump photon to create a pair of daughter photons) is uniform throughout the crystal. This allows us to assign a rectangular function to describe the probability amplitude of this process. Transitioning from a *real-space* to a *k-space* representation via a Fourier transform naturally preserves the probability amplitude representation, and hence it becomes evident that the downconversion probability as a function of wave vector momentum is described by a $sinc(x)$ function with respect to the variable Δk.

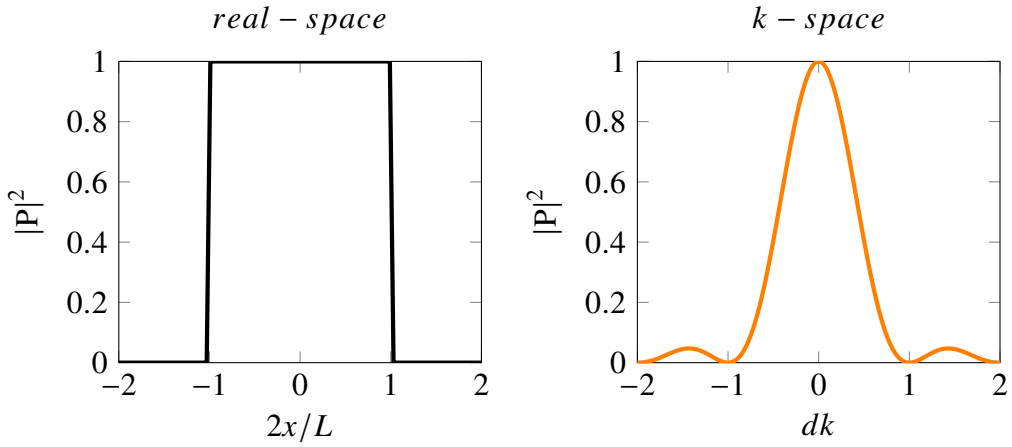

Figure 3.2: Transformation of the rectangular crystal function in real-space to that of its Fourier dual in k-space which is $sinc(k) = \frac{sin(k)}{k}$. Note that plotted here are the intensities of the above functions (i.e. $|f(x)|^2$).

Unfortunately in most cases multiplication by *sinc* functions makes analytical treatment difficult, in particular compared to functions such as pure Gaussians. As a result of this, it is most often extremely convenient to rely on an approximation by a Gaussian function of the form e^{ikx}. The approximation is valid so long as the phase-mismatch is sufficiently small such that the two functions are overlapping well enough. [1]

To somewhat explain the background of this, let us again take the process of parametric fluorescence. The output state observed in this interaction can be derived as per [6] to take the following functional form:

$$|\Psi\rangle \approx C_0 \,|0_1, 0_2\rangle + C_1 \int\int d^3k_1 d^3k_2 \Phi(\vec{\boldsymbol{k}}_1, \vec{\boldsymbol{k}}_2)\hat{a}^\dagger(\vec{\boldsymbol{k}}_1)\hat{a}^\dagger(\vec{\boldsymbol{k}}_2)\,|0_1, 0_2\rangle\,. \quad (3.24)$$

Here $\Phi(\vec{\boldsymbol{k}}_1, \vec{\boldsymbol{k}}_2)$ describes the two-photon wavefunction consisting of two terms

$$\Phi(\vec{\boldsymbol{k}}_1, \vec{\boldsymbol{k}}_2) = \alpha(\vec{\boldsymbol{q}}_1 + \vec{\boldsymbol{q}}_2)\phi(\frac{\Delta k_z L_z}{2}). \quad (3.25)$$

$\alpha(\vec{\boldsymbol{q}}_q + \vec{\boldsymbol{q}}_2)$ being the transverse momentum profile of pump beam described by a Gaussian and $\phi(\Delta k_z)$ the phase matching function of the form $sinc(\Delta k_z)$ specific to the nonlinear medium as discussed in detail before. Letting the angle between the pump wave vector $\vec{\boldsymbol{k}}_p$ and the signal/idler wave vectors $\vec{\boldsymbol{k}}_s$ and $\vec{\boldsymbol{k}}_i$ be small enough

[1] However even this has not been a strict requirement in the past as evidenced by the theoretical results of a lot of publications in recent years.

such that a small-angle approximation can be used, we can write down the following relationships under the assumption of conservation of momentum:

$$\vec{k}_p = (\vec{k}_1 + \vec{k}_2)cos(\theta) - \Delta\vec{k}_z \tag{3.26}$$

$$\frac{|\vec{q}_1 - \vec{q}_2|}{2} = \vec{k}_1 sin(\theta) \tag{3.27}$$

which subsequently yields:

$$\Delta\vec{k}_z \approx -\frac{|\vec{q}_1 - \vec{q}_2|}{2\vec{k}_p}. \tag{3.28}$$

This allows us to re-write the two-photon wavefunction in terms of only the transverse momenta $\vec{q}_1$ and $\vec{q}_2$.

$$\Phi(\vec{q}_1, \vec{q}_2) = exp(-|\vec{q}_1 + \vec{q}_2|^2)sinc(|\vec{q}_1 - \vec{q}_2|^2). \tag{3.29}$$

As mentioned previously, the form of such *sinc*-Gaussian type functions makes them difficult to work with analytically. Instead, in most cases the choice to approximate the phase-matching function by a Gaussian with a forced "smudge factor" is a reasonable compromise to make. A comparison between a Gaussian and *sinc* function with quadratic arguments is shown in Fig.3.3 to display the discrepancy between the two.

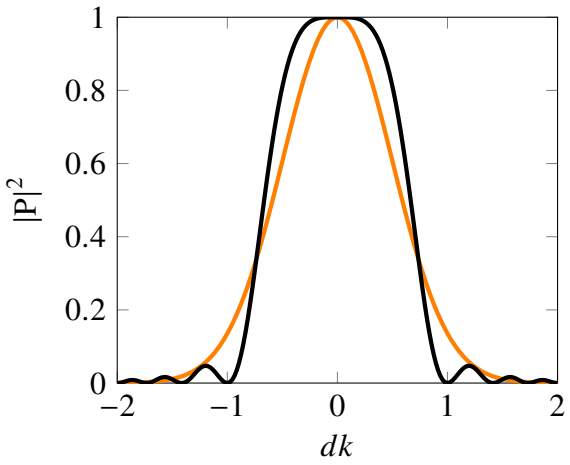

Figure 3.3: Comparison of a $sinc(x^2)$ (black) and a Gaussian function (orange). Note that the argument of both functions is quadratic in this case.

3.4 SPDC Quantum States

SPDC correlation function

Following the general treatment presented in [7], the quantum state generated in the process of SPDC can be derived via first-order perturbation theory. By starting

from the vacuum state:

$$|\psi\rangle = -\frac{i}{\hbar}\int_{-\infty}^{\infty} dt\mathcal{H}\,|0\rangle \tag{3.30}$$

where $\mathcal{H}$ is the interaction Hamiltonian of the following form:

$$\mathcal{H} = \epsilon_0\chi^{(2)}\int_V d^3\mathbf{r}E_p^{(+)}E_s^{(-)}E_i^{(-)} + h.c. \tag{3.31}$$

$E_p^{(+)}$ is the pump laser field that we take to be monochromatic and classical. Propagating it in z and assigning a frequency Ω_p,

$$E_p^{(+)} = \mathcal{E}_p exp\left[i\left(k_p z - \Omega_p t\right)\right]. \tag{3.32}$$

Furthermore, $E_{s,i}^{(-)}$ is the quantized field operator for the signal and idler modes, respectively. With the assumption that these two modes also propagate along z with some frequency $\omega_{s,i}$, we can write

$$E_{s,i}^{(-)} = \int_V d^3\mathbf{k}\mathcal{E}_{s,i}a_{s,i}^{\dagger}(\omega_{s,i})exp\left[i\left(k_{s,i}z - \omega_{s,i}t\right)\right]. \tag{3.33}$$

The final output SPDC state can thus be calculated to be:

$$|\psi\rangle = \int d\omega_s d\omega_i sinc\left(\frac{\Delta kL}{2}\right)e^{-i\frac{\Delta kL}{2}}a_s^{\dagger}(\omega_s)a_i^{\dagger}(\omega_i)\,|0\rangle \tag{3.34}$$

with $\Delta k = k_{pz}(\Omega_p) - k_{sz}(\omega_s) - k_{iz}(\omega_i)$, and L being the total length of the nonlinear crystal.

This generalized state encapsulates two important factors. One is the phase-matching term described by the *sinc* function and the exponential term, which is entirely defined by the properties of the nonlinear material and the wavelengths being utilized. The second is a here omitted factor, which in practical terms is hidden due to the fact that it is a δ-function in frequency-space and was implicitly included in the derivation when we constrained our field equations Eq.3.32 and Eq.3.33 to be monochromatic. The product of these two terms is what defines the previously mentioned joint-spectral-amplitude, $\gamma\left(\omega_s,\omega_i\right) = \mu\left(\omega_s,\omega_i\right)\times\phi\left(\omega_s,\omega_i\right)$, where μ is the *pump-envelope function* and ϕ the *phase-matching amplitude* [8].

SPDC Phase-Matching

Considering the result described in the phase-matching document (attach later), we can see that the functional description of the phase-matching takes on the following form:

$$\int_0^L e^{i\Delta kz}dz = \frac{sin(\Delta kL/2)}{\Delta k}. \tag{3.35}$$

For type-II and non-degenerate type-I SPDC, we have:

$$F_{II}(\Omega) = \frac{sin(DL\Omega/2)}{DL\Omega/2} \tag{3.36}$$

with D being the inverse group velocity difference between the signal and idler photons. For type-I frequency-degenerate SPDC, this spectral amplitude function modifies to:

$$F_{I}(\Omega) = \frac{sin(D''L\Omega^2/2)}{D''L\Omega^2/2} \tag{3.37}$$

where D'' denotes the second derivative of the dispersion dependence $k(\omega)$ in the nonlinear medium for the signal and idler photons, taking into account that the second-order correlation function $G^{(2)}$ is only dependent on $\tau \equiv [t_2 - (z_i/u_i + r_2/c)] - [t_1 - (z_s/u_s + r_1/c)]$. Hence if one now considers the Fourier transforms of the previous two equations (i.e. $F(\tau)$), then one obtains the expected unfiltered lineshapes of the interference patterns in an HOM type setup.

$$\mathcal{F}_x\left[sinc^2(x)\right](\omega) = \sqrt{\frac{\pi}{2}}\Lambda\left(\frac{\omega}{2}\right) \tag{3.38}$$

3.5 Entangled State HOM Interference

The resultant state from parametric downconversion is fundamentally always entangled in its frequency degree-of-freedom. Since the two photons originate from the same space-time location and are constrained in their possible frequency sums due to energy conservation, both superposition and correlation criteria are fulfilled in order to obtain an entangled state as the output. Although restricted in the frequency sum, the two daughter photons can be emitted in any two frequency modes. The most general form of the energy entangled state produced by SPDC is:

$$|\Psi\rangle = \int dE\ \Phi(E)\,|E\rangle_1\,|E_0 - E\rangle_2 \tag{3.39}$$

or equivalently in the frequency domain representation:

$$|\psi\rangle = \int d\omega\ \phi(\omega)\,|\omega\rangle_1\,|\omega_0 - \omega\rangle_2\,. \tag{3.40}$$

Here, $\phi(\omega)$ is the joint-spectral-amplitude (JSA) which is a symmetric weight function responsible for describing the spectral distribution of the signal and idler photons in the downconversion process. It is composed of the product of two functions, one of which is the pump spectrum and the other is the phase-matching function that is dictated by the nonlinear crystal in which the parametric process takes place. From this, it is easy to see that one obtains a highly entangled state with a discrete number

of terms proportional to the bandwidth of the SPDC spectrum. Simultaneously, it is worth noting that $\phi(\omega)$ dictates which frequencies are accessible in the entangled state.

We can simplify the state in Eq.3.40 significantly by only focusing on a single pair of conjugate frequencies such that the discrete two-frequency entangled state which we end up with looks strongly reminiscent of a polarization entangled state with a Schmidt number, $K = 2$. The frequency entangled biphoton state is thus represented by the following expression:

$$|\Psi\rangle_{\omega_1,\omega_2} = \frac{1}{\sqrt{2}}\left(|\omega_1\rangle_s\,|\omega_2\rangle_i + e^{i\theta}\,|\omega_2\rangle_s\,|\omega_1\rangle_i\right) \tag{3.41}$$

where $\theta = (\omega_1 - \omega_2)\,d\tau$ is the relative difference in arrival time between the signal and idler photons at the beamsplitter. Obviously for a frequency degenerate state, $\theta = 0$ regardless of the time delay $d\tau$ which leads to a maximally entangled EPR state. For any amount of frequency difference between signal and idler, proper adjustment of the time-delay allows for the creation of some arbitrary entangled state at the output of the two ports of the beamsplitter. This can in principle then be post-selected for via a coincidence measurement.

Frequency beat note Ou-Mandel Interference

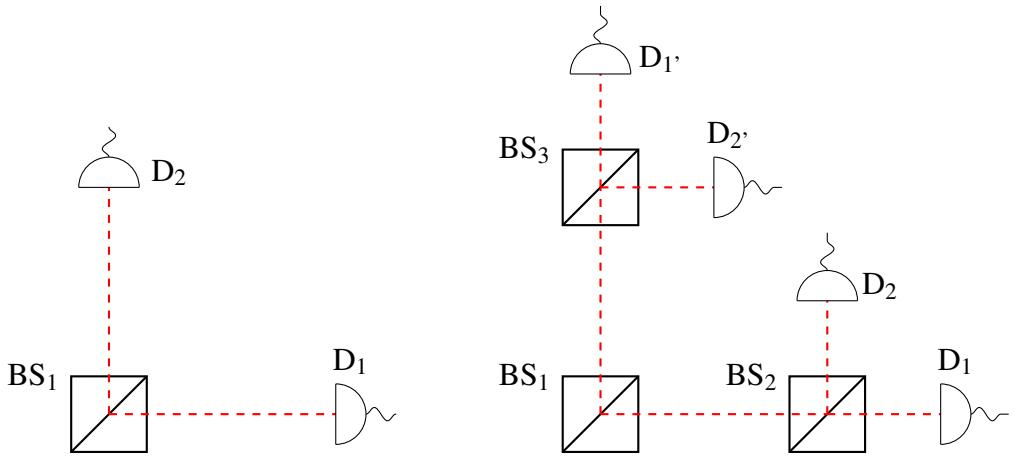

Figure 3.4: Left: traditional HOM setup with one single beamsplitter and two photodetectors measuring coincidence counts resulting from the interference of probability amplitudes, Right: cascaded setup where the relative phases in the two output arms can be investigated via coincidence detection between different detector combinations

Of note is that this original experiment did not use the potential of entangled state

generation in the down-conversion process. Instead, a product state of the form

$$|\Psi\rangle = |H\rangle\,|V\rangle \tag{3.42}$$

was created via the 90° rotation in one arm of the interferometer. This state was then used in its separated form as the input of a beamsplitter. After the beamsplitter, the state formed is

$$|\Psi\rangle = \frac{1}{2}\left[|H\rangle_1\,|V\rangle_2 + |V\rangle_1\,|H\rangle_2 - i\,|H\rangle_1\,|V\rangle_1 + i\,|H\rangle_2\,|V\rangle_2\right]. \tag{3.43}$$

Thus if only coincidences are measured for this output state, the last two terms which represent bunched photons do not contribute to the coincidence count defined as:

$$P_{12} \propto \left[T^2 + R^2 - 2TRe^{-\sigma^2\delta t^2/2} cos\left(\left(\omega_1 - \omega_2\right)\delta t\right)\right] \tag{3.44}$$

where σ is the rms width of either the downconverted signal/idler spectra, or if narrower, the rms bandwidth of interference filters used to spectrally narrow the bandwidth of measurement. δt is the temporal displacement in the arrival times of the photons at the beamsplitter. Substituting $T = R = 0.5$ for a balanced 50:50 beamsplitter then yields:

$$P_{12} \propto \left[0.5 - 0.5e^{-\sigma^2\delta t^2/2} cos\left(\left(\omega_1 - \omega_2\right)\delta t\right)\right]. \tag{3.45}$$

By taking some SPDC process which produces a frequency degenerate pair of photons (i.e. $\omega_1 = \omega_2$), the coincidence rate which is measured by two photodetectors displays the prototypical HOM dip characterized by a negative Gaussian (blue) centered around the zero delay position corresponding to the beamsplitter position which ensures that both photons are incident in two input ports at the same time.

The results above are based on the Gaussian function dictating the coincidence count probability P_{12} due to the narrowband filter's lineshape applied to the signal/idler fields. If we were to apply no filtering and use a cw source to generate our SPDC spectrum in a type-II phase-matched crystal, the $sinc(\omega)$ shaped phase-matching function would be what determines the measured coincidence count curve. In this case, transitioning over into the temporal domain via a Fourier transform returns a triangular pulse function $\Lambda(t)$ orange:

$$F(t) = \mathcal{F}_\omega\left[sinc^2(\omega)\right](t) = \frac{1}{\sqrt{2\pi}}\int_{-\infty}^{\infty} sinc^2(\omega)e^{i\omega t}d\omega = \frac{1}{\sqrt{2\pi}}\Lambda\left(\frac{t}{2}\right). \tag{3.46}$$

In contrast, in the frequency non-degenerate case ($\omega_1 \neq \omega_2$) we recover the sinusoidal beating pattern (at the frequency of the difference) of the coincidence function which still displays a Gaussian envelope Fig.3.6. There are certain requirements that need to be satisfied in order to observe this interference effect:

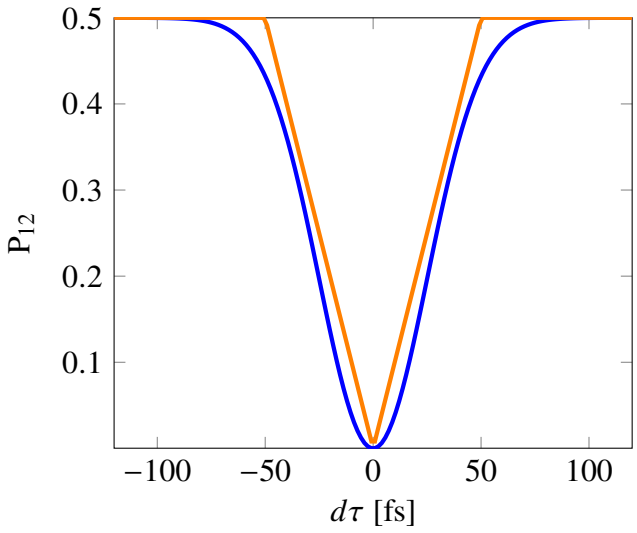

Figure 3.5: Frequency degenerate ($\omega_1 = \omega_2$) Hong-Ou-Mandel interference patterns corresponding to no filtering which retains the *sinc* functional phase-matching dependence (orange), and the case where a Gaussian spectral filter has been applied (blue).

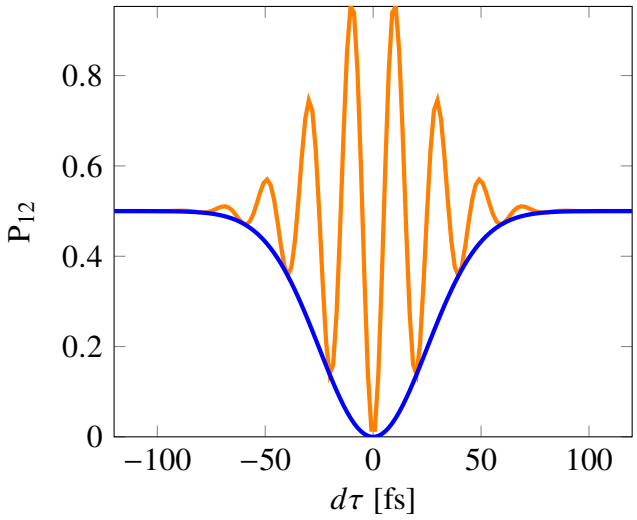

Figure 3.6: Frequency non-degenerate ($\omega_1 \neq \omega_2$) Hong-Ou-Mandel interference pattern displaying a frequency beat-note (orange), with its corresponding envelope function (blue).

- The spatial distributions of the two light fields must overlap and must not be orthogonal.
- The polarization states also must not be orthogonal.
- The optical frequency difference must be within the bandwidth of the pho-

todetector.

- Wavelengths must be within the range where the photodetector is sensitive.

An interesting observation to be made is that for an entangled photon pair originating from a type-I downconversion process, different arrangements of the detector pairs, that is, when the two detectors are placed on the same side of the beamsplitter which is responsible for the HOM interference (Fig.3.4 right, with only D1 and D2 being used), the beamsplitter changes the π-phase shift between two two-photon probability amplitudes. This can be viewed as a Bell-type measurement based on frequency, rather than polarization post-selection. This π-phase shift would then be observable in a frequency resolved interference measurement as a flip in the vertical position of the absolute interference minimum Fig. 3.7.

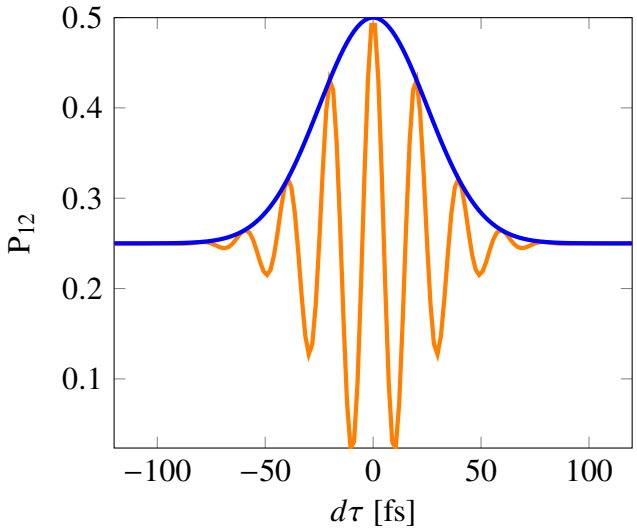

Figure 3.7: Frequency non-degenerate ($\omega_1 \neq \omega_2$) Hong-Ou-Mandel interference pattern with a beamsplitter induced π-phase shift (and a correspondingly different detector configuration) displaying a frequency beat-note (orange), with its corresponding envelope function (blue).

Broadband SPDC HOM

If one transitions away from the discrete two-frequency state to a highly entangled state stemming from a broadband SPDC process (i.e. $cos\left((\omega_1 - \omega_2)\,\delta t\right) = cos(kx)$ for $k = [-a, a]$ where $[-a, a]$ now represents some continuous **symmetric** SPDC bandwidth about $\omega_1 = \omega_2$), then integrating w.r.t. k yields:

$$\int_{-a}^{a} cos(kx)dk = \frac{2sin(ax)}{x} \rightarrow \frac{2sin(ax)}{2ax} \tag{3.47}$$

such that it is normalized, where $a \propto \Delta SPDC$. This is a *sinc* function with parameter a dictated by the downconversion bandwidth. As an example, we can model the coincidence count probability P_{12}^{BB} for such a broadband SPDC state for a number of arbitrary bandwidths. Note that the exponential term responsible for the Gaussian filter is removed.

$$P_{12}^{BB} \propto \left[0.5 - 0.5\frac{2sin\,(a\delta t)}{2ax}\right] \tag{3.48}$$

This behaviour is, of course, also evident if one simply assumes a broadband SPDC

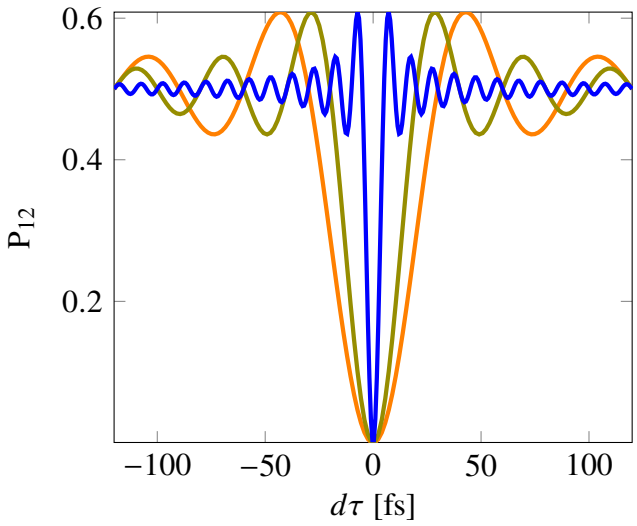

Figure 3.8: Broadband Hong-Ou-Mandel interference pattern for three different SPDC bandwidths. The respective bandwidths increase from (orange), to (green), to (blue).

spectrum modelled by $rect(\omega) \equiv \Pi(\omega)$ which, if Fourier transformed, yields:

$$F(t) = \mathcal{F}_\omega\left[\Pi(\omega)\right](t) = \frac{1}{\sqrt{2\pi}}\int_{-\infty}^{\infty}\Pi(\omega)e^{i\omega t}d\omega = \frac{1}{\sqrt{2\pi}}sinc\left(\frac{t}{2}\right). \tag{3.49}$$

Curiously, if one were to re-introduce the narrowband filter into the experiment after the broadband HOM interference has taken place, the ultrashort temporal resolution remains intact and the only change observed is the disappearance of the 'high' frequency modulation as shown below in Fig. 3.9.

$$P_{12}^{BB} \propto \left[0.5 - 0.5e^{-\sigma^2\delta t^2/2}\frac{2sin\,(a\delta t)}{2ax}\right] \tag{3.50}$$

Next, let us assume that the downconverted SPDC spectrum is **asymmetric** around

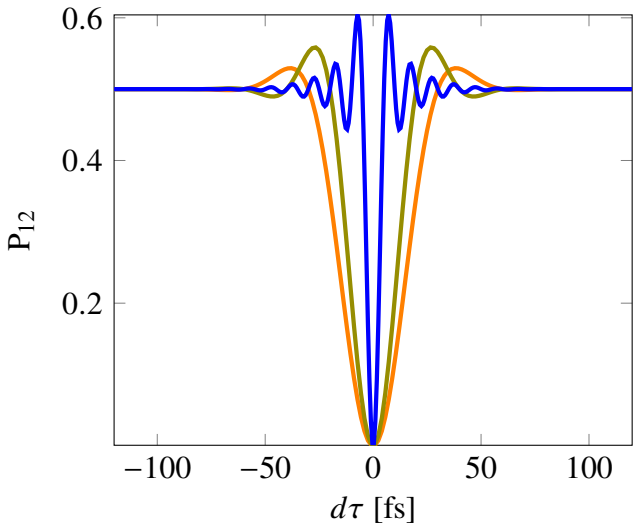

Figure 3.9: Broadband Hong-Ou-Mandel interference pattern for three different SPDC bandwidths with additional spectral filtering after the beamsplitter interaction. The respective bandwidths increase from (orange), to (green), to (blue).

the degeneracy $\omega_1 = \omega_2$. Integration of the frequency beat note cosine term now yields:

$$\int_{-a}^{b} cos(kx)dk = \frac{sin(ax) + sin(bx)}{x} \rightarrow \frac{sin(ax) + sin(bx)}{(a+b)x} \tag{3.51}$$

such that it is normalized in amplitude. Taking values $a = 2$ and $b = 3$ as example values, we can plot the observed coincidence counts for such asymmetric frequency distributions. Obviously it is somewhat immediately clear that extracting the frequency information from the signal can be achieved via a Fourier transformation of the signal pattern.

3.6 SPDC Power Spectral Density

Determining the amount of power, and thus the number of entangled photon pairs, that can be produced through the SPDC process is a crucial element to the design process. In particular if considerations need to be made regarding the photon number occupation of frequency modes, such as is the case in quantum spectroscopy where interactions from uncorrelated pairs can arise in certain situations if the entangled photon generation rate is too high. Therefore, to estimate the power scaling, emission bandwidth, and entangled photon generation rate, we resort to the formalism of Fermi's golden rule in order to calculate the transition rate from the ground-state (in this case the vacuum field), to a specific energy eigenstate (the state where two photons occupy conjugate modes) [9]. As a result of the SPDC process being such

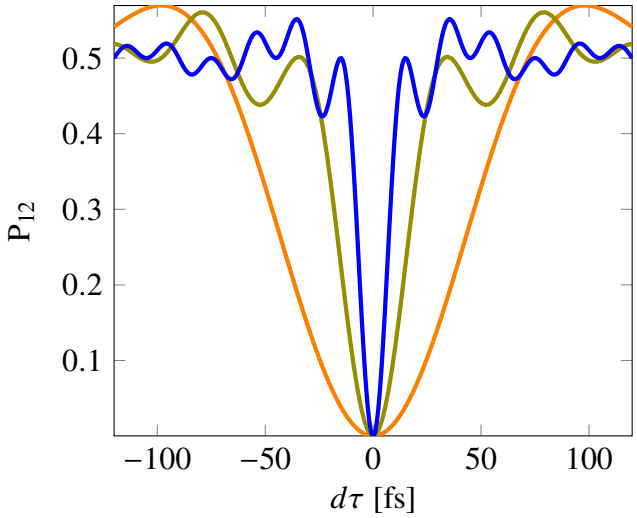

Figure 3.10: Asymmetric broadband Hong-Ou-Mandel interference pattern for three different SPDC bandwidths. The respective bandwidths increase from (orange), to (green), to (blue).

an inefficient process, the usual requirement of being in the weak perturbation limit is somewhat inherently satisfied. The obtained transition rate can be taken to be independent of time. The strength of the coupling between the initial and final states is described by the nonlinear dielectric tensor elements of the material that is used, as well as the density of states that are available to make the transition to.

Here, we specifically focus on the waveguided case, however the approach for free-space gratings is essentially identical and requires only slight modifications. In practice, the same final result could be used by making adjustments for the transverse phase matching component, given the deviation from the paraxial regime when using a focused beam. We begin by writing down the monochromatic field equations following the treatment in [10].

$$\mathbf{E}_{s,i}(\mathbf{r},t) = i\sum_{k}\left(c_k u_k(\mathbf{r})e^{-i\omega^{(k)}t} + C.C.\right). \tag{3.52}$$

Here, u_k satisfies the following three conditions:

$$\begin{aligned}\left(\nabla^2 + \frac{(\omega^{(k)})^2}{n^2c^2}\right)u_k &= 0\\ \nabla\cdot u_k &= 0\\ \int_V u_k^* u_k &= 1\end{aligned} \tag{3.53}$$

with u_k being defined as

$$u_k(\mathbf{r}) = \frac{1}{\sqrt{\Gamma}} U^{(k)}(x,y) e^{i\beta^{(k)} z} \tag{3.54}$$

with Γ being the length of the quantization volume along the propagation axis z. $U^{(k)}(x,y)$ is the k-th transverse mode profile, satisfying the same normalization condition as the pump beam (Eq. 8). The signal and idler beams can be quantized by introducing the electric field operator for each.

$$\hat{\mathcal{E}}_{s,i} = \frac{1}{2}\left[\hat{E}_{s,i}(\mathbf{r},t) + \hat{E}^{\dagger}_{s,i}(\mathbf{r},t)\right] \tag{3.55}$$

$$= \frac{i}{2}\sum_k \left[\left(\frac{2\hbar\omega^{(k)}_{s,i}}{n^2_{s,i}\epsilon_0}\right)^{1/2} \frac{1}{\sqrt{\Gamma}} U^{(k)}_{s,i}(x,y) e^{i(\beta^{(k)}_{s,i} z - \omega^{(k)}_{s,i} t)} \hat{a}^{(i)}_{s,i} + H.C\right]. \tag{3.56}$$

Similarly, the pump beam can be written as follows:

$$\mathcal{E}_p = \frac{1}{2}\left[E_p(\mathbf{r},t) + E^*_p(\mathbf{r},t)\right] \tag{3.57}$$

$$= \frac{1}{2}\left[\sqrt{\frac{2P}{cn_p\epsilon_0}} U_p(x,y) e^{i(\beta_p z - \omega_p t)} + H.C\right]. \tag{3.58}$$

With the assumption that

$$\int dxdy \left|U_p\right|^2 = 1 \tag{3.59}$$

and normalization by

$$P = \int dxdy cn_p\epsilon_0 \left|E_p\right|^2/2 = 1. \tag{3.60}$$

The interaction Hamiltonian can then be written as:

$$\hat{H}_I = -\frac{\epsilon_0 d}{2}\int_V d^3\mathbf{r}\left\{\hat{E}_p\hat{E}^{\dagger}_s\hat{E}^{\dagger}_i + H.C.\right\} \tag{3.61}$$

$$= \frac{\hbar d\sqrt{2}}{\sqrt{\epsilon_0 cn_p n^2_s n^2_i}} \frac{\sqrt{P}}{\Gamma} \sum_{j,k} \sqrt{\omega^{(j)}_s \omega^{(k)}_i} \ldots$$

$$\ldots \int_V d^3\mathbf{r}\left[U_p \left(U^{(j)}_i\right)^* \left(U^{(k)}_s\right)^* e^{i\left(\beta_p - \beta^{(k)}_s - \beta^{(j))}_i\right)z} e^{-i\left(\omega_p - \omega^{(k)}_s - \omega^{(j))}_i\right)t} \hat{a}^{(i)\dagger}_s \hat{a}^{(j)\dagger}_i + H.C.\right]. \tag{3.62}$$

At this point, it is easy to simplify the overall problem by assuming momentum and energy conservation having to be satisfied. Therefore the complex exponential with

wavevectors gets simplified to $\Delta k = \beta_p - \beta_s^{(k)} - \beta_i^{(j)}$, and the complex exponential involving the angular frequencies becomes unity as a result of $E_p = E_s + E_i$.

$$\left|\left\langle f\left|\hat{H}_I\right|i\right\rangle\right| = \left|\left\langle 00\left|\hat{a}_s^{(l)}\hat{a}_i^{(m)}\hat{H}_I\right|00\right\rangle\right| = \left|\left\langle 11\left|\hat{H}_I\right|00\right\rangle\right| \tag{3.63}$$

$$\left|\left\langle f\left|\hat{H}_I\right|i\right\rangle\right| = \frac{d\hbar\sqrt{2\omega_s\omega_i P}}{\sqrt{\epsilon_0 c n_p n_s^2 n_i^2}}\frac{1}{\Gamma}\int_V d^3\mathbf{r} U_p\left(U_i\right)^*\left(U_s\right)^* e^{i\Delta kz} \tag{3.64}$$

$$\left|\left\langle f\left|\hat{H}_I\right|i\right\rangle\right| = \frac{d\hbar\sqrt{2\omega_s\omega_i P}}{\sqrt{\epsilon_0 c n_p n_s^2 n_i^2}\Gamma}\frac{L}{\sqrt{A}} sinc\left(\frac{\Delta kL}{2}\right) d\omega_s \tag{3.65}$$

In a length scale of L, the one dimensional density of states for either signal or idler field is given by:

$$d\mathcal{N}_{s,i} = \frac{Ln_{s,i}}{2\pi\hbar c} dE_{s,i}. \tag{3.66}$$

The density of states for the two-photon output is then the convolution of the individual density of states for signal and idler fields (with the additional condition of $dE_s = -dE_i$)

$$\rho = \left(\frac{L}{2\pi}\right)^2 \frac{n_s n_i}{\hbar c^2} d\omega_s \tag{3.67}$$

$$\Omega = \frac{2\pi}{\hbar}\left|\left\langle f\left|\hat{H}_I\right|i\right\rangle\right|^2 \rho = \frac{d^2\omega_s\omega_i L^2 P}{\epsilon_0\pi c^3 n_p n_s n_i A} sinc^2\left(\frac{\Delta kL}{2}\right) d\omega_s \tag{3.68}$$

subsequently substituting $P_{(s,i)} = \hbar\omega_{(s,i)}\Omega$

$$dP_{WG,s} = \frac{\hbar d^2\omega_s^2\omega_i L^2 P}{\epsilon_0\pi c^3 n_p n_s n_i A} sinc^2\left(\frac{\Delta kL}{2}\right) d\omega_s \tag{3.69}$$

which can be re-written in the wavelength domain, via the substitution of $\omega_i = \frac{2\pi\lambda_i}{c}$

$$dP_{WG,s} = \frac{16\pi^3\hbar c d^2 L^2 P}{\epsilon_0 n_p n_s n_i \lambda_s^4 \lambda_i A} sinc^2\left(\frac{\Delta kL}{2}\right) d\lambda_s. \tag{3.70}$$

References

[1] John F Clauser et al. “Proposed experiment to test local hidden-variable theories”. In: *Physical review letters* 23.15 (1969), p. 880.

[2] Bas Hensen et al. “Loophole-free Bell inequality violation using electron spins separated by 1.3 kilometres”. In: *Nature* 526.7575 (2015), pp. 682–686.

[3] Albert Einstein, Boris Podolsky, and Nathan Rosen. “Can quantum-mechanical description of physical reality be considered complete?” In: *Physical review* 47.10 (1935), p. 777.

[4] Artur Ekert and Peter L Knight. “Entangled quantum systems and the Schmidt decomposition”. In: *American Journal of Physics* 63.5 (1995), pp. 415–423.

[5] Zhe-Yu Jeff Ou. *Multi-photon quantum interference*. Vol. 43. Springer, 2007.

[6] Carlos Henrique Monken, PH Souto Ribeiro, and Sebastiao Pádua. “Transfer of angular spectrum and image formation in spontaneous parametric down-conversion”. In: *Physical Review A* 57.4 (1998), p. 3123.

[7] Morton H Rubin et al. “Theory of two-photon entanglement in type-II optical parametric down-conversion”. In: *Physical Review A* 50.6 (1994), p. 5122.

[8] Kevin Zielnicki et al. “Joint spectral characterization of photon-pair sources”. In: *Journal of Modern Optics* 65.10 (2018), pp. 1141–1160.

[9] Paul Adrien Maurice Dirac. “The quantum theory of the emission and absorption of radiation”. In: *Proceedings of the Royal Society of London. Series A, Containing Papers of a Mathematical and Physical Character* 114.767 (1927), pp. 243–265.

[10] Daniel F Walls and Gerard J Milburn. *Quantum optics*. Springer Science & Business Media, 2007.

Chapter 4

DESIGN AND IMPLEMENTATION OF A FIBER-OPTIC ENTANGLED PHOTON INTERFEROMETER

4.1 Introduction

While typical implementations of experiments utilizing SPDC are based on bulk crystals (BPM) or free-space gratings (QPM), they suffer from numerous disadvantages. Namely, the comparatively low interaction volumes limit the attainable entangled photon brightness which is further complicated by the highly dispersive and divergent profile of the downconverted signal, making efficient collection a challenge. Furthermore, the non-trivial behavior of the associated beam profile, most appropriately approximated by a Laguerre-Gauss (LG) mode with $l \neq 0$, results in free-space beams that are difficult to control, particularly as the bandwidth increases. These LG ($l \neq 0$, $p = 0$) mode profiles are also commonly called donut modes (see Fig.4.1) and have a single, annular-ring intensity distribution with the radius of this ring given by $r_l(z) = w(z)\sqrt{\frac{l}{2}}$. Provided the SPDC bandwidth remains small, the angular distribution will be correspondingly sharp and thus manageable using simple optics. However, broadband SPDC poses the additional challenge of yielding an extended, highly wavelength dependent intensity distribution (more on this in Chapter 5). In most experiments utilizing free-space optical implementations, these issues are overcome by spatially filtering two conjugate points of the ring, selecting entangled photon pairs in the process. These points are then treated as Gaussian beams that are used in the experiment downstream. Obviously the major drawback of this approach is the loss of large proportions of the entangled photon flux. This "wastefulness" is particularly undesirable in imaging applications where high fluxes of entangled photons would indeed be critical for optimal performance.

A somewhat natural solution to these aforementioned issues is to transition away from free-space optics and exploit the highly confined nature of nanophotonic and fiber-optic setups. By utilizing a periodically-poled nonlinear waveguide to generate entangled photon pairs, the inherent mode confinement allows for both co-propagating modes (signal and idler) to be efficiently fiber coupled out of the device. Correspondingly, on the input side, the single-mode injection of the pump wavelength via a single-mode fiber enables the parametric downconversion process

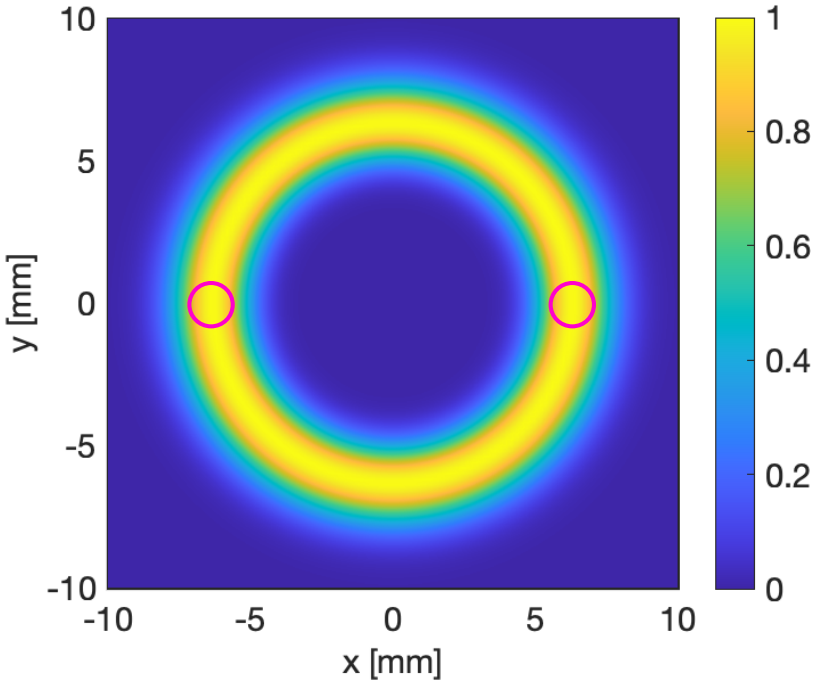

Figure 4.1: SPDC LG(1,0) mode profile intensity distribution and the most commonly used approach to spatially select (pink circles) entangled photon pairs for subsequent downstream manipulation.

to be particularly efficient on a W^{-1} basis. Besides this improvement in coupling and mode-matching efficiency, waveguide SPDC sources are also substantially more efficient than their bulk (grating) counterparts owing to the strong modal overlap between the optical field and the waveguide cross-sectional area. As it will be shown later, the efficiency scaling is particularly strong with respect to the waveguide guided mode area.

The specific implementation of our setup is based on a periodically poled lithium niobate waveguide, designed for type-II quasi-phase-matching a 406nm-812nm conversion. The choice of wavelengths is primarily dictated by optical transitions in two dyes of interest, *R6G* with a virtual state transition and *ICG* with a real sequential transition process, as well as to act as a point of comparison to the free-space setups described in the next chapter. Lithium niobate was selected as the host material for the waveguide due to its high second order nonlinear coefficient and to support the design and development steps for future generation, entirely on-chip nanophotonic architectures that would implement additional photonic components (beamsplitters, modulators, etc.) to enhance overall functionality. As a result of the fiber-coupled output, the experimental setups required for characterization, sample

interactions, and photon measurements are all optical fiber based and thus facilitate a high-brightness, high-efficiency, low-loss, and highly compact platform, which in addition is also entirely maintenance free subsequent to initial alignment. It is these strengths that are leveraged with a nanophotonic/fiber-optic system implementation.

Of particular note regarding the photon-pair source is that in order to substantiate its usefulness, it has to be capable of generating photon-pairs at a high rate, while also ensuring their indistinguishability. By this we mean how little information we possess about the underlying characteristics of the generated photons. An experimental measure of this property is the Hong-Ou-Mandel interference as described in Chapter 3. In practice, the less distinguishing information there is available about the photons being interfered (e.g. frequency, polarization, time-of-arrival), the more likely it is that they undergo boson bunching and therefore display signatures of two-photon interference. The reason for the importance of this is that for our particular application of nonlinear spectroscopy, atomic/molecular two-photon absorption will only occur if two-photon interference manifests itself to a very high degree at the point of interaction. By design, this point is the center of a 50:50 beamsplitter (when performing a HOM type interference experiment) which can be replaced by a two-photon absorptive medium with similar effect.

Lastly, it is interesting to consider the fact that while the implicit photonic entanglement obtained from our photon-pair source is in the time-energy degree of freedom, due to the fiber-optic implementation it becomes trivial to re-configure the fiber-optic circuit such that polarization entangled states are produced as the output of the interferometer. Although this is not (to our knowledge) of practical importance with regards to two-photon absorption events, higher-order entanglement has been studied for its unique properties such as inherent topological protection. Furthermore, entanglement in multiple degrees-of-freedom can increase the information content per photon and display unusually high noise tolerance which scales very favourably with the size of the Hilbert space [1].

4.2 Waveguide SPDC Source

The SPDC source used for the entangled photon interferometer is a periodically poled 5%MgO doped lithium niobate ridge waveguide (see Fig.4.2 for the refractive index curves and associated group-velocity parameters in bulk). The cross-sectional dimensions are $10\mu m$ x 10 μm, with the bottom surface being up against 300nm of SiO2. The other three sides are surrounded by several μm of glass-like epoxy. The

poling period is 1.87μm, corresponding to a type-II quasi-phase-matched configuration for 406nm-812nm. The total length of the waveguide is 20mm, chosen such that it yields a ~20%/W conversion efficiency at the expense of a narrower emission bandwidth.

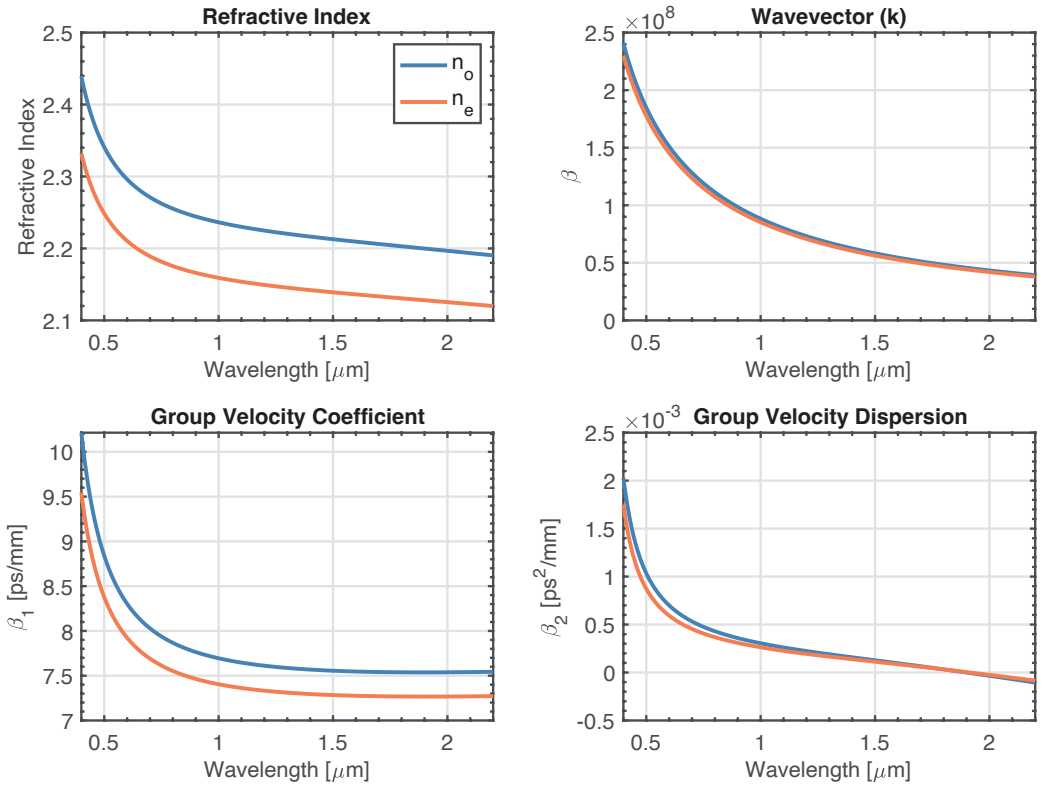

Figure 4.2: Bulk 5%MgO doped-lithium niobate refractive index curves and GVD.

For the specific downconversion process of this source, the input pump field is required to be along the crystallographic Y axis. Correspondingly, due to the type-II phase-matching process, the signal and idler fields are polarized along the Y and Z axes. The mode profiles of the pump, signal, and idler modes are shown in Fig.4.3a,b,c, where it is easy to see the total confinement of the guided modes as a result of the relatively large waveguide geometry. The mode indices (effective refractive index) of each mode are extracted from the FEM simulations and are $n_p = 2.43$, $n_s = 2.2531$, and $n_i = 2.1735$, respectively. Correspondingly, these simulations are used to calculate the group velocity dispersions, v_g, since waveguide dispersion has to be taken into account for the calculation of the appropriate poling period. When accounting for these effects, the poling period of 1.87μm efficiently phase-matches the SPDC process at 73°C. The effective refractive index curves

and group velocity dispersions for our specific waveguide geometry are shown in Fig.4.3b.

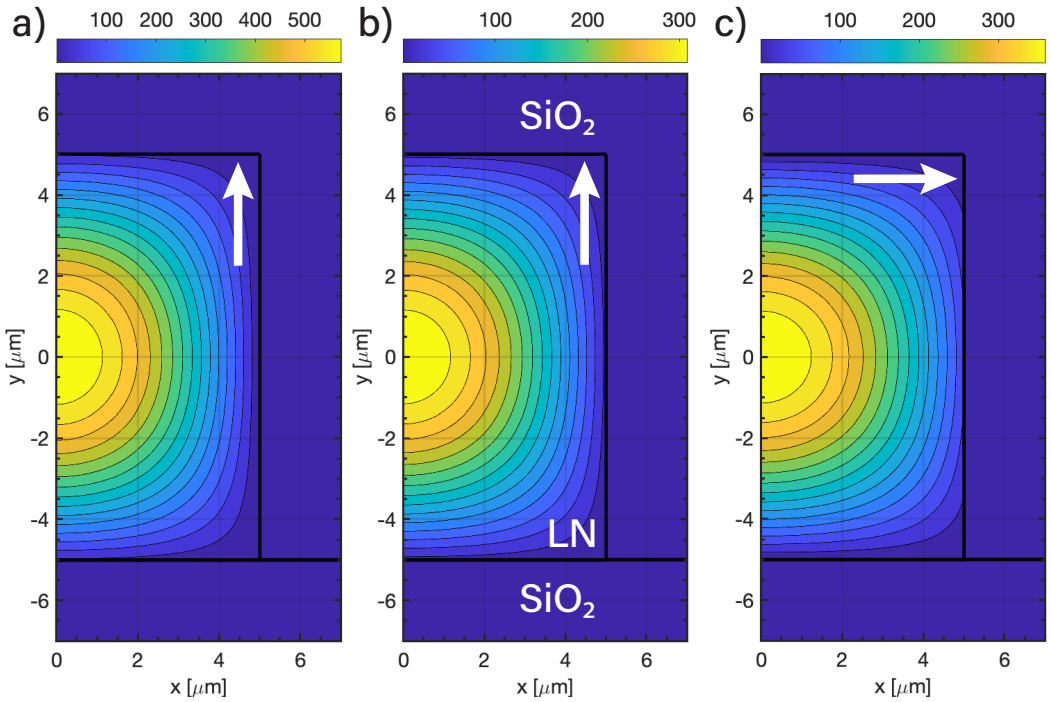

Figure 4.3: Contour plot of the LN waveguide electric-field mode profiles for all three interacting fields. (a) 406nm pump mode, (b) 812nm signal mode, and (c) 812nm idler mode. The respective polarizations for each mode are shown using the white arrows.

Fiber coupling of the light into and out of the waveguide is done using butt-coupled single mode fibers. At the input, a Corning PM400 type fiber is used which has a mode field diameter of $\sim 3.5 \pm 0.5\mu m$. The output is collected using a Corning PM850 fiber with a mode field diameter of $\sim 5.5 \pm 0.5\mu m$. Both fibers are polarization maintaining PANDA fibers, and thus preserve the polarization states of both the light used to pump the waveguide, as well as the orthogonally polarized SPDC photons. The fiber coupling efficiencies can be analytically estimated via the overlap integral of the fiber and waveguide fundamental mode distributions Eq.4.1.

$$\eta = \frac{\left|\int E_1^* E_2 dA\right|^2}{\int |E_1|^2 dA \int |E_2|^2 dA}. \tag{4.1}$$

Here, E_1 and E_2 are the complex electric fields that are supported by the fiber and waveguide, respectively. The field distributions can be easily extracted from FEM simulations given the geometry, while that of the fiber is approximated through the

mode field diameter quoted in the specifications of the fiber. The effective coupling efficiencies are approximately 60% at both ports, which were obtained by including the losses stemming from the finite divergence of the fiber mode. The coupling efficiencies were verified experimentally.

By the nature of the fiber coupling being optimal for the fundamental modes of both the fiber and the waveguide, the SPDC process will primarily be pumped by the TE_{00} mode. Given that the mode area is a factor in the effective downconversion efficiency as shown in the theory section, the maximum flux of of entangled photons is obtained when all three interacting fields are in their fundamental propagating modes. While higher-order modes are obviously also supported given the (relatively) large waveguide geometry, these are assumed to fiber-couple inefficiently, in addition to not participating in the SPDC process very strongly due to their reduced interaction areas.

The periodic poling used for the waveguide was determined by calculating the phase-mismatch given a 406nm pump wavelength. This is shown as a surface plot in Fig.4.5a where the red iso-line signifies values where $\Delta k = 0$. The phase-matching temperature for this poling period is ~73C as shown in Fig.4.4.

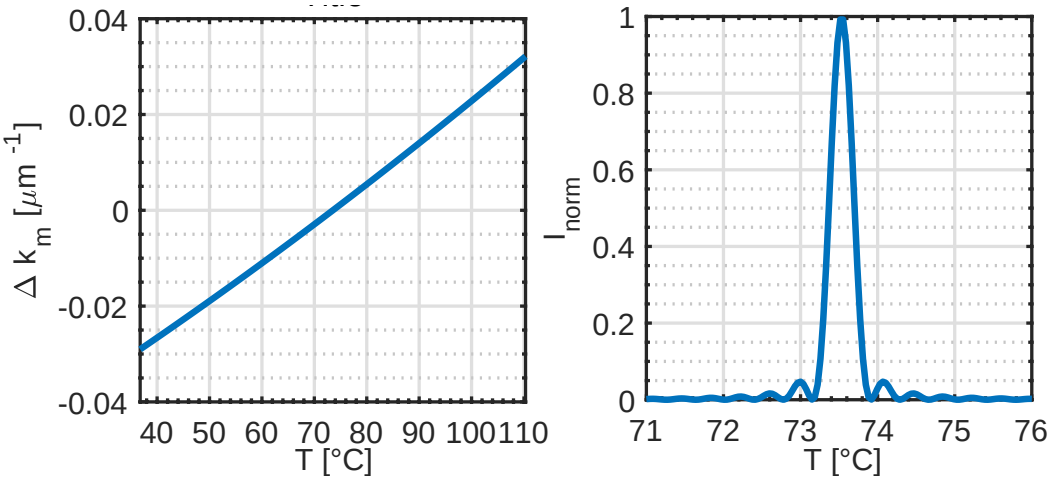

Figure 4.4: Temperature dependent phase-mismatch (left) and the expected relative output signal intensity (right).

To calculate the expected SPDC output spectrum, we follow the theoretical derivation described in detail in Ch.3, whereby we carry out the quantization of the electromagnetic fields involved in the three-field interaction and subsequently use Fermi's golden rule to arrive at the transition rate, Ω, between our initial and final states, corresponding to the pump and signal/idler fields, respectively. The transition

rate is then used to define the power available in each signal wavelength mode.

$$dP_{WG,s} = \frac{16\pi^3\hbar c d^2 L^2 P}{\epsilon_0 n_p n_s n_i \lambda_s^4 \lambda_i A} sinc^2\left(\frac{\Delta k L}{2}\right) d\lambda_s. \tag{4.2}$$

Given the Type-II phase-matching process, the nonlinear optical coefficient used is the tensor element $d_{31} = d_{15} = 5.95$pm/V [2]. As a result of the quasi-phase-matching implementation used, this coefficient has to be adjusted by a factor of $\frac{2}{\pi}$, yielding an *effective* nonlinear optical coefficient, $d = \mathbf{d}_{eff} = 3.79$pm/V. Estimating

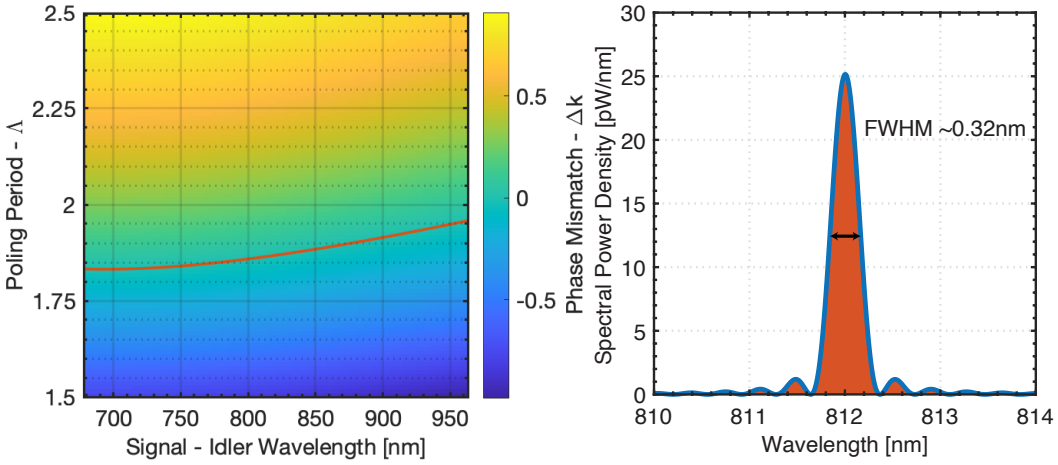

(a) (b)

Figure 4.5: (a) Quasi-phase-matching surface plot for our ppLN waveguide using a 406nm pump wavelength, with the zero-Δk iso-line being shown in red. At 812nm, the poling period is found to be $1.87\mu m$. (b) Theoretically calculated spectral power density for our waveguide at 1mW input pump power, with the corresponding extracted FWHM value. The total area (shaded in orange) is used to determine the theoretical pair generation rate of the source.

the pair generation rate is then possible by integrating Eq.4.2 with respect to the wavelength variable, calculating the area under the curve in Fig.4.5b.

$$P_{WG} = \int P_{WG,s} d\lambda_s. \tag{4.3}$$

Subsequently, the pair generation rate, R_{pg}, is defined as

$$R_{pg} = \frac{P_{WG}\lambda}{hc}[pairs/s/mW]. \tag{4.4}$$

For our ppLN waveguide source, we calculated $R_{pg} = 3.66 \times 10^7$ pairs/s/mW.

Due to the temperature dependence of the refractive index of the material [3], the downconverted signal is particularly sensitive to temperature fluctuations. In

comparison, KTP shows a less severe temperature dependence and is thus quite well suited for room-temperature operation where no active temperature stabilization is utilized. For the ppLN waveguide used here, the phase-matching temperature bandwidth is extremely narrow as shown in Fig.4.4. This is further complicated by the fact that the emission bandwidth is predicted to be less than 0.5nm, and therefore the spectral overlap as a function of temperature will have to be very accurate.

4.3 Entangled Photon Characterization

To characterize the waveguide source and its performance, we utilized a simple coincidence counting setup. The main advantage of this is that coincidence counting is highly selective to the measurement of photon pairs which have some underlying temporal correlation as we discussed in Ch.3. Therefore, in order to prove the existence of entangled photon pairs generated via SPDC, we can analyze the coincidence histogram from a TCSPC. The experimental setup is shown in Fig.4.6, and fundamentally consists of a long-pass filter, a fiber-optic polarization beamsplitter, and two SPADs. The long-pass filter removes any residual 406nm pump light, after which the polarization beamsplitter is used to separate the orthogonally polarized photons into two spatial modes. The SPADs are then used to monitor the arrival of the two entangled photons and using the technique of TCSPC, create a histogram showing the relative timing statistics. Both SPADs are operated in free-running mode, meaning that there is no applied temporal gating and therefore the measurements are only limited by the associated dead-times (~45ns). The spectral sensitivity of the avalanche diodes is shown in the Appendix, with an expected detector efficiency at 810nm of ~50%. Given the extreme sensitivity of the SPADs, we enclosed them in light-tight boxes to shield from ambient light, and thus reduce the measured dark counts. Experimentally observed dark counts were regularly at, or below the level of ~10Hz. To extract the pair generation rate, R_{pg}, from a coincidence counting measurement, we need to normalize by the overall detection efficiency for the signal and idler photons together. In addition, we also divide by the input pump power to obtain a per mW value, leading to the expression,

$$R_{pg} = \frac{R_c}{\eta_s \eta_i P}. \tag{4.5}$$

The detection efficiencies for each photon are a product of the coupling, transmission, and detection efficiencies starting at the output of the waveguide, all the way to the detectors themselves. The approximate characterization of these losses was done using a coherent source in conjunction with relying on manufacture specified values

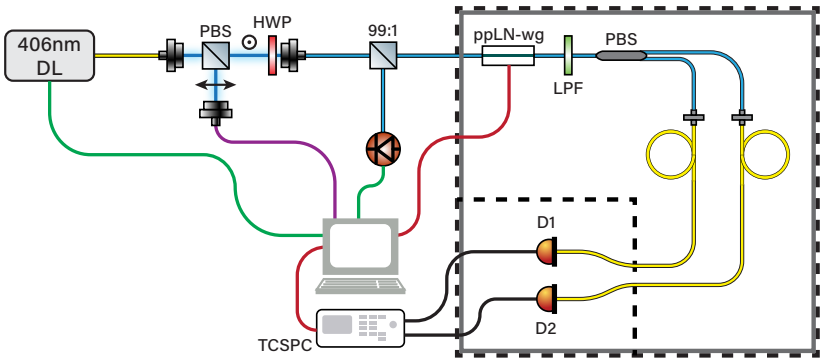

Figure 4.6: Fiber optic coincidence counting setup for characterization of the ppLN SPDC waveguide.

where appropriate. Multiplying all of the individual losses together, we obtain $\eta_s = 10\%$, and $\eta_i = 11\%$. To note is that these efficiencies are specific to only the coincidence counting scheme used as shown in Fig.4.6. The extension of the setup to include both interferometer arms drastically further reduces these values to $\sim 1\%$. By directly taking the output of our waveguide and filtering the SPDC signal with a 1nm bandpass filter to remove most of the fluorescence background, we have calculated and R_{pg} of $\sim 4.09 \times 10^7$ pairs/s/mW, which is in reasonable agreement with our theoretically predicted value. One reason for the discrepancy is the extremely narrow SPDC bandwidth of only ~0.3nm, which means that our 1nm bandpass filter still allowed some fluorescence photons to be sent to the detector. Furthermore, the estimated detection efficiencies may not be perfectly accurate due to polarization dependent coupling effects. As expected, the measured value is orders of magnitude larger than those obtained from traditional bulk gratings, owing to the tight confinement of the waveguide geometry.

An example coincidence histogram is shown in Fig.4.7. The finite width of the peak can be attributed to the detector and time-tagging electronics jitter, as well as the bandwidth of the source resulting in a dispersive broadening of the simultaneous arrival of photon pairs. Given the timing resolution of 1000ps of our SPADs, the coincidence window within which we can consider the simultaneous arrival of two photons to be a true event is chosen as $3 * 512$ps=1536ps. The 512ps factor is defined as a result of the time-tagging electronics' resolution, with the multiplier of 3 chosen such that the two bins adjacent to the peak are taken into consideration. This window is highlighted in orange. The position of the peak at ~17ns is experimentally enforced through the introduction of an electronic delay so as to place it away from the 0ns point. To distinguish between true and accidental coincidences, we

perform a Riemann sum of the data points being used and subtract the noise floor average multiplied by the coincidence window. This average is calculated away from the coincidence peak using a wide time-window ≫1ns. To characterize the

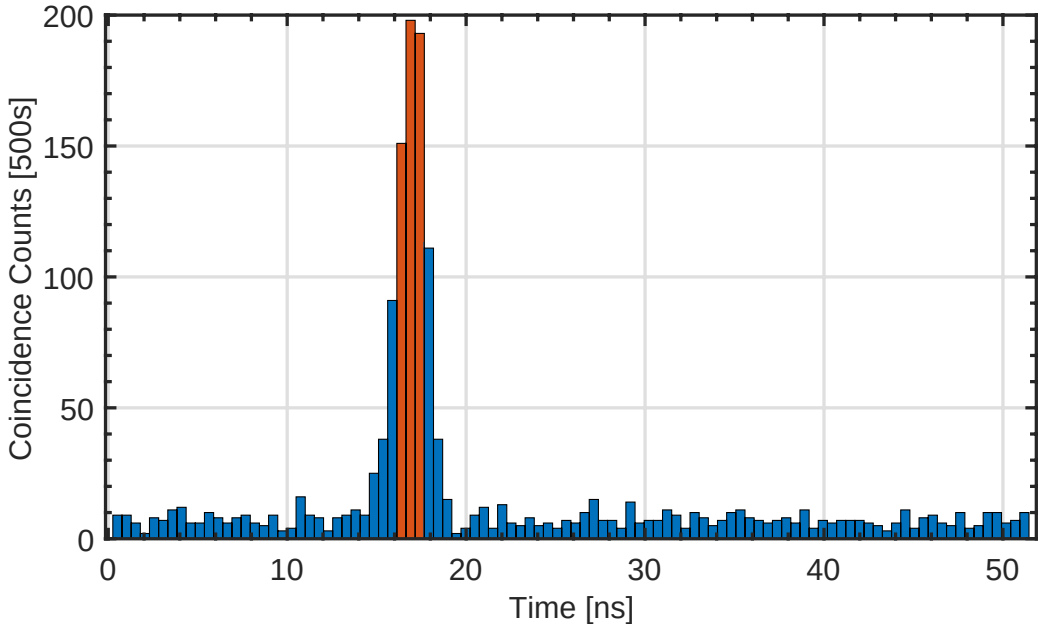

Figure 4.7: Coincidence counting histogram. Orange colored bars highlight the coincidence window in which the simultaneous arrival of two photons is taken to be a true coincidence. Away from this window, the events are registered as accidental coincidences due to background noise.

power dependence of the waveguide and its generated SPDC signal, we performed coincidence counting measurements across a wide range of input pump powers. The resulting scalings of the true and accidental coincidences are shown in Fig.4.8. Fitting the experimental data reveals the linear and quadratic scaling of the raw and accidental coincidences, respectively. A particularly useful metric to define for the SPDC source in use is a "pseudo" signal-to-noise ratio. By taking the ratio of the true and accidental coincidences, we calculate the "coincidence-to-accidental ratio" (CAR). The extracted CAR at various pump powers is shown in Fig.4.9, where the degradation at higher powers is clearly visible. This is a result of the previously observed quadratic scaling of the accidental coincidences, which start to dominate at higher pump powers and thus raise the noise-floor at a faster rate than the true coincidences are able to scale. While not shown in the plot, at even lower pump powers, the CAR value begins to drastically decrease again as the generation rate of entangled photon pairs no longer provides a significant contribution. The plot effectively shows that there is a region of optimal operation at low pump powers

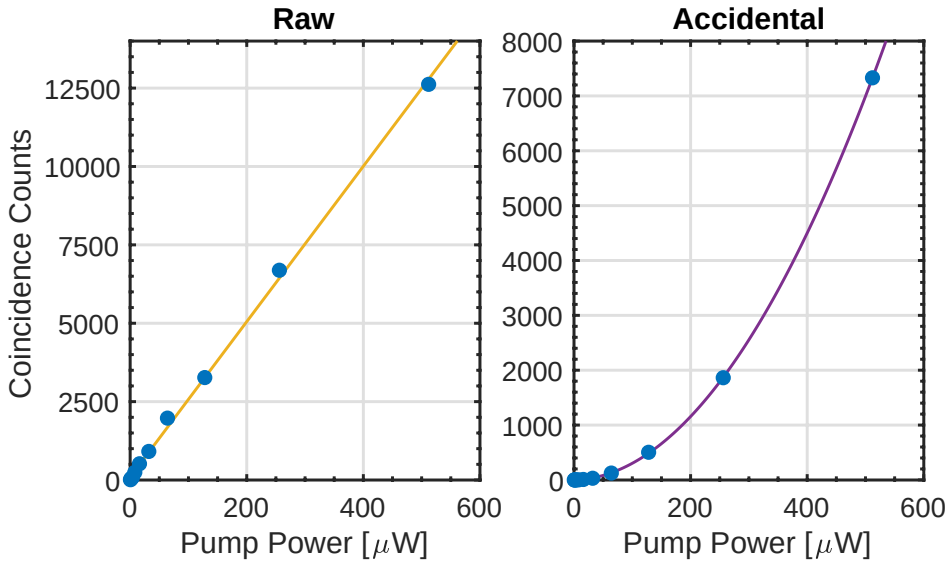

Figure 4.8: Power scalings of the raw (i.e. real) and accidental coincidences as extracted from the histograms produced above. The line fits demonstrate the linear and quadratic scaling of each, respectively, which leads to the relationship that dictates the coincidence-to-accidental ratio as shown in Fig.4.9

where the source is utilized in a way so as to maximize its "noise-resistance."

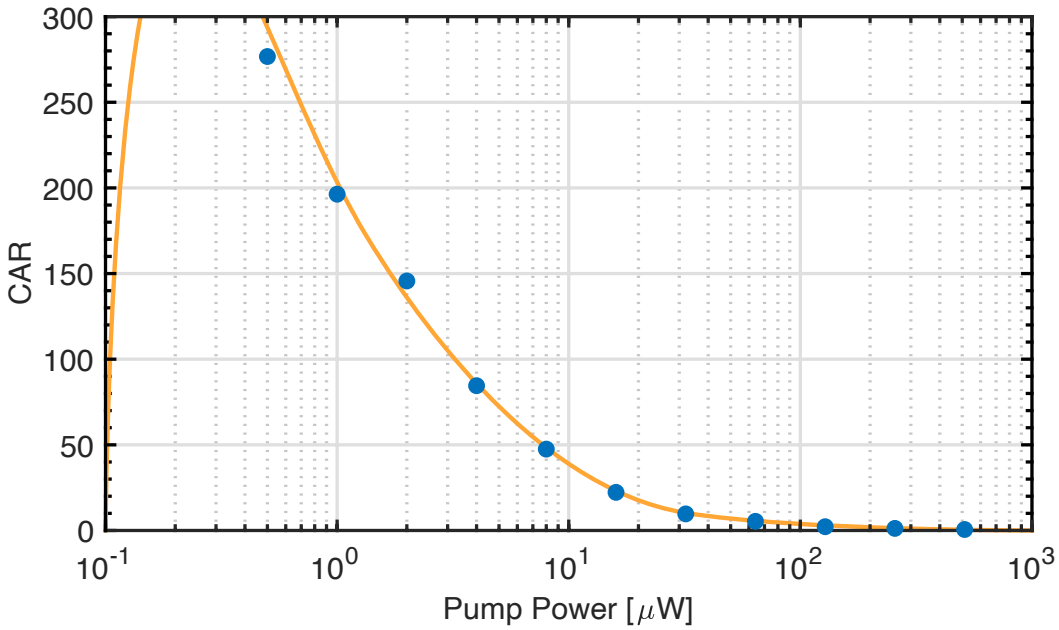

Figure 4.9: Coincidence-to-accidental ratios for a range of input pump powers. At low powers, the true coincidences outnumber the background, and provide a better effective signal-to-noise ratio. As the pump power is increased, the accidental coincidences caused by fluorescence photons begin to dominate and deteriorate the CAR value.

4.4 HOM Interference Experiment

The experimental setup used for demonstrating two-photon interference is based on a fiber-optic Mach-Zehnder Interferometer (MZI). In this scheme, two beamsplitters are used to split, and subsequently recombine the input signal. The main advantage of this layout is that no signal is lost due to back-propagation as it would be the case in a Michelson scheme using only a single beamsplitter. The conceptual layout for a fiber-optic MZI is shown in Fig.4.10a. To systematically study the interference pattern created between the signals in both arms, the phase of one arm is adjusted relative to that of the other. By doing so, in the classical case with a cw signal, the two sine waves are shifted such that they either constructively or destructively interfere. This manifests itself as a modulation of the detected power in the two output arms of the second beamsplitter. The interferometric signal can then be written as:

$$V = V_0 \left(1 + \nu cos\phi cos\theta\right) \tag{4.6}$$

where V_0 is the measured signal amplitude when no interference occurs. The quality of the interference, or contrast, is given by the so-called visibility, ν.

$$\nu = \frac{I_{max} - I_{min}}{I_{max} + I_{min}} \tag{4.7}$$

The phase ϕ is a function of the difference between the lengths of the interferometer arms (reference and control). θ is the angular variable signifying the polarization alignment difference between the two interacting fields. Thus, when the polarization are orthogonal, no interference is observed.

As is clear from the equation, the modulation depth is primarily determined by the relative powers in both arms, how accurately the relative phase is set, and how well the polarzations are aligned with respect to each other. Fig.4.10b shows how these parameters dictate the value of V. While in principle the use of polarization-maintaining optical fibers would somewhat simplify the MZI, due to limitations in available wavelength specific components as well as greater experimental freedom, the interferometer is built using regular single-mode fibers. As such, the polarization degree-of-freedom needs to be accounted for, which will be discussed later. An important point when dealing with classical interference is to consider the coherence length of the source used. Interference between the two arms is only possible if the relative path-length difference between the two arms is within the coherence length, defined as

$$L_{coh} = c\tau_{coh} = \frac{c}{\pi \nu_{FWHM}}. \tag{4.8}$$

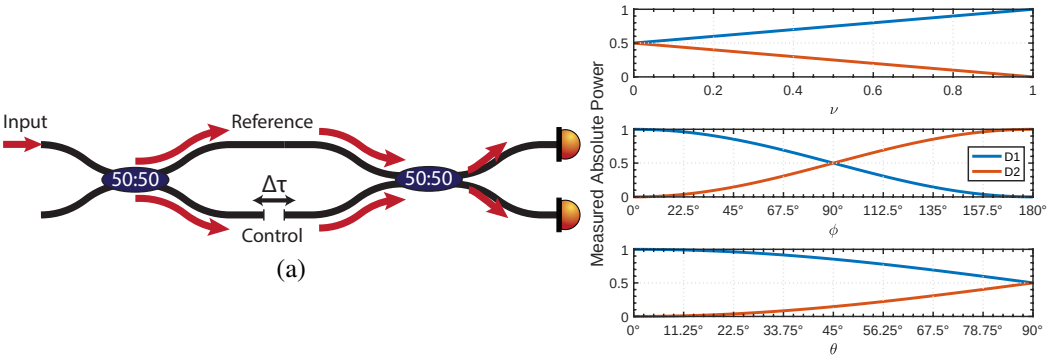

Figure 4.10: (a) Schematic layout of a fiber-optic MZI. One port of a 50:50 beamsplitter is used as the input, which then effectively results in a homodyne detection scheme. The "reference" arm is used as the local oscillator, while the "control" arm is set up so as to allow sensing, phase-adjustment via an optical delay, and polarization control to match the properties of the adjacent arm. (b) Plots showing the dependence of V on the free parameters ν, ϕ, and θ. The blue and orange curves reflect the detectors D1 and D2, respectively.

Thus, narrow-linewidth lasers which have extremely long coherence lengths are less sensitive to path-length differences between the interferometer arms. In contrast, broadband sources, with short coherence lengths, require the arm lengths to be matched very precisely. This property of narrow-linewidth lasers proves useful for the purposes of aligning the MZI prior to utilizing single photon states as the input. The obvious downside to this is that the interferometer arms need to be correctly measured to within the delay stage throw distance. Alternatively, broadband sources with very short coherence lengths, such as SLDs can be used to accurately align the arm lengths and find the zero time-delay point quickly.

Without access to broadband light sources, in order to help with the process of equating the MZI arm-lengths, it is quite useful to rely on calculating the approximate timing diagram for each arm. For this, we calculate the propagation times of each photon as a function of the medium it is traversing. As such, we can plot the accumulated time that each photon needs to make it through either arm of the MZI and subsequently arrive at the interfering 50:50 beamsplitter. By taking the delay stage range as the minimum/maximum that this arrival time can be shifted by, it becomes much simpler to match the arm lengths when using some off-the-shelf components which prohibit easy fiber-splicing. The photon timing diagram for the MZI used here is shown in Fig.4.11.

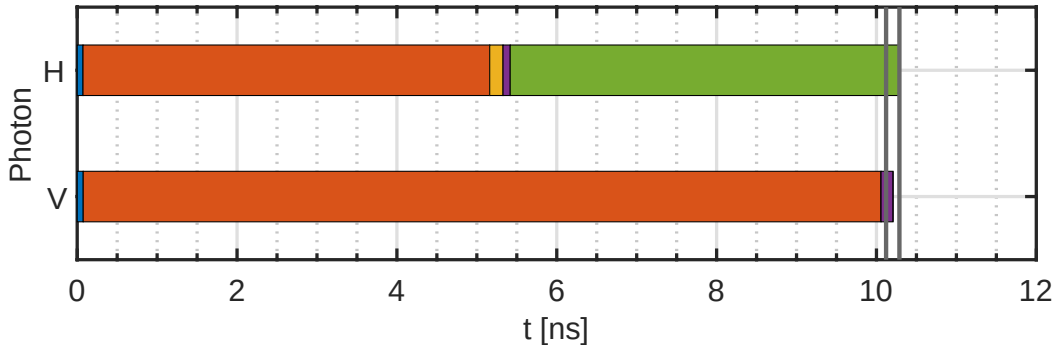

Figure 4.11: Photon timing plot for calculating interferometer arm lengths and corresponding delay lengths. From left to right, for the horizontal polarization H, we have: (blue) ppLN waveguide, (orange) 104cm optical fiber, (yellow) 5cm free-space, (purple) 2.7cm delay-stage internal delay, (green) 100cm optical fiber. For the vertical polarization, we have: (blue) ppLN waveguide, (orange) 205cm optical fiber, (purple) 4.5cm static free-space compensation. The vertical gray lines represent the minimum and maximum possible positions of the delay-stage, bounding the range within which the interferometer arms need to fall.

Analogous to how quantum interference fundamentally relies on the indistinguishability of the two interacting photons, with coherent signals it is also necessary to match their properties. Under the assumption that the MZI is operated in a homodyne scheme, the equivalence in frequency is a given. Further, the balancing of the interferometer arm-lengths ensures that the phase/delay is appropriate such that the two waves interfere. This leaves us with the polarization degree-of-freedom being the last variable to align. In order to do so, we take advantage of a Ti:Sapp laser and its corresponding long coherence length. This helps in two major ways. Firstly, the signal strengths of a coherent signal can be set such that the overall system efficiency of the MZI does not hinder in detecting interference using a regular photo-diode. Second, the long coherence length provides a certain amount of tolerance in the initial position of the delay stage. Therefore, even if the arm-lengths are not perfectly made to match by designating a "time-zero," it is still possible to optimize the polarization degree-of-freedom to a high degree. Experimentally, owing to the simplicity provided by the fiber-optic implementation, the alignment procedure is easily carried out by re-configuring the circuit to utilize the "B" ports shown in Fig.4.12. These correspond to the outputs of a polarization beamsplitter that has as its input, the narrow-linewidth Ti:Sapp laser. Rotating the input polarization by 45°, we obtain an even split of the input power and thus a balanced output with orthogonal polarization states. Subsequently these are then used as the inputs of the

MZI, where a motorized three-paddle polarization controller is adjusted to obtain perfect interference. Long term polarization drift has not been observed as a specific issue and therefore only a single initial alignment is required. After the alignment

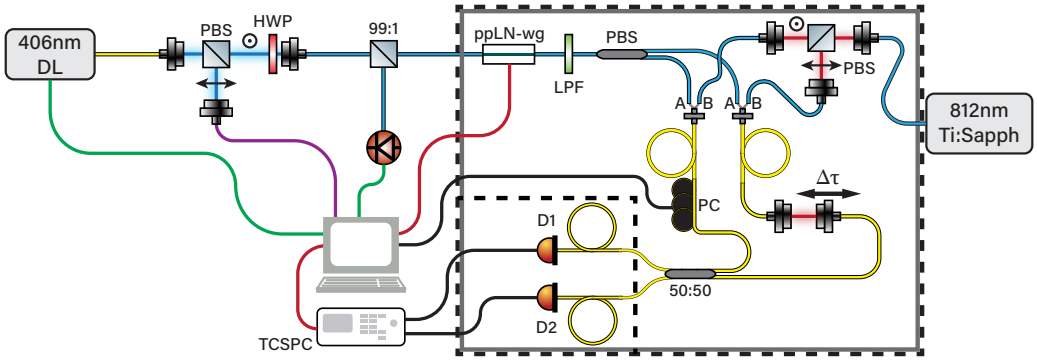

Figure 4.12: Experimental layout of the fiber optic entangled photon interferometer used to demonstrate Hong-Ou-Mandel interference. The fiber-coupled 406nm diode laser is polarization conditioned using a PBS and HWP. The ppLN input pump power is monitored using a 99:1 beamsplitter. The ppLN output is filtered using a LPF to remove residual 406nm pump light. The orthogonally polarized photon pairs are separated using a PBS and directed into the two arms of a MZI. The reference arm consists of a variable air-gap delay stage with matched fiber collimators. The control arm has a motorized three-paddle polarization controller to allow the adjustment of the photon polarization to match the reference arm. The two arms are recombined on a fiber-optic 50:50 beamsplitter. The outputs are fed into two fiber-coupled SPADs that are part of a coincidence counting setup using a TCSPC module. Calibration of the MZI is performed using a narrow linewidth 812nm Ti:Sapp laser which is used as the input to a polarization based power splitter to produce a balanced interferometer signal.

procedure is carried out using the coherent source, simply re-configuring the input ports of the MZI to use the outputs of the polarization beamsplitter which separates our orthogonally polarized entangled photons is all that is needed. Connecting ports "A" sends the entangled photon pair from our ppLN waveguide through the aligned and calibrated MZI, in essence making it a Hong-Ou-Mandel Interferometer (HOMI). As a result of the entirely single-mode fiber guided setup, the spatial degree-of-freedom is here implicitly taken care of and requires no further attention.

As discussed in previous chapters, the entangled two-photon states generated via SPDC have an associated "coherence time" which is directly related to the spectral bandwidth of the downconverted spectrum. A particular feature of HOMI is that by its nature of being a fourth-order interference effect, it is highly selective to the interference of the correlated two-photon state. As a result, the incoherent

background "noise" stemming from fluorescence photons does not play a part in the HOM interference. This is especially advantageous if one contrasts it to a regular spectral measurement using a spectrometer. In this case, the background noise could feasibly wash-out the contribution of the actual signal and therefore make spectral characterization challenging. This is supported by our experience when attempting to measure the output spectrum of the waveguide directly by utilizing an emCCD-spectrometer. Although the measured signal was strong enough to be picked up by the detector, the incoherent contribution from fluorescence made it exceedingly difficult to resolve the SPDC photons. The relationship between the coherence time measured in a HOMI and the corresponding SPDC spectral bandwidth is given by Eq.4.9.

$$\Delta\lambda = \frac{\lambda^2}{2c\tau_c}. \tag{4.9}$$

Owing to the very narrowband spectrum of our source (~0.3nm), no further spectral filtering was implemented to eliminate the existence of common satellite peaks. Such extremely narrow passband filters would have required further free-space elements which was undesirable. A potential solution for performing high rejection-ratio filtering would include the use of a fiber-optic circulator and a fiber-Bragg-reflector (FBR) immediately after the waveguide.

The overall experimental layout for the HOMI is shown in Fig.4.12. We use a diode laser which is single-mode fiber-coupled as our pump source. We ensure the pump wavelength is exactly centered at 406nm by monitoring the horizontally polarized portion of the output using a tabletop spectrometer and adjusting the diode temperature to shift the output spectrum. The vertical polarization is then passed through a half-waveplate to adjust the polarization angle relative to the fast and slow axes of the polarization maintaining fiber into which we couple our light. We then use a 99:1 fiber-optic beamsplitter to pick of the majority of our power, which we monitor using a power meter. This allows for the injected power into the waveguide to be monitored and adjusted during experiments if needed. The 1% output of the beamsplitter is sent to the input fiber of the ppLN waveguide. The waveguide itself is mounted on top of a TEC/heating element, which is actively temperature stabilized using a PID loop. The output of the waveguide, now consisting of the SPDC signal together with the remaining 406nm pump, is passed through a long-pass filter to remove the residual pump. After the filter, the orthogonally polarized entangled photon pairs are separated using a fiber-optic polarization beamsplitter. The outputs of this beamsplitter are PM fibers which ensure that the polarizations of each photon

are kept intact. At this point, the HOMI is entirely built using standard single-mode fibers which do not maintain the polarizations of the states but rather let them evolve freely as a function of the topology of the fibers. One of the interferometer arms (reference arm) has a free-space delay stage consisting of two collimators which are aligned with high precision so as to minimize the stage position dependent coupling loss. The polarization in this arm is left to freely evolve. The adjacent interferometer arm (control arm) has a motorized paddle polarization controlled, which is used to align the polarization of the photons to match that of the reference arm. The two arms are then connected to a fiber-optic 50:50 beamsplitter which acts as the point where interference and therefore boson-bunching is to occur. The outputs of of the 50:50 beamsplitter are connected to a pair of fiber-coupled single-photon avalanche detectors (SPADs) operated in free-running mode, which have their peak sensitivity at $\approx$ 800nm. The electrical signal from the SPADs firing is directed to a time-correlated single-photon counting circuit, which time-tags the electrical pulses and bins them according to their coincidence event time-bins similar to the experiments done in Sec.4.3.

As discussed in Sec.4.3, there is balance that needs to be met between using higher pump powers and the corresponding acquisition time lengths. Obviously higher pump powers yield more coincidence events, however this is at the expense of a higher background noise level due to more fluorescence photons as well as temporally overlapping photon pair generation inside the waveguide. Correspondingly, lower pump powers result in a significant improvement in SNR/CAR, however the integration time of the experiment has to scale up to make up for the loss in overall coincidence events being detected. For our HOM interference measurements, the overall system (interferometer) efficiency of $\sim$1% requires the input pump power to be at the $\sim 200\mu W$ level to produce significant SPAD counts in the $\sim 10^5$ range so as to reduce the overall integration time per delay position to realistic timescales (5-10mins). To obtain experimentally significant photon interference statistics, the total integration time at each delay-stage position is set to be 250s. The measurement is subsequently repeated for each delay-stage position for a total acquisition time-length of 4 hours. Fig.4.13 shows a measured HOM interference plot for a delay-stage range close to the zero relative time-delay point. The triangular shape of the interference pattern is a result of the rectangular two-photon wave function in type-II SPDC processes [4]. From the plot, the two-photon coherence time is estimated to be 3.15ps. This would correspond to the two-photon bandwidth to be $\sim$0.35nm, which is in reasonable agreement with the theoretically calculated value

using the Sellmeier equations for 5% doped MgO:LN.

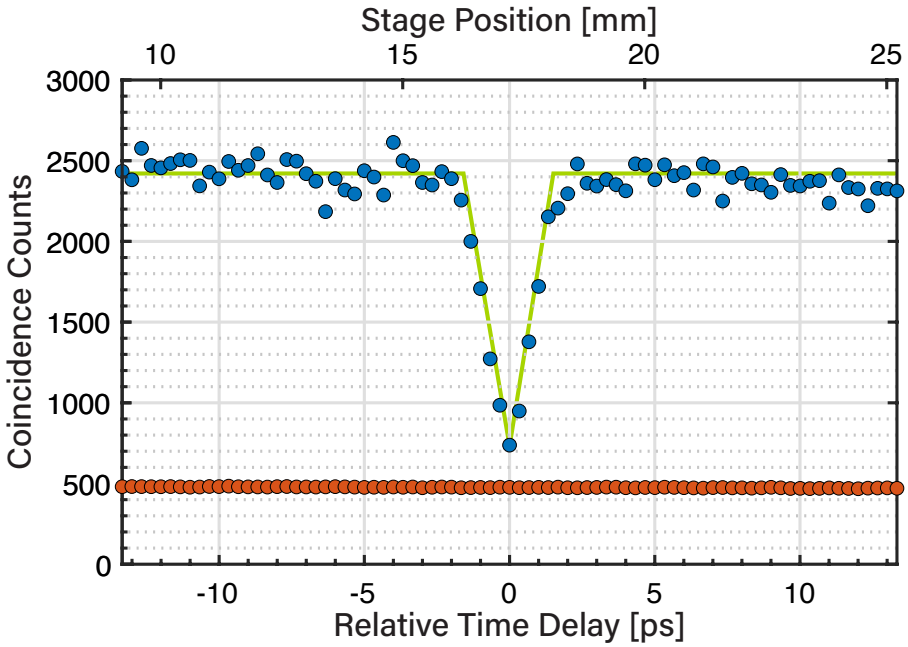

Figure 4.13: HOM interference for our type-II SPDC waveguide source. The blue markers represent real coincidences, while the orange markers defining the baseline are the extracted accidental coincidences. The green triangular fit to the data allows the two-photon coherence time to be determined.

A particular experimental consideration for such a fiber-optic implementation is the fact that non-polarization-maintaining single-mode fibers are particularly sensitive to local temperature fluctuations [5]. Temperature induced polarization drift can degrade the interferometer performance on short time-scales, provided the fibers are allowed to thermalize through a large sink, such as the optical table itself. This condition is further improved by taping down fibers to the table and making sure the overall interferometer footprint is kept as small as possible to avoid large temperature gradients. Furthermore, to isolate the system from the laboratory environment, and thus any air-flows resulting from the HVAC system or day-to-day use of the space, we enclosed the interferometer in a light-tight box which was covered in 1/2" of polyurethane foam insulation on the inside. The performance of this setup was verified by calibrating the MZI using the Ti:Sapp source for near-perfect visibility and subsequently checking the interference pattern after 24 and 48 hours, with no observed changes. Therefore once the polarization alignment is done and the ports are switched to convert the MZI into a HOMI, the system remains stable for multiple days of measurements.

Since the visibility of the HOM interference is strongly dependent on the spectral overlap of the signal and idler photons, and regular spectral characterization using a spectrometer is challenging given the weak SPDC signal and corresponding strong fluorescence background, we repeated the same measurement at different phase-matching temperatures. By sweeping through the crystal temperature degree-of-freedom, we optimized the spectral overlap by finding the point at which our HOM visibility was optimized. Owing to the very narrow bandwidth of the SPDC signal, the temperature sensitivity of the HOM dip was very strong. In contrast, broader downconversion signals can be more easily spectrally filtered to enforce an identical signal-idler spectrum.

4.5 Conclusion

Here, we demonstrated the experimental implementation of a fiber-optic HOMI which utilizes a ppLN waveguide source that produces orthogonally polarized entangled photon pairs at 812nm. We carried out numerical simulations to predict the properties of the source, including mode field distributions, quasi-phase-matching calculations, as well as the expected power spectral density spectrum of the SPDC signal. The source itself was then characterized using a coincidence counting scheme which looked at the detection of simultaneous photon arrivals in order to post-select for the two-photon states. This technique enabled us to extract crucial parameters, such as the generation rate of $\sim 4.09 \times 10^7$ pairs/s/mW, and a coincidence-to-accidental ratio (CAR) of ~350. The experimentally measured generation rate was in reasonable agreement with our theoretically calculated value, with the discrepancy being primarily attributed to difficult to characterize component/system losses, the lack of narrowband filtering of the SPDC signal, resulting in a large flux of residual background/fluorescence photons being detected, and the potential effective loss of real coincidences due to photon pairs being generated at a high enough rate.

The HOM interference measurements performed showed a visibility of ~78%, which was limited by the imperfect spectral overlap of the signal and idler photons given their very narrow bandwidth and high phase-matching temperature sensitivity. Furthermore, the large number of fluorescence photons resulted in a degradation of the photon counting statistics that could be easily improved through the implementation of narrowband tunable filters. The relatively low overall system efficiency due to fiber connectors being used instead of direct fiber-splices also had a significant impact on all the presented measurements. The consequence of this is two-fold.

First, in order to make up for the photon losses in the interferometer, a higher pump power needed to be used, which comes at the expense of higher fluorescence photons being generated as well as pushing the effective generation rate to be so high that temporally overlapped photon pair generation becomes a significant issue. In this case, measurements of uncorrelated photon pairs as real coincidences contribute to the real signal and skew the measurement statistics. Second, the total measurement times become particularly long due to each sample step requiring an integration time of multiple minutes. This is unavoidable as enough coincidences need to be registered to be able to draw significant statistical conclusions from the data. Here, lower system losses, which also includes the detection efficiency, would lead to a significant improvement in both the signal quality as well as the total experimental run-times. Particularly as single-photon losses in a single arm of the interferometer are just as bad as the two-photon case, since the loss of one half of the pair immediately leads to a lost coincidence event. Given that these single-photon losses affect either arm, the tolerance scales quadratically.

Immediate improvements to the overall setup would be best directed towards decreasing the propagation losses through the use of fusion splices. These can have insertion losses as little as 0.03dB and thus >99% transmission. Given that in the current setup, each interferometer arm has ~5 fiber connections, the improvement would be on the order of 3x (32% vs. 97% overall transmission with connectors vs. splices, respectively). As mentioned before, the 3x reduction in loss would subsequently carry with it an effective system-level improvement of ~9x due to each independent interferometer arm. A second near-term goal with regards to increasing the efficiency of the setup would entail the implementation of tunable fiber-optic filters. These would allow the systematic elimination of any residual fluorescence from the nonlinear crystal, as well as make it possible to very accurately align the signal and idler spectra such that their overlap is maximal. Hence leading to higher quality quantum interference and an improved HOM visibility. Furthermore, the use of custom length cleaved optical fibers would significantly simplify the interferometer arm length alignment. As a result of the entirely fiber-optic design, both of these are simple to implement and would not require a significant re-build of the setup.

References

[1] Feng Zhu et al. “Is high-dimensional photonic entanglement robust to noise?” In: *AVS Quantum Science* 3.1 (2021), p. 011401.

[2] Ichiro Shoji et al. “Absolute scale of second-order nonlinear-optical coefficients”. In: *JOSA B* 14.9 (1997), pp. 2268–2294.

[3] Shai Emanueli and Ady Arie. “Temperature-dependent dispersion equations for KTiOPO 4 and KTiOAsO 4”. In: *Applied optics* 42.33 (2003), pp. 6661–6665.

[4] AV Sergienko, YH Shih, and MH Rubin. “Experimental evaluation of a two-photon wave packet in type-II parametric downconversion”. In: *JOSA B* 12.5 (1995), pp. 859–862.

[5] BW Hakki. “Polarization mode dispersion in a single mode fiber”. In: *Journal of lightwave technology* 14.10 (1996), pp. 2202–2208.

Chapter 5

DESIGN OF HIGH-POWER, OCTAVE SPANNING ENTANGLED PHOTON SOURCES FOR QUANTUM SPECTROSCOPY

Adapted from: Szilard Szoke et al. "Designing high-power, octave spanning entangled photon sources for quantum spectroscopy". In: *The Journal of Chemical Physics* 154.24 (2021), p.244201

ABSTRACT

Entangled photon spectroscopy is a nascent field that has important implications for measurement and imaging across chemical, biology, and materials fields. Entangled photon spectroscopy potentially offers improved spatial and temporal-frequency resolutions, increased cross sections for multiphoton and nonlinear measurements, and new abilities in inducing or measuring quantum correlations. A critical step in enabling entangled photon spectroscopies is the creation of high-flux entangled sources that can use conventional detectors, as well as provide redundancy for the losses in realistic samples. Here, we report a periodically poled, chirped, lithium tantalate platform that generates entangled photon pairs with a $\sim 10^{-7}$ efficiency. For a near Watt level diode laser, this results in a near μW-level flux. The single photon per mode limit that is necessary to maintain non-classical photon behavior is still satisfied by distributing this power over up to an octave-spanning bandwidth. The spectral-temporal photon correlations are observed via a Michelson-type interferometer that measures the broadband Hong-Ou-Mandel two-photon interference. A coherence time of 245 fs for a 10 nm bandwidth in the collinear case and a 62 fs for a 125 nm bandwidth in the non-collinear case is measured using a CW pump laser, and, essentially, collecting the full photon cone. We outline in detail the numerical methods used for designing and tailoring the entangled photons source, such as changing center wavelength or bandwidth, with the ultimate aim of increasing the availability of high-flux UV-Vis entangled photon sources in the optical spectroscopy community.

5.1 Introduction

An entangled photon pair is generated by splitting a single photon into two photons via spontaneous parametric down conversion (SPDC) [1]. The quantum correlations between the two photons have several effects. First, when coherently recombined in time and space, the two entangled photons behave as the initial pump photon. In other words, the two entangled photons can be thought of as acting like a single photon in light-matter interactions [2]. As a result, two entangled photons leave the same side of a beamsplitter [3] and diffract from a grating at the wavelength of the pump photon [4, 5, 6]. Entangled photon pairs also linearize multiphoton and nonlinear spectroscopy, as has been well-studied in two photon absorption and fluorescence [7, 8, 9, 10, 11, 12, 13]. Entangled photons also have non-Fourier reciprocal spectral-temporal resolutions and are able to yield spatial resolutions which scale inversely with the number of correlated entangled photons N [14, 15, 16, 17, 18].

These properties, plus the more well known sub-shot noise and classical light rejection behaviors, make entangled photons tempting for use in ultrafast laser spectroscopy [19, 20]. The fragility of the entangled states, and the difficulty and expense associated with single photon counting, necessitates a need for high flux (nW-μW) entangled photon sources that would easily interface with existing ultrafast optics setups [21]. However, commonly used nonlinear crystals (BBO, KDP), usually have entangled photon creation efficiencies in the 10^{-10} to 10^{-12} range [22, 23, 24]. Reliance on 'birefringent phase matching' limits the highest usable nonlinear coefficients of the crystal as well as the bandwidth of entangled photons that can be created [25, 26, 27]. The possible phase-matching conditions result in bandwidths in the tens of nanometers range, which corresponds to 100s of femtoseconds to picoseconds in correlation times in experiments. Given the current assumption that the entangled photon correlation time must be less than a molecule or material's de-phasing time to allow a nonlinear or multiphoton enhancement, the narrow bandwidth of birefringent phase matching presents critical limits on entangled spectroscopy's feasibility [19, 28, 29].

In contrast, the ferroelectric properties of materials such as KTP and lithium niobate allow the crystals to be periodically poled and utilize a 'quasi phase-matching' (QPM) technique [30, 31, 32]. Quasi-phase-matching allows the use of Type-0 collinear phase matching [33], SPDC efficiencies of 10^{-6} to 10^{-10} [34, 35], a broadly tunable center wavelength (set by the grating period instead of crystal angle) [36],

and easy implementation of waveguides that can saturate single photon detectors with ~mW of CW diode laser input power [37]. Broad bandwidth phase matching is achieved by introducing a chirp into the poling period of the structure. The nonlinear poling allows for more wavelengths to be phase matched, while also retaining the benefits associated with longer crystals, namely a larger downconverted photon flux. The increased bandwidth directly affects the effective temporal resolution of experiments [38, 39, 40]. The broad bandwidth also allows increased power densities, as the the single photon per wavelength mode occupation limit necessary for non-classical effects is not exceeded (calculated as the flux in photons/s divided by the bandwidth in Hz) [41, 42]. While KTP and lithium niobate have been the primary workhorse for entangled photon generation in quantum information system settings, they have limitations with regards to their damage thresholds and UV cut-offs. In contrast, lithium tantalate is more ideal for physical chemistry and materials research because it has higher power handling capabilities (240 MW/cm^2) [43] and a lower UV absorption edge (≈280 nm) [44, 45].

To accelerate the adoption of entangled photon techniques, we outline how to create an entangled photon source that can achieve near μW powers of entangled photons down to UV wavelengths with temporal resolutions of tens of femtoseconds. These entangled photon fluxes are high enough to be visible by eye when starting from a 1W CW pump laser, greatly facilitating the alignment of entangled experiments. Here, the generated photon pairs are centered around a degenerate wavelength of 812 nm, resulting from a 406 nm pump source, but this wavelength can be tuned as outlined by the formulas in the paper. The 8% MgO doped congruent lithium tantalate (CLT) gratings use a Type-0, collinear quasi-phase matching configuration. A Michelson type interferometric scheme [46] measures the fourth-order interference of the entangled photons and gives coherence times of 245 fs for a bandwidth of 10 nm and 62 fs for a bandwidth of 125 nm. Of course, simply producing a broad bandwidth of entangled photons is not the same as carrying out experiments using them. We discuss our attempts to utilize the full SPDC cone and bandwidth in subsequent experiments, emphasizing where optics development is still needed to achieve maximum temporal resolution and flux. Using the full cone is in contrast to most experiments where irises are used to select two points from the SPDC cone, thereby severely reducing the total photon flux at the gain of state purity. The paper aims to give quick access to the sources needed for the emerging field of nonlinear entangled photon optics as well as outlining the next steps needed in the field.

5.2 Theory

Designing Broadband SPDC in chirped nonlinear materials

Prior to quantifying the experimental behavior of the SPDC sources, we lay out the theoretical and numerical details used in their design.

In SPDC, the creation of two entangled photons arises from the quantum mechanical process of a single pump photon mixing with the underlying vacuum state. The two down-converted daughter photons display strong correlations in time, energy, and momentum due to the parametric mixing process [1, 47]. The time and energy correlations originate from the individual photons being generated simultaneously from the pump photon:

$$E_p\left(\omega_p\right) = E_s\left(\omega_s\right) + E_i\left(\omega_i\right) \tag{5.1}$$

$$\therefore \;\; \omega_i = \omega_p - \omega_s \tag{5.2}$$

where ω_p, ω_s, and ω_i are the frequencies of the pump, signal, and idler photon, respectively. The momentum correlation is dictated by the phase matching condition, which is a consequence of the wave-like nature of the interacting fields. Each field has a corresponding wave vector defined via its respective phase velocity $v_p = c/n\left(\omega, T\right)$ in the medium:

$$k\left(\omega, T\right) = \frac{\omega n\left(\omega, T\right)}{c} \tag{5.3}$$

with $n\left(\omega, T\right)$ being the frequency and temperature dependent refractive index of the material. The following vector sum, the longitudinal component of which is depicted in Fig.5.1, should be satisfied in order to ensure that a proper phase relationship between the interacting waves is maintained throughout the nonlinear crystal.

$$\begin{aligned}\Delta\boldsymbol{k}\left(\omega_p, \omega_s, \omega_i\right) = \boldsymbol{k}_p\left(\omega_p, n_p\left(\omega_p, T\right)\right) - \boldsymbol{k}_s\left(\omega_s, n_s\left(\omega_s, T\right)\right) \\ -\boldsymbol{k}_i\left(\omega_i, n_i\left(\omega_i, T\right)\right)\end{aligned} \tag{5.4}$$

It is only when this relationship holds true ($\Delta k = 0$) that constructive interference between the propagating waves can occur and energy is transferred dominantly in one direction, rather than oscillating back and forth between the two optical modes [48].

A natural extension of this phase-matching principle, termed quasi-phase-matching, is apparent if one considers the duality between position and momentum space. A periodic lattice in position space directly corresponds to a well-defined wave

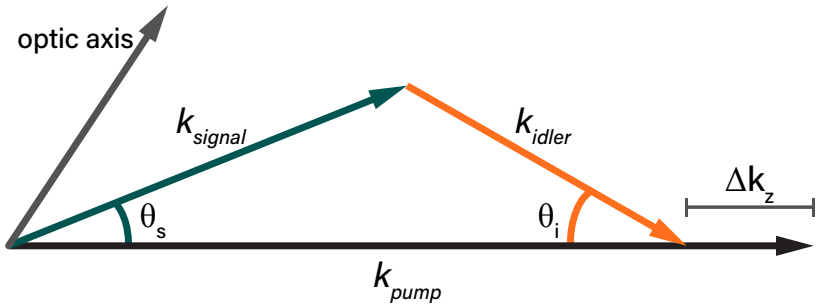

Figure 5.1: Phase-matching diagram for a two-photon downconversion process, showing the longitudinal phase-mismatch component Δk_z. The entangled photons (signal and idler) are each shown to have their distinct wave vectors k and emission angles θ. The phase-mismatch component must be compensated to create entangled photons by spontaneous parametric down conversion (SPDC).

vector $\boldsymbol{k}$ in momentum space via a Fourier transform. Therefore, if the nonlinear dielectric tensor domains of ferroelectric nonlinear crystal are modulated with a specific periodicity Λ, a quasi-momentum term $\Gamma(\Lambda)$ arises, which can be used to satisfy a non-phase-matched nonlinear interaction.

$$\Delta\tilde{\boldsymbol{k}}\left(\omega_p, \omega_s, \omega_i\right) = \Delta\boldsymbol{k}\left(\omega_p, \omega_s, \omega_i\right) - \Gamma(\Lambda) \tag{5.5}$$

The quasi-phase-matching term $\Gamma(\Lambda)$ also has an additional advantage, in that it can be chosen to be higher-*order*. Here, the order of the configuration is defined by m.

$$\Gamma(\Lambda) = \frac{2\pi m}{\Lambda},\ m \in 2\mathbb{Z} + 1\ (\neg 0) \tag{5.6}$$

This serves a particular experimental benefit as it allows for nonlinear interactions to be phase-matched (albeit with lower efficiency), even if the required 1^{st} order periodicity is too small to be fabricated [49].

We now describe the design of a grating in congruent lithium tantalate with the design goal of a 406 nm pump wavelength that creates a >400 nm bandwidth around the degenerate 812 nm SPDC point. The source must also be capable of creating near μW powers given a 1 W input power. The first step is to obtain the Sellmeier equations that describe the frequency and temperature dependent refractive indices of the material [50]. The numeric values and a representative plot are found in the supplementary information. Using the Sellmeier equations, the phase mismatch (Eq.5.5) is then evaluated for a wide range of pump-signal/idler wavelength configurations while keeping one entangled photon frequency a constant. External conditions such as the desired temperature range and minimum achievable

poling periodicity are also enforced such that the parameter space remains within experimentally realistic boundaries. The root of Eq.5.5 can then be found by a root-finding algorithm. For the congruent lithium tantalate and a 406-812 SPDC process, and imposing a realistic < 200°C temperature condition, solving for the root of Eq.5.5 yields a poling period of 9.5 μm at 133°C (see figure in SI for the graphical solution).

Quasi-phase-matching is a strongly temperature dependent technique. By solving Eq.5.5 for a range of temperatures near the calculated degeneracy point (133°C), the splitting and tuning of the SPDC spectrum can be calculated. Tuning the SPDC spectrum via the crystal temperature is useful for controlling what intermediate states are involved in, the magnitude of, and the temporal resolution of an entangled two photon process. The temperature dependent behavior is shown in Fig.5.2. Here, the transition between the degenerate and non-degenerate domains is clearly observable, with lower temperatures corresponding to a weaker degenerate emission profile. The lower plot of Fig.5.2 also clearly shows a very strong narrowing of the signal and idler bandwidths as one temperature tunes further away from degeneracy.

Additionally, both signal and idler have an inherent angular emission property determined by the momentum conservation condition in Eq.5.5. The strong frequency dependence of the outgoing angles can be numerically calculated from the momentum conservation equation if one decomposes the wave vectors into their longitudinal and transverse components, and solves the trigonometric equations for transverse phase-matching. Subsequently computing the emission angle for each frequency of interest, in conjunction with the frequency dependent refractive index of the nonlinear crystal, the SPDC cone's spectral characteristic for various crystal temperatures can be plotted (Fig.5.3). As predicted, at the degenerate emission temperature of 133°C, the plot shows that the emission angle of the 812 nm signal and idler photons is 0°. More importantly however, comparing the results to those in Fig.5.2, the shaded non-degenerate region also corresponds to a collinear emission profile. Vice versa, temperatures below 133°C display a (albeit weak) degenerate, non-collinear character. In a chirped crystal, the bandwidth of the down-converted entangled photons is increased by changing the poling period throughout the crystal. The increasing width elements correspond to different phase-matched wavelength configurations of Eq.5.5 (Fig.5.4). The photons still add up to the narrow linewidth of the pump laser but the temporal resolution is given by the temporal alignment and down-converted bandwidth of the entangled photons. This is why entangled photon

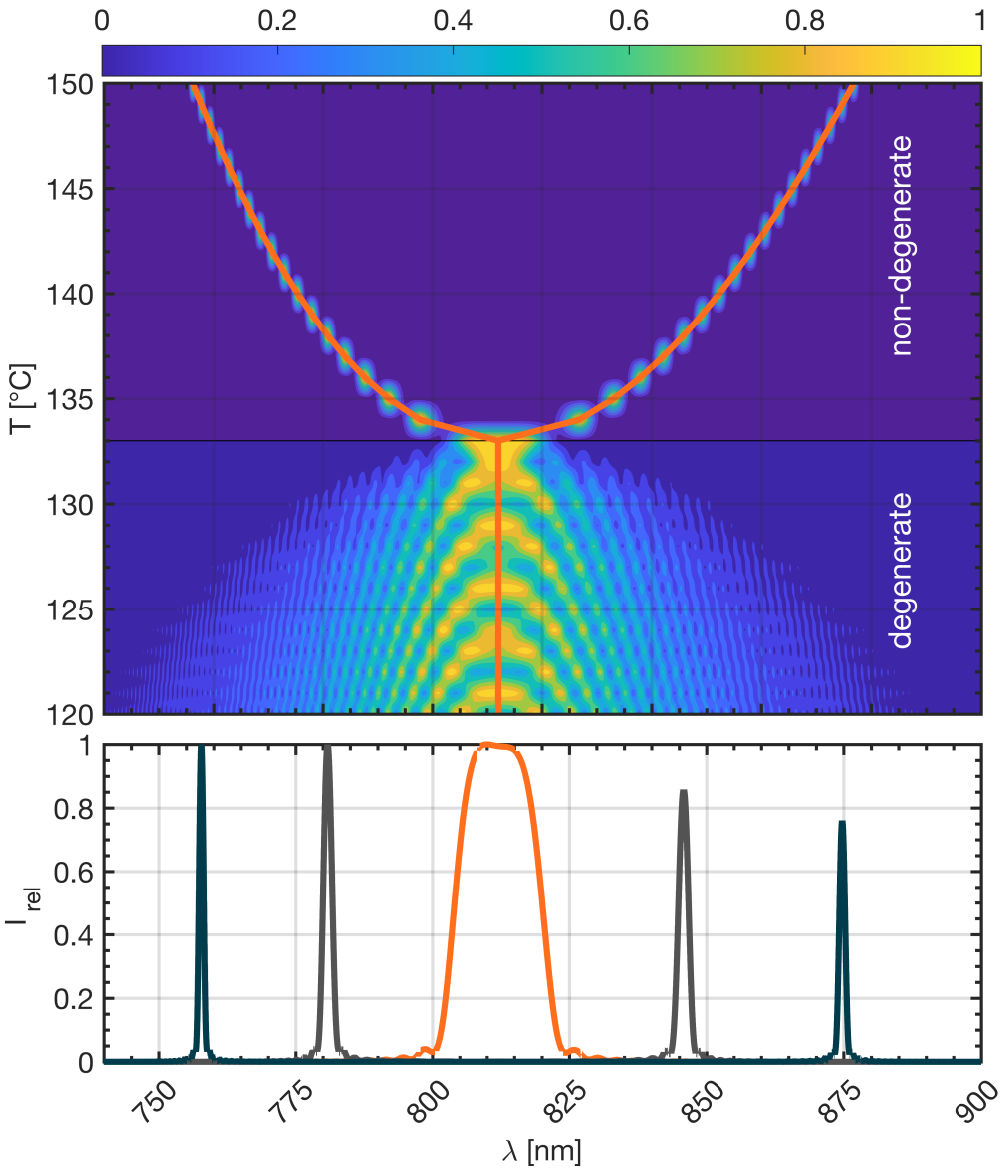

Figure 5.2: SPDC emission spectrum for ppCLT at various phase-matching temperatures showing transition from degenerate to non-degenerate downconversion. Bottom plot showing spectra at three temperatures corresponding to cross sections of the 2D plot. The phase matching temperature results in the broadest bandwidth.

experiments are said to have independent spectral and temporal resolutions. The importance of the pump laser's linewidth in determining the entangled photon state's purity, and thus the access to non-classical spectroscopic properties, is discussed in the SI.

Following a similar treatment to [51], the crystal can be decomposed into its individual domains, in each of which the downconversion amplitude follows the usual

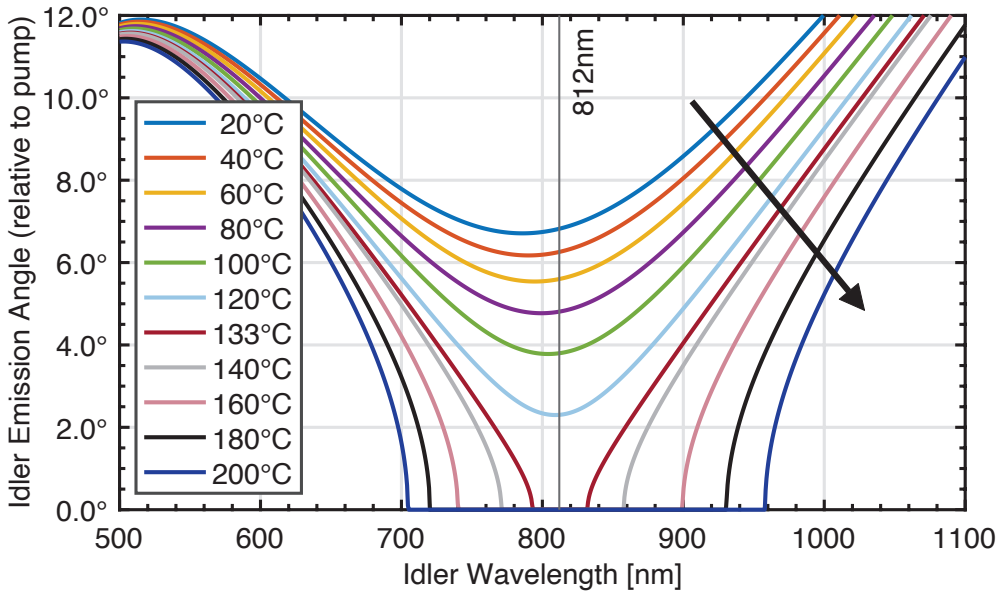

Figure 5.3: Broadband signal/idler emission angles in ppCLT with 9.5 μm poling period, showing how the SPDC source does not act as an ideal dipole emitter when broadband entangled photon pairs are desired. Points where curves reach a value of zero correspond to collinear, non-degenerate emission. Note that at certain temperatures, there need not be any SPDC emission in certain directions, governed by the spectral emission characteristics in Fig.5.2. Arrow indicating direction of increasing temperature.

sinc function-like phase-matching dependence [52]. This is attributed to the Fourier transform of a rectangular function in real-space representing the probability of a downconversion event occurring inside the crystal element

$$A_n\left(\omega_s, \omega_i\right) = L_n sinc\left(\frac{L_n \Delta k}{2}\right) \tag{5.7}$$

with L_n being the length of the n^{th} crystal element. Similarly, a cumulative-phase term can be defined, which is related to a forward propagating wave with phase-mismatch Δk traversing a crystal length L_{prop} after it has been generated in the SPDC process at crystal element n.

$$\varphi = \Delta k L_{prop} = \Delta k \left(\frac{L_n}{2} + \sum_{m=n+1}^{N} L_m\right) \tag{5.8}$$

Carrying out a sum over all individual crystal elements then allows for the resulting SPDC spectrum to be calculated (Eq.5.9) and thereby observe the effects of different chirping parameters. For lithium tantalate, this is shown in Fig.5.5. In the case of CLT, a ±10% chirp around the degenerate poling periodicity calculated above yields

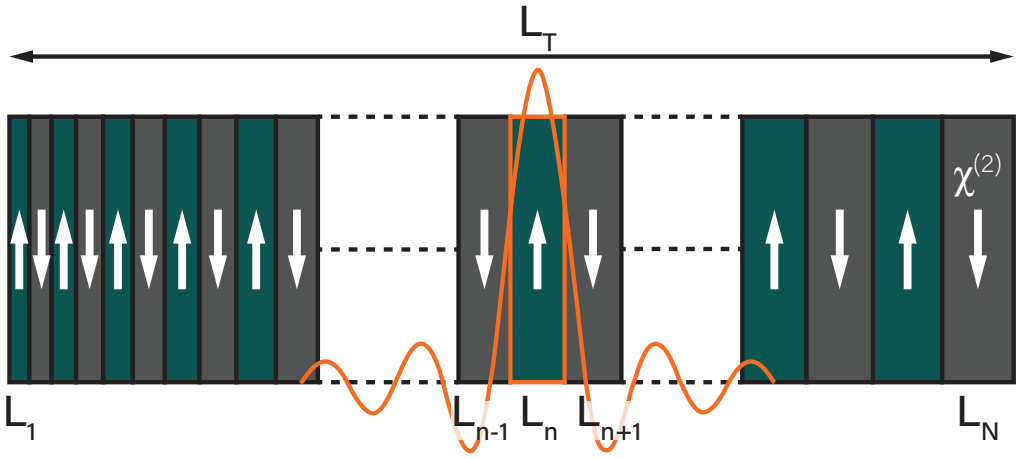

Figure 5.4: Depiction of a chirped periodically poled crystal with total length L_T. Each crystal segment of length L_n is associated with a *sinc*-shaped downconversion amplitude around a different center wavelength. Equivalently to a normal periodically poled crystal, the domain orientation is reversed in adjacent elements.

a full octave spanning SPDC bandwidth. Trivially, in the limit of no chirp, where all crystal elements are equal in size, the solution for a periodically poled crystal of length L is recovered.

$$A(\omega_s, \omega_i) = \chi_0 \sum_{n=1}^{N} (-1)^n L_n sinc\left(\frac{L_n \Delta k}{2}\right) \times e^{-i\Delta k\left(\frac{L_n}{2} + \sum_{m=n+1}^{N} L_m\right)} \tag{5.9}$$

By plotting the solution of Eq.5.9 as a function of the position inside the crystal along the propagation direction, we can gain some intuition for how the constructive interference results in a broadened spectrum. In the case of CLT, a ±10% chirp around the degenerate poling periodicity calculated above yields a full octave spanning SPDC bandwidth as shown in Fig.5.6. Here we used a total grating length of 18 mm equal to the chip used in subsequent experiments.

The 2D plot in Fig.5.6 provides some additional insight into how modulation of the poling period affects the build-up of the emitted spectrum. In particular, it is important to note that while the first 8mm length of the crystal appears to show no downconversion taking place, this is indeed not the case. While all crystal elements in this region satisfy a particular phase-matching condition, it is only after a certain propagation length that the phases of each spectral mode coherently sum to a strong enough amplitude that would be perceivable on the plot. Furthermore,

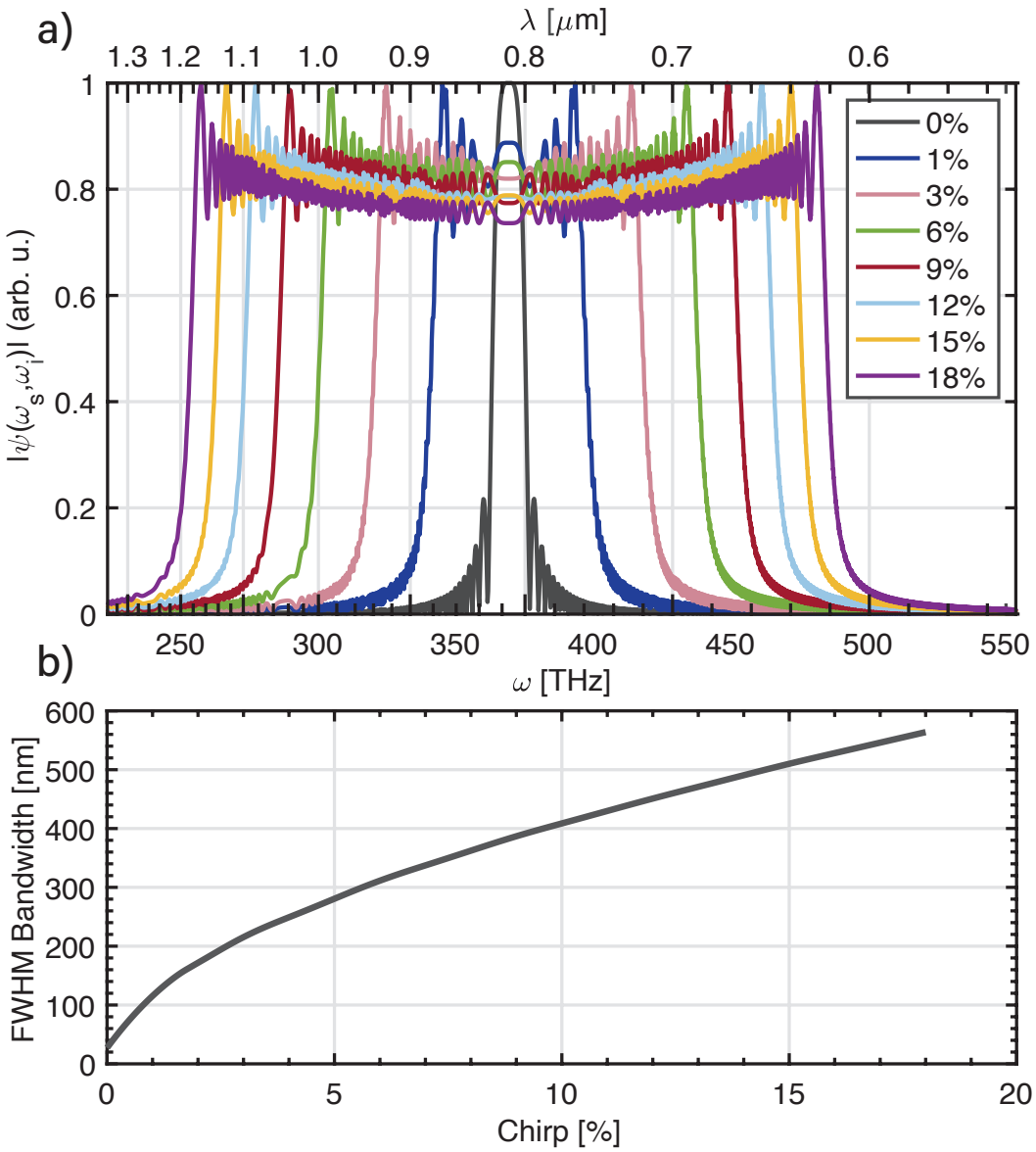

Figure 5.5: (a) SPDC emission bandwidth broadening as a function of chirp parameter, defined as total percentage deviation from the degenerate poling period. (b) Numerically calculated FWHM bandwidth trend as a function of poling period chirp.

the broadening of the downconverted bandwidth does have a particular drawback, in that the frequencies close to degeneracy become weaker in intensity. This is best observed in the line cuts for positions L3 and L4, where instead of a constant intensity across all frequencies, the emission spectrum peaks at the lower and higher cut-offs but begins to droop more severely as the bandwidth increases. Thus, increasing the chirping of the poling period indefinitely does not necessarily yield a flat power

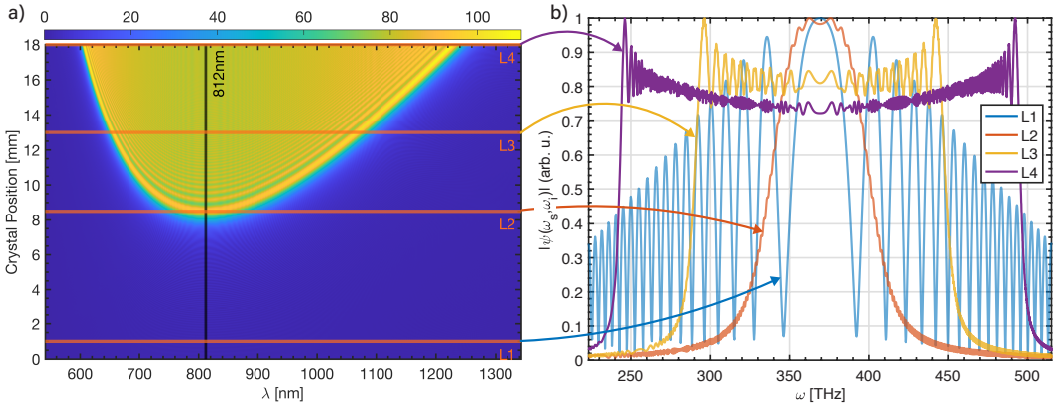

Figure 5.6: (a) Build up of the collective SPDC spectrum as a function of the position inside a chirped ppCLT grating in the direction of propagation. (b) Line cuts across the 2D spectrum plot in a) showing the normalized spectrum (in frequency space) at the positions designated as L1, L2, L3, and L4 respectively.

spectral density. It should be pointed out that this issue can be addressed via chirp profiles which follow not a linear but some higher order functional form [53].

In contrast to narrowband SPDC where the emission angles for the photon pairs are well confined within the two narrow arcs satisfying momentum conservation, such extremely broadband downconversion poses inherent difficulties in the spatial degree of freedom due angular (chromatic) dispersion of the resulting beam. As Fig.5.3 shows, the emission angles increase quickly away from degeneracy. This presents several experimental issues, as the beam no longer represents an ideal point source, which will be discussed in the experimental section below. Taking into account the physical dimensions of the grating cross section (detailed in the experimental section below), it is easy to see that the output aperture of the grating can at most only accommodate $arctan(0.15mm/9mm) \approx 1°$ of emission in the horizontal axis, and $arctan(0.5mm/9mm) \approx 3.2°$ along the vertical axis relative to the center point of the crystal where we focus. Beyond this, large parts of the SPDC emission cone will begin to interact with the domain boundaries which form the grating channel. While in principle the refractive index is the same for both un-poled and poled crystal regions, the periodic poling process causes some stress at the domain walls. Therefore, the edge of the each pattern in the lateral direction acts as a kind of scattering center, possibly resulting in unwanted interference patterns. Therefore special attention should be paid to accommodate the spatial distribution of the cone as it diverges inside the channel.

A final point to consider is that the total length of the grating is to be chosen by considering two interlinked criteria. Firstly, the expected power spectral density of the entangled photons at the output scales as L^2. Emission intensity can therefore be significantly increased by utilizing longer structures. Conversely, the expected power spectral density also depends on a $sinc\left(\frac{L_n \Delta k}{2}\right)$ multiplicative factor. Hence, longer gratings result in narrower emission bandwidths. This 'dual'-argument also applies to poling patterns which have a chirp, as while increasing the amount of variation in the poling periodicity serves to broaden the emission bandwidth, each spectral component will be less populated with photons and thus less brilliant. Particularly for entangled photon spectroscopy, the optimal flux is around the single photon per mode limit. Above this, the quantum and entangled effects will start to blur out due to classical effects. So, to maximize the entangled flux such that it remains within the single photon per mode limit, it is crucial that higher total fluxes (due to increased grating lengths) are spread out across broader bandwidths (via stronger chirps). An unchirped or bulk crystal will blur out quantum effects quicker than the chirped crystal with increasing length. The length reported here is to balance these effects.

5.3 Experiment

SPDC Characterization

The periodically poled congruent lithium tantalate gratings were manufactured by HC Photonics. The unchirped chip consists of 8 gratings with different poling periods (8.5, 9, 9.5, 10, 10.5, 11, 11.5, 12 μm). It is 20 mm long and each channel has a 0.9 mm by 0.5 mm cross section. The chirped chip consists of 6 gratings with varying chirp parameters and entrance poling periods (Table 5.1). Each grating is 18 mm long and has a 1 mm by 0.3 mm cross section. The gratings are AR-coated on both input and output faces at 406nm(R<0.5%)/812nm(R<0.5%).

Grating	$\Lambda_1[\mu m]$	$\Lambda_c[\mu m]$	$\Lambda_2[\mu m]$	Chirp
1	9.000	9.45	9.900	10%
2	9.048	9.50	9.952	10%
3	9.095	9.55	10.005	10%
4	9.143	9.60	10.057	10%
5	9.190	9.65	10.110	10%
6	9.238	9.70	10.162	10%

Table 5.1: Chip parameters

The experimental setup, as illustrated in Fig.5.8, consisted of a computer-tunable, CW Ti:Sapphire laser (M2 SolsTiS) and an external SHG cavity to act as the pump source. The maximal output power of the SHG at 406 nm was 1.15 W with a 0.89 nm linewidth. The pump beam is focused through the ppCLT grating using an aspheric lens with a 40 cm focal length. This focal length is chosen such that the size of the focused beam was smaller than the grating's cross sectional dimension and further optimized for peak SPDC brightness. The position of the crystal can be finely adjusted in the XYZ directions using a piezoelectric stage, which is critical for maximizing the entangled photon flux. The angular deviation of the grating's long axis relative to the input beam was not as crucial as the X-Y centering of the chip around the focused beam and the z-control over exact focal point positioning. The temperature of the crystal is controlled by a ceramic heater and PID loop (Covesion) to an accuracy of 10 mK.

To measure the SPDC spectrum as well as the power of the downconverted flux, the output of the grating is passed through a total of three OD-4 500 nm longpass filters (Edmund Optics) to eliminate the residual 406 nm pump. The SPDC cone is collimated with an off-axis parabolic mirror and then focused into a USB spectrometer (Thorlabs). For more detailed characterization, the SPDC cone is collimated with a telephoto lens and then focused into a spectrometer (Princeton Instruments IsoPlane) with a 15cm focal length lens. In this configuration, spectral and power measurements are performed with an electron multiplying intensified CCD camera (emICCD, Princeton Instruments MAX4). For the broadband spectral measurements, spectra are collected and stitched together as a 800 nm blazed grating with 150 grooves/mm is scanned across several center wavelengths. These spectra are then background corrected, quantum efficiency corrected according to the detection efficiency of the emICCD camera, and normalized.

Fig.5.7 (a) depicts the SPDC spectra for the 9.50 μm unchirped grating as the temperature of the crystal is varied from 60°C to 160°C. Above 150°C, the shift from degenerate to non-degenerate emission conditions is apparent from the decrease in intensity around the degenerate wavelength region of 812 nm (gray dashed line). In comparison, as shown in Fig.5.7 (b), at 145 °C, the chirped chip (blue curve) exhibits much broader and flatter emission than the unchirped counterpart (red curve). The ratio of the flux produced by the chirped grating to that produced by the unchirped grating is ∼1.7. This increased flux is due to the lower wavelength components, as shown in Fig.5.7b. The occupation per spatial mode was not estimated here because

of the difficulty of collimating the full SPDC cone.

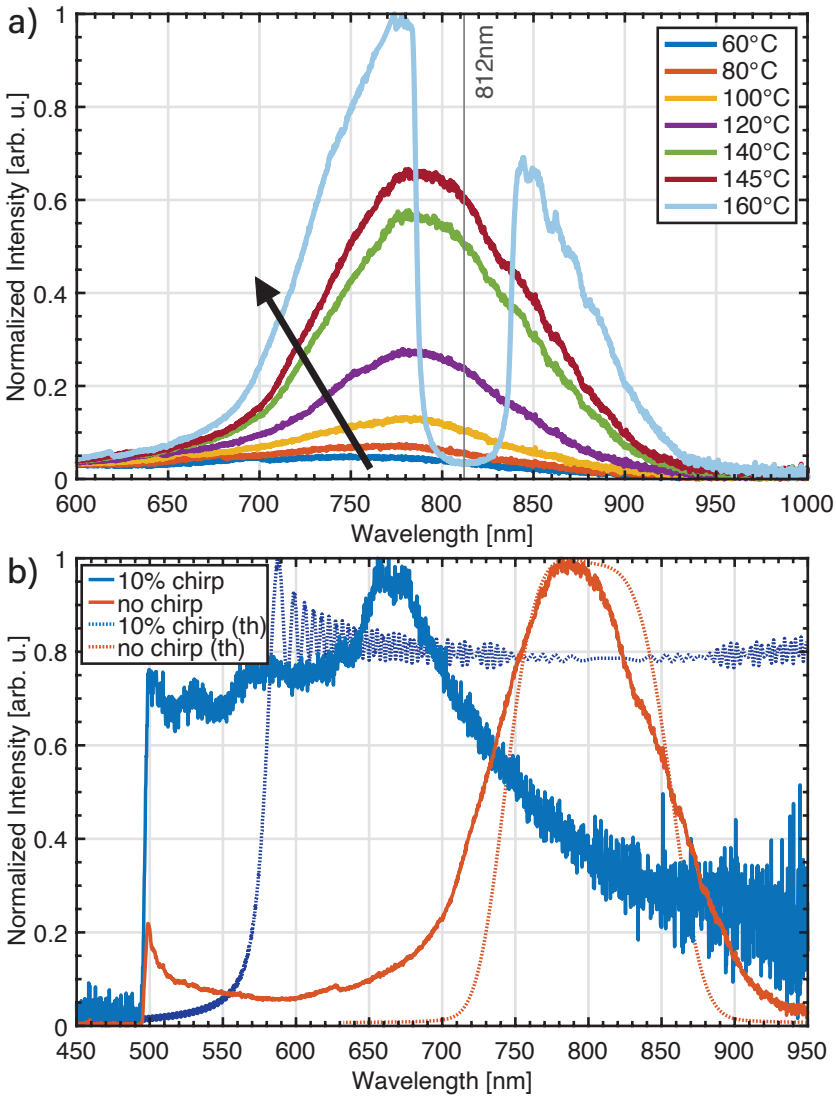

Figure 5.7: (a) SPDC spectra for a 9.50 µm unchirped grating, gray reference line marks the degenerate wavelength of 812 nm. Arrow a guide in the direction of increasing temperature. (b) Experimental (solid) and theoretical (dashed) SPDC spectra for a chirped grating with a 9.50 µm center poling period and 10% chirp rate. Both spectra taken at a temperature of 145°C. The chirped emission is broader and has a flatter top than the unchirped emission. Note the detector cut-off at 900 nm.

Two-Photon Interference

The fourth-order interference between entangled photon pairs was quantified with a two-photon Michelson interferometer, depicted in Fig.5.8. The Michelson interferometer is chosen because the configuration allows a broader bandwidth of

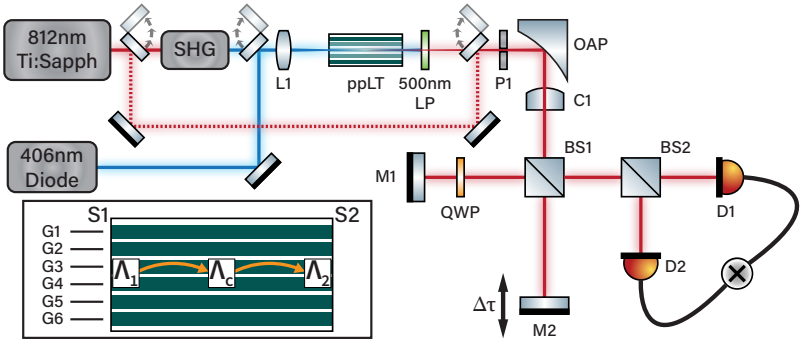

Figure 5.8: Entangled photon pair Michelson interferometer used to measure the fourth order interference. SHG: second harmonic generation unit, L1: focusing lens, ppLT: periodically poled lithium tantalate chip, LP: longpass filter, OAP: off-axis parabolic mirror, C1: cylindrical lens, BS1 and BS2: 50:50 beamsplitters, M1 and M2: mirrors, QWP: quarter-wave plate, D1 and D2: multimode fiber coupled single photon avalanche diodes connected to coincidence counting unit. The flip mirrors allow re-configuring such that the Ti:Sapph output is picked off and used for aid in alignment of downstream optics. A 406 nm diode laser is used as an alternate pump source. (Inset) Chip diagram showing the grating layout and their corresponding entrance (Λ_1), center (Λ_c), and end (Λ_2) poling periodicity locations in reference to Table.5.1.

the SPDC cone to be easily utilized, in contrast to a Mach-Zehnder configuration. Following the end of the ppLT chip, the entangled photons are collimated with an off-axis parabolic mirror and a cylindrical lens. These photons are directed through a broadband nonpolarizing 50:50 beamsplitter (BS1, Layertec) which separates the incident photons into two paths. In the reflected path, the photons pass through an achromatic quarter-waveplate (Thorlabs) twice to rotate their polarizations. The optical path length difference between the two arms is adjusted by scanning a mirror mounted to a linear stage in the transmitted arm. Coincidence counts vs. optical path length difference are then collected at one of the output arms of BS1. The coincidence counting setup consists of a second broadband 50:50 beamsplitter (BS2, Layertec), and two free-space-to-fiber coupling setups connecting to single-photon avalanche diodes (SPADs, Laser Component COUNT) and time-tagging electronics (PicoHarp 300). Because of the high SPDC flux, the pump beam must first be dimmed by three orders of magnitude to avoid SPAD saturation (counting rate 10^6 photons/s). Full counting rate experiments can be completed using the CCD alone [54, 55] but were not implemented at the time of writing this paper.

The free-space-to-fiber coupling setups each consist of 2 mirrors to align the beamsplitter outputs through a 4.51 mm focal length asphere, which then focuses the

beam into a multimode fiber (105 μm core diameter, 0.22 NA) connected to the SPADs. For these measurements, the coincidence time-bin resolution is set to 8 ps and coincidences are summed within a 10 ns window. Fourth-order interferograms were measured for different bandwidths of entangled photon pairs. For the first experiment, bandpass filters centered at 810 nm with a 10 nm FWHM are mounted to the front of each of the fiber coupling units. Note that this filter is not at the 812nm degenerate wavelength and reduces the degree of entanglement. For the second experiment, the 810 nm bandpass filters are removed to couple the broadband, collinear SPDC into the SPADs. Finally, the oven is allowed to cool to the non-collinear but degenerate temperature of 150°C, and broadband two-photon interference was measured again. Note that due to the large bandwidth of the SPDC, the fiber coupling efficiency of the non-degenerate photons is also poor at less than 10% of total power. Thus, 42% of the overall SPDC flux was lost before reaching the fibers connecting to the SPADs. Over 20% of the loss was due to the high angular dispersion of the beam, while the other ~20% of the loss was due to the reflective optics such as the aluminum OAP and silver mirrors. As discussed at the end of this section, optics development is still needed similar to using classical broadband ultrafast lasers.

Fig.5.9 shows the simulated fourth-order interferences using the produced bandwidth of the SPDC source and then the measured fourth-order interferences for two collinear bandwidths and a third non-collinear, full spectrum measurement. When the quarter-wave plate is set to 0°, the photons arriving at BS1 have the same polarization, and interfere coherently as correlated pairs. The interference pattern is robust against pump power fluctuations. When the quarter-wave plate is rotated to 45°, the reflected arm becomes perpendicularly polarized to the transmitted arm, the interference pattern disappears, and the coincidence counts follow the average pump power reading collected before and after the coincidence detection (SI Fig.8-9). The resulting coherence length of the total flux can be determined from the width of the interference peak. Table 5.2 summarizes the theoretical and measured coherence lengths.

For the measurement with 810-(10) nm bandpass filters mounted to the front of the fiber coupling units, shown in Fig.5.9(d), the coherence length is approximately 73 μm (or 245 fs). The simulated interference pattern as well as the coherence length of 60μm (200 fs), shown in Fig.5.9(a), agree fairly with the measurement given that the 10nm bandpass filter is offset from the degenerate wavelength of 812 nm. Note that

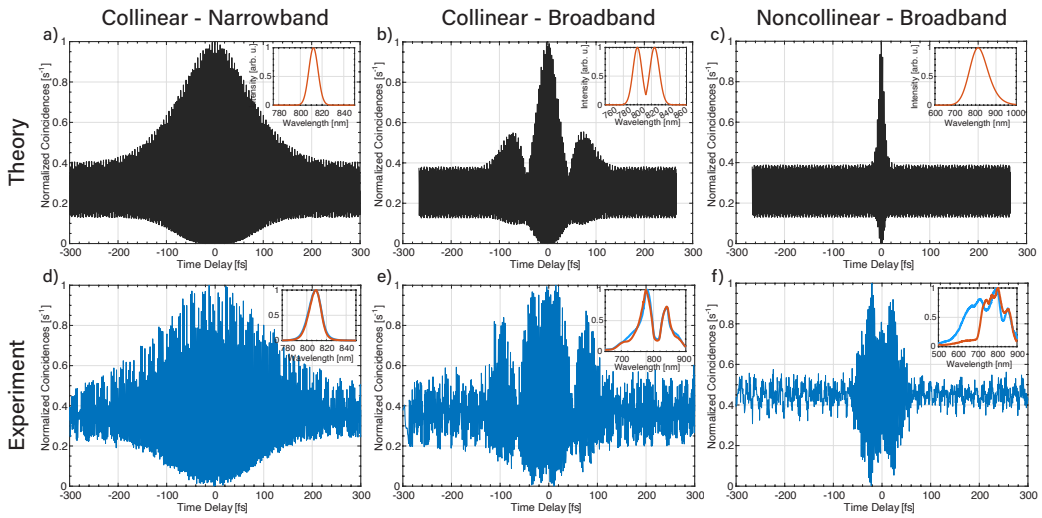

Figure 5.9: Simulated (top row) and measured (bottom row) fourth-order interference for narrowband collinear (a,d), broadband collinear (b,e), and broadband non-collinear (c,f) entangled photons. Coincidence counts are measured with 15 s integration time. The insets in each figure depict the SPDC spectra used to simulate or measure the corresponding interference in each detector arm. For simulations, Gaussian functions are used to approximate SPDC spectral envelopes. As shown in Table 5.2, the theroretical and measured coherence times are 200 fs and 245 fs for collinear narrowband, 45 fs and 57.4 fs for collinear broadband, 18 fs and 62 fs for non-collinear broadband. The growing difference between expected time resolution from the SPDC bandwidth and the measured interference is due to the difficulty with fiber coupling the full cone emission profile.

	Collinear narrowband	Collinear broadband	Non-collinear broadband
Theoretical coherence time [fs]	200	45	18
Measured coherence time [fs]	245	57.4	62

Table 5.2: Coherence times of different configurations and bandwidths of SPDC

the measured bandwidth after the fiber is roughly double what it actually is because the spectrometer slit had to be run wide to get sufficient flux for spectral analysis after the fiber coupling. The theoretical plot uses the correct bandwidth. Fig.5.9(e) shows the interference from collinear broadband SPDC flux without bandpass filters. The bandwidth is reduced and the SPDC spectrum is split (nondegenerate) because the phase matching temperature is maintained at the elevated collinear emission

(Fig.5.2). From the width of the center peak, the coherence length is approximately 17.2 μm (or 57.4 fs). For reference, the simulated coherence length is approximately 13 μm (45 fs). Similarly, Fig.5.9(f) shows the lower temperature non-collinear broadband interference. Here, the full 200 nm bandwidth of the SPDC source is attempted to be used (expected temporal width 8fs). However the spectrum reaching the detector is limited to 125 nm because of collimation issues, upstream optics, and fiber coupling. The coherence length calculated from the measured width of the peak is 18.9 μm (or 62 fs). This indicates that the degree of entanglement has degraded due to poor fiber coupling at non-collinear temperatures and other upstream optics. For example, the spectrum after the multiple beamsplitters is not balanced (Fig.5.9(f), inset) as compared to the other cases. The increased temporal width is also indicative of the need for dispersion management upstream, just as is similar to a broadband ultrafast laser pulse of an expected ~20 fs pulse. The same would be true for the chirped (>200 nm) SPDC source so an interferogram is not shown here. Note that the measured broadband spectra in the insets do not well match the theoretical spectra. This is because 1) fiber coupling of the broad bandwidth was not optimal and 2) the free space spectrometer slit was opened wide to increase the measurement fluxes which leads to a spectral broadening by a factor of 2.

The lack of fiber coupling efficiency in the broadband, non-collinear case is not simply one of input optics. Immediately following the chip, the spatial profile of the entangled photons is cone-like with a wavelength-dependent distribution (Fig.5.10 left). The measured angular deviation with wavelength matches the simulated entangled photon emission. Within a non-degenerate pair, the idler photon has a larger emission angle than the signal photon. The wavelength-dependent angular emission cone present a challenge in the implementation of free-space broadband entangled photon setups because the emission does not act like single point source. We attempted to collimate the emission cone using a variety of free-space optical configurations and found that a telephoto lens or an off-axis parabolic mirror (sometimes with an additional cylindrical lens for beam shaping) provides the best long range spatial profiles. After a propagation length of 45 cm into the far field, the entangled photon cone collapses (Fig.5.10 middle). This spatial profile collapse is most likely due to the interference of photon pairs created along the length of the crystal and scattering effects near the domain boundaries of the grating. The end result shows characteristics of somewhere between a Laguerre and a Hermite mode which would match the circular emission in a square profile created by the source.

The beam profile will likely be improved by using adaptive optics. The far field effects could also be reduced by using a waveguide instead of a grating; however, nanophotonic implementations cannot handle the high input powers used in this paper and fiber coupling of the broadband emission spectrum from waveguides is not yet well developed. Another obvious option is, instead of using fiber coupled SPADs for the detection, is to move to emICCD photon counting techniques that would not require focusing of the collapsed beam profile. However, this approach still needs exploration and requires an emICCD even more costly than SPADs. A necessary future development for the broadband entangled photon source is the clean-up of the SPDC spatial mode. Following the output of the bulk crystal, several possible improvements can be implemented including a spatial light modulator (SLM) to imprint phase and intensity shifts on the SPDC cone [56]. Alternatively, a combination of diffraction gratings and lenses could be used to correct the angular dispersion of the broadband wavelengths. The SPDC output could also be coupled into a broad bandwidth photonic crystal fiber such that the photons are propagating in a single spatial mode. Further, the spatial mode of the input pump beam could be modulated with an SLM or combinations of lenses/axicons to achieve the desired output SPDC spatial mode. Further investigation into the creation and collimation of broadband entangled photons is critical for the implementation of short temporal length, high flux entangled photon spectroscopy.

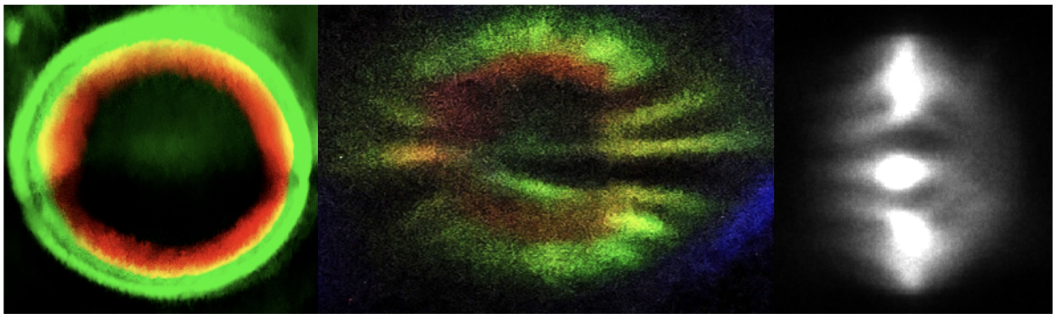

Figure 5.10: Images of collimated SPDC emission cone at 145 °C in the near field (left), far field (middle) after collimation with an off axis parabolic mirror, and far field after collimation and focusing by a 15.45cm focal length lens (right). The left and middle images are collected with a standard cell-phone camera, the right image is collected with an emICCD.

5.4 Conclusion

Quasi-phase-matching in periodically poled crystals offers significant benefits in the experimental implementation of broadband entangled photon sources for use

in spectroscopy. Simulated parameters for unchirped, periodically poled lithium tantalate gratings were utilized to design and construct a broadband entangled photon source spanning nearly an octave in frequency. This broadband source was characterized by measuring the output spectra of the grating and the fourth order interference by a two-photon Michelson interferometer. The two-photon Michelson interferometer was used to emphasize where further optics and detector development is still need to utilize the broadband and short temporal width sources. As in, the SPDC spectrum can be reliably created from the designed chip, however, the downstream optics and detectors still need development to fully utilize this source. Given the theoretical and experimentally demonstrated advantages of entangled photons in studies of chemical, biological, and material systems, we anticipate the widespread applicability of this particular energy-time entangled photon source.

5.5 Additional Information

CLT Refractive Indices

The Sellmeier equations [50] describing the frequency and temperature dependent refractive indices of the material are plotted in Fig.5.11.

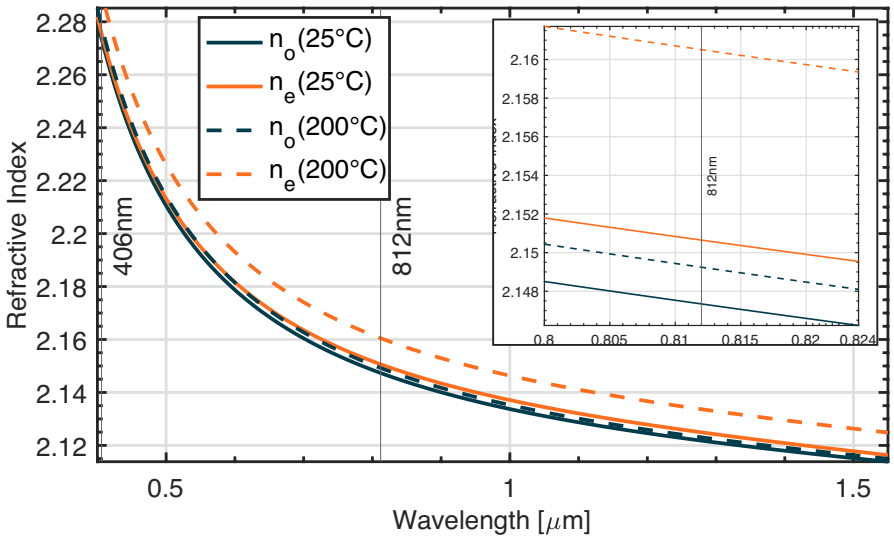

Figure 5.11: Congruent lithium tantalate refractive indices for ordinary and extraordinary polarizations at two different temperatures.

Quasi-Phase-Matching

Based upon these values, the poling periodicity was calculated for a collinear 3^{rd}-order Type-0 QPM configuration with a degenerate wavelength of 812nm.

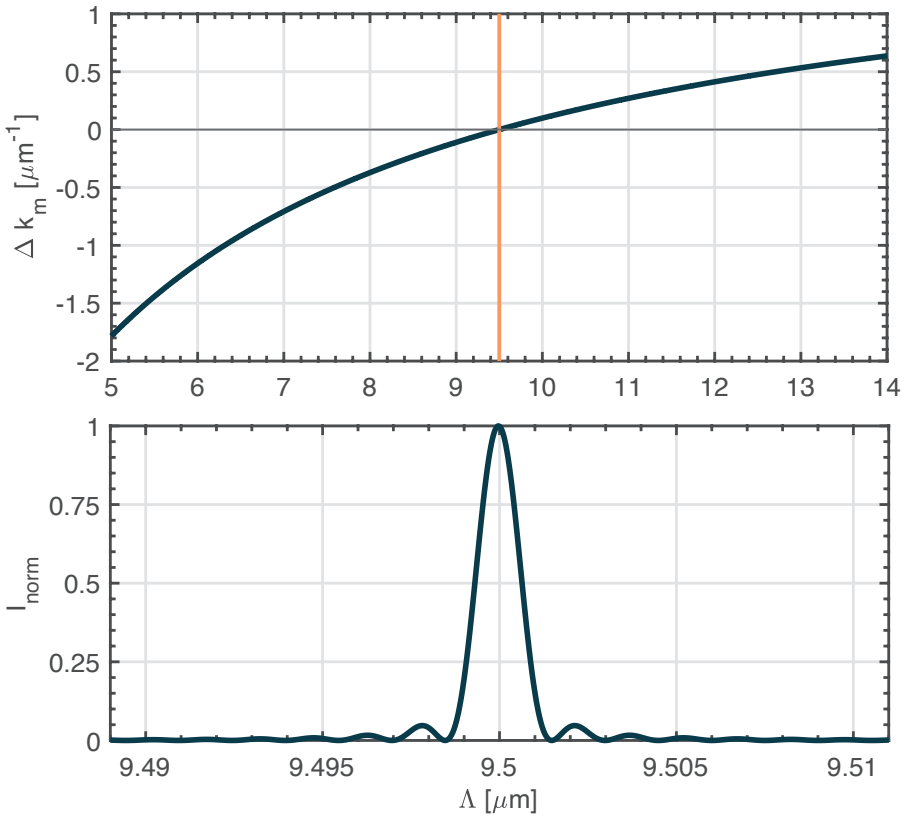

Figure 5.12: calculated poling period for 406nm-812nm at 133°C - CLT

Phase-matching Amplitude

Once the required poling period for our specific crystal and configuration has been determined, the two-dimensional phase-matching amplitude can be calculated by again evaluating Eq.5 and Eq.7 in the main text for a wide range of wavelength combinations. The result is the contour plot in Fig.5.13, which shows the downconversion intensity for photon pairs near the 812 nm degeneracy point. The inset of Fig.5.13 is a wide-range plot displaying the characteristic shape of the phase-matching curve for a Type-0 process. The contour provides some important information regarding the resultant output of the SPDC process. Mathematically, the output state of the downconversion process can be described as:

$$|\Psi\rangle = \int \int \gamma\left(\omega_s, \omega_i\right) d\omega_s d\omega_i a_s^{\dagger} a_i^{\dagger} |0\rangle \tag{5.10}$$

whereby the *joint spectral amplitude* (JSA), $\gamma\left(\omega_s, \omega_i\right)$ is the product of two terms, the *pump-envelope function* $\mu\left(\omega_s, \omega_i\right)$ and the *phase-matching amplitude* $\phi\left(\omega_s, \omega_i\right)$ [57]. Here the phase-matching amplitude function is solely determined by the crystal and the desired downconversion configuration. The pump-envelope function on the other hand is dictated by, as the name implies, the spectral characteristic of the pump

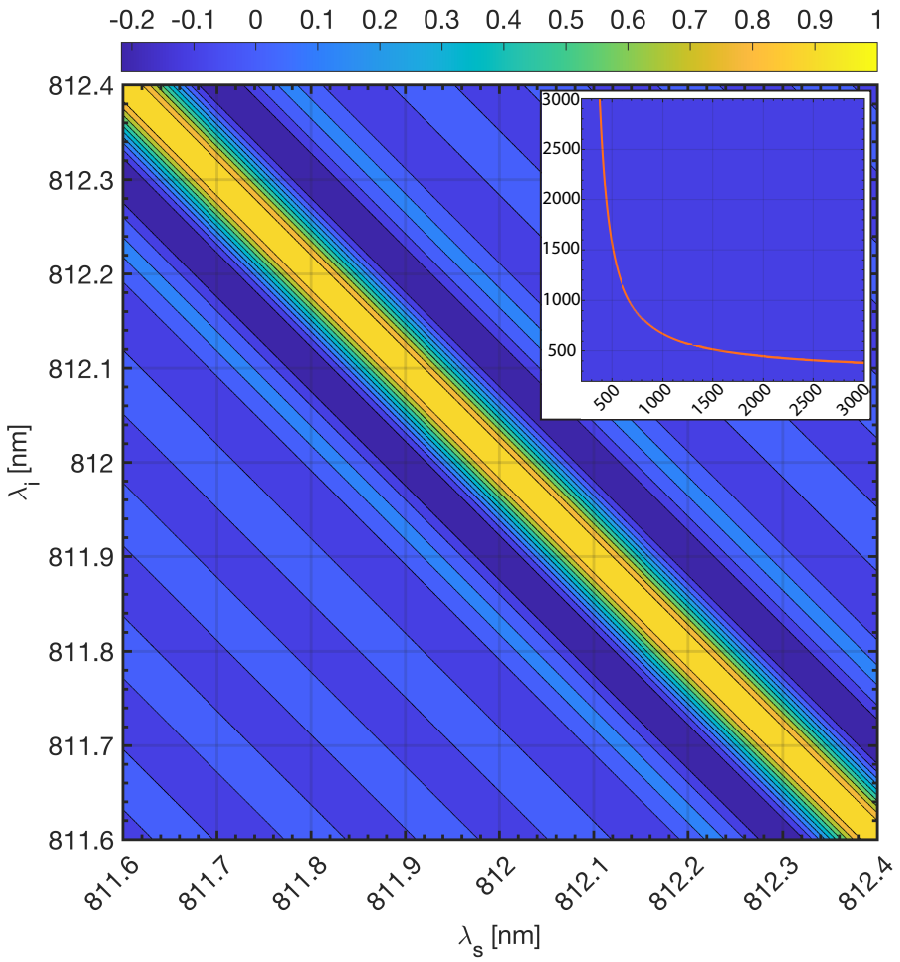

Figure 5.13: Phase matching amplitude contour plot for a 20 mm long ppCLT grating with a 9.5 μm poling period at 133C. Inset showing wide range phase matching curve across a larger wavelength range for the Type-0 phase matching configuration.

beam. Obviously due to conservation of energy, μ will be diagonal in its orientation if plotted as a function of the signal and idler wavelengths.

The strongly diagonal direction of ϕ is advantageous as its overlap with the pump-envelope along the diagonal allows for a wide range of anti-correlated signal and idler photon pairs to be phase-matched. This is of particular importance in experiments where this anti-correlation is necessary for achieving two-photon absorption processes which occur via an intermediate energy level transition [58]. This can be viewed in contrast to applications where highly spectrally pure photon states are desired, such as in single photon sources. Here, obtaining a lack of frequency correlations by designing an anti-diagonal direction of ϕ is of primary concern.

Entanglement and Purity

Given the output state as defined in Eq.5.10, the joint spectral amplitude allows for the prediction of the SPDC spectrum obtained for a given configuration of μ and ϕ by carrying out an integral across all signal/idler wavelengths with respect to a corresponding idler/signal wavelength held constant. For our specific 20 mm long ppCLT grating with a 9.5 μm poling period, the pump bandwidth has a distinct effect on not only the resulting emission spectrum's bandwidth, but also more profoundly on the entanglement of the photonic state. This is characterized by the purity,

$$P = \frac{1}{K} \tag{5.11}$$

with

$$K = \frac{1}{\Sigma_i \lambda_i^2} \tag{5.12}$$

being the Schmidt number equal to the rank of the reduced single particle density matrix. This value can be interpreted as a weighted measure (weights being the eigenvalues λ_i) of the number of modes required to represent the mixed state, and therefore how entangled it is [59]. The eigenvalues themselves are obtained via a singular value decomposition of the joint spectral amplitude matrix. As shown in Fig.5.14 (top), the SPDC spectrum trivially narrows as the pump bandwidth is decreased up to a limiting point. Below this value, the intersection of the pump envelope μ with the phase matching amplitude ϕ no longer causes a decrease in the spectral width which is being carved out by μ. Fig.5.14 (bottom) shows the calculated FWHM of the SPDC spectrum as a function of the pump bandwidth, as well as the corresponding purity of the output state. As is evident, the purity of the state decreases with increasing pump bandwidths, and therefore conversely the entanglement of the overall state increases. While this is advantageous from the perspective of producing a state which displays more/stronger anti-correlations between photon pairs, the significant drawback is that the spectral resolution with which optical atomic and molecular transitions are able to be addressed is directly determined by the bandwidth of the pump laser driving the SPDC process. Thus, for highly spectrally resolved measurements, the figure of merit will be dictated by the pump laser.

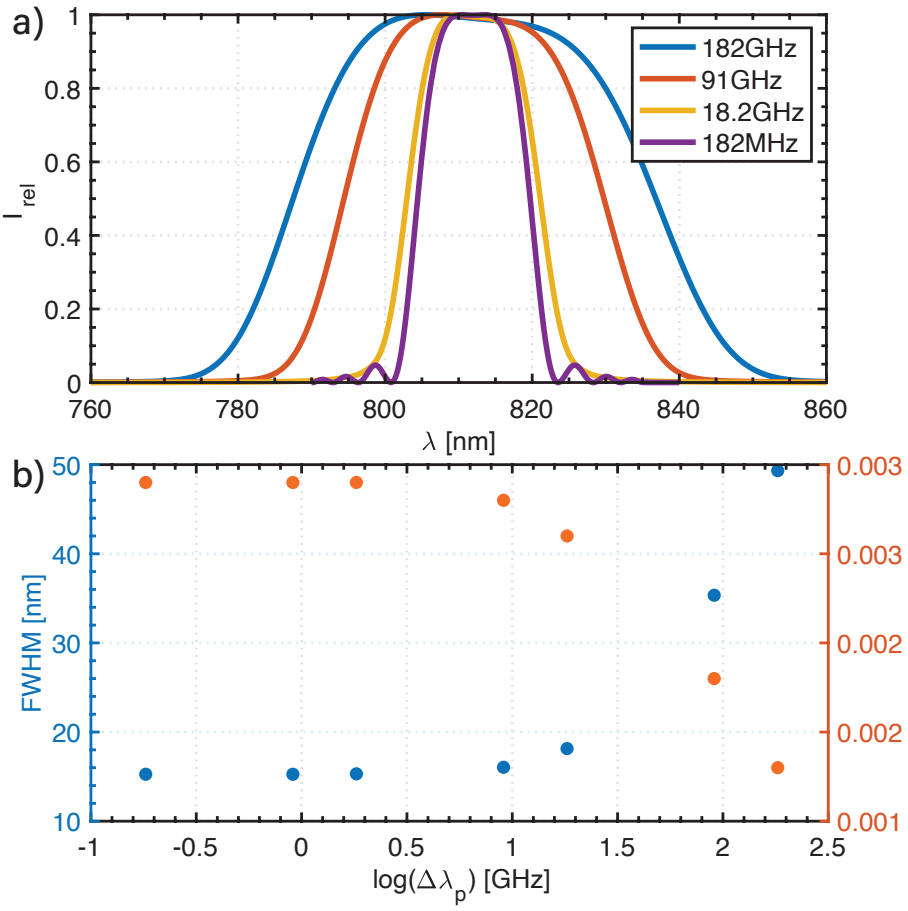

Figure 5.14: (a) SPDC emission spectrum as a function of the pump bandwidth. (b) The corresponding broadening of the spectrum (left y-axis) at larger bandwidths carries with it a degradation of the photon state purity (right y-axis) which is of advantage where strong (anti-)correlation between photon pairs is desired.

References

[1] David C. Burnham and Donald L. Weinberg. “Observation of Simultaneity in Parametric Production of Optical Photon Pairs”. In: *Phys. Rev. Lett.* 25 (2 July 1970), pp. 84–87.

[2] Szilard Szoke et al. “Entangled light–matter interactions and spectroscopy”. In: *J. Mater. Chem. C* 8 (31 2020), pp. 10732–10741.

[3] C. K. Hong, Z. Y. Ou, and L. Mandel. “Measurement of subpicosecond time intervals between two photons by interference”. In: *Phys. Rev. Lett.* 59 (18 Nov. 1987), pp. 2044–2046.

[4] Valentin Mitev et al. “Discrimination of entangled photon pair from classical photons by de Broglie wavelength”. In: *Scientific Reports* 10.1 (Apr. 2020), p. 7087.

[5] Ryosuke Shimizu, Keiichi Edamatsu, and Tadashi Itoh. “Quantum diffraction and interference of spatially correlated photon pairs generated by spontaneous parametric down-conversion”. In: *Phys. Rev. A* 67 (4 Apr. 2003), p. 041805.

[6] A F Abouraddy et al. “Double-slit interference of biphotons generated in spontaneous parametric downconversion from a thick crystal”. In: *Journal of Optics B: Quantum and Semiclassical Optics* 3.1 (Feb. 2001), S50–S54.

[7] Juha Javanainen and Phillip L. Gould. “Linear intensity dependence of a two-photon transition rate”. In: *Phys. Rev. A* 41 (9 May 1990), pp. 5088–5091.

[8] Barak Dayan et al. “Nonlinear Interactions with an Ultrahigh Flux of Broadband Entangled Photons”. In: *Phys. Rev. Lett.* 94 (4 Feb. 2005), p. 043602.

[9] Juan P. Villabona-Monsalve, Ryan K. Burdick, and Theodore Goodson. “Measurements of Entangled Two-Photon Absorption in Organic Molecules with CW-Pumped Type-I Spontaneous Parametric Down-Conversion”. In: *The Journal of Physical Chemistry C* 124.44 (2020), pp. 24526–24532.

[10] M. G. Raymer et al. “Entangled Photon-Pair Two-Dimensional Fluorescence Spectroscopy (EPP-2DFS)”. In: *The Journal of Physical Chemistry B* 117.49 (2013). PMID: 24047447, pp. 15559–15575.

[11] D. Tabakaev et al. “Energy-time-entangled two-photon molecular absorption”. In: *Phys. Rev. A* 103 (3 Mar. 2021), p. 033701.

[12] Tian Li et al. “Squeezed light induced two-photon absorption fluorescence of fluorescein biomarkers”. In: *Applied Physics Letters* 116.25 (2020), p. 254001.

[13] Gyeongwon Kang et al. “Efficient Modeling of Organic Chromophores for Entangled Two-Photon Absorption”. In: *Journal of the American Chemical Society* 142.23 (2020), pp. 10446–10458.

[14] Agedi N. Boto et al. “Quantum Interferometric Optical Lithography: Exploiting Entanglement to Beat the Diffraction Limit”. In: *Phys. Rev. Lett.* 85 (13 Sept. 2000), pp. 2733–2736.

[15] Ole Steuernagel. “On the concentration behaviour of entangled photons”. In: *J. Opt. B: Quantum Semiclass* 6.6 (May 2004), S606–S609.

[16] Hisaki Oka. “Selective two-photon excitation of a vibronic state by correlated photons”. In: *The Journal of Chemical Physics* 134.12 (2011), p. 124313.

[17] Hisaki Oka. “Enhanced vibrational-mode-selective two-step excitation using ultrabroadband frequency-entangled photons”. In: *Phys. Rev. A* 97 (6 June 2018), p. 063859.

[18] Frank Schlawin, Konstantin E. Dorfman, and Shaul Mukamel. “Entangled Two-Photon Absorption Spectroscopy”. In: *Accounts of Chemical Research* 51.9 (2018), pp. 2207–2214.

[19] Konstantin E. Dorfman, Frank Schlawin, and Shaul Mukamel. “Nonlinear optical signals and spectroscopy with quantum light”. In: *Rev. Mod. Phys.* 88 (4 Dec. 2016), p. 045008.

[20] Jean-Philippe W. MacLean, Sacha Schwarz, and Kevin J. Resch. “Reconstructing ultrafast energy-time-entangled two-photon pulses”. In: *Phys. Rev. A* 100 (3 Sept. 2019), p. 033834.

[21] Magued B. Nasr et al. “Generation of high-flux ultra-broadband light by bandwidth amplification in spontaneous parametric down conversion”. In: *Optics Communications* 246.4 (2005), pp. 521–528. ISSN: 0030-4018.

[22] Paul G. Kwiat et al. “New High-Intensity Source of Polarization-Entangled Photon Pairs”. In: *Phys. Rev. Lett.* 75 (24 Dec. 1995), pp. 4337–4341.

[23] S. Friberg, C. K. Hong, and L. Mandel. “Measurement of Time Delays in the Parametric Production of Photon Pairs”. In: *Phys. Rev. Lett.* 54 (18 May 1985), pp. 2011–2013.

[24] Paul G. Kwiat et al. “Ultrabright source of polarization-entangled photons”. In: *Phys. Rev. A* 60 (2 Aug. 1999), R773–R776.

[25] Suman Karan et al. “Phase matching in beta-barium borate crystals for spontaneous parametric down-conversion”. In: *Journal of Optics* 22.8 (June 2020), p. 083501.

[26] D. N. Nikogosyan. “Beta barium borate (BBO)”. In: *Applied Physics A* 52.6 (June 1991), pp. 359–368. ISSN: 1432-0630.

[27] J E Midwinter and J Warner. “The effects of phase matching method and of crystal symmetry on the polar dependence of third-order non-linear optical polarization”. In: *British Journal of Applied Physics* 16.11 (Nov. 1965), pp. 1667–1674.

[28] Oleksiy Roslyak and Shaul Mukamel. “Multidimensional pump-probe spectroscopy with entangled twin-photon states”. In: *Phys. Rev. A* 79 (6 June 2009), p. 063409.

[29] Stefan Lerch and André Stefanov. “Experimental requirements for entangled two-photon spectroscopy”. In: *arXiv preprint arXiv:2103.10079* (2021).

[30] S. Wang et al. “First-order type II quasi-phase-matched UV generation in periodically poled KTP”. In: *Opt. Lett.* 24.14 (July 1999), pp. 978–980.

[31] Nan Ei Yu et al. “Broadband quasi-phase-matched second-harmonic generation in MgO-doped periodically poled LiNbO3 at the communications band”. In: *Opt. Lett.* 27.12 (June 2002), pp. 1046–1048.

[32] Jintian Lin et al. “Broadband Quasi-Phase-Matched Harmonic Generation in an On-Chip Monocrystalline Lithium Niobate Microdisk Resonator”. In: *Phys. Rev. Lett.* 122 (17 May 2019), p. 173903.

[33] Jun Chen et al. “A versatile waveguide source of photon pairs for chip-scale quantum information processing”. In: *Opt. Express* 17.8 (Apr. 2009), pp. 6727–6740.

[34] Matthias Bock et al. “Highly efficient heralded single-photon source for telecom wavelengths based on a PPLN waveguide”. In: *Opt. Express* 24.21 (Oct. 2016), pp. 23992–24001.

[35] Bao-Sen Shi and Akihisa Tomita. “Highly efficient generation of pulsed photon pairs with bulk periodically poled potassium titanyl phosphate”. In: *J. Opt. Soc. Am. B* 21.12 (Dec. 2004), pp. 2081–2084.

[36] J. A. Armstrong et al. “Interactions between Light Waves in a Nonlinear Dielectric”. In: *Phys. Rev.* 127 (6 Sept. 1962), pp. 1918–1939.

[37] S. Tanzilli et al. “Highly efficient photon-pair source using periodically poled lithium niobate waveguide”. In: *Electronics Letters* 37 (1 Jan. 2001), pp. 26–28.

[38] Magued B. Nasr et al. “Ultrabroadband Biphotons Generated via Chirped Quasi-Phase-Matched Optical Parametric Down-Conversion”. In: *Phys. Rev. Lett.* 100 (18 May 2008), p. 183601.

[39] Avi Pe’er et al. “Temporal Shaping of Entangled Photons”. In: *Phys. Rev. Lett.* 94 (7 Feb. 2005), p. 073601.

[40] Z. Y. Ou and Y. J. Lu. “Cavity Enhanced Spontaneous Parametric Down-Conversion for the Prolongation of Correlation Time between Conjugate Photons”. In: *Phys. Rev. Lett.* 83 (13 Sept. 1999), pp. 2556–2559.

[41] Robert H. Hadfield. “Single-photon detectors for optical quantum information applications”. In: *Nature Photonics* 3.12 (Dec. 2009), pp. 696–705. ISSN: 1749-4893.

[42] Stefan Lerch and André Stefanov. “Observing the transition from quantum to classical energy correlations with photon pairs”. In: *Communications Physics* 1.1 (2018), pp. 1–6.

[43] Georgii M Zverev et al. “Laser-Radiation-Induced Damage to the Surface of Lithium Niobate and Tantalate Single Crystals”. In: *Soviet Journal of Quantum Electronics* 2.2 (Feb. 1972), pp. 167–169.

[44] V. A. Antonov et al. “Colour centres in single crystals of lithium tantalate”. In: *physica status solidi (a)* 28.2 (1975), pp. 673–676.

[45] J.-P. Meyn and M. M. Fejer. “Tunable ultraviolet radiation by second-harmonic generation in periodically poled lithium tantalate”. In: *Opt. Lett.* 22.16 (Aug. 1997), pp. 1214–1216.

[46] Dorilian Lopez-Mago and Lukas Novotny. “Coherence measurements with the two-photon Michelson interferometer”. In: *Phys. Rev. A* 86 (2 Aug. 2012), p. 023820.

[47] D. N. Klyshko, A. N. Penin, and B. F. Polkovnikov. “Parametric Luminescence and LIght Scattering by Polaritons”. In: *JETP Lett.* 11 (1 Jan. 1970), pp. 11–14.

[48] R.W. Boyd and D. Prato. *Nonlinear Optics*. 3rd ed. Elsevier Science, 2008. ISBN: 9780080485966.

[49] M. M. Fejer et al. “Quasi-phase-matched second harmonic generation: tuning and tolerances”. In: *IEEE Journal of Quantum Electronics* 28.11 (1992), pp. 2631–2654.

[50] Konstantinos Moutzouris et al. “Temperature-dependent visible to near-infrared optical properties of 8 mol% Mg-doped lithium tantalate”. In: *Opt. Mater. Express* 1.3 (July 2011), pp. 458–465.

[51] Giovanni Di Giuseppe et al. “Entangled-photon generation from parametric down-conversion in media with inhomogeneous nonlinearity”. In: *Phys. Rev. A* 66 (1 June 2002), p. 013801.

[52] A. V. Burlakov et al. “Interference effects in spontaneous two-photon parametric scattering from two macroscopic regions”. In: *Phys. Rev. A* 56 (4 Oct. 1997), pp. 3214–3225.

[53] Agata M. Brańczyk et al. “Engineered optical nonlinearity for quantum light sources”. In: *Opt. Express* 19.1 (Jan. 2011), pp. 55–65.

[54] Matthew Reichert, Hugo Defienne, and Jason W. Fleischer. “Massively Parallel Coincidence Counting of High-Dimensional Entangled States”. In: *Scientific Reports* 8 (1 May 2018), pp. 2045–2322.

[55] Yingwen Zhang et al. “Multidimensional quantum-enhanced target detection via spectrotemporal-correlation measurements”. In: *Phys. Rev. A* 101 (5 May 2020), p. 053808.

[56] Baenz Bessire et al. “Versatile shaper-assisted discretization of energy–time entangled photons”. In: *New journal of physics* 16.3 (2014), p. 033017.

[57] Kevin Zielnicki et al. “Joint spectral characterization of photon-pair sources”. In: *Journal of Modern Optics* 65.10 (2018), pp. 1141–1160.

[58] Bahaa E. A. Saleh et al. “Entangled-Photon Virtual-State Spectroscopy”. In: *Phys. Rev. Lett.* 80 (16 Apr. 1998), pp. 3483–3486.

[59] Artur Ekert and Peter L. Knight. “Entangled quantum systems and the Schmidt decomposition”. In: *American Journal of Physics* 63.5 (1995), pp. 415–423.

Chapter 6

GENERATION OF DEEP-UV CONTINUOUS-WAVE RADIATION USING $LaBGeO_5$

6.1 Introduction

In recent years, SPDC has predominantly been utilized at the visible, and telecom wavelengths, driven mainly by investigations of condensed matter systems with small bandgaps. To explore novel problems in chemistry and photochemistry, there is an inherent need to be able to reach into the UV to deep-UV spectral ranges, allowing for higher energy excitations to be driven in a quantum-controlled manner. This includes both cases where the summed wavelengths fall within the UV domain for two photon absorption studies, as well as where the individual downconverted photon wavelengths are in this spectral range, the latter being significant for investigations of photoexcited effects via the interference of two entangled photons. UV sources in general also find uses in applications where single-photon control is not necessarily required, such as laser-induced breakdown spectroscopy [1], UV Raman spectroscopy [2], and photoluminescence [3, 4]. The issues of atmospheric absorption and lack of optics generally hamper spectroscopies in these ranges where many atoms and molecules exhibit strong dipole-allowed transitions. Owing to the particularly high photon energies and attainable peak field intensities when properly focused, these sources also play an important role in highly-controlled "destructive" and tissue-damaging applications, such as biological micro-dissection [5, 6], or laser surgeries [7, 8].

There are a few different approaches for the realization of sources within this wavelength range of interest (100nm-400nm), such as excimer, argon-ion, nitrogen or gallium nitride (GaN) based lasers. However, most have significant disadvantages, making them either expensive, bulky, or vastly under-powered for practical applications in spectroscopy. The primary challenges in producing coherent sources at these wavelengths are material absorption, and the significant increase in spontaneous emission which causes threshold pump powers for lasing to set in to be exceedingly high. Although both of these constraints can be mitigated through high-power operation, the associated deleterious effects, such as severe heating, power and temperature instabilities, and short timescale drifts due to optical ele-

ment related wavefront distortions make UV lasers a challenging field of research. In addition, the high-quality UV optics required can quite heavily limit the lifetime of these sources. Although not always an experimental hindrance, most sources rely on pulsed operation, with highly-coherent cw sources usually being low in power.

Continuous-wave deep-UV laser sources in most fields have been relying on the frequency-quadrupling of Nd:YAG lasers, or alternatively the frequency-doubling of argon-ion lasers. In both situations, the nonlinear crystal being used is BBO, in conjunction with either intra-cavity or external-cavity enhanced layouts. Unfortunately, both implementations suffer from numerous disadvantages as a result of either needing two up-conversion steps, or requiring gas lasers as the pump, making experimental footprints large and system lifetimes short.

Over the past few decades, cesium lithium borate (CLBO) and beta barium borate (BBO) have been the primary workhorses for nonlinear optical frequency conversion at these unique wavelengths utilizing pulsed sources. Specifically, the generation of cw 266nm coherent radiation has so far been primarily restricted to implementations which employ CLBO. While conversion efficiencies as high as ~50% have been reported for green to UV frequency doubling using mode-locked lasers, the cw implementations fundamentally suffer from low single-pass conversion efficiencies ($\sim 1\%$) and therefore require some resonant cavity enhancement.

Another particular drawback to these nonlinear materials is that they necessarily rely on BPM techniques, and as such suffer from narrow spectral bandwidths and spatial walk-off effects, which limit the useful interaction length and correspondingly the attainable conversion efficiency. Noncritical phase-matching methods, specifically QPM, would then allow for both more efficient conversion processes, as well as a wider range of wavelengths of interest to be generated without beam walk-off effects being a concern. In contrast to SHG, SPDC processes would additionally benefit from being able to utilize chirped poling patterns to produce broad bandwidth signals. These could then enable ps to fs scale temporal resolutions in UV spectroscopies using entangled photons.

As such, in order to explore and take advantage of the interesting science that this wavelength domain has to offer, we look to utilize the techniques (specifically QPM) used in previous experiments of this thesis to implement sources capable of generating deep-UV cw radiation. Subsequently we look to utilize these coherent cw sources as the basis for the generation of entangled photons using SPDC for uses in quantum spectroscopic experiments that, for example, aim to look at chemical

reactions corresponding to σ-bonding as well as the more delocalized π-bonding in complex compounds amongst others [9, 10, 11, 12, 13].

Our proposed UV source utilizes $LaBGeO_5$ (LBGO), a relatively new nonlinear-optical ferroelectric material which has a transparency window extending down to ~195nm. This low cut-off wavelength makes the material particularly suitable for applications involving parametric downconversion processes and frequency mixing applications where the target wavelengths fall within the deep-UV regions. For our particular source, we have chosen a type-0 phase-matching process for 532nm-266nm frequency conversion, where all three interacting fields have identical, extraordinary, polarizations. The phase-matching is achieved through a first-order periodic poling of the crystal with a period of $\sim 2.1\mu m$. The relevant second order nonlinear optical coefficient d_{33} is approximately 0.96pm/V along the direction orthogonal to the periodic poling. Although this value is somewhat lower compared to leading edge nonlinear materials such as lithium niobate, optical pumping setups relying on free-space beams are well suited to generate sufficiently high entangled photon fluxes due to the very high pump-power budget available. The total length of the crystal is chosen to be 10mm, with each grating having a width of 1mm. These dimensions are currently pushing the experimental fabrication capabilities in this material, therefore improvements in the future are expected to enhance the nonlinear conversion efficiencies. The crystal and grating geometry constrain the emission profile of the SPDC cone to range from fully collinear, to non-collinear with a maximum opening half-angle of $\sim 2^\circ$, tunable via the adjustment of the working temperature of the crystal. The gratings were manufactured by Oxide Corporation.

As an immediate extension of this work, we have simultaneously also designed a second nonlinear frequency conversion experiment which is phase-matched for a type-0, 440nm-220nm configuration. The exploration of this even more challenging implementation was targeted to succeed the initial 266nm crystal once the general experimental validation of LBGO being a viable cw radiation, and SPDC source, is established. Together with the additional obstacles of increased material absorption, required custom mirror and lens coatings, as well as atypical diode laser wavelength to serve as the pump (which thus requires the frequency doubling of a Ti:Sapp laser), it was deemed too large an immediate experimental step for such a new material. The following chapter therefore specifically focuses on the generation of 266nm cw radiation, however with the overall approach more or less being identical for the second grating.

6.2 Design

Given the relative novelty of the material, many of the properties of LBGO are still currently under study. Of special importance are the Sellmeier equations describing the refractive indices as a function of the wavelength of light. As these are used to determine not only the phase-matching conditions for the specific conversion process of interest, but also the dispersive properties of the material, they are key to the initial design process. These empirical equations are dictated by experimental measurements which varyingly focus on different portions of the frequency spectrum depending on the regions of interest. As such, the Sellmeier equations for LBGO near the lower cut-off, which is of primary importance to us, have not been well characterized yet, making the theoretically calculated phase-matching conditions potentially inaccurate. To accommodate any problems related to this, the fabricated LBGO chip comprises a number of gratings with different poling periods around the nominal value. The Sellmeier equations used for all the following design considerations are taken from the work of Umemura et al. [14]

$$n_o^2 = 3.2187 + \frac{0.03194}{\lambda^2 - 0.01039} - 0.00661\lambda^2 \tag{6.1}$$

$$n_e^2 = 3.3650 + \frac{0.03080}{\lambda^2 - 0.01946} - 0.01176\lambda^2 \tag{6.2}$$

$$(0.266 \leqslant \lambda \leqslant 1.064)\,. \tag{6.3}$$

These equations are shown in Fig.6.1, with the additional change of the refractive index at a higher temperature also being shown in the bottom figure. Although the lower end of the cited range is at the wavelength of our interest, our proposed 440nm-(SHG)-220nm-(SPDC)-440nm frequency conversion relies on the extrapolation of the above curves.

Correspondingly, the temperature dependence of the refractive indices is defined via the following thermo-optic dispersion equations.

$$\frac{\mathrm{d}n_o}{\mathrm{d}T} = \left(\frac{0.1859}{\lambda^3} - \frac{0.9308}{\lambda^2} + \frac{1.6877}{\lambda} + 0.4327\right) \times 10^{-5} \left(^\circ C^{-1}\right) \tag{6.4}$$

$$\frac{\mathrm{d}n_e}{\mathrm{d}T} = \left(\frac{0.1127}{\lambda^3} - \frac{0.5543}{\lambda^2} + \frac{1.0902}{\lambda} + 0.2343\right) \times 10^{-5} \left(^\circ C^{-1}\right) \tag{6.5}$$

$$(0.266 \leqslant \lambda \leqslant 1.064) \tag{6.6}$$

By defining the phase-matching configuration to be of Type-0, corresponding to all three interacting fields having extraordinary polarizations, we can calculate the

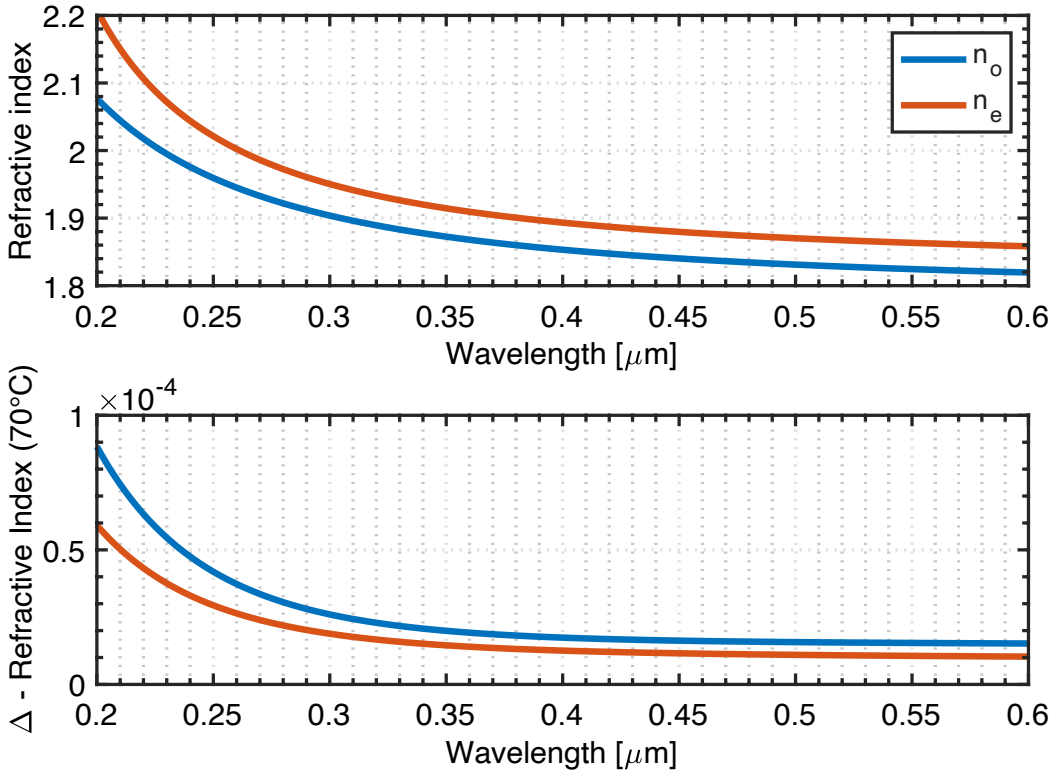

Figure 6.1: (top) LBGO refractive index curves for the ordinary (n_o) and extraordinary (n_e) polarizations. (bottom) Relative change in the refractive index value at a given temperature of 70°C across the same wavelength range.

phase mismatch for the 532nm-266nm SHG process including the poling period parameter Λ. This is determined through the phase-matching equations outlined in the theory section of this work. The crossover point at which $\Delta k = 0$ then signifies the poling period required to obtain perfect phase-matching as shown in Fig.6.2, with the associated phase-matching intensity being shown in the right plot. In order to estimate how the wavelength of the second harmonic changes as a function of the poling period Λ, we calculated the effective phase-mismatch Δk for a wide range of values. The contour plot displaying the phase-mismatch is shown in Fig.6.3. The red curve signifies the $\Delta k = 0$ iso-line. It is evident from the curvature of the line, that the wavelength sensitivity of the periodic poling is not very severe. Thus, the temperature dependent changes in the poling period of the grating should not ultimately limit the wavelength stability, and hence the performance of the source. The narrow phase-matching intensity curve shown in Fig.6.2 further reveals that the second harmonic signal intensity itself would be far more sensitive to poling period (and therefore temperature) variations, before shifts and fluctuations of the wavelength become significant. In addition to the grating periodicity, another

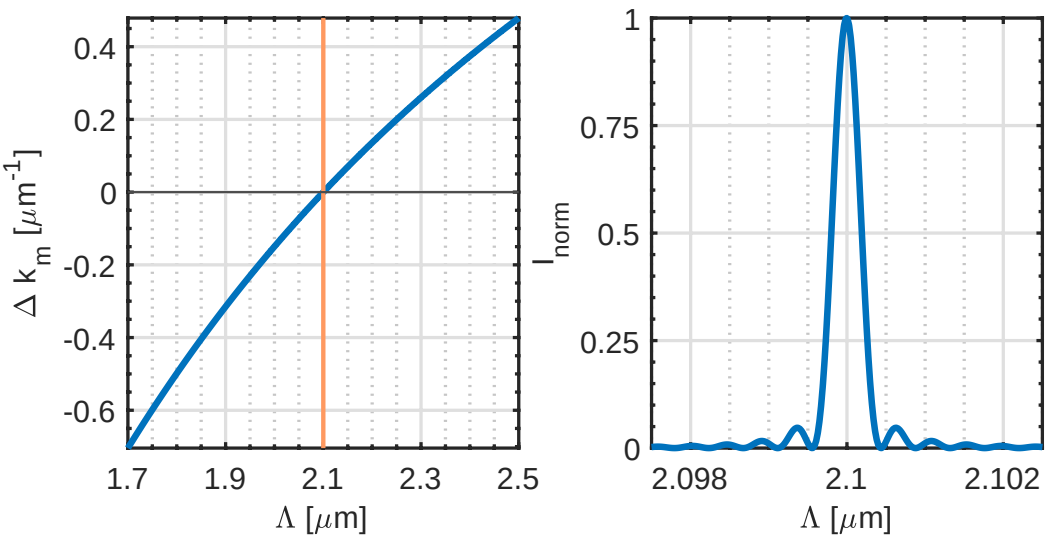

Figure 6.2: (left) Phase-mismatch curve for Type-0, 532nm-266nm frequency conversion. (right) Phase-matching intensity as a function of poling period.

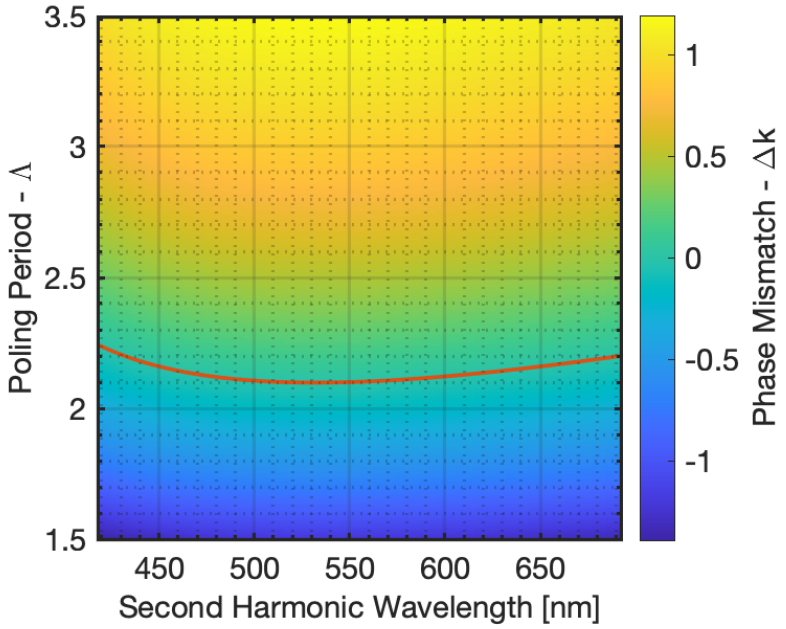

Figure 6.3: Contour plot showing the phase mismatch Δk as a function of the fundamental pump wavelength and the poling period, Λ. The orange curve shows the $\Delta k = 0$ iso-line, which at 532nm is equal to the $2.1\mu m$ poling period value.

important design consideration is the effective interaction volume and the associated optimal focusing condition of the pump field. As per the specifications provided by the company, the experimentally realizable grating cross-section is 1mm(W) x 0.3mm(H). With the total crystal length being 10mm, we rely on the theoretical treatment by Boyd-Kleinman [15] to determine the optical focusing element which

yields the optimal focusing parameter for the most efficient generation of the second harmonic under the assumption of no pump depletion. Although primarily meant for bulk crystals that utilize BPM, the theoretical approach is still useful as long as the beam waist is chosen so as to match the grating cross-section at the focus. The focusing parameter ζ is defined as,

$$\zeta = \frac{L_c}{b} \tag{6.7}$$

where L_c is the total length of the crystal, and b the confocal parameter for a Gaussian beam.

$$b = 2z_R = \frac{2\pi w_0^2}{\lambda_\omega} \tag{6.8}$$

The variables w_0 and z_R are the beam waist and Rayleigh range, respectively, with

$$2w_0 = \frac{4\lambda_\omega f}{\pi D} \tag{6.9}$$

for a given focusing optical lens with focal length f and input beam diameter D.

Per their derivation from first principles, the optimal effective nonlinearity E_{NL}, corresponding to the situation where the pump field is focused sufficiently strong enough while at the same time utilizing the largest possible volume of the grating, is found at a value of $\zeta = 2.84$.

This result allows us to calculate the ideal focal length lens to be utilized for a wide range of wavelengths and input beam diameters. The Millenia eV 15W DPSS laser intended to be used for the pumping of the crystal has a manufacturer specified beam diameter of ~2.3mm. It thus becomes trivial to evaluate the optimal lens focal length value of ~17cm for our specific experimental configuration.

6.3 Experimental SHG Characterization

In order to characterize the performance of our LBGO crystal, we utilize a relatively simple experimental setup depicted in Fig.6.4. It consists of a 15W DPSS laser source which is passed through a polarization conditioning step, consisting of a polarizer and half-waveplate, after which the power is monitored using a 99:1 beamsplitter. The beam is subsequently focused through the grating using a 10cm focal length lens. The reason for the shorter focal length used here in contrast to the optimal value calculated in the design section is the experimentally measured smaller beam diameter (1.3mm) of the 532nm laser source. The grating is mounted on top of a PID-loop controlled heating element, that sits on top of an XYZ translation

stage to ease alignment. The output, now consisting of the generated 266nm second harmonic and the residual 532nm pump beam, is collimated using a short focal length lens in order to keep the beam diameter small. The collimated beam is then passed through a filter stack consisting of multiple short-pass filters to remove as much of the residual pump beam as possible. The filtered 266nm signal is then fiber coupled into a multimode fiber which is used as the input to either a spectrometer for spectral characterization, or a UV sensitive photodiode to measure the generated power.

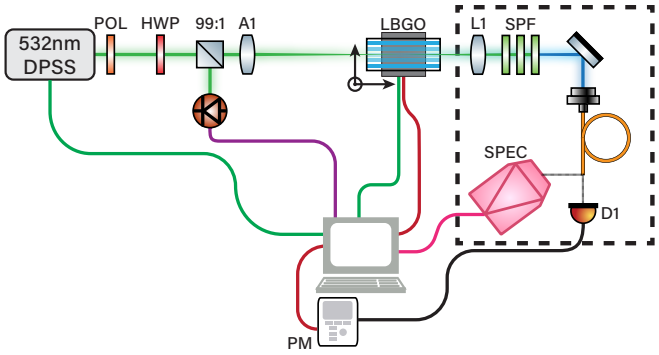

Figure 6.4: SHG characterization setup. It consists of a 15W 532nm DPSS laser source which is polarization conditioned using a polarizer (POL) and a half-waveplate (HWP). The power is then monitored using a beamsplitter (99:1), and the light is focused through the grating (LBGO) using an aspheric lens (A1). The grating sits on top of a PID-loop controlled heating element, which is mounted on top of an XYZ translation stage to aid alignment. The second harmonic output is then collimated using a short focal length lens (L1). The collimated beam is passed through a filter stack consisting of three short-pass filters (SPF) to remove the residual 532nm pump light. The filtered 266nm signal is then fiber coupled into a multimode fiber (orange) and directed towards a spectrometer (SPEC) or a UV sensitive photodiode (D1) to measure the power (PM).

After observation of a weak second harmonic signal and subsequent optimization of the input coupling into the grating, we performed a temperature scan of the crystal to characterize the temperature dependence of the phase-matching as shown in Fig.6.5. For the 2.1μm poling period of our crystal, we expected the perfect phase-matching temperature to be around 70°C. The experimentally measured value which resulted in the strongest 266nm signal was found to be 57°C. We attribute this discrepancy to the fact that continuous cw pumping has a significant contribution to dissipating power as heating in the crystal. Therefore, the required temperature to be set for the heating element would necessarily be lower as the tightly focused pump field provides a certain element of additional heat.

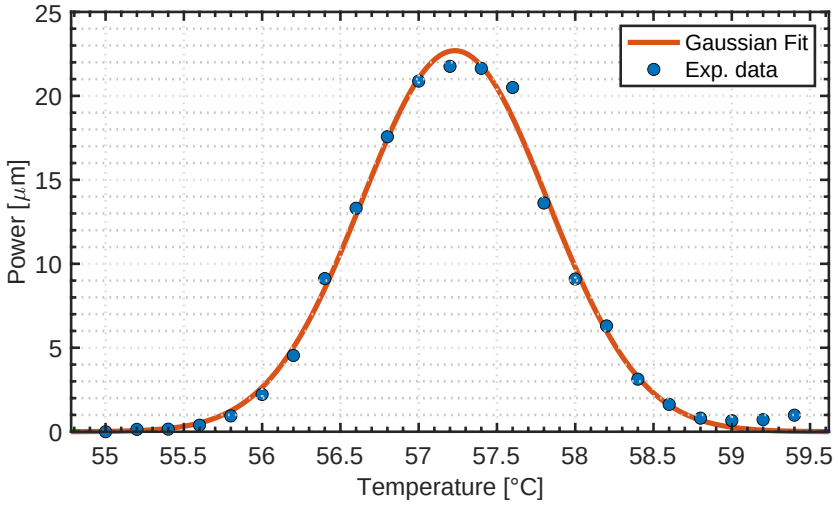

Figure 6.5: Temperature characterization of the generated 266nm second harmonic signal. Blue data points are experimentally measured values with the orange curve a Gaussian fit of the data.

The experimental setup used is also ideal for the characterization of the single-pass efficiency of the LBGO crystal. As the most recent implementations of LBGO for the generation of 266nm all utilized pulsed laser sources as the input pump, there is no available data for expected cw pumped conversion efficiencies. We define the single-pass conversion efficiency ϵ as

$$\epsilon = \frac{P_{OUT}}{P_{IN}} \tag{6.10}$$

with P_{OUT} and P_{IN} being the output and input powers at 266nm and 532nm, respectively.

To determine ϵ, we varied the input 532nm pump power and recorded the measured 266nm output signal. The results are plotted in Fig.6.6. As expected, the SHG power scaling follows a quadratic trend with the data being fitted with the curve in orange. The calculated single-pass efficiency for the cw pumped case is thus calculated to be $\sim 1^{-4}$. This value is found to be prohibitively low for generating enough 266nm signal to pump a second, identical grating for the generation of entangled photon pairs. In particular, as although the input power could feasibly be increased to $> 1W$, and thus generate μW levels of 266nm light, the associated strong laser induced heating effects could be detrimental to the crystal and result in critical damage. Therefore, the simple single-pass pumping scheme would not be suitable for long-term experimental implementations. The most effective way to obtain second harmonic power levels that would be usable in SPDC experiments

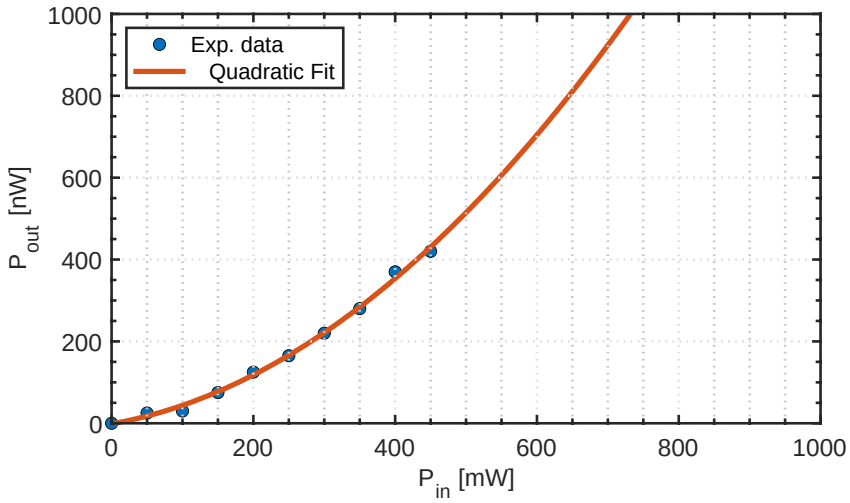

Figure 6.6: Power characterization of the generated 266nm second harmonic signal. Blue data points are experimentally measured values with the orange curve a quadratic fit of the data.

is through the implementation of a resonant cavity around the grating. This would yield an enhancement of the SHG conversion efficiency through the re-circulation of the light inside the resonator. The low single-pass efficiency is thereby overcome without a required increase in the fundamental input pump power that could result in the damage or destruction of the crystal.

6.4 Cavity Enhanced SHG

Resonant cavity enhanced SHG is a common technique to obtain moderate to high nonlinear conversion efficiencies at experimentally realistic input powers. The cavity consists of a series of mirrors set up in such a way so as to allow the light inside to circulate with minimal losses. The standing wave that is supported in such a resonator ensures that photons which have not participated in a nonlinear interaction as a result of a low single-pass efficiency get recycled and are allowed multiple passes through the crystal. As a result of this, the input pump power requirements remain more conservative.

Cavities are primarily characterized for their performance through their finesse, $\mathfrak{F}$, which is a measure of how narrow the supported cavity resonances are relative to the free spectral range of the resonator. In simple terms, the sharper a resonance, i.e. smaller FWHM, the higher the value of the finesse, defined as

$$\mathfrak{F} = \frac{\pi}{2arcsin\left(\frac{1-\sqrt{\rho}}{2\sqrt[4]{\rho}}\right)} \tag{6.11}$$

where ρ is the remaining circulating power after a single round-trip and thus $1-\rho$ is the cavity round-trip loss. It is easy to see from this that lower internal cavity losses lead to higher finesse cavities, as less of the light is lost per round-trip. A related metric also commonly used is the so-called Q-factor which includes a scaling with respect to the average optical frequency.

Fig.6.7 shows the calculated cavity finesse for a range of round-trip loss values. As is evident from the plot, the more reflective the mirrors constituting the cavity are made, the lower the round-trip losses are and therefore lead to a higher finesse. Experimentally, the higher the cavity finesse, the more efficient a nonlinear conversion process becomes due to the higher ratio of recycled pump photons.

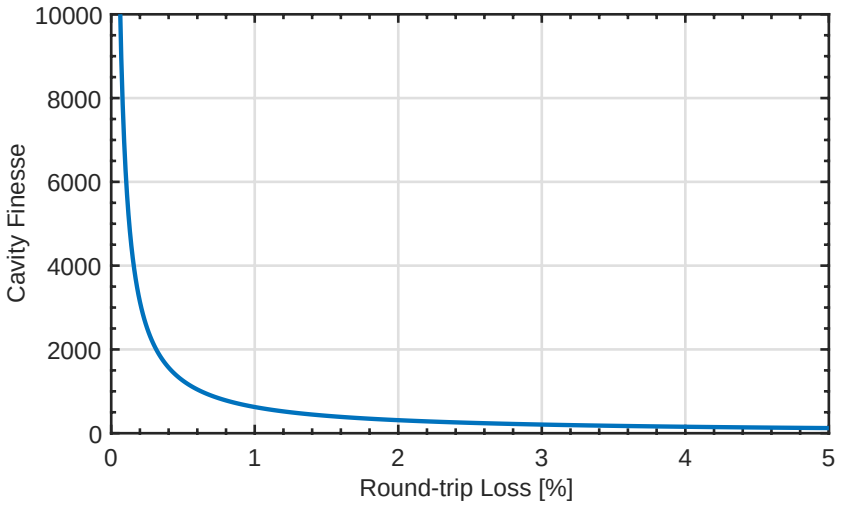

Figure 6.7: Plot of Eq.6.11 showing the scaling of the cavity finesse as a function of the cavity round-trip loss percentage.

Following the work of Ashkin et al. [16], the overall conversion efficiency in a resonant cavity is defined as

$$\sqrt{\epsilon} = \frac{4T_1\sqrt{E_{NL}P_1}}{\left[2-\sqrt{1-T_1}\left(2-L-\sqrt{\epsilon E_{NL}P_1}\right)\right]^2} \tag{6.12}$$

where E_{NL} is the single-pass conversion efficiency, and T_1 is the input coupler transmission coefficient. The factor L specifies the overall linear losses of the resonator (not including T_1).

Given our experimentally measured single-pass conversion efficiency of $E_{NL} = 1^{-4}$, we can use Eq.6.12 to calculate the expected second harmonic output power as a function of the input pump power used, and the linear cavity losses. Fig.6.8

shows the contour plot of the relationship between these free parameters. Similarly, transforming the linear cavity losses into the more practical measure of the cavity finesse, $\mathfrak{F}$, we can alternatively display the contour plot as a function of this variable shown in Fig.6.9. The above figures demonstrate that for reasonably modest

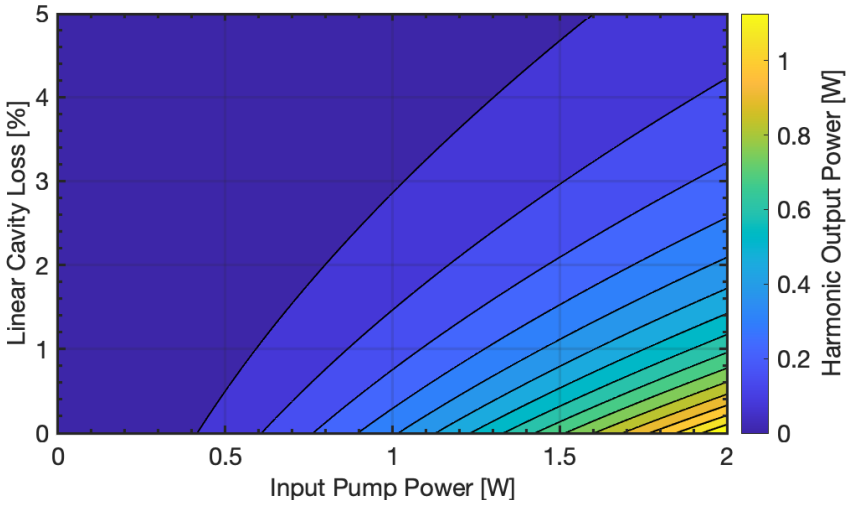

Figure 6.8: Contour plot of Eq.6.12 showing the expected harmonic output power as a function of the input pump power and the linear cavity loss parameter.

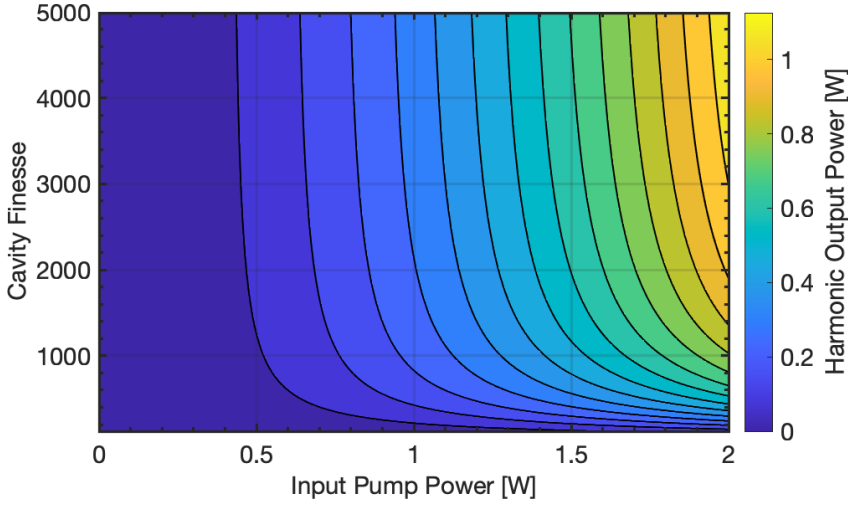

Figure 6.9: Contour plot of Eq.6.12 redefined to be showing the expected harmonic output power as a function of the input pump power and the cavity finesse parameter.

cavities with finesses of ~500, we can obtain an expected cavity enhanced nonlinear conversion efficiency of ~25%. The requirement to achieve this would be mirror reflectivities ~99.6% which are fairly easy to obtain for the Nd:YAG harmonic wavelength of 532nm. Custom, high-quality coatings would allow cavity finesses

of >1000 (ϵ ~50%) and therefore close to Watt-level 266nm signal generation at safe pump powers <2W.

Coupling of the pump light into the cavity is achieved through an input coupler mirror which is partially transmissive. The transmissivity of this mirror is an important parameter as it both sets how much light is allowed to be fed into the resonator, and also contributes to the linear cavity losses. To determine the optimal value of T_1 which maximizes the resonantly-enhance conversion efficiency, we can solve Eq.6.12 for this parameter. The optimal value of T_1 yielding ϵ_{max} is then given as follows.

$$T_1^{opt} = \frac{L}{2} + \sqrt{L^2/4 + E_{NL}P_1} \tag{6.13}$$

Fig.6.10 shows the contour plot of how T_1^{opt} scales as a function of the input pump power and the linear cavity loss parameters. It is easy to see that higher finesse cavities require less input power to be coupled into the resonator as a result of the better photon recycling due to lower losses. The experimental implementation of our

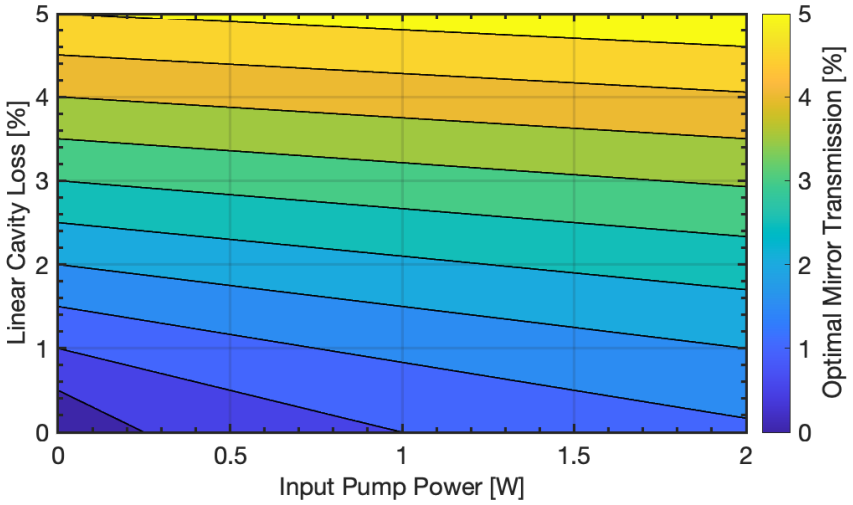

Figure 6.10: Contour plot showing the optimal mirror transmission parameter T_1^{opt} as a function of the input pump power and the overall linear cavity loss percentage.

resonator is based on a bow-tie cavity shown in Fig.6.11 which slightly modifies the SHG characterization setup used. It consists of four mirrors, M1-M4, in total (two flat and two concave). The two concave mirrors, M3 and M4, are chosen such that their focal points lie at the center of the LBGO grating. Mirror M1 corresponds to the input coupler, which is needed to allow some pump light into the cavity. Mirror M2 is the output coupler of the cavity, and it is fully reflective at the fundamental wavelength, while being transmissive at the second harmonic. To achieve mode-matching into the cavity, the aspheric lens has been replaced with lens L1 with a

longer focal length to loosely focus at the concave mirror surface M3. At the second harmonic output of the cavity M3, we utilized a lens L2 to collimate the 266nm light. Subsequently we still retained the short-pass filter stack from before to clean up the beam and remove any residual 532nm pump light.

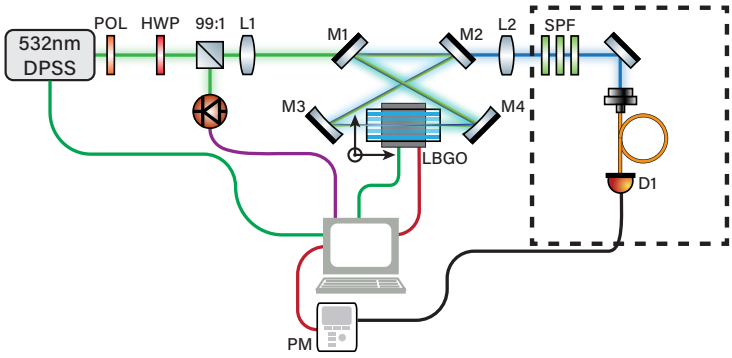

Figure 6.11: Cavity enhanced SHG setup; consisting of a 15W 532nm DPSS laser source which is polarization conditioned using a polarizer (POL) and a half-waveplate (HWP). The power is then monitored using a beamsplitter (99:1), and the light is focused and mode-matched into the cavity (LBGO) using a lens (L1). The grating is positioned inside a bow-tie cavity, composed of four mirrors, M1, M2, M3, and M4. The mirrors M3 and M4 are concave mirrors which focus the circulating light inside the cavity through the grating. M1 is the weakly transmissive input coupler that allows light to be coupled into the resonator. M2 is the output coupler, which is fully reflective at 532nm, however transmits 266nm light. The grating sits on top of a PID-loop controlled heating element, which is mounted on top of an XYZ translation stage to aid alignment. The now cavity enhanced second harmonic output is collimated using a lens (L2). The collimated beam is passed through a filter stack consisting of three short-pass filters (SPF) to remove any residual 532nm pump light. The filtered 266nm signal is then fiber coupled into a multimode fiber (orange) and directed to a UV sensitive photodiode (D1) to measure the power (PM).

6.5 Deep-UV Pumped SPDC at 532nm

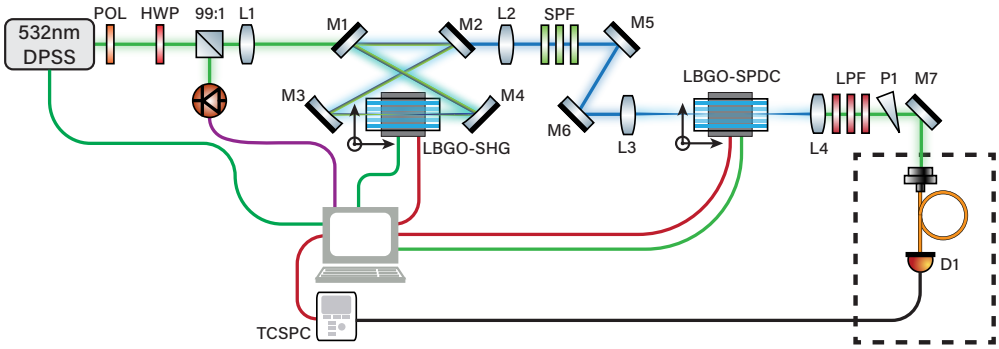

Figure 6.12: Cavity enhanced SHG setup followed by UV pumped SPDC; the cavity enhanced SHG follows the exact same experimental layout as described in 6.11, see its caption for details. The UV pumped SPDC is implemented by introducing mirrors M5 and M6 to steer the 266nm output and focus it through the LBGO grating (LBGO-SPDC) using lens (L3). The grating sits atop a ceramic heating element and is phase-matched for degenerate, collinear downconversion at 532nm. The SPDC output is the subsequently collimated using a lens (L4) and passed through a stack of long-pass filters (LPF) as well as a prism (P1) to dispersively filter any residual 266nm pump light. The collimated SPDC signal is then fiber-coupled and sent to a UV-sensitive SPAD (D1).

6.6 Conclusion

In conclusion, we have shown that using periodically poled LBGO and quasi-phase-matching techniques is a feasible route towards the generation of cw radiation in the UV wavelength range. By characterizing the gratings for their phase-matching properties, we have found that the theoretical calculations used in the design phase are experimentally well supported. Therefore, the numerical simulations can be utilized further to refine the source properties, such as potential non-degenerate or broadband wavelength emission characteristics. By the nature of utilizing cw pumping with low peak power, measurement of the single-pass conversion efficiency yielded an expectedly low value of $\sim 1e^{-4}$. Thus, the potential to generate significant second-harmonic power with pump power levels that are not critically high so as to cause laser induced damage to the crystal through impurity absorption is not possible without resonant enhancement.

The implementation of an external bow-tie cavity to mitigate the effects of the low single-pass conversion efficiency is currently under process. The theoretical treatment presented, aimed to estimate the cavity dependent enhancement of the second harmonic generation, showed that SHG conversion efficiencies as high as

50% are realistic using relatively modest cavity finesses. As such, cavity-enhanced SHG using ppLBGO is expected to be able to produce the $\sim 1W$-level powers that are needed for a subsequent SPDC process to be pumped. Given the measured temperature stability of the phase-matching in LBGO, in conjunction with the moderate pump power levels required, the designed setup is showing excellent long-term stability, however with active cavity-stabilization possibly being a requirement. In bow-tie cavities, this can be achieved in a straightforward manner using a single electrically actuated mirror element.

The characterization of the SPDC process in ppLBGO remains yet to be fully accomplished, once sufficiently high power levels are obtained.

References

[1] Andrzej W Miziolek, Vincenzo Palleschi, and Israel Schechter. *Laser induced breakdown spectroscopy*. Cambridge university press, 2006.

[2] Sanford A Asher. "UV resonance Raman spectroscopy for analytical, physical, and biophysical chemistry. Part 2". In: *Analytical chemistry* 65.4 (1993), 201A–210A.

[3] Hongbin Liang et al. "VUV–UV photoluminescence spectra of strontium orthophosphate doped with rare earth ions". In: *Journal of Solid State Chemistry* 167.2 (2002), pp. 435–440.

[4] Challa SSR Kumar. *UV-VIS and photoluminescence spectroscopy for nanomaterials characterization*. Springer, 2013.

[5] G Isenberg et al. "Cell surgery by laser micro-dissection: A preparative method". In: *Journal of Microscopy* 107.1 (1976), pp. 19–24.

[6] Silvia Hernández and Josep Lloreta. "Manual versus laser micro-dissection in molecular biology". In: *Ultrastructural pathology* 30.3 (2006), pp. 221–228.

[7] Motowo Tsukakoshi et al. "A novel method of DNA transfection by laser microbeam cell surgery". In: *Applied Physics B* 35.3 (1984), pp. 135–140.

[8] Moishe S Kitai et al. "The physics of UV laser cornea ablation". In: *IEEE journal of quantum electronics* 27.2 (1991), pp. 302–307.

[9] Charles S Dulcey et al. "Deep UV photochemistry of chemisorbed monolayers: patterned coplanar molecular assemblies". In: *Science* 252.5005 (1991), pp. 551–554.

[10] Zhengmao Zhu and Michael J Kelley. "IR spectroscopic investigation of the effect of deep UV irradiation on PET films". In: *Polymer* 46.20 (2005), pp. 8883–8891.

[11] Andrey S Mereshchenko et al. "Ultrafast photochemistry of copper (II) monochlorocomplexes in methanol and acetonitrile by broadband deep-UV-to-near-IR femtosecond transient absorption spectroscopy". In: *The Journal of Physical Chemistry A* 120.11 (2016), pp. 1833–1844.

[12] Yukihiro Ozaki and Satoshi Kawata. *Far-and Deep-ultraviolet spectroscopy*. Springer, 2015.

[13] William J Abbey et al. "Deep UV Raman spectroscopy for planetary exploration: The search for in situ organics". In: *Icarus* 290 (2017), pp. 201–214.

[14] Nobuhiro Umemura et al. "Temperature-dependent quasi phase-matching properties of periodically poled LaBGeO 5". In: *Optical Materials Express* 9.5 (2019), pp. 2159–2164.

[15] GD Boyd and DA Kleinman. “Parametric interaction of focused Gaussian light beams”. In: *Journal of Applied Physics* 39.8 (1968), pp. 3597–3639.

[16] A Ashkin, G Boyd, and J Dziedzic. “Resonant optical second harmonic generation and mixing”. In: *IEEE Journal of quantum electronics* 2.6 (1966), pp. 109–124.

Chapter 7

TOWARDS NANOPHOTONIC IMPLEMENTATIONS OF ENTANGLED PHOTON SPECTROSCOPY

7.1 Introduction

In specific circumstances, such as it is in the case of entangled photon interferometry, the transition from free-space optics to optical fibers carries with it a lot of useful advantages. In particular, the easy to re-configurable circuit architecture makes fiber implementations unusually flexible. This is especially beneficial in the scope of extremely low-power entangled photon setups, where alignment of these difficult to measure signals is a challenge. Although medium-power coherent sources can aid in this endeavour, their integration into table-top experiments can be unnecessarily impractical. First and foremost as the cascaded nature of free-space optics means that changes to the optical system upstream inherently carries with it a downstream re-alignment step. Therefore, coherent sources at the correct downconversion wavelength of choice are wholly indispensable.

As demonstrated in the chapter pertaining to the implementation of the fiber-optic entangled photon interferometer (Ch.4), the confinement of light to optical waveguides practically removes the need for any re-alignments once any (potential) free-space optical elements have been adjusted to maximize transmission. In the extreme case of being entirely independent of free-space components, long-term system, and therefore experiment stability is a given. Furthermore, the experimental footprint, weight, and portability aspects are additional advantages of this change in architecture.

Unfortunately, such as it is, optical fibers themselves carry some unwanted disadvantages. Standard single-mode fibers are notoriously sensitive to environmental fluctuations, like vibrations and temperature gradients. The effective modulation of the refractive index of the fiber through these effects causes, most notably, drifts in the polarization state of the field being guided. While polarization maintaining fibers serve as a good solution for this problem, they are not always practical to implement in an experiment. Furthermore, unless spliced together, the number of fiber connections involved in an experiment carries a significant loss budget with it. Even small-scale circuits composed of only a few handfuls of distinct fiber components

dramatically scale in the total system efficiency. As mentioned, this can however be mitigated through fiber splicing methods.

The general industry trend towards absolute miniaturization of optical systems is one that has significant merit. Nanophotonic implementations take advantage of low power budgets, extremely small footprints, easily scalable circuit architectures, and unique optical components with superior performances just to name a few. Unfortunately this comes at a cost, in that the initial design and fabrication barrier can be prohibitive. In lieu of this, taking advantage of the possibilities that nanophotonics has to offer, alongside its integration into the larger world of CMOS compatible technologies, means that there are numerous new scientific areas that could be explored. These range from single-molecule spectroscopy, to integration of microfluidics, or even the implementation of molecular qubit systems.

Recent work on the nanophotonic integration of entangled photon interferometers has been increasing in pace. While initial implementations already exist, there are numerous ways that these systems can be envisioned. Here, I would like to provide some nanophotonic design principles for the implementation of certain specific elements within the overall photonic integrated circuit. Owing to the fact that the design process for quasi-phase-matched waveguide has been discussed at length in other chapters, this will not be further elaborated on. I hope that the information contained in this chapter will serve as a helpful basis for extending the work which is currently beginning to take roots in our lab.

7.2 System Architecture

Our proposed monolithic, lithium niobate nanophotonic platform comprises multiple elements, as shown in Fig.7.1: (a) An adiabatic coupler and mode converter for high-efficiency fiber/free-space coupling. (b) A quasi-phase-matched waveguide used to generate MHz level entangled photons, here for the sake of concreteness chosen to be at 1550nm. This wavelength allows the use of common 775nm laser diodes. (c) An in-line photonic crystal filter for high suppression of the residual 775nm pump wavelength. (d) A complete on-chip Mach-Zehnder interferometer circuit to allow deterministic photon state manipulation. The interferometer consists of 2-by-2 couplers for probabilistically splitting/recombining the entangled photon pairs into separate arms, with polarization or spatial-mode de-multiplexing also a possible option. (e) Electro-optic phase shifters or electrically tunable high-Q ring-resonators for introducing the relative time-delays needed for spectroscopy.

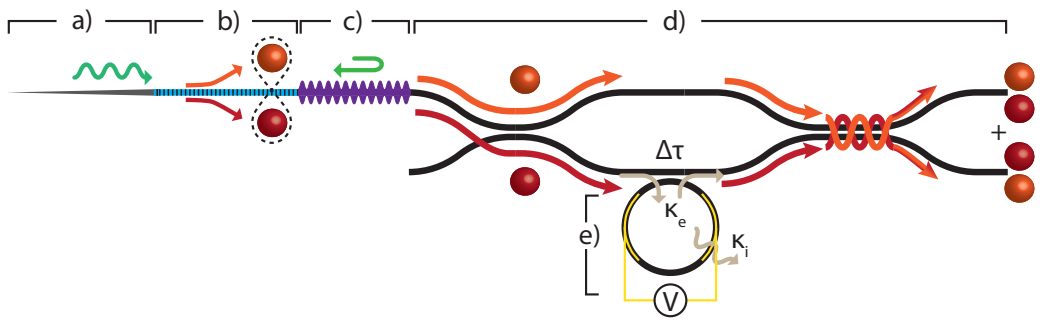

Figure 7.1: Schematic integrated circuit layout for a proposed monolithic HOM interferometer. From left to right; (a) adiabatic coupler and mode converter, (b) periodically-poled waveguide section for SPDC, with poling electrodes and example spectrum shown, (c) photonic crystal filter element with simulated band-diagram and unit cell shown, (d) Mach-Zehnder interferometer circuit consisting of 2x2 couplers with (e) tunable time-delay in one arm via an electrically controlled high-Q ring-resonator (resonator coupling strength and intrinsic loss defined by κ_e and κ_i respectively). The generated entangled N00N-state due to two-photon interference is shown at the output.

7.3 Photonic Crystal Filters

Immediately following the SPDC process in the periodically poled region of the waveguide, the input pump beam which served as the seed for the downconversion process no longer has any use. Therefore we require a strategy to stop these photons from further propagating in the integrated circuit. While it would be possible to filter out the specific pump wavelength using a resonant drop filter, or even a cascade of them, this would not necessarily be the most efficient or "safest" way to handle this. Obviously one thing to keep in mind is that the lithographically simplest solution is usually the best. Going down the route of elaborate photonic elements is likely to cause more of a headache in the end when further modifications are needed.

Therefore, the proposed route to achieve efficient filtering of the pump beam is to utilize in-line photonic crystal filters. Photonic crystals have the major advantage that they are easily scalable from the point of view that in order to obtain a higher rejection-ratio, simply more unit cells can be appended onto the periodic structure. By designing a photonic crystal waveguide with a bandgap at the particular frequency of interest, it becomes evident that the simplicity of the approach is also reflected in its function. The entangled photon pairs, which are located far away from the bandgap, effectively see the region as transparent and therefore will not be effected. The pump frequencies which fall inside the region where propagation is forbidden, will effectively encounter a mirror element. After reflection, even though the pump

field will traverse the periodically poled region again and therefore generate more entangled photon pairs, all three of these fields will have k-vectors which are in the opposite direction. Although the back-propagation of the pump towards the laser source is usually undesirable, since the coupling efficiency into a collimated mode after exiting the waveguide coupler is effectively zero, this should pose no risk. If it is deemed to be necessary after all, a simple method to deal with the backwards propagating mode is to utilize an optical isolator, consisting of a polarization beamsplitter and a Faraday rotator.

Although the design process for a photonic crystal waveguide may seem daunting at first given the number of free parameters, there are some general rules of thumb that can be followed to zero-in on a potential design. Here, we will show two slightly different implementations that perform equally well, however from a fabrication perspective differ somewhat in their difficulties. Both designs will be implemented on lithium niobate and will be targeted at a rejection wavelength (i.e. the middle of the bandgap) of 775nm.

Nanobeam design

First, we look at the most conventional unit cell design, which consists of a rectangular beam section with a hole in the middle. The periodicity generated by the holes lifts the degeneracy of the dielectric and air modes at the Brillouin zone edge, that would normally exist in the case of an unpatterned waveguide. The emergence of this bandgap where no guided modes exist is what requires to be placed precisely at the frequency location of interest. The primary parameter which determines the location of the bandgap is the lattice-constant a. This parameter is effectively responsible for introducing interference between adjacent unit cells. When beginning to search for a reasonable value, it is worth noticing that the condition for interference can be distilled down to the lattice-constant being comparable in scale to the effective wavelength of light. As such, a can be evaluated to fall near $\lambda = c/nf_0$, where n is the refractive index of the material and f_0 the frequency. For lithium niobate, at 386.8THz, we get $a \sim 350nm$.

Next, the size of the bandgap Δf is dictated by the index contrast between the material and the surrounding medium. The way this manifests itself in the geometry is in the beam thickness, t, and the hole-size, parameterized by $h_x and h_y$ that signify the lateral and longitudinal hole radii. While it is useful to have a constraint placed up t, this is sometimes not the most realistic path to follow. The device layer

thickness is ultimately dictated by a number of other, higher order, considerations, like the fundamental guided modes in the rest of the circuit or the fabrication specific requirements. Regardless, it can be useful to have a rough idea about reasonable values that would maximize the given parameter and so the thickness t should approximately be equal to the lattice constant a. To optimize the bandgap, the thickness can be slowly adjusted downwards up to a value of $\sim 0.5a$. Optimal Δf will be located somewhere in-between.

Given that the hole-size is parameterized by two values, it might be tempting to treat both independently, however the bandgap is quite robust with respect to the particular shape used. To further elucidate on this, the hole shape is more applicable when both optical and mechanical modes need to be taken into consideration. Mechanical resonances are particularly sensitive to the hole deformation and therefore phononic bandgaps are tune through the additional adjustment of the two hole radii separately. For our optical bandgap of interest, the crucial element is actually simply the ratio between the area of suspended by the hole and the total area of the unit cell (i.e. $a \times w$). Although this is not strictly true for *all* bandgaps in general, the ideal ratio which results in the largest TE bandgap is found between 0.2-0.25.

Following these design considerations, we can perform a three-dimensional FEM simulation in COMSOL to determine the bound and leaky modes of a structure at various values of the wavevector k. By enforcing a periodic condition at both end surfaces of the unit-cell, we can treat the system as quasi-infinite and thereby extract a dispersion relation for a specific design. A semi-optimized (one where the guided modes at the SPDC frequencies still require pulling down below the light-line) bandstructure for a nanobeam photonic crystal is shown in Fig.7.5. As is obvious, the dielectric and air modes form a TE bandgap around our frequency of interest. The TM mode which is located inside the gap is not necessarily of any worry as there should be negligible coupling to orthogonal polarization modes.

When searching for a bandgap with a given structure, it is most often helpful to be cognizant of the electric field shape and distribution of the modes themselves. It is easy to get lost in parameter space where seemingly no bandstructure is being reproduced that makes sense, only to realize that there are no longer any bound modes to speak of due to some geometrical parameter being outside of the required parameter space. Therefore to help with this, Fig.7.3 shows the three lowest order modes of the nanobeam photonic crystal for reference.

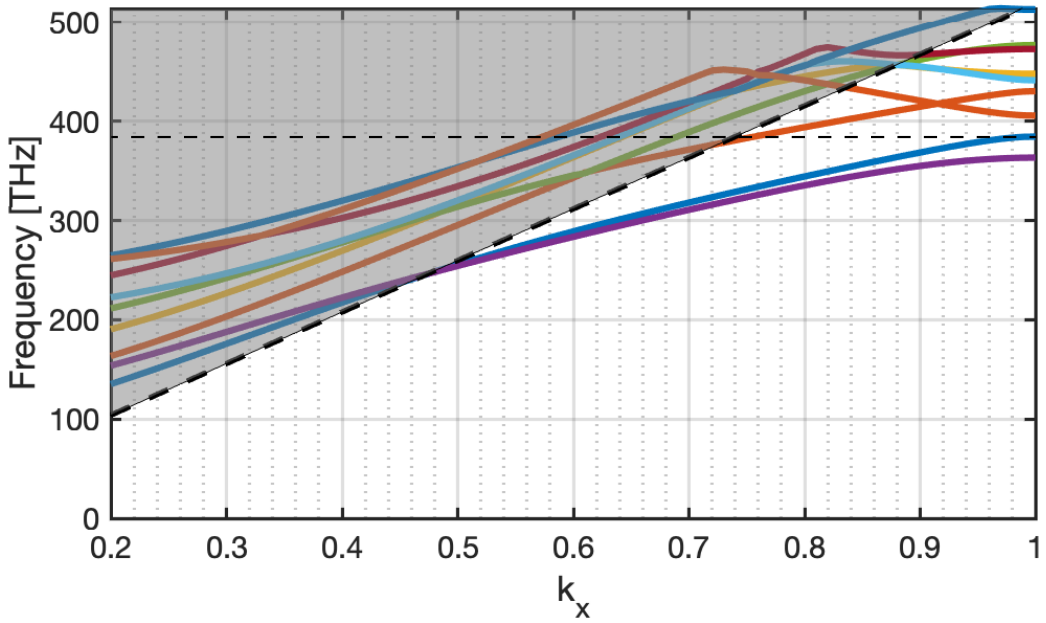

Figure 7.2: Lithium niobate nanobeam photonic crystal bandstructure with design parameters; a=270nm, t=300nm, w=400nm, h_x=h_y=90nm.

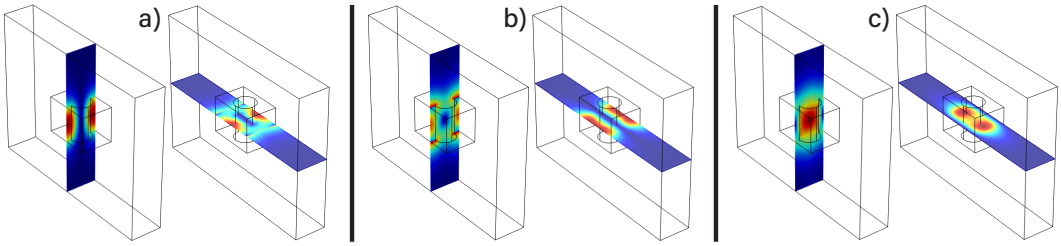

Figure 7.3: Lithium niobate nanobeam photonic crystal electric field distributions for the (a) TE dielectric mode, (b) TM dielectric mode, and (c) TE air mode.

Fishbone design

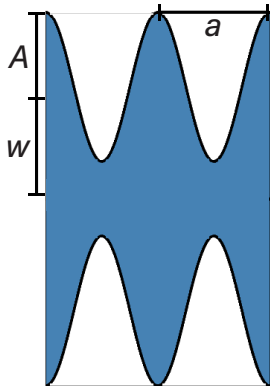

Figure 7.4: Fishbone geometry parameterization.

The second practical design which has advantages in particular from a fabrication

perspective is the so-called 'fishbone'. Here, instead of holes forming the periodic lattice along a nanobeam, it is instead a sinusoidal modulation of the outer edges that leads to Bragg diffraction. The design and parameterization is shown in Fig.7.4. The particular downside to this design is that it works better for thinner dielectric films. Film thicknesses above 500nm make it exceedingly challenging to open up band gaps in the dispersion relation at the visible-near IR wavelengths. To demonstrate a potential (un-optimized - again one where the guided modes at the SPDC frequencies still require pulling down below the light-line) design, we have chosen to reduce the film thickness to 200nm. This allowed for proper gap placement around 775nm and ensured that the aspect ratio of unit cell was not too extreme.

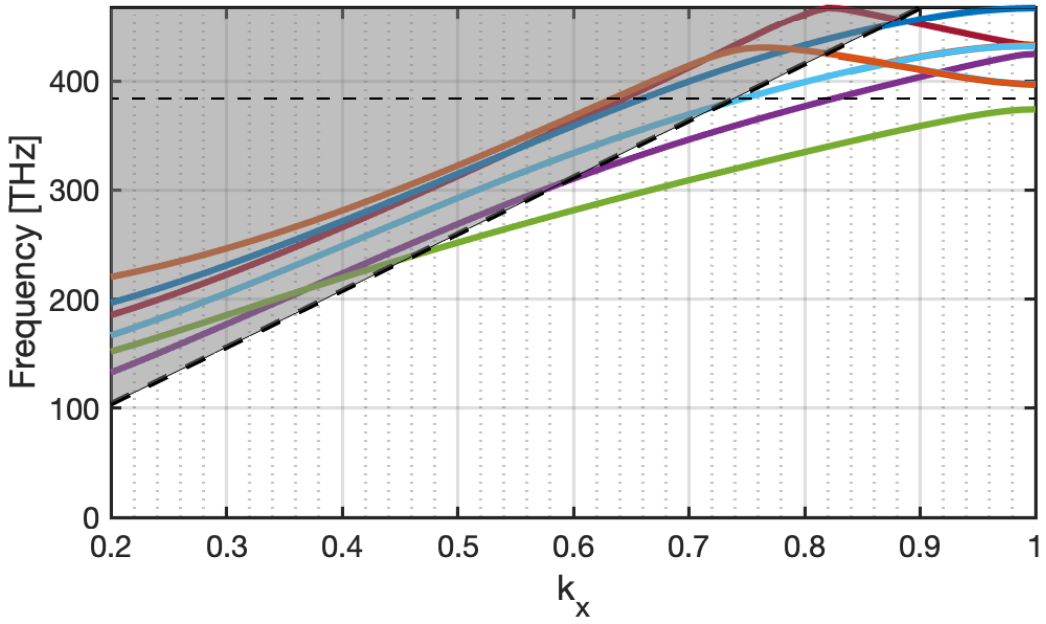

Figure 7.5: Lithium niobate 'fishbone' photonic crystal bandstructure with design parameters; a=270nm, t=200nm, w=200nm, A=150nm.

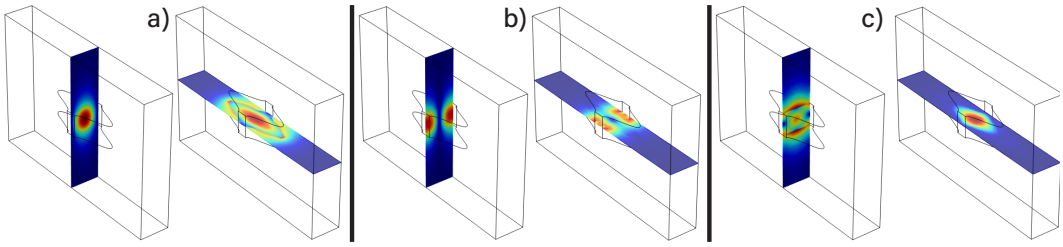

Figure 7.6: Lithium niobate 'fishbone' photonic crystal electric field distributions for the (a) TE dielectric mode, (b) TE air mode, and (c) TM dielectric mode.

These fishbone structures are generally very useful. In contrast to the nanobeams containing holes, the critical features which modulate the bandgap are located at the

edges and are thus less prone to be be affected by aspect-ratio dependent etching (ARDE) for example. The tolerances during lithography are similarly favourable, as deviations in the dosing (particularly overdosing) have been observed to have a negligible effect on the amplitude parameter, A. This general robustness and relatively simple design makes these fishbone devices a great testing platform, such as for high-Q cavities or filters.

The relative tuning of the optical properties as a function of the changes in the geometry are relatively easy to ascertain. Given that there are only really two free variables (the lattice constant a is usually not changed unless the center frequency of the bandgap needs to be shifted) available which are the amplitude A, and the width w, the free parameter space is fairly restricted. In effect, tweaking parameter w primarily shifts the bandgap center frequency f_0, while changes to A affect the stopband width Δf. Therefore once the appropriate lattice constant has been found, it becomes quite straightforward to position the bandgap precisely.

7.4 Resonators

Optical resonators play an important part in not just nanophotonics but also on the macro-scale. Their ability to confine light to a volume of space for extended periods of time make them applicable to increasing sample-interactions, the resonant enhancement of nonlinear processes, optical beamforming, or even to act as optical buffers to delay signals in their arrival times. Applications in which they are used as optical delay lines (ODL) require them to be not only easily tunable, but also to operate over a broad bandwidth with insertion losses kept as low as possible. Although they can be implemented in a variety of different ways, here we shall briefly focus on and describe ODLs that are complementary with our on-chip nanophotonic entangled-photon interferometer.

More specifically, we highlight the use of ring resonators which can be tightly integrated on-chip, and offer advantages such as low cost, (relatively) small size, and low power consumption. Furthermore, their operation speeds can be vastly superior to what is possible in traditional optical implementations. An obvious downside is that from a practical point-of-view, the time-bandwidth product remains a constant. Thus for an individual device, there is a balance between how long the effective delay can be vs. how broadband the working range is. This can be easily understood from the perspective of a high-Q resonator. The sharper the resonance (i.e. the narrower the bandwidth over which resonant frequencies exist), the longer

the time lifetime of the cavity, and vice versa. Irrespective of this bottleneck, for near-term implementations relying on narrowband SPDC, we can take advantage of the simpler design considerations associated with ring resonators coupled to a straight waveguide as shown in Fig.7.1e.

Using ring-resonators in conjunction with thermo-optic tuning to achieve our initial goals to have tunable optical delays in our circuit is a realistic approach. In order to effectively tune the delay along the waveguide in one arm, it is sufficient to tune the external coupling rate κ_e of the resonator, whereas the internal rate κ_i defines the intrinsic losses of the resonator. By definiton, we then take $\kappa_t = \kappa_e + \kappa_i$. In essence this means that the resonator is tuned into a state where the waveguide-resonator coupling is effectively strong. Detuning κ_e reduces the amount of light that is cross-coupled between the systems and therefore mitigates an optical delay effect. The associated change in the operating bandwidth is a result of the constant time-bandwidth product mentioned. The reflection intensity and phase shift of a waveguide-resonator coupled system can be well visualized as shown in Fig.7.7a and 7.7b.

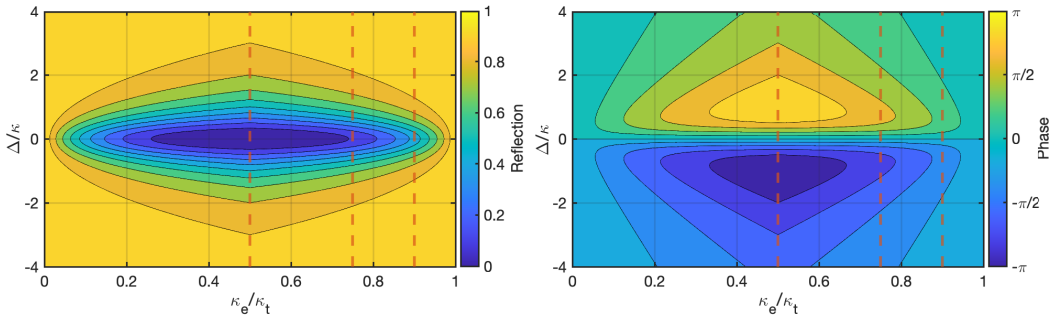

(a) (b)

Figure 7.7: (a) Contour plot showing the intensity of the reflection for a resonator as a function of the parameter κ_e/κ_t (x-axis) and the relative frequency detuning Δ/κ (y-axis); (b) the corresponding phase shift.

The contour plots show that there are two regions of interest $\kappa_e/\kappa_t < 0.5 and > 0.5$. These are the under-, and overcoupled cases, respectively, where the effective coupling rate κ_e is either too small or too large. At the crossover point, the coupling into the resonator is ideal, termed the 'critically'-coupled point. This is the situation when all of the light coupled into the resonator is eventually recovered. The dashed lines displayed on the contour plots represent slices along the frequency detuning relative to the cavity resonance as shown in Fig.7.8a and 7.8b.

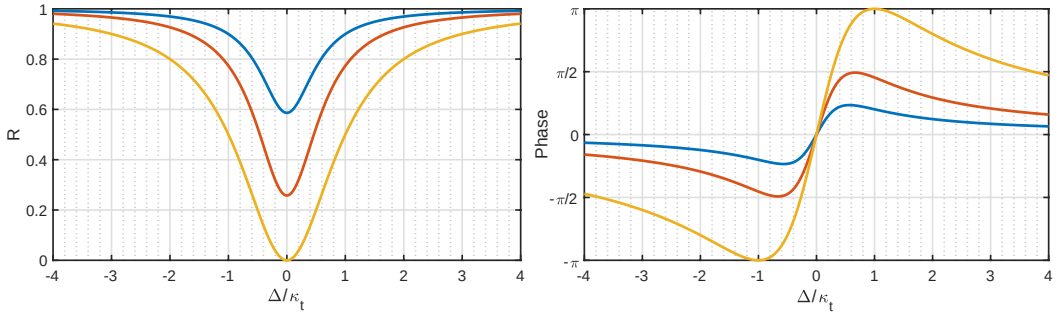

(a) (b)

Figure 7.8: (a) Slices along the dashed lines shown on the contour plots, showing the intensity of the reflection for a resonator as a function relative frequency detuning Δ/κ (y-axis); (b) the corresponding phase shift.

Investigation of the intrinsic and extrinsic cavity coupling rates can be done using FEM simulations in COMSOL. By appropriately setting up an input coupling waveguide with a closely positioned ring resonator, it is possible to estimate the required gap distances and ring resonator dimensions for achieving the desired amount of optical time delay/buffering. An example of a critically coupled system is shown in Fig., where we have designed the ring to be resonant with the specific input wavelength of the waveguide. The gap distance between the waveguide and resonator was then subsequently swept to find the optimal point where $\kappa_e = \kappa_i$.

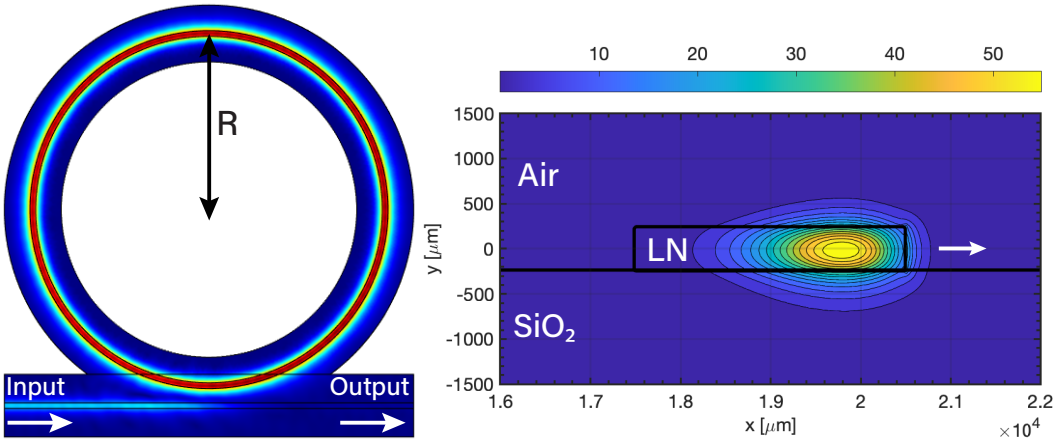

(a) (b)

Figure 7.9: (a) Waveguide-ring resonator coupling FEM simulation showing the critical coupling of the waveguide input mode into the resonant mode of the cavity (b) correspnding electric field mode profile for the cross-section of the thin-film LN ring resonator

In order to increase the total available optical delay that is possible in the circuit, the

easiest solution is to stack these resonators. Following the methodology of SCISSOR (side-coupled integrated spaced sequence of resonators), the time-bandwidth product can be effectively increased. In this architecture, multiple, identical resonators are side coupled to the same input waveguide, thus providing a total possible delay equal to their sum. The bandwidth constraint however remains the same as with a single device. Thus, this technique is a simple yet effective way of increasing the available optical delay by a factor N. Of special note is that slow-light effects obviously lead to dispersion effects becoming more severe due to group velocity differences. Therefore increasing the number of resonators indefinitely is only viable in the narrowband wavelength domain. Special techniques to compensate for this dispersion in the case of broader signals entail the detuning of cavity resonances in opposite directions along the cascade.

To briefly conclude this section, we would like to point out that in terms of performance, such ring resonator based designs satisfy our specific requirements in excess. It has been shown that optical delays $> 100ps$ are experimentally possible, which is, of course, orders of magnitude larger than what our picosecond to femtosecond scale coherence time entangled photons require. The ~GHz level bandwidths that these systems are capable of will likely pose a challenge in the implementation.

7.5 Slow-light Photonic Crystals for Sample Interactions

Following the foundations set out by atomic light-matter systems, the simplest method to achieve an interaction between the two sub-systems is via a free-space coupling. The downside to this is the naturally weak interaction that is dictated by the diffraction limit. Since for atoms, the optical cross section is given as $\sigma_0 \approx \frac{\lambda^2}{2}$, and the smallest area that a beam can be focused down to using free-space optics is $A \approx \lambda^2$, we get a sub-optimal coupling rate as a result of the dipole radiation pattern having a poor overlap with that of the free-space propagating mode.

Cavity systems consisting of an optical cavity (such as Fabry-Pérot cavities) being incorporated around the emitter enhance the interaction rate N-fold, due to the multiple passes that the light inside the cavity has to interact with the atom/molecule. Figure of merit here is the cooperativity, C. Given that cavities with Q-factors of $> 10^5$ are easily achievable, the strong-coupling regime is more or less easily obtained in cavity-QED (cQED). The major drawback of cavity systems is that they are difficult to scale. Especially if one is looking for systems with a large number of distinct samples to interact with. The design and subsequent precise implementation

of optical layouts with a substantial number of cavities that are all precisely aligned to be resonant with the sample systems of interest is an experimentally very challenging and daunting endeavour.

A current paradigm that AMO systems try to exploit is that of waveguide-QED (wQED). A departure from free space optics allows one to really take advantage of the small size scales offered by nanophotonics. In contrast to the approaches in cQED where the coupling is enhanced via the N-fold interaction of the optical mode with that of the atom, wQED aims to achieve this via a minimization of the photonic mode volume that interacts with the emitter. By more tightly confining the light near the atom/molecule system, the mode overlap between the dipole radiation pattern and that of the photonic mode becomes particularly strong. As a result the coupling rate increases substantially. While this enhancement is, of course, also present in small mode-volume cavity systems, the scalability enabled by wQED makes it a much more lucrative approach.

While fiber-optic guided modes are a prime resource for implementing these scalable systems, the downside is that they are missing some very interesting physics. Namely bandgaps. In contrast, nanophotonics offers a significant advantage in the way structures can be modified to display novel properties. Thus, instead of relying on a tapered optical fiber that only has guided modes to be utilized, we can design waveguides with a periodic lattice structure. Now, in addition to the traditional guided modes supported by a simple rectangular waveguide, the introduced periodicity opens up a bandgap in the dispersion relation. Inside this bandgap, the photonic modes are forbidden to propagate and therefore take on exponentially decaying functional forms. Near the band-edge, the slope of the dispersion relation approaches zero and therefore leads to novel slow-light conditions. These increase the effective interaction time with the emitter, similar to the re-circulation of light inside a cavity.

The main benefit of this added complexity is that if the band edges are tuned to the transition frequencies of the proposed atomic or molecular system, not only can we take advantage of the enhancement provided by the slow-light effects, but can also explore emitter-photon bound states. Here, by (for example electrically) tuning the atomic/molecular resonance to be inside the bandgap, the system could only emit a photon into an evanescently decaying photonic mode that has an exponential profile. This means that instead of a guided mode of the form e^{ikx} being coupled into the waveguide, a bound-state of the form $e^{-\kappa x}$ is formed. Therefore one can

imagine the situation where multiple atoms or molecules are coupled to a single photonic crystal waveguide, and the emission profiles of each individual node could be adjusted in-situ. Furthermore, since the exponential decay length of the bound state depends on how deep inside the bandgap the emission frequency happens to lie, the coupling strength J_{ij} between nearest (or next-nearest) neighbor emitters i and j could be controlled with high precision. This would subsequently facilitate the implementation of dynamic interaction Hamiltonians.

7.6 Bottom-up Fabrication

Nanofabrication techniques using common dielectrics such as silicon or silicon nitride fundamentally rely on a top-down approach, where material is removed through etching to define the desired structure. This carries with a potential issue with respect to etch induced sidewall roughness and ion bombardment damage to the top-surface of the device layer. The predominant reason why these issues are encountered is because of the geometric constraint placed up nanophotonic structures to support the desired guided modes at the wavelength of operation. This means that the films need to be sufficiently thick *apriori* and therefore require etching times to be long (>3 mins). The longer the physical etching using reactive ions is taking place, the higher the likelihood of potential damage being inflicted onto the high-quality material. As photonic design is usually carried out with the film thickness being taken as somewhat of a static variable, this ultimately could pose certain limitations.

Here, we investigate the potential for atomic-layer-deposition (ALD) to be a viable tool for reversing the usual nanofabrication process and fabricate high-quality photonic structures from the bottom up. ALD is a technique that allows for single atomic layers to be grown using a two-step reaction process which includes a metallic precursor gas and a reactant in the form of water vapour. By pulsing each gas into a heated chamber kept under vacuum, with a certain amount of purging being used as a quasi-'dead-time' to allow proper saturation of the surfaces, we can grow atomically thin layers of photonics compatible materials such as Al2O3 (alumina).

We begin by significantly reducing the nominal device layer thickness of the SiN wafer, down to only 100nm. This is less than 50% of the regular thickness commonly used in most device geometries. This extremely thin film should enable the corresponding reactive-ion etch times to be shortened and therefore hopefully mitigate the usual issues mentioned before. However, even if the etch process re-

sults in some induced sidewall roughness, we hypothesise that the pristine material growth that ALD is capable of, will ideally passivate the surface and smooth out any imperfections that carry with them a high-frequency spatial character.

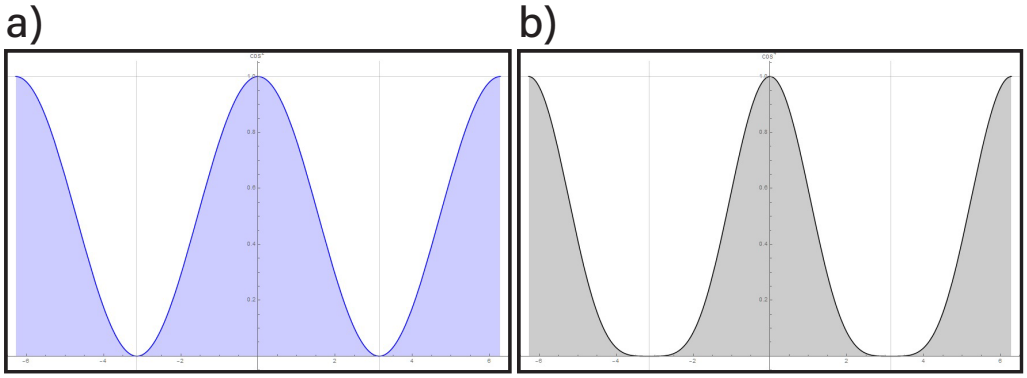

Figure 7.10: Outer edges of the 'fishbone' photonic crystal device with (a) no pre-compensation and (b) pre-compensation for N layers of material growth.

As our test system, we chose the familiar 'fishbone' photonic crystal design. To ensure that the devices being fabricated end up being optically usable, we need to account for the material growth in our device designs and thus pre-compensate our designs as shown in Fig.7.10. In order to do so, we have developed a robust mathematical framework implemented in MATLAB that approximates a layer-by-layer growth process. It does so by taking as its input a 'skeleton' design, and evaluating the normal vector at every infinitesimal surface element. This produces a three-dimensional vector field that determines the growth direction of an infinitesimally thin material layer everywhere along the device. By incorporating a realistic value for a single growth-layer thickness, we can recursively call our function to iterate the growth process for a number of cycles, N. We show an example of the simulated growth outcome in Fig.7.11.

By having this numerical tool developed and at our disposal, we can begin to utilize it in simulations to predict how photonic structures would behave as material growth is incorporated into the design. We utilized finite element simulations in COMSOL to investigate both the bandstructure and the ultimate device performance of our pre-compensated fishbones. The simulations were set-up so as to make use of the material growth script, with an example three-dimensional cross-section of the implemented device geometry, inclusive of ALD growth, being shown in Fig.7.12.

Next, the bandstructures of the fully covered fishbone unit cells were calculated using MEEP, to determine the device geometries needed for building a nanophotonic

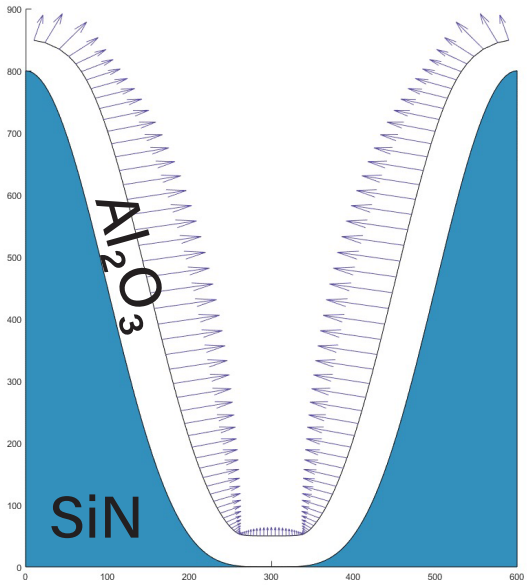

Figure 7.11: Simulated material growth on top of a pre-compensated photonic device using the numerical technique described in the text.

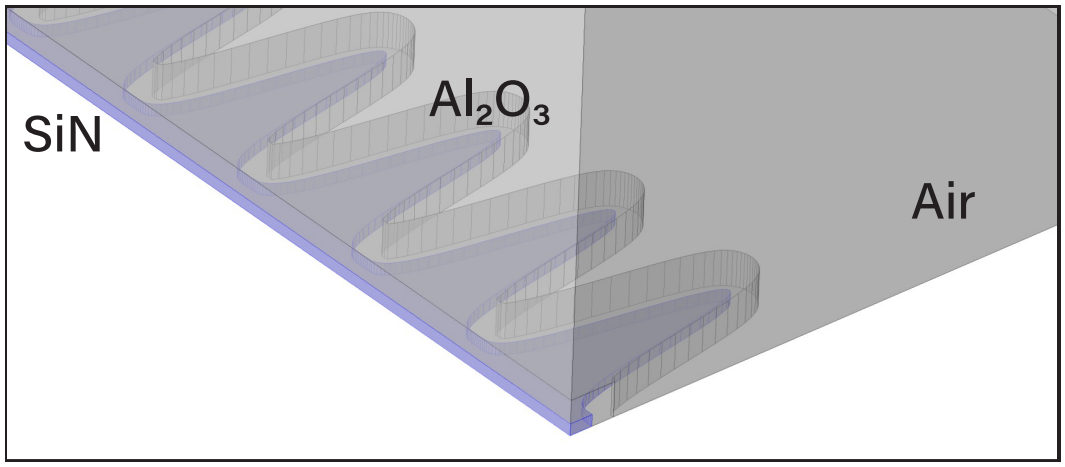

Figure 7.12: Three-dimensional cross-section of the fishbone device geometry, inclusive of ALD grown outer 'hull.' Highlighted in blue is the 100nm SiN device layer.

cavity comprised of two highly reflective mirror regions at either end, two adiabatic tapering regions consisting of unit cells with slightly adjusted lattice constants, and a cavity region. The cavity was designed by first determining the optimal unit cell that has a well-centered and reasonably large bandgap (10%) at 1550nm. Subsequently, through slight adjustments to only the lattice constant, we pulled the dielectric TE

mode into the bandgap center. This is shown in Fig.7.13.

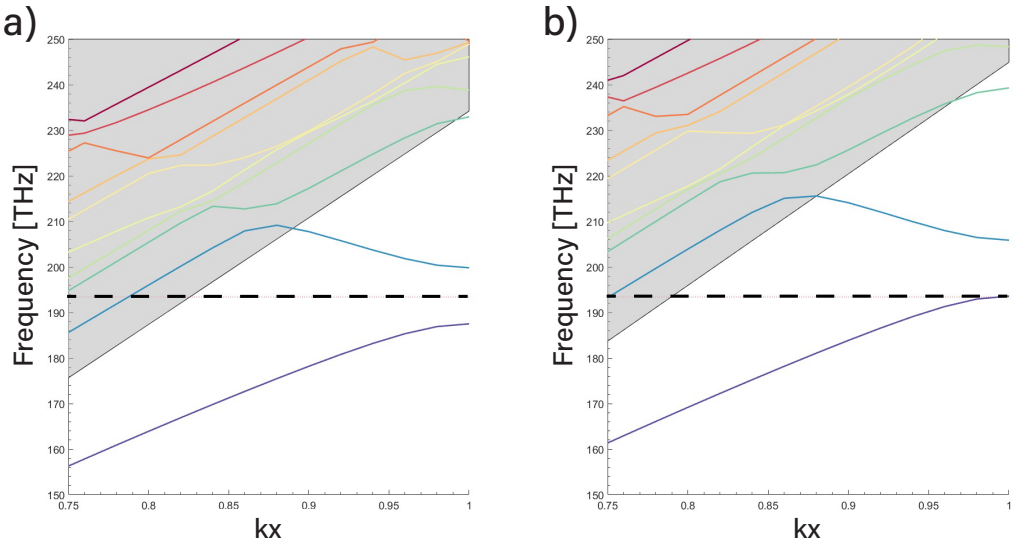

Figure 7.13: Band diagrams for the mirror unit cell (a), and the cavity unit cell (b). The bandgap center is shown using the black dashed line.

With the optimal unit cell dimension having been determined, we then carried out fully three-dimensional FEM simulations to investigate the theoretical behavior of the cavity and analyze how its performance, i.e. the cavity Q-factor, scales as a function of both the number of mirror cells, as well as the number of taper cells leading from the mirror region to the cavity region. These two variables are the strongest knobs that can be tweaked, as the number of mirror cells strongly affects the total reflectivity of the cavity, while the number of taper cells is correlated with the amount of scattering that the resonant mode undergoes. Longer taper regions allow for a smoother evolution of the mode profile, and thereby decrease the amount of power lost. While naively one would assume that longer device geometries simultaneously also increase the propagation losses (which is true), the relative increase in the effective length of the cavity scale more favourably as a function of the reduction of scattering losses. The simulation results showing the scalings for both unit cell types as a function of their quantity are plotted in Fig.7.14 and 7.15.

With these simulation results predicting good device performances, we fabricated our pre-compensated SiN fishbones on 100nm thick films using the process outlined in the Appendix. In short, the device geometries were defined on ZEP520A resist using electron-beam lithography and subsequently etched using an ICP-RIE process with a C_4F_8/SF_6 gas combination. The devices were then undercut by locally etching away the SiO_2 substrate underneath the devices using a vapor-HF technique. The

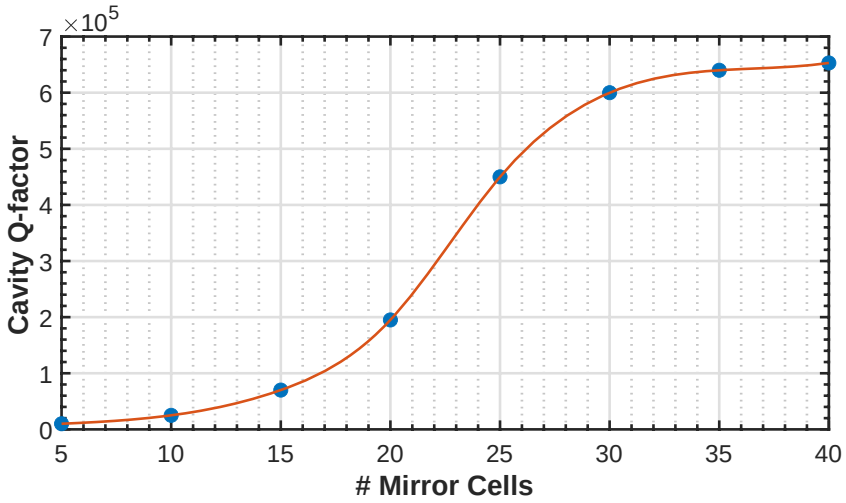

Figure 7.14: Simulation results showing the scaling of the cavity Q-factor as a function of the number of mirror unit cells.

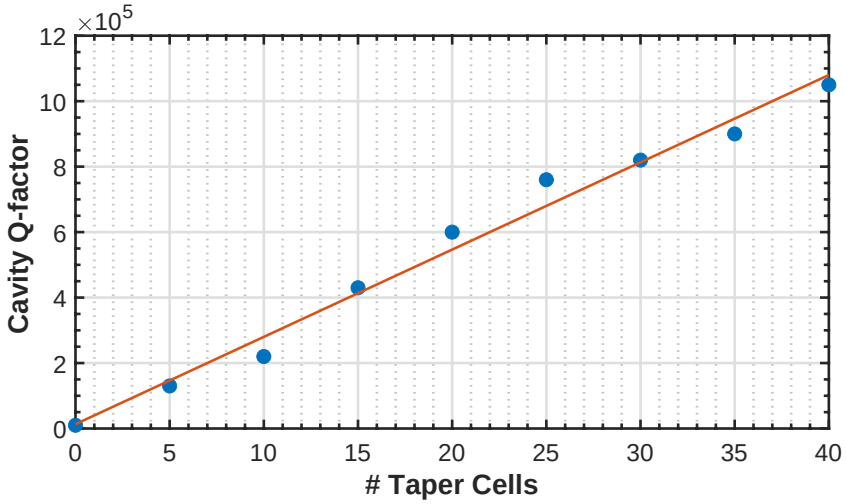

Figure 7.15: Simulation results showing the scaling of the cavity Q-factor as a function of the number of taper unit cells.

devices were then cleaned using a piranha step. The finished, pre-compensated devices are shown in Fig.7.16.

After the final clean, the finished devices were transferred into an O2-plasma cleaner to prepare them for the ALD growth step. Once the ALD system was conditioned for the Al2O3 growth process and ready to go, the devices were transferred into the main chamber of the ALD, where they were again one last time O2 plasma cleaned. The devices were then coated in 100nm thick Al2O3 over the course of a few hours. SEM images of the finished devices are shown in Fig.7.17.

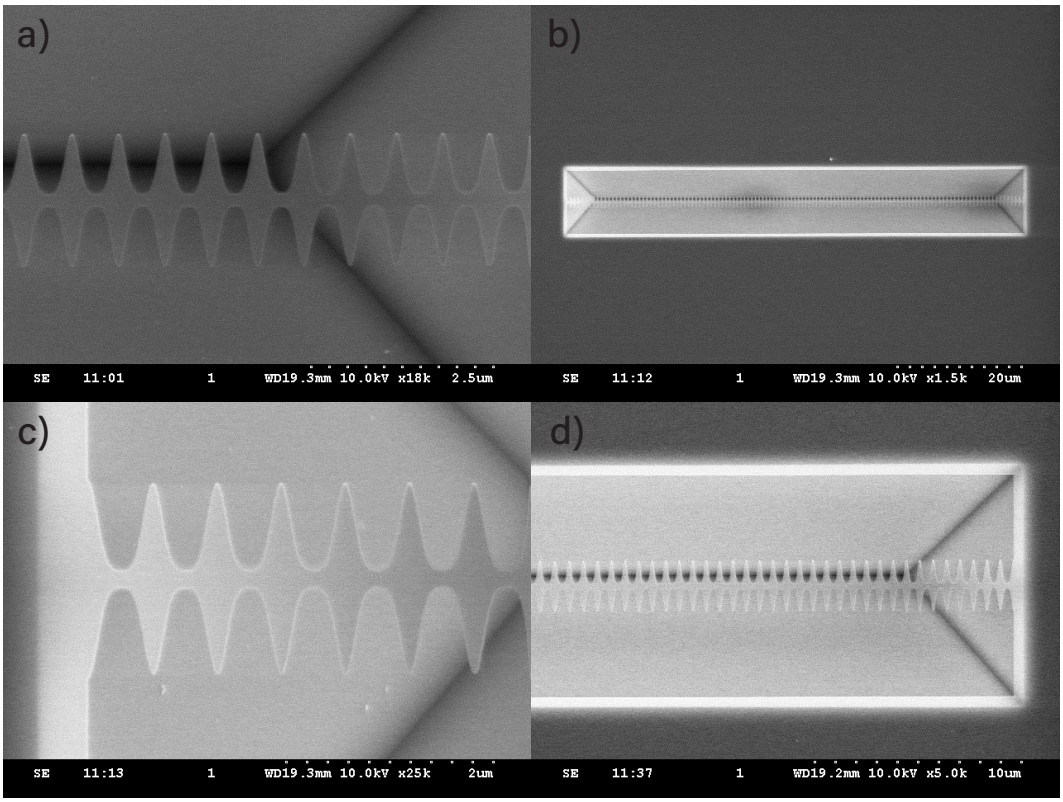

Figure 7.16: SEM images of the finished pre-compensated fishbone photonic crystal cavities.

The photonic crystal cavities were then optically characterized by measuring the normalized optical transmission of a tapered optical fiber that was placed in the near-field of the center of the cavity. The observed drop in transmission as a result of coherently coupling light into the resonant mode of the cavity then allowed for the Q-factor to be determined by fitting the spectrum using a Gaussian function. An example measurement is shown in Fig.7.18, with the extracted intrinsic Q-factor, Q_i, being $\sim 2.27 \times 10^5$. This is a fairly promising result given the uniqueness of this fabrication process and the fact that this was a first-run.

To briefly conclude this section, it is worth pointing out that while the implementation of 'pre-compensation' techniques and ALD growth is far from trivial, it offers some very unique advantages. As is to be expected, it is not necessarily compatible with the design and fabrication flow of all types of photonic devices. However, the benefits of finely tunable and adjustable cavity resonances through an atomically thin growth process, or the associated chemical passivation properties of amorphous oxides to temporarily protect sensitive photonic devices from corrosive and highly reactive atomic and molecular species could prove to be very beneficial. Especially

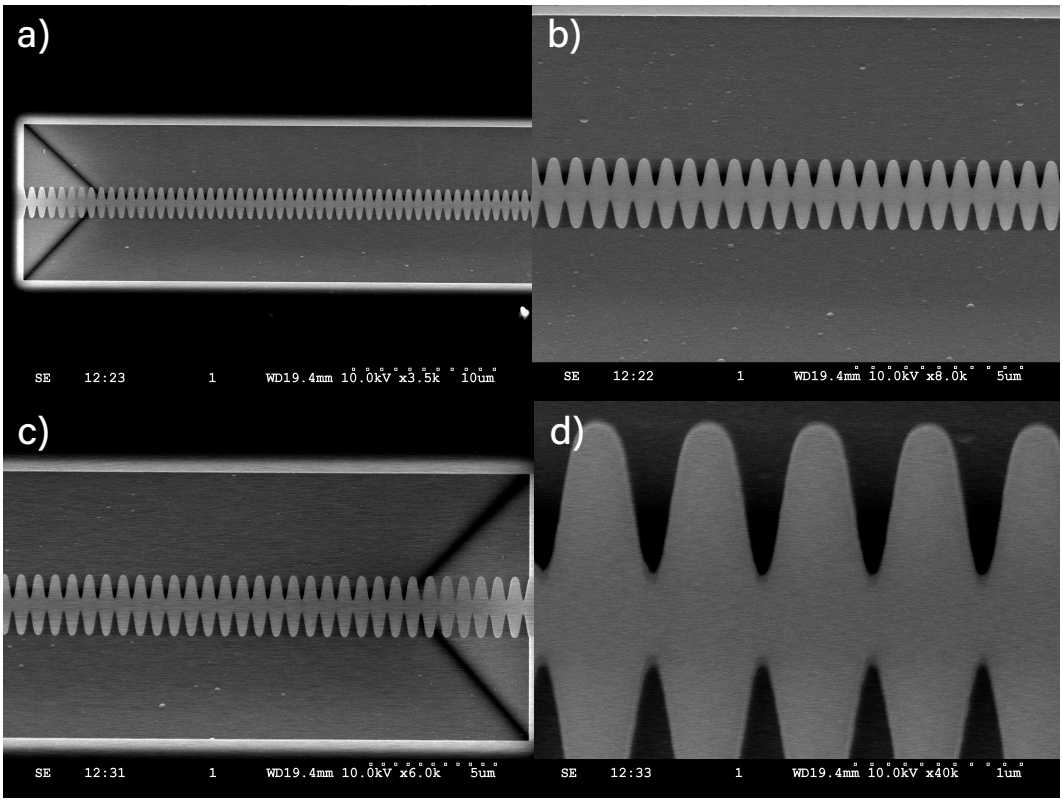

Figure 7.17: SEM images of the finished devices with 100nm of Al2O3 grown around the pre-compensated skeleton structure.

in the context of entangled photon spectroscopy, where the potential for implementing photonic crystal cavities to resonantly enhance two-photon absorption processes could pave the way to novel sensing applications. In particular as uniquely designed cavities could allow two-photon processes to be resonant not only with the final state of the sample but rather with some far-off-resonant transition that would be impossible to address without an enhancement in the density of optical states near it. In these situations, the extremely finely tunable properties of such cavities may outweigh the challenging and cumbersome additional design elements that come with it.

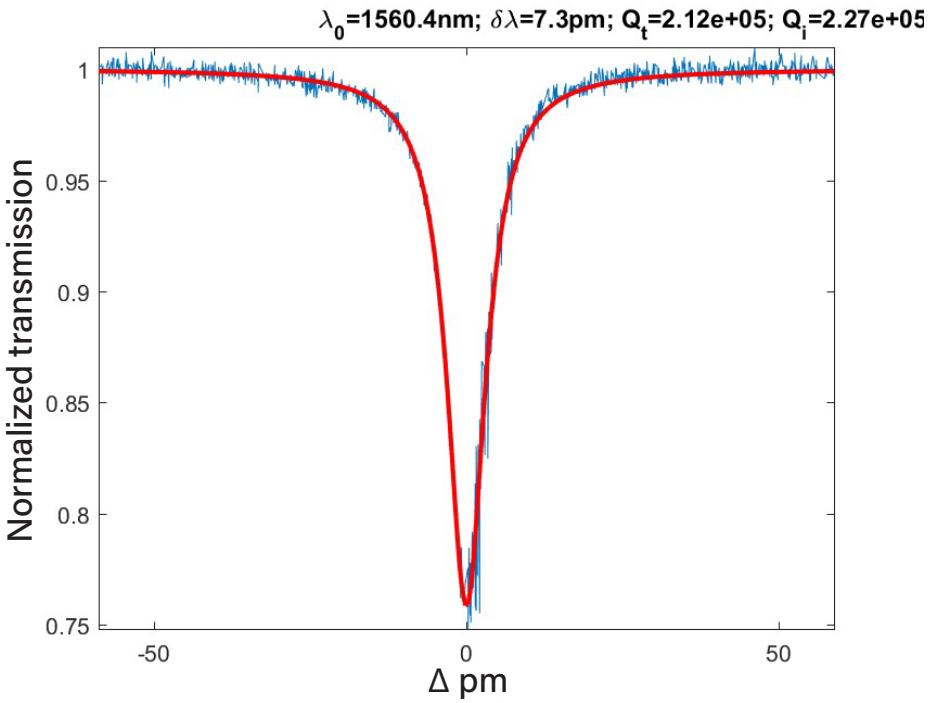

Figure 7.18: Optical characterization of a finished device using near-field coupling with a tapered optical fiber as a function of the laser detuning. The dip on resonance characterizes the cavity's response and allows for the determination of the cavity Q-factor. The extracted intrinsic Q-factor, Q_i, is $\sim 2.27 \times 10^5$.

Chapter 8

TELECOM-BAND QUANTUM OPTICS WITH YTTERBIUM ATOMS AND SILICON NANOPHOTONICS

Adapted from: Jacob P Covey et al. "Telecom-band quantum optics with ytterbium atoms and silicon nanophotonics". In: *Physical Review Applied* 11.3(2019), p.034044

ABSTRACT

Wavelengths in the telecommunication window ($\sim 1.25 - 1.65\ \mu$m) are ideal for quantum communication due to low transmission loss in fiber networks. To realize quantum networks operating at these wavelengths, long-lived quantum memories that couple to telecom-band photons with high efficiency need to be developed. We propose coupling neutral ytterbium atoms, which have a strong telecom-wavelength transition, to a silicon photonic crystal cavity. Specifically, we consider the $^3P_0 \leftrightarrow ^3D_1$ transition in neutral ^{171}Yb to interface its long-lived nuclear spin in the metastable $^3P_0$ 'clock' state with a telecom-band photon at 1.4 μm. We show that Yb atoms can be trapped using a short wavelength (≈ 470 nm) tweezer at a distance of 350 nm from the silicon photonic crystal cavity. At this distance, due to the slowly decaying evanescent cavity field at a longer wavelength, we obtain a single-photon Rabi frequency of $g/2\pi \approx 100$ MHz and a cooperativity of $C \approx 47$ while maintaining a high photon collection efficiency into a single mode fiber. The combination of high system efficiency, telecom-band operation, and long coherence times makes this platform well suited for quantum optics on a silicon chip and long-distance quantum communication.

8.1 Introduction

Efficient interfaces between single atoms and single photons could enable long-distance quantum communication based on quantum repeaters [1, 2, 3, 4, 5, 6, 7] and constitute a novel platform for many-body physics with long-range interactions [8, 9]. While most atom-photon interfaces to date operate at visible or near-infrared wavelengths ($\sim 700 - 1000\,\mathrm{nm}$), compatibility with telecom wavelengths ($\sim 1.25 - 1.65\ \mu\mathrm{m}$) is highly desired; both for quantum communication due to low propagation loss in fiber-optic cables, and for compatibility with silicon-based photonics. Accordingly, most approaches to quantum communication require frequency conversion of single photons into the telecom window, which often results in additional noise photons and reduced efficiencies [10, 11, 12]. A platform combining *both* long atomic coherence times and high emission bandwidth at telecom wavelengths has yet to be developed.

Atom-like defects in solids [13, 14, 15, 16, 17] and trapped neutral atoms [18, 19, 20, 21, 22] coupled to photonic crystal cavities hold promise to achieve such light-matter interactions. Atom-like defects in solids require no external trapping potential since they are held in the crystal field of the host solid-state environment. However, this environment has drawbacks, such as inhomogeneous broadening, phonon broadening, and spectral diffusion [23, 24]. Hence, these systems require cooling to cryogenic temperatures to reduce phonon broadening, and spectral tuning to achieve indistinguishability [13]. Moreover, the atom-like defects investigated to date are either outside of the telecom window, have short coherence times, or have low emission bandwidths [24].

Optically trapped atoms in free space offer the prospect of significantly improved coherence properties since inhomogeneous broadening and spectral diffusion are negligible. However, an outstanding challenge is to reliably trap an atom sufficiently close to a photonic device. Previous trapping efforts were based on evanescent fields that confine the atom near the device [25, 26, 18], or by forming a standing wave trap via reflection from the device [19, 27]. Surface effects such as Van der Waals forces [28, 29], surface patch charges [30], and Casimir-Polder forces [31, 32, 33] complicate these approaches. Moreover, the emission wavelengths of the atomic species used to date – rubidium and cesium – are $\sim 800\,\mathrm{nm}$, well outside the telecom window.

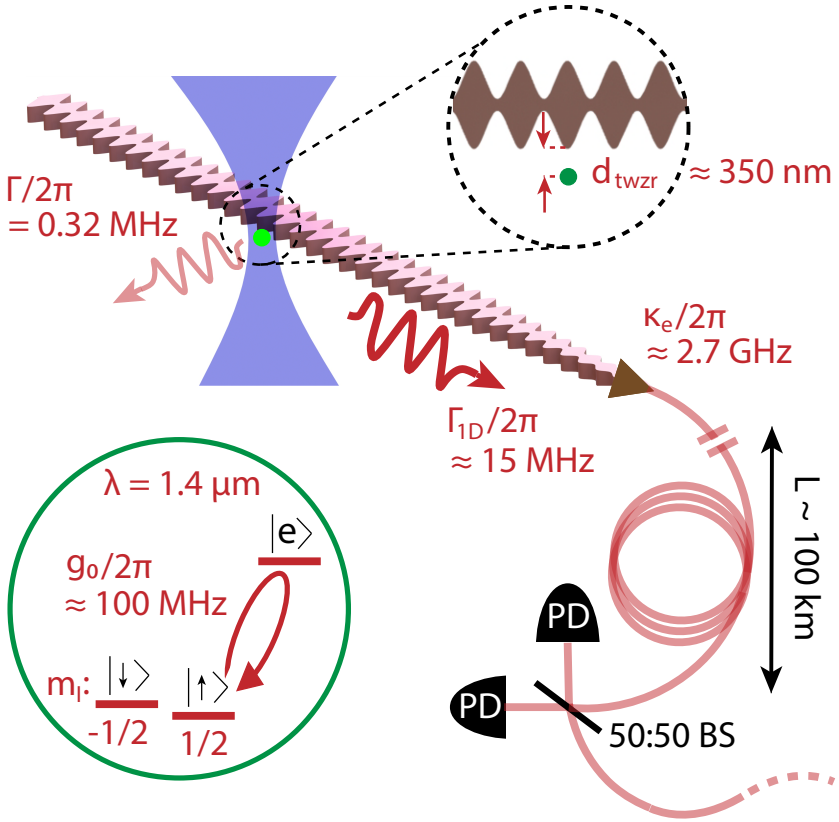

Figure 8.1: Schematic overview. Silicon photonic crystal cavity with an ^{171}Yb atom trapped nearby in an optical tweezer. The minimum atom-device separation $d_{\mathrm{twzr}} \approx 350$ nm allowed by our approach corresponds to an atom-cavity system on a strong telecom-band transition with vacuum Rabi frequency $g_0/2\pi \approx 100$ MHz and emission bandwidth of $\Gamma_{1\mathrm{D}}/2\pi \approx 15$ MHz, for a partially-open cavity with external coupling $\kappa_e/2\pi \approx 2.7$ GHz and atomic free-space linewidth of $\Gamma/2\pi = 0.32$ MHz. The nuclear spin projections m_I are of the $I = 1/2$ nuclear spin of ^{171}Yb. The photon in the cavity is coupled to an optical fiber with length $L \sim 100$ km. This system constitutes a node in a telecom quantum repeater in which entanglement between nodes is established by a Bell state measurement using a 50:50 beamsplitter (BS) and single-photon detectors (PD).

8.2 Overview of the System

We propose a platform based on short-wavelength optical tweezer trapping [34, 35, 36] to hold an Yb atom near a silicon photonic crystal in order to obtain strong atom-cavity interactions. The atomic transition is from the metastable 'clock' state, and has a wavelength of $\lambda = 1.4$ μm. Compared to previous work with tweezers operating at $\lambda_{\mathrm{twzr}} \approx 800$ nm [20], we use $\lambda_{\mathrm{twzr}} \approx 470$ nm to obtain tighter focusing. Further, the use of a $\sim 2\times$ longer wavelength transition results in a larger spatial extent of the evanescent cavity field. Accordingly, we propose to trap the atom

without the use of reflection from the device. We use a larger distance from the device compared to previous work [36] (d_{twzr} = 350 nm), at which surface forces are reduced by a factor of > 10. The larger disparity between the trapping- and the telecom-transition-wavelengths in Yb enables both a five-fold increase in cooperativity and more robust atom trapping.

We focus on quantum communication as a specific application of this platform, and we envision an Yb atom coupled to a silicon nanophotonic cavity as a node in a quantum repeater network (Fig.8.1). To this end, we propose a partially-open cavity design which enables the emission of ≈ 15 MHz-bandwidth photons entangled with the nuclear spin of ^{171}Yb that serves as a long-lived quantum memory. Further, we also consider a fiber gap Fabry-Pérot cavity rather than a photonic crystal, which may offer a simpler alternative, but is not compatible with on-chip silicon photonics.

We highlight the use of silicon for the photonic crystal cavity not only due to low losses but also its maturity as a fabrication technology [37]. Robust and high-yield electronic, mechanical, and optical devices have been realized in silicon-based systems utilizing a wide array of highly developed micro- and nano-fabrication techniques. Indeed, custom silicon devices are increasingly commercially available from fabrication foundries (see e.g. Ref.[38]). Moreover, silicon is compatible with other photonic technologies [39] such as electro-optomechanical [40, 41] and opto-mechanical [42, 43] systems.

The precise control of single atoms in this approach enables scalable extension to multiple atoms by employing recently-demonstrated techniques with tweezer arrays [44, 45, 27]. This would enable photonic coupling within an array of atoms, which could lead to a novel platform for many-body physics [46, 47], quantum nonlinear optics [21, 22], and photon-mediated quantum gates [48]. The latter application is relevant to quantum repeaters, where deterministic two-qubit gates in each node could enhance entanglement distribution rates by realizing efficient Bell state measurements for entanglement swapping operations. Note that two-qubit gates could also be accomplished using local exchange [49, 50, 51] or Rydberg [52] interactions.

The strong telecom-wavelength transition of Yb is from a metastable state with lifetime $\tau \approx 26$ sec (Fig. 8.2), which is the crucial state in the optical clock transition [53]. We focus on the 1.4 μm ($^3P_0 \rightarrow {}^3D_1$) transition which is shown with the orange double arrow (see Appendix I). Concerning the other transitions available, the one at 1.5 μm ($^3P_1 \rightarrow {}^3D_1$) is hampered by the short lifetime of $^3P_1$, which restricts

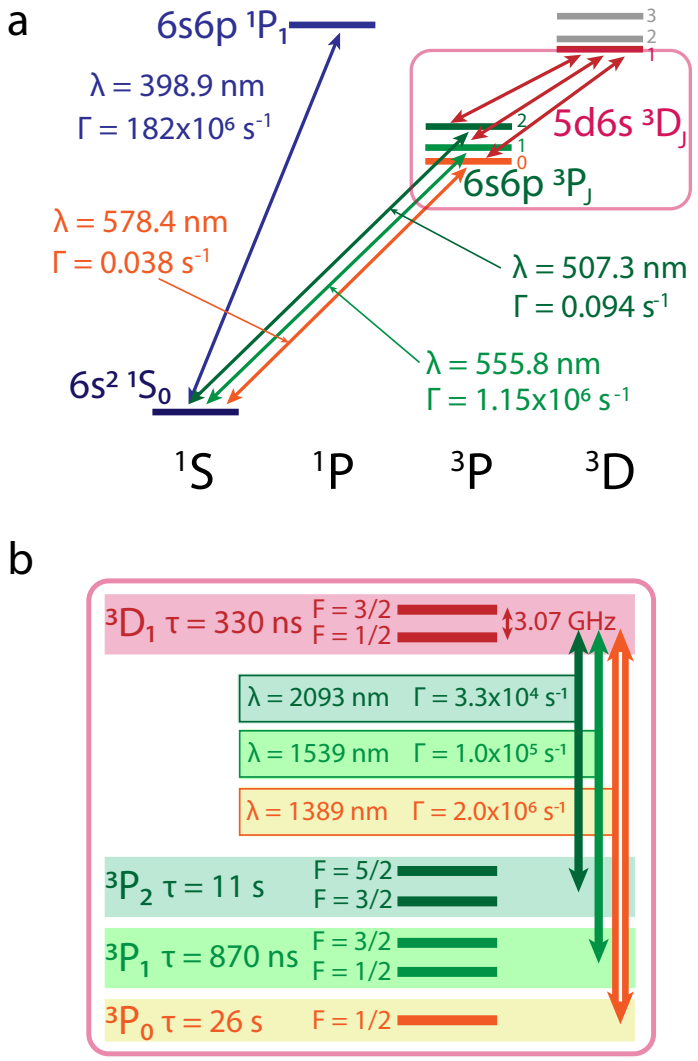

Figure 8.2: Level diagram of the relevant states of ^{171}Yb. (a) Low-lying states of Yb in the singlet and triplet manifolds. The telecom transitions from the metastable 6s6p ^{3}P$_J$ states to the 5d6s ^{3}D$_1$ state are highlighted in the red box. (b) Zoom-in of the highlighted transitions. The nuclear spin in ^{171}Yb is $I = 1/2$, so the hyperfine states are given by $F = 1/2$ when $J = 0$ and $F = \{J+1/2, J-1/2\}$ when $J \geq 1$. The lifetimes of the ^{3}P$_J$ states, transition wavelengths, transition linewidths, as well as lifetime and hyperfine splitting of the ^{3}D$_1$ state are given. We employ the transition shown with the orange double arrow.

its use to more complex protocols. Finally, the 2.1 μm transition (^{3}P$_2 \rightarrow ^3$D$_1$) is not suitable for fiber-optic communication. However, it is an interesting candidate for free-space communication given the relatively high atmospheric transmission at this wavelength. We define the states of interest as $|\downarrow\rangle \equiv {}^3\mathrm{P}_0\,|F = 1/2, m_F = -1/2\rangle$, $|\uparrow\rangle \equiv {}^3\mathrm{P}_0\,|F = 1/2, m_F = 1/2\rangle$, and $|e\rangle \equiv {}^3\mathrm{D}_1\,|F = 3/2, m_F = 3/2\rangle$ (see

Figs. 8.1 and 8.3). Note that care must be taken to correctly account for mode overlap with the cavity field, particularly in the case of circularly-polarized emission.

8.3 Dipole Matrix Elements and Polarization Considerations

In order to quantify the coupling to a cavity we must calculate the dipole matrix element of the desired atomic transition: $^3\mathrm{P}_0\ |F = 1/2, m_F = 1/2\rangle \leftrightarrow\ ^3\mathrm{D}_1\ |F = 3/2, m_F = 3/2\rangle$ (see Sec. 8.4 for detailed quantum repeater scheme). The $^3\mathrm{P}_0 \leftrightarrow ^3\mathrm{D}_1$ transition has been carefully measured because of its relevance to Yb clock precision [54]. Given that $\Gamma_{^3\mathrm{D}_1 \rightarrow ^3\mathrm{P}_0} = 2 \times 10^6\ \mathrm{s}^{-1}$, we arrive at $\mu = \langle\ F = 1/2\ m_F = 1/2|e\hat{\mathbf{r}}_q|F' = 3/2\ m_{F'} = 3/2\rangle = 1.38 \times 10^{-29}$ C-m, or 1.63 a_0-e, in which the polarization is taken to be $q = +1$ (σ^+) [55]. However, purely circular polarization cannot be supported by the modes of the photonic structure (see Sec. IV), and so the effective dipole matrix element is reduced by $\sqrt{2}$ upon decomposing σ^+ into a combination of linear polarizations. The 'quantization axis' is assumed to be determined by the electric field of the optical tweezer $\mathrm{E}_{\mathrm{twzr}}$ (see Sec. IV), and the external magnetic field $\mathrm{B}_{\mathrm{ext}}$ (see Sec. 8.4) is assumed to be parallel. To drive the σ^+ transition, we require the electric field of the mode in the cavity $\mathrm{E}_{\mathrm{cavity}}$ to be perpendicular to the quantization field axis $\mathrm{E}_{\mathrm{cavity}} \perp \mathrm{E}_{\mathrm{twzr}},\ \mathrm{B}_{\mathrm{ext}}$.

Finally, we study the emission branching ratio from $^3\mathrm{D}_1$ to $^3\mathrm{P}_J$, for $J = 0,\ 1,\ 2$ as shown in Fig. 8.2. On the basis of fine structure alone, the branching ratio from $^3\mathrm{D}_1$ to $^3\mathrm{P}_0$, $^3\mathrm{P}_1$, and $^3\mathrm{P}_2$ is 60:3:1, respectively. Therefore, in the absence of Purcell enhancement, the probability of emitting the desired photon from $^3\mathrm{D}_1$ is 93.3%. The Purcell enhancement for the decay to $^3\mathrm{P}_0$ based on our analysis is 47, and the corresponding branching ratio becomes 2820:3:1. Hence the probability of emitting the desired photon with Purcell enhancement is 99.9%. However, when the hyperfine structure is included in this analysis and decay from the specific state of interest $^3\mathrm{D}_1$ $|F = 3/2, m_F = 3/2\rangle$ is considered, a more detailed calculation is required [55], upon which we find the following values. In the absence of Purcell enhancement, the branching ratio is 20.9:1.9:1, for which the probability of emitting the desired photon is 88%. With Purcell enhancement the branching ratio is 982:1.9:1, for which the probability of emitting the desired photon is 99.7%.

8.4 Application in a Quantum Repeater

Quantum repeater implementation

In this section, we describe a quantum repeater based on a network of ^{171}Yb atoms coupled to photonic crystal cavities. The repeater involves dividing a long channel

of length L into 2^n elementary links of length L_0 that are connected by nodes which feature a pair of trapped atoms. The integer n is often referred to as the number of nesting levels [56]. Atom-atom entanglement that spans L is achieved by entangling atoms that are separated by L_0 and by performing entanglement swapping between atoms that are located at each node. Fig. 8.3b depicts two elementary links and entanglement swapping at one node. We consider the scheme of Barrett and Kok [57, 58] for generation of remote spin-spin entanglement and then calculate the rate of distribution of a Bell state.

Level scheme and protocol

We consider the three-levels of ^{171}Yb shown in Fig. 8.3a using solid colors. These consist of an excited $m_F = 3/2$ Zeeman level of the $^3D_1$ manifold and a pair of $m_F = \pm 1/2$ nuclear spin levels of the $^3P_0$ manifold that form the ground level. The $^3P_0$ state can be populated from the $^1S_0$ ground state by using the 'clock' transition [53], or by multi-photon processes [59]. The $m_F = 3/2$ and $m_F = 1/2$ Zeeman levels of the $^3D_1$ level are separated by 0.47 MHz/G, which is much larger than the 752 Hz/G splitting of the $m_F = \pm 1/2$ levels of $^3P_0$.

The first step of the repeater is to generate spin-photon entanglement and then, using two-photon detection, spin-spin entanglement between atoms that are separated by one elementary link. We begin by preparing each atom in an equal superposition of the $m_F = \pm 1/2$ nuclear states of the $^3P_0$ ground level: $1/\sqrt{2}(|\uparrow\rangle + |\downarrow\rangle)$. This is accomplished by a RF field despite the relatively small gyromagnetic ratio of the spin $\gamma_N/2\pi = 752$ Hz/G. Nonetheless, this favorably results in a weak coupling of the spin to the environment [60, 61]. We propose to split these states with a magnetic field of $B_{ext} = 200$ G. With the fabricated micro-stripline resonator [62] described in Sec. V, we expect Rabi frequencies of tens of kilohertz using tens of Watts of RF power. This allows π-pulses to be performed on timescales that are much less than the time to establish entanglement over an elementary link (see Subsec. B).

Next, each atom is excited by a short laser pulse that is resonant with the $|\uparrow\rangle \rightarrow |e\rangle$ transition, as indicated by λ_{cavity} in Fig. 8.3a. As described in Sec. V, this transition is strongly-coupled to the cavity, and thus the resultant spontaneous emission locally entangles the spin and photon number in the Bell state $1/\sqrt{2}(|\uparrow, 1\rangle + |\downarrow, 0\rangle)$, in which 1(0) represents the presence (absence) of an emitted photon.

The photons that are emitted by each atom are directed to a beam splitter which is located half-way between nodes, see Fig. 8.3b. If the photons that are emitted

by each atom are indistinguishable, detection of one photon after the beam splitter heralds spin-spin entanglement or, due to potential loss and imperfections, a spin-spin product state between each atom [57, 58]. To avoid the latter, a π-pulse inverts the $m_F = \pm 1/2$ spins and the transition is optically excited a second time. The detection of a photon in both rounds heralds the creation of a spin-spin Bell state between each atom $1/\sqrt{2}(|\uparrow,\downarrow\rangle_{AB} \pm |\downarrow,\uparrow\rangle_{AB})$, in which the relative phase is defined according to whether both photons were detected on the same or different output ports of the beam splitter.

Entanglement swapping is accomplished by performing a similar procedure as to generate heralded entanglement– optical excitation, single photon detection, spin flip, and detection of a second photon. This procedure limits the swapping efficiency to at most 50% [63]. A deterministic swapping process, which allows improved scaling, could be achieved by trapping two atoms using two tweezers within a single cavity and exploiting photon-mediated deterministic intracavity gates [46].

A limitation of this process will be the isolation of the $|\uparrow\rangle \rightarrow |e\rangle$ transition relative to the other transitions in the $^3D_1$ state (see Fig. 8.3a). The splitting between the $m_F = 3/2$ and $m_F = 1/2$ states is 470 kHz/G, and this must be compared to the Purcell-enhanced linewidth Γ_{1D}. We choose a field of $B_{ext} = 200$ G for which $\Delta = 2\pi \times 93$ MHz. For $\Gamma_{1D} = 2\pi \times 15$ MHz and Rabi frequency $\Omega = \Gamma_{1D}$, the off-resonant scattering rate is $\Gamma_{SC} = 2\pi \times 600$ kHz. The read-out fidelity is assumed to be $\mathcal{F}_{RO} = 1 - \Gamma_{SC}/\Gamma_{1D}$, which is > 0.99. Note that this value is even slightly improved when considering the Clebsch-Gordan coefficients for the different pathways.

Entanglement distribution rate

We quantify the distribution rate of a Bell state using our repeater scheme, showing that it outperforms an approach based on the direct transmission of photons. We denote the success probability for an atom to emit a photon into a single mode fiber (e.g. system efficiency) to be p, which includes the probability to prepare the initial state, the spontaneous emission of a photon into the cavity mode, and the coupling into a fiber. The probability of the two-photon measurement at the center of the elementary link is given by $P_0 = \frac{1}{2} p^2 {\eta_t}^2 {\eta_d}^2$ in which $\eta_t = e^{-L_0/(2L_{att})}$ is the fiber transmission with attenuation length $L_{att} = 12$ km. This corresponds to losses of 0.35 dB/km at 1.4 μm using hydrogen-aged single mode fiber, which has been recently deployed for modern infrastructure (see, e.g., Corning SMF-28e for ITU-T G.562D standards [64]).

The spin-spin entanglement creation step is repeated at time intervals of the communication time L_0/c, in which $c = 2 \times 10^8$ m/s is the speed of light in fiber. Thus, the average time to produce entanglement that spans an elementary link is $T_{L_0} = \frac{L_0}{c}\frac{1}{P_0}$. Using the beam splitter approach depicted in Fig. 8.3b, the efficiency of the entanglement swapping operation is $P_s = \frac{1}{2}p^2{\eta_d}^2$, while a deterministic gate allows $P_s = 1$, assuming the gate fidelity is unity. Therefore, the total time for the distribution of an entangled pair over distance $2L_0$ is given by $T_{2L_0} = \frac{3}{2}\frac{L_0}{c}\frac{1}{P_0 P_s}$, and the average time to distribute an entangled pair over distance L is $T_L \approx \left(\frac{3}{2}\right)^{n-1}\frac{L_0}{c}\frac{1}{P_0(P_s)^n}$. The factor of 3/2 arises because entanglement has to be created over two links before the swapping is performed [65, 56].

For the discussion in Sec. 8.7 we assume $p = 0.8$, which is given by the $\eta_{\text{ext}} \cdot \eta_{\text{taper}} \cdot \eta_{\text{AC}}$ estimated in Sec. IV, a detection efficiency of 0.9, and that the lifetime of the $^3\text{P}_0$ level is much longer than the distribution time. This detection efficiency is straightforwardly achieved using superconducting nanowires, which have been demonstrated at 1.5 μm [66]. Note that the spontaneous Purcell-enhanced emission time from $^3\text{D}_1$ is $1/\Gamma_{1\text{D}} \approx 11$ ns, which is negligible compared to the time to distribute entanglement over an elementary link. Figs. 8.3c and 8.3d show the repeater performance based on this analysis, plotted versus total distance for 2^4 nodes (8.3c) and versus number of nodes for a total distance of 600 km (8.3d).

In our analysis, we assumed that the emission bandwidths of each Yb atom-cavity system is identical. However, variations in the cavity properties and tweezer-cavity distance will result in a variation in the Purcell-enhanced decay rate. For our proposed remote entanglement generation scheme, this variation causes a reduction in the entanglement generation efficiency, but does not impact the entanglement fidelity. This could be achieved by applying a standard frequency, e.g. fiber-Bragg grating, or temporal filter to the two-photon coincidence signal [67, 68].

As an example, we consider utilizing our system in a quantum repeater architecture by entangling an ^{171}Yb nuclear spin and a telecom photon using the Barret-Kok scheme with time-bin photonic qubits [57, 58]. The key parameters of our system that impact the entanglement generation rate and fidelity are summarized in Table 8.1. We describe in detail in the following sections how these values are achieved in our platform.

Our system allows a bandwidth of $\Gamma_{1\text{D}} = 2\pi \times 15$ MHz, which is sufficiently high to not limit performance of the repeater. High bandwidth emission increases the

Table 8.1: The values relevant for a quantum repeater with a photonic crystal cavity, and the sections of the text in which they are described.

Parameter	**Section**	**Value**
Bandwidth	IV	$2\pi \times 15$ MHz
Wavelength	II	1.39 μm (0.35 dB/km)
System efficiency	IV	0.80
Memory	II, AII	≤ 26 sec
Read-out fidelity	AII	> 0.99

detection fidelity since the acquisition time is reduced and detection of dark counts can be mitigated. While most emitter platforms have sufficient bandwidth, many of the platforms operating in the telecom band, such as rare-earth ions in crystals, have slow emission rates. The bare linewidth of erbium (Er) ions, for instance, is $\Gamma/2\pi \approx 14$ Hz [69], and thus large Purcell enhancement in high-Q nanophotonic cavities [70, 71] is required to enhance the emission rate.

The long-lived memory of the nuclear spin qubit is one of the strengths of our platform. Some atom-like defects such as nitrogen vacancy (NV) centers in diamond also have long memory [72, 73], but their optical transitions are at visible wavelengths and are hampered by phonon broadening. Further, many of the solid-state systems whose optical transitions are in the telecom band have short memories [74]. In our system, the memory is assumed to be limited to the lifetime of the $^3P_0$ state, though care must be taken to mitigate various heating mechanisms associated with tweezer trapping. A unique feature of alkaline-earth (-like) atoms is the possibility of cooling via electronic states while preserving coherence of the nuclear spin [50].

Another important characteristic for determining the quantum repeater performance is the system efficiency, which describes the probability that a photon emitted by the atom is acquired into the fiber network. This includes the coupling to the cavity, the extraction from the cavity into the waveguide, and the coupling to a fiber. All these values are described in Sec. IV, and the total photon system efficiency is expected to be $\eta_{\text{tot}} \approx 0.80$.

As a concrete demonstration of the potential of this system, we calculate the entanglement distribution rate in a network as shown in Fig. 8.3a and 8.3b, and compare it to direct communication without repeaters. For a repeater system of 16 nodes we find that the distribution rate exceeds that of direct communication with a 10 GHz single photon source [56, 75] for a minimum total distance of 550 km. The correspond-

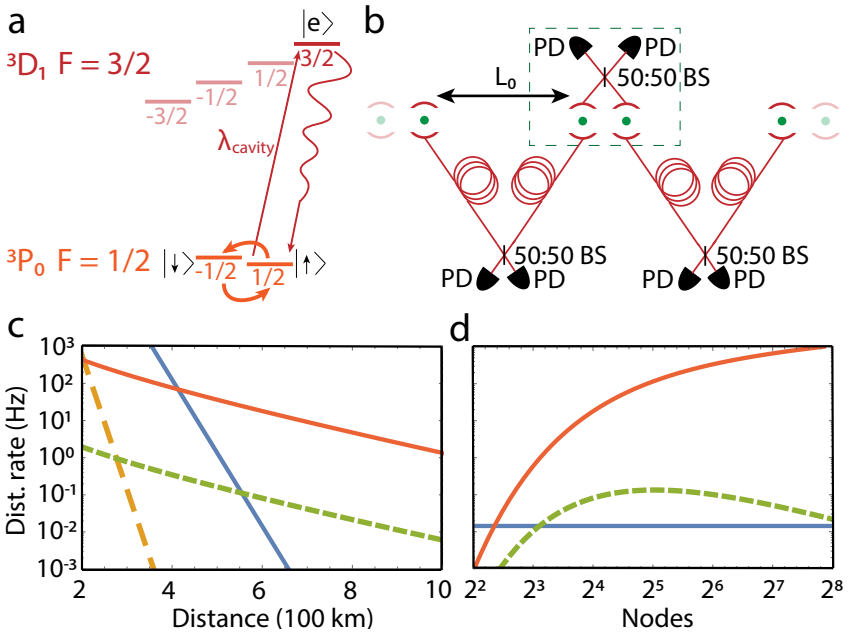

Figure 8.3: Spin-photon entanglement scheme and quantum repeater operation. (a) The relevant (irrelevant) hyperfine states are shown in solid (semi-transparent) colors. The cavity-enhanced transition wavelength is λ_{cavity}. (b) A single trapped ^{171}Yb atom in a cavity is represented by a green dot inside two curved semi-circles. Local node pairs are shown in the dashed box. Node pairs are separated by L_0. BS: beamsplitter, PD: single photon detector. (c) The entanglement distribution rate versus total distance via direct communication at 10 GHz for 1550 nm (solid blue) and 1390 nm (large-dashed orange) and via a quantum repeater with 2^4 nodes with (without) local deterministic entanglement, solid red (short-dashed green). Note that a 10 GHz rate for the direct transmission scheme [56] can be interpreted as an information-theoretic bound for information distribution without quantum repeaters if an ideal single photon source with a 10 GHz/1.44=6.9GHz repetition rate is employed [75]. (d) The entanglement distribution rate over 600 km versus number of nodes via direct communication at 10 GHz for 1550 nm (solid blue) and 1390 nm (large-dashed orange, not visible) and via a quantum repeater with (without) local deterministic entanglement, solid red (short-dashed green).

ing entanglement distribution rate is 0.1 Hz. However, when local entanglement swapping at a node can be realized using two-qubit gates rather than probabilistic photon detection-based schemes, the distribution rate could be enhanced to 25 Hz. The distribution rate versus distance for 16 nodes is shown in Fig. 8.3c, and the rate versus number of nodes for 600 km is shown in Fig. 8.3d. These findings indicate that this platform is a competitive quantum repeater technology in the telecom band. Note that the fiber gap Fabry-Pérot alternative also performs well (see 8.7).

As a specific point of reference, we compare to a system with the same cavity QED

parameters in Table 8.1 but operating at half the wavelength, in the visible band. Due to the large attenuation loss of ≈ 3.5 dB/km, such a system would require frequency conversion into the telecom window. Typical conversion efficiencies realized in alkali-atom [10], trapped ion [11], and nitrogen-vacancy-center [12] systems are $\approx 25\%$. We account for this by including it in the overall system efficiency, which goes from 0.8 to 0.2. Based on the equations above, the corresponding entanglement distribution rate for 16 nodes becomes becomes 110 nHz (1.6 Hz) in the case of probabilistic (deterministic) local entanglement swapping. This simple comparison shows the power of starting with a photon whose wavelength is in the telecom-band, particularly when local entangling gates are not available. We also note that frequency conversion results in additional noise photons owing to the presence of a strong pump field, which can cause false photon coincidences and reduced entanglement fidelity.

8.5 The Silicon Photonic Crystal Cavity

We now describe the design of the partially-open cavity, and the resulting coupling strength to an Yb atom. We consider a photonic crystal geometry based on a nanobeam with an external corrugation [76]. The sinusoidal modulation along the outer edges induces a photonic bandgap, which in turn enables the creation of a cavity via the introduction of a defect cell in the lattice to break the translational symmetry of the crystal. This enables the formation of modes localized in space around the defect region. For our chosen photonic crystal geometry, this is achieved by using a lattice constant $a_{\text{mirror}} = 454$ nm. This is then subsequently tapered down to $a_{\text{cavity}} = 433$ nm such that the relevant band-edge of the mirror region is tuned into the bandgap and hence establishes a cavity region.

Details of the photonic crystal geometry are shown in Fig. 8.4a and b. The different colors show the different sections of the cavity. From left to right: purple is the input section of the cavity which transitions from a single mode waveguide to the photonic crystal geometry enabling the coupling of light in and out; medium blue is the left cavity mirror with higher transmission; dark green is the cavity taper region from the mirror cell lattice constant a_{mirror} to the center cavity cell lattice constant a_{cavity}; light green is the central cavity unit cell; dark green is the taper to the backside mirror; and blue is the backside mirror with very high reflectivity. The tapering is done in such a way as to produce an effective quadratic potential for localized cavity photons, providing the optimal balance between localization in the plane of the device and radiation out-of-plane [77, 78, 79]. The device thickness is

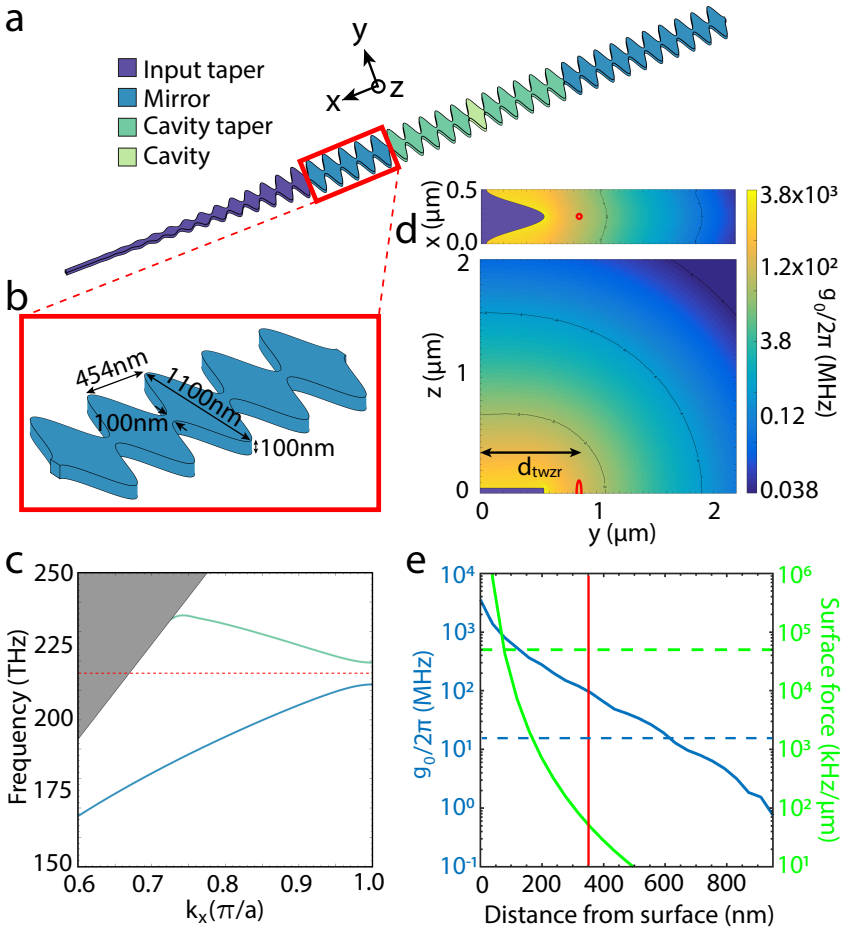

Figure 8.4: Design and characterization of the Si cavity. (a) Schematic of the photonic crystal cavity. The different colors show the different sections of the cavity. (b) A zoom-in of the first mirror section of the photonic cavity. (c) The TE mode band structure of the air (green) and dielectric (blue) mode. The red dashed line is the atomic resonance, and the shaded gray region is outside the light cone. (d) The coherent coupling rate g_0 shown on a color map as a function of distance in the y and z directions from the center antinode of the photonic cavity ($x = 0$) in the bottom image, and the profile along the x direction across the center tooth in the top image. The red ellipse and circle show the size of the atomic motional wavefunction (see Sec. V). (e) Blue - left vertical scale: A line cut of the coherent coupling rate for $x = z = 0$ versus the distance from the surface. The dashed line represents the value of g_0 for which $C_0 = 1$. Green - right vertical scale: The surface force from the photonic crystal on the atom. The curve is meant to show the qualitative scaling only. The dashed line shows the maximum restoring force from an optical tweezer of depth 1 mK and waist of $\approx$ 330 nm. The vertical red line shows the proposed position of the atom at $d_{\mathrm{twzr}} = 350$ nm.

chosen to be 100 nm to extend the evanescent field due to weaker confinement inside the dielectric, hence allowing for a greater distance between the photonic crystal

and the atom.

This design has a radiation limited quality factor of 3.5×10^6 in simulations. However, we anticipate that the quality factor will be limited by intrinsic fabrication imperfections to $Q_i \leq 7 \times 10^5$, whose corresponding intrinsic cavity linewidth is $\kappa_i = 2\pi \times 300$ MHz [80]. We design the cavity to be partially open on one side (as in Fig. 8.4a) to efficiently extract the cavity photons [81, 82, 48]. Specifically, we consider 5 mirror cells on the front mirror and 10 on the back mirror. The collection efficiency η_{coll} of extracting the photon into the waveguide mode is given by $1 - Q_e/Q_i$, where the subscript 'e' denotes external coupling. In our design we have chosen a modest $Q_e = 8 \times 10^4$, for which $\eta_{\text{coll}} = 0.89$ and $\kappa_e = 2\pi \times 2.7$ GHz.

We now consider the photonic mode profile. The transverse electric (TE) photonic band structure containing a bandgap centered on the atomic transition at $\lambda = 1388.8$ nm (215.9 THz) is shown in Fig. 8.4c. The evanescent field profile of the dielectric mode is shown in Fig. 8.4d, where the simulated electric field per photon $\mathrm{E}_{\text{cavity}}$ is converted to the vacuum Rabi frequency (i.e. coherent coupling rate) by $g_0 = \mu \cdot \mathrm{E}_{\text{cavity}}/\hbar$. μ is the dipole matrix element described in Appendix I. The red ellipse and circle show the $1/e^2$ size of the atomic motional wavefunction, to be discussed in the next section. A line cut of the coherent coupling rate is shown in Fig. 8.4e for $x = z = 0$ versus the distance from the surface, and we find an exponential length scale of $\lambda_{\text{Si}} \approx 170$ nm, determined by fitting $g_0(d) = g_0(0)e^{-d/\lambda_{\text{Si}}}$, where d is the distance between the surface and the atom. The smoothness of the curve is limited by numerical resolution, but the data provides an accurate quantitative estimate over ≈ 100 nm length scales. This is consistent with estimates for the mode dispersion based on the band structure (Fig. 8.4c). The position of the atom is represented by the vertical red line.

The maximal evanescent coupling occurs at the surface of the photonic crystal, where the electric field per photon is $\mathrm{E}_{\text{cavity}} = 2.6 \times 10^5$ V/m. The coherent coupling rate can then be calculated to be $g_0(0) = 2\pi \times 3.8$ GHz at this location, and $g_0(d_{\text{twzr}}) = 2\pi \times 100$ MHz at the chosen location of the atom $d_{\text{twzr}} = 350$ nm, as explained in Sec. V. The single-atom cooperativity defined here as $C_0 = 4g_0^2/\kappa\Gamma$ between a Yb atom and the silicon photonic crystal cavity can be estimated using the cavity linewidth $\kappa = \kappa_i + \kappa_e$ and the atomic linewidth $\Gamma = 2\pi \times 0.32$ MHz. This corresponds to a cooperativity for an atom located at d_{twzr} of $C_0 = 47$. The Purcell-enhanced emission rate $\Gamma_{1\text{D}}$ is given by the Purcell factor $P = C_0$ and the atomic decay rate Γ as $\Gamma_{1\text{D}} = P\Gamma$, which for this system gives $\Gamma_{1\text{D}}/2\pi = 15$ MHz.

The probability of spontaneously emitting a photon into the cavity mode P_{cavity} is given by $C_0/(C_0 + 1)$, which is 0.98. Thus, the total efficiency of extracting the photon from the atom into the waveguide mode is given by $\eta_{\text{ext}} = P_{\text{cavity}} \cdot \eta_{\text{coll}}$, which is 0.87. We design the photonic cavity to taper to a nanobeam waveguide which can then be coupled to an optical fiber using a microlens or adiabatic coupler. Efficiencies for the latter are $\eta_{\text{AC}} \approx 0.95$ [83]. These parameters result in a total system efficiency of ≈ 0.80.

8.6 Trapping a Single Yb Atom Near a Photonic Crystal

We now show that an Yb atom can be trapped close to the photonic crystal using only a tightly-focused optical tweezer.

Analysis of the optical tweezer trap

Single-atom detection and addressing of alkaline earth (-like) atoms is a growing area of research interest. Quantum gas microscopy of Yb has been demonstrated [84], and large two-dimensional tweezer arrays of Yb [85] and strontium (Sr) [86, 87] have recently been reported. Further, cooling of single alkaline-earth (-like) atoms close to the motional ground state of an optical tweezer has recently been demonstrated for Sr [86, 87], and cooling of alkali atoms optically trapped $\approx$ 300 nm from a room-temperature surface has recently been observed [88].

For a tweezer wavelength of $\lambda_{\text{twzr}} \approx$473 nm (depending on the tweezer polarization [86]), there is a 'magic' wavelength for which the polarizability of $^1\text{S}_0$ and $^3\text{P}_1$ are identical [54, 89]. This is particularly useful for cooling the atom in the tweezer [86, 87]. Coincidentally, the polarizability of $^3\text{P}_0$ is also similar [90]. Moreover, the polarizability at this wavelength is large, which allows deep traps to further mitigate surface forces. As such, we propose to use the $\approx$ 473 nm wavelength for generating tightly-focused optical tweezers, although easily accessible wavelengths such as 532 nm are an alternate as they have been used in a similar magic configuration [84, 85].

In order to further understand the design constraints and tweezer trap properties, we describe here the polarizability at the trapping wavelength λ_{twzr}, and the tweezer waist that can be generated with numerical aperture NA$\approx$ 0.7 objective [84]. The polarizability of $^1\text{S}_0$ and $^3\text{P}_1$ at λ_{twzr} is $\alpha = -18$ Hz/(W/cm^2) [90]. For an objective of NA$\approx$ 0.70, the $1/e^2$ waist radius of a tweezer that can be generated with this wavelength is $w_{\text{twzr}} \approx 330$ nm, and the corresponding Rayleigh range is $R_{\text{twzr}} \approx 730$ nm. An optical power of 1.0 mW is required for a trap depth of $U_{\text{twzr}} \approx 0.5$ mK,

and the trapping frequencies are $\omega_R \approx 2\pi \times 150$ kHz and $\omega_z \approx 2\pi \times 48$ kHz. The polarizability of the ^{3}D$_1$ state is not well known, but it is only populated during a π-pulse for photon-spin entanglement and during read-out (see Sec. 8.4). To mitigate deleterious effects from a polarizability mismatch on the ^{3}P$_0 \leftrightarrow ^3$D$_1$ transition, we propose to switch the trap off during excitation [20]. Atom survival probability in the absence of a trap is known to be high for times of several μs [91], which is much longer than the Purcell enhanced emission timescale $\Gamma_{1D}^{-1} = 11$ ns.

The temperature of a typical Yb magneto-optical trap (MOT) operating on the ^{1}S$_0$ - ^{3}P$_1$ transition is $< 10\ \mu$K [90, 84]. This temperature would correspond to $n_R = 0-1$ motional quanta in the radial direction and $n_z = 2-3$ motional quanta in the axial direction, and further cooling in a tweezer has been demonstrated with Sr [86, 87]. Such conditions lead to thermal $1/e^2$ atomic wavefunction radii of $\sigma_R \approx 30$ nm in the radial direction and $\sigma_z \approx 80$ nm in the axial direction. The circles in Figs. 8.4d are meant to roughly represent the size of the atomic wavefunction and illustrate how small it is compared to the mode profile of the cavity field. Note that the nodal spacing of the cavity is larger here compared to previous work [19] because of the longer wavelength, and thus the evanescent field coupling is expected to be more homogeneous over the tweezer trap volume.

Atom trapping and imaging near the photonic crystal

We consider a tweezer focused at a distance $d_{twzr} = 350$ nm from the photonic crystal, as shown in Fig. 8.5a and 8.5b. This was chosen to be slightly larger than the waist of the tweezer $w_{twzr} \approx 330$ nm to minimize the impact of scattered fields from the photonic crystal. Further, we propose to use the chip geometry shown in Fig. 8.5c and discussed in the next subsection, which allows the tweezer to be translated with respect to the cavities on the chip and the MOT [19] using an acousto-optic deflector or spatial light modulator. This is advantageous since atomic flux on the device is known to have detrimental effects on photonic structures [92, 93].

A significant difference between alkali- and alkaline-earth(-like) atoms is the size and temperature of their MOTs. For alkalis, typically only one atomic transition is used for laser cooling and optical molasses. Conversely, alkaline-earth(-like) atoms are typically laser cooled in two stages: the broad ^{1}S$_0 \leftrightarrow ^1$P$_1$ transition for initial loading and the narrow ^{1}S$_0 \leftrightarrow ^3$P$_1$ transition for cooling to $< 10\ \mu$K [90, 84] as mentioned above. Further, the narrow linewidth of the cooling transition in the second stage allows for flexibility in the MOT size and position by adjusting the

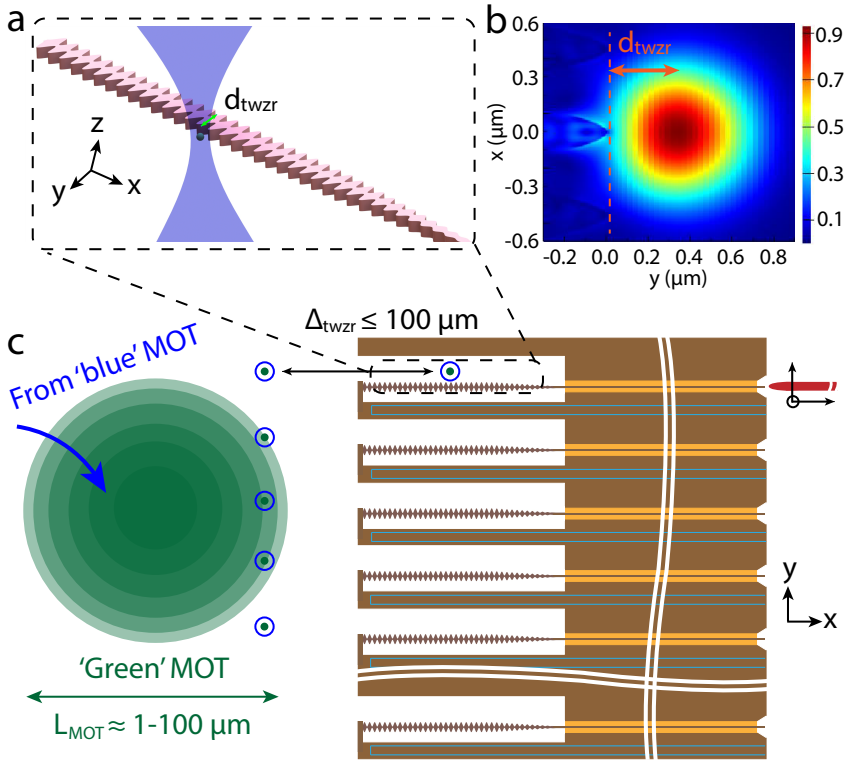

Figure 8.5: Coupling a Yb atom to a silicon photonic crystal cavity via an optical tweezer trap. (a) A zoom-in illustrating the atom in a tweezer near the device at a distance d_{twzr}. (b) The electric field magnitude of the tweezer trap in arbitrary units at a distance of $d_{\mathrm{twzr}} = 350$ nm from the edge of the device. (c) Schematic of the silicon chip. The silicon top layer is brown, and the insulator layer below is orange. The blue microstrips on the chip are used for Ohmic temperature control and applying RF magnetic fields. The lensed fiber on the right can be coupled to any cavity using a 3D translation stage. Wavy white lines indicate cuts to show the entire chip. The green circle on the left is the Yb MOT, and atoms can be shuffled between it and the device using optical tweezers. This architecture allows simultaneous operation of multiple Yb-cavity nodes on a single device.

magnetic field gradient and offset. Hence, a small and cold second-stage 'green' MOT could be moved to within ≈ 100 μm of the silicon chip using magnetic fields, which is within the field of view of typical microscope objectives. This enables easy tweezer transport with acousto-optic deflectors [45] (see Fig. 8.5), and does not require translation of the objective. The large first-stage 'blue' MOT could be millimeters from the chip at all times. This approach will reduce atomic flux onto the device compared to previous work [19, 18], and also mitigates the detrimental effect of the photonic structure on the MOT.

Surface effects on the atom are substantially mitigated in our approach compared

to previous work [19]. Operating at 350 nm from the surface instead of 200 nm decreases the surface potential to $\approx$ 13%, and surface force to $\approx$ 7% to that of previous work [19] (see Supplementary Material in Ref. [19], and Ref. [94] for electric dipole polarizabilities at imaginary frequencies used in this calculation). In addition, the external corrugation used in our photonic crystal design further reduces the effective surface area interacting with the atom where only the surface areas at the antinodes (see Fig. 8.1 and 8.5b) contribute significantly to the surface force. We show the qualitative scaling of the surface force with distance in Fig. 8.4e, but we leave a quantitative assessment for further study. We can compare this surface force with the dipole force in the tweezer potential. We expect the surface force at d_{twzr} to be $\approx$ 100 kHz/μm or less, while the maximum dipole force for a tweezer as described above with 1 mK depth is $\approx$ 50 MHz/μm, and the use of deeper traps is possible.

Now we consider absorption of the tweezer light by the silicon nanocavity. Absorption can have two deleterious effects: it can cause heating of the structure that will alter the cavity properties, and it can generate free-carriers which increase the optical absorption in the telecom band [95, 96]. The absorption coefficient of silicon at a wavelength of $\approx$ 470 nm is $\alpha_{\mathrm{Si}} \approx 2 \times 10^4$ cm^{-1} [97], which means that $\approx$ 18% of incident tweezer light will be absorbed by our cavity of 100 nm thickness. For a 1 mW tweezer of waist $w_{\mathrm{twzr}} = 330$ nm at a distance from the surface of $d_{\mathrm{twzr}} = 350$ nm, we estimate that < 3 μW is incident on the device, and thus < 530 nW is absorbed. Given the thermal conductivity of silicon and the dimensions of the proposed nanocavity we expect a ≈ 0.3 K temperature difference in the vicinity of the tweezer relative to the chip which serves as a thermal reservoir. The temperature dependence of the index of refraction causes a shift in the cavity resonance frequency at the 10^{-5} /K level [95]. Hence, we expect $\approx 3 \times 10^{-6}$ fractional shift in the cavity resonance, which is much less than $1/Q_e > 10^{-5}$ for the cavity.

To mitigate the effect of free-carrier generation in the silicon nanocavity, we propose to switch the tweezer off during the telecom-photon emission phases, such as spin-photon entanglement and read-out. The weak tweezer illumination onto the device will cause free electron-hole pairs which will decay within 10's of ns [95, 96]. This is fast compared to the allowed free expansion time of the atom with high probability re-trapping (several μs), so waiting for 100's of ns to ensure electron-hole pair decay is feasible. Since the recoil energy of a telecom photon is low, we expect heating of the atom during these pulses to be sufficiently small.

Coherent scattering from the nanocavity must also be considered because it could alter the trapping potential. We calculate the trapping potential in the presence of scattering from the silicon device using a finite-difference time-domain simulation. We simulate a gaussian beam with a waist of 330 nm focused at a distance of $d_{\mathrm{twzr}} = 350$ nm from the edge of the photonic crystal cavity. The results are shown in Fig. 8.5b, where the magnitude of the electric field is shown on a relative scale. The trap perturbations are below $|\mathrm{E}_{\mathrm{twzr}}| \approx 0.2$ ($I_{\mathrm{twzr}} \approx 0.1$), and they occur only at distances of $\geq d_{\mathrm{twzr}}$ from the center of the tweezer. This effect is negligible, particularly for a cold atom.

The ability to have many photonic cavities per chip facilitates fabrication error and device degradation to be overcome, but also opens the possibility to couple an array of atoms in optical tweezers [45] to an array of cavities. This would enable multi-qubit repeater nodes as discussed in Sec. 8.4, 8.7. An array of cavities can be fabricated such that their separation is as small as ≈ 10 μm (as in Fig. 8.5c). The cavities are coupled to a microlens coupler or adiabatic coupler, and the fiber could be aligned and coupled to any individual cavity on the chip using a three-axis stage as shown in Fig. 8.5c. Each cavity is independently temperature controlled with its own tungsten heating strip (light blue lines in Fig. 8.5c), and thus each cavity in the array could be individually tuned into resonance with the atomic transition [98]. This strip is also used for applying radio-frequency (RF) pulses to control the nuclear spin.

8.7 Coupling Yb to a Fiber Gap Fabry-Pérot Cavity

In this section, we discuss an alternative approach to efficiently interface a single atom with a single telecom photon in a fiber using fiber based Fabry-Pérot (FP) resonator [99, 100, 101]. While fiber based Fabry-Pérot resonators have significantly larger mode volumes ($\sim 1000\lambda^3$) that result in reduced vacuum Rabi frequencies, we show that they can achieve high enough cooperativities necessary to extract single photons directly into a telecom fiber with sufficiently high efficiency.

We begin by considering the geometry of fiber FP cavities, as shown in Fig. 8.6a. Typical heights H of the cavity claddings are 125 μm, so in order to focus a tweezer and image an atom inside with high NA, we assume a cavity length $L = 150$ μm. We choose radii of curvature R of the cavity mirrors to be $R = 100$ μm, which is a typical value for such CO_2-laser etching techniques [101]. This geometry at a wavelength of $\lambda = 1388.8$ nm gives a mode waist of $\omega_0 = 4.4$ μm and a mode

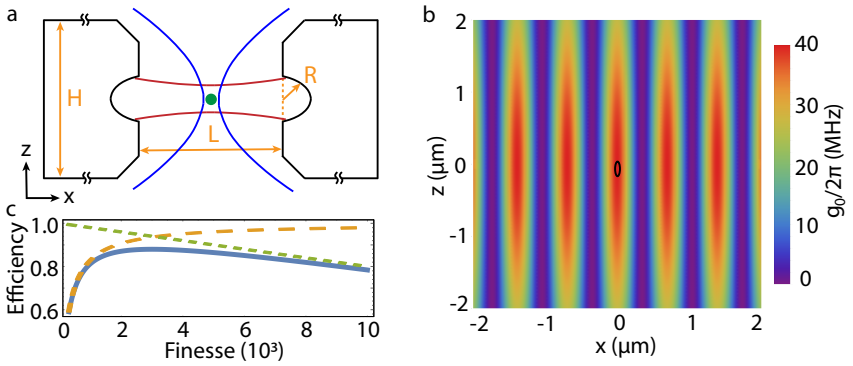

Figure 8.6: Tweezer trapping in a fiber Fabry-Pérot cavity. (a) The geometry of the fiber FP cavity, and the tweezer trap at the center. (b) A zoom-in of the center ± 2 μm of the cavity mode. The black ellipse shows a liberal estimate of the atomic wavefunction in a tweezer trap as described in the previous section. (c) The efficiencies associated with the fiber cavity vs F_e (see text). P_{cavity} (orange long dash), η_{coll} (green short dash), and their product η_{ext} (blue line).

volume of $V_m = 2.3 \times 10^{-15}$ m^3, or $842\lambda^3$.

We also analyze the mode profile in this cavity in a similar way to the photonic cavity, and a zoom-in of the central ± 2 μm is shown in Fig. 8.6b. The black ellipse shows a liberal estimate of the atomic wavefunction in a tweezer as described in the previous section. The only requirement in this system is that the atom is centered on the antinode as shown in Fig. 8.6b. Noting that the y-axis into the page has the same profile as the z-direction, this system requires an overall less precise alignment than the photonic cavity.

The coherent coupling rate g_0 between the cavity and the atom is given by [101]

$$g_0 = \sqrt{\frac{d^2\omega}{2\hbar\epsilon_0 V_m}}, \tag{8.1}$$

where d is the reduced dipole matrix element, ω is the angular frequency of the cavity and the atomic transition, ϵ_0 is the permittivity of free space. For this geometry and the value of d discussed above, we obtain a coherent coupling rate of $g_0 = 2\pi \times 39$ MHz. Note that here the cavity supports two degenerate polarizations, so the cavity field can have perfect polarization overlap with the transition dipole. As with the photonic crystal cavity, we design the fiber cavity such that one mirror has lower reflection and allows for coupling photons into and out of the cavity [81, 82, 48]. Now we choose a finesse of $F_e = 2000$, which is well below maximum finesse values of $> 10^5$ [101]. The cavity linewidth $\kappa_e = \pi\, c/(LF)$ for these values is $\kappa = 2\pi \times 500$ MHz, and the free spectral range FSR $= 2\pi\, c/(2L) = 2\pi \times 1.0$ THz.

Table 8.2: The values relevant for a quantum repeater with a fiber FP cavity, and the sections of the text in which they are described.

Parameter	**Section**	**Value**
Bandwidth	8.7	$2\pi \times 13$ MHz
Wavelength	II	1.39 μm (0.35 dB/km)
System efficiency	8.7	0.80
Memory	II, AII	≤ 26 sec
Read-out fidelity	8.7	> 0.99

We can now estimate the single-atom cooperativity [101], defined here for consistency with the photonic crystal as $C_0 = \frac{4g_0^2}{\kappa\Gamma}$. For our values we arrive at $C_0 = 39$, for which the probability of emission of a spontaneous photon into the cavity mode is $P_{\text{cavity}} = C_0/(C_0 + 1) = 0.97$. We assume an intrinsic finesse of $F_i = 5 \times 10^4$ [101, 81], for which we can again define a collection efficiency η_{coll} of extracting the photon into the waveguide mode, which is given by $\eta_{\text{coll}} = 1 - F_e/F_i$. For $F_e = 2000$ this corresponds to $\eta_{\text{coll}} = 0.96$. The efficiency of extracting a photon from the atom into the waveguide mode is given by the product of these $\eta_{\text{ext}} = P_{\text{cavity}} \cdot \eta_{\text{coll}}$, which is 0.94. η_{ext} is maximized for $F_e = 2000$, as is shown in Fig. 8.6c.

However, another factor emerges because we require the waveguide mode of the optical fiber to be single-mode (SM). This is necessary since indistinguishable photons are required for Bell state measurements. Representative efficiencies for coupling a photon in a cavity similar to our design into a SM fiber are $\eta_{\text{SM}} \lesssim 0.85$ [101]. The photon acquisition efficiency is thus $\eta_{\text{PA}} = \eta_{\text{ext}} \cdot \eta_{\text{SM}} = 0.80$.

As with the photonic crystal in the main text, we show a table for the fiber FP cavity of the quantities relevant for a quantum repeater in Table 8.2. The Purcell-enhanced linewidth is given by $\Gamma_{1D} = (1 + P)\Gamma$, where $P = C_0$. For the fiber FP cavity $\Gamma_{1D} = 2\pi \times 13$ MHz. For the same $B_{\text{ext}} = 200$ G and for $\Omega = \Gamma_{1D}$, we get $\Gamma_{\text{SC}} = 2\pi \times 390$ kHz, and $\mathcal{F}_{\text{RO}} > 0.99$.

8.8 Telecom Networks with Yb^+ Ions

We now discuss the possibility of using Yb^+ ions in fiber FP cavities. Yb^+ has strong telecom transitions that remain largely unused in experiments. Yet, they have been studied carefully by theorists because Yb is a platform for parity violation measurements [102, 103, 104, 105, 106]. Similar to the scheme in neutral Yb, the telecom transitions in Yb^+ are from metastable states $^2D_{3/2}$ and $^2D_{5/2}$, which are strongly coupled to a higher-lying state $^2P_{3/2}$ via wavelengths of 1346 nm and 1650

nm, respectively. The relevent level structure is shown in Fig. 8.7a. The metastable $^2D_{3/2}$ and $^2D_{5/2}$ states are very weakly connected to the ground state via 'clock'-like transitions, similar to the case of neutral Yb.

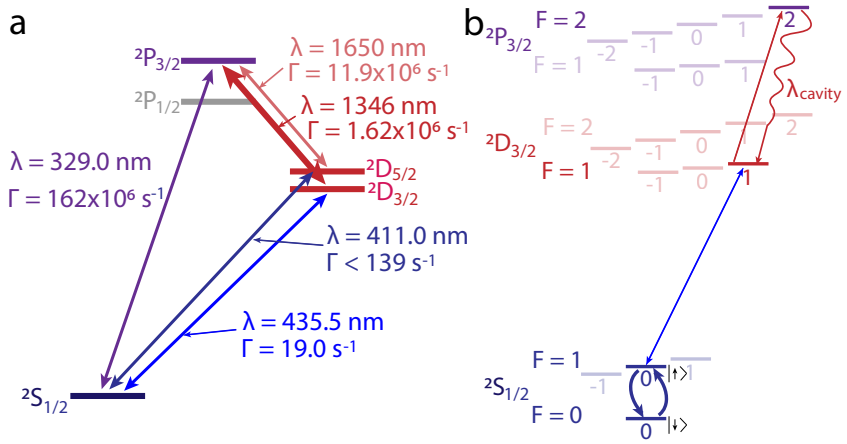

Figure 8.7: Yb^+ level structure, and excitation scheme for $^{171}Yb^+$. (a) The relavent levels of Yb^+, showing their wavelengths and linewidths. The thick red line shows the proposed telecom transition. (b) Three-level scheme by which quantum information in the ground state can be entangled with a telecom photon via the proposed telecom transition resonant with the cavity mode.

The scheme described in Fig. 8.7b is designed to include the ground-state hyperfine qubit, which has become the workhorse of quantum information processing with trapped ions. One of these qubit states can be mapped to the $^2D_{3/2}$ manifold by driving the electric quadrupole (E2) 'clock' transition [107]. An excitation from this state to the $^2P_{3/2}$ allows one of the ground hyperfine qubit states to be entangled with a telecom photon that is strongly coupled to the cavity. The mapping back to the ground state is done by performing a π-pulse with the 'clock' laser.

We choose the $^2D_{3/2}$ state rather than $^2D_{5/2}$ because it is easier to eliminate other decay pathways from the $^2P_{3/2}$ excited state. The hyperfine splitting is 430 MHz for $^2D_{3/2}$ but only 64 MHz for $^2D_{5/2}$ [106]. This latter value is comparable to the Purcell-enhanced linewidth for the decay into the cavity mode. Note that the dipole matrix is 4.2 a_0-e for the transition from $^2P_{3/2}$ to $^2D_{5/2}$ and 1.3 a_0-e for the transition to $^2D_{3/2}$ [105]. The Purcell-enhanced linewidth for the $^2D_{3/2}$ state in a fiber FP cavity is well below the hyperfine splitting of 430 MHz.

Using the analysis outlined in Appendix I and Ref. [55], we can arrive at the exact DME for the specific scheme described in Fig. 8.7b. This gives $DME_{|1,1\rangle\rightarrow|2,2\rangle}$ = 0.41 a_0-e. This is smaller than the case for neutral Yb by a factor of > 3 even though

the linewidth Γ is similar. This is because $J > 0$, and thus there is hyperfine splitting and more states that contribute to the total linewidth.

We believe that the fiber FP cavity considered above and in Fig. 8.6 is also suitable for Yb^+. Indeed, a Yb^+ ion has already been trapped inside a fiber cavity, where the fiber length is ~ 200 μm [108]. In that work, the same metastable state $^2D_{3/2}$ was used, but it was coupled to an even higher excited state $^3D[3/2]_{1/2}$ (not shown), with a transition wavelength of 935 nm. The atomic wavefunction in an ion trap is of similar size to that in an optical tweezer, so the entire discussion above and in Fig. 8.3 applies here as well.

As for the neutral Yb scheme described above, this scheme for Yb^+ ion could be used for creating a clock network. This transition is already used for atomic ion frequency standards [107], and so the development of a commercial technology based on this system may be more straightforward. Further, such a scheme could allow direct telecommunications between trapped ion quantum computers to facilitate the realization of a quantum computing network [1], and it could also be used with multiple qubits at each node of the network, for which gate operations between qubits can be employed for error correction or decoherence free subspaces [109].

8.9 Conclusion and Outlook

We have illustrated that silicon-based photonics combined with tweezer-trapped ^{171}Yb atoms are a candidate system for quantum optics in the telecom-band. The strong 1.4 μm transition from the $^3P_0$ 'clock' state of Yb enables 15 MHz-bandwidth emission when coupled to a silicon photonic cavity, and the nuclear spin allows for a coherent quantum memory. Further, we propose a simple and robust trapping protocol which enables atoms to be coupled to silicon nanophotonics, and even facilitates an array of atoms coupled to an array of cavities. Furthermore, we illustrate the potential of our platform for quantum repeaters.

Moreover, there are several other applications of this system which include quantum photonic circuits, novel platforms for long-range interactions, and many-body physics [46]. Our system may enable the direct integration of neutral-atom quantum computers into a quantum network, in which quantum gates can be performed using local exchange [50, 51] or Rydberg [52] interactions. Further, this system opens the possibility to implement an optical clock network [110] by using the $^1S_0 \leftrightarrow {}^3P_0$ optical clock qubit [53].

Alternative cavity designs based on free-space optics could offer different possi-

bilities, and we consider a fiber Fabry-Pérot cavity in Sec. 8.7. Finally we note that a similar telecom-wavelength atomic system could be created with Yb^+ ions, where a group of transitions from a metastable state has convenient wavelengths of 1450 and 1650 nm. We analyze a Yb^+ ion coupled with a fiber Fabry-Pérot cavity in Appendix IV, but we note that ion trapping near dielectric materials poses other technical challenges.

References

[1] L.-M. Duan and C. Monroe. "Colloquium: Quantum networks with trapped ions". In: *Rev. Mod. Phys.* 82 (2 2010), pp. 1209–1224.

[2] Andreas Reiserer and Gerhard Rempe. "Cavity-based quantum networks with single atoms and optical photons". In: *Rev. Mod. Phys.* 87 (4 2015), pp. 1379–1418.

[3] J. I. Cirac et al. "Quantum State Transfer and Entanglement Distribution among Distant Nodes in a Quantum Network". In: *Phys. Rev. Lett.* 78 (16 1997), pp. 3221–3224.

[4] S. J. van Enk, J. I. Cirac, and P. Zoller. "Photonic Channels for Quantum Communication". In: *Science* 279.5348 (1998), pp. 205–208.

[5] H. J. Kimble. "The quantum internet". In: *Nature* 453 (2008), pp. 1023–1030.

[6] Stephanie Wehner, David Elkouss, and Ronald Hanson. "Quantum internet: A vision for the road ahead". In: *Science* 362.6412 (2018).

[7] Manuel Uphoff et al. "An integrated quantum repeater at telecom wavelength with single atoms in optical fiber cavities". In: *Applied Physics B* 122.3 (2016), p. 46.

[8] Olivier Alibart et al. "Quantum photonics at telecom wavelengths based on lithium niobate waveguides". In: *Journal of Optics* 18.10 (2016), p. 104001.

[9] D. E. Chang et al. "Colloquium: Quantum matter built from nanoscopic lattices of atoms and photons". In: *Rev. Mod. Phys.* 90 (3 2018), p. 031002.

[10] Xavier Fernandez-Gonzalvo et al. "Quantum frequency conversion of quantum memory compatible photons to telecommunication wavelengths". In: *Opt. Express* 21.17 (2013), pp. 19473–19487.

[11] M. Bock et al. "High-fidelity entanglement between a trapped ion and a telecom photon via quantum frequency conversion". In: *Nature Communications* 9 (2018), p. 1998.

[12] Anaıs Dréau et al. "Quantum Frequency Conversion of Single Photons from a Nitrogen-Vacancy Center in Diamond to Telecommunication Wavelengths". In: *Phys. Rev. Applied* 9 (6 2018), p. 064031.

[13] A. Sipahigil et al. "An integrated diamond nanophotonics platform for quantum-optical networks". In: *Science* 354.6314 (2016), pp. 847–850.

[14] A. M. Dibos et al. "Atomic Source of Single Photons in the Telecom Band". In: *Phys. Rev. Lett.* 120 (24 2018), p. 243601.

[15] F. Kimiaee Asadi et al. "Quantum repeaters with individual rare-earth ions at telecommunication wavelengths". In: *Quantum* 2 (2018), p. 93. ISSN: 2521-327X.

[16] Kutlu Kutluer, Margherita Mazzera, and Hugues de Riedmatten. “Solid-State Source of Nonclassical Photon Pairs with Embedded Multimode Quantum Memory”. In: *Phys. Rev. Lett.* 118 (21 2017), p. 210502.

[17] Tian Zhong et al. “Nanophotonic rare-earth quantum memory with optically controlled retrieval”. In: *Science* 357.6358 (2017), pp. 1392–1395.

[18] A. Goban et al. “Atom-light interactions in photonic crystals”. In: *Nature Communications* 5 (2013), p. 3808.

[19] J. D. Thompson et al. “Coupling a Single Trapped Atom to a Nanoscale Optical Cavity”. In: *Science* 340 (2013), pp. 1202–1205.

[20] T. G. Tiecke et al. “Nanophotonic quantum phase switch with a single atom”. In: *Nature* 508 (2014), pp. 241–244.

[21] D. E. Chang, V. Vuletic, and M. D. Lukin. “Quantum nonlinear optics - photon by photon”. In: *Nature Photonics* 8 (2014), pp. 685–694.

[22] A. Goban et al. “Superradiance for Atoms Trapped along a Photonic Crystal Waveguide”. In: *Phys. Rev. Lett.* 115 (2015), p. 063601.

[23] I. Aharonovich, D. Englund, and M. Toth. “Solid-state single-photon emitters”. In: *Nature Photonics* 10 (2016), pp. 631–641.

[24] D. D. Awschalom et al. “Quantum technologies with optically interfaced solid-state spins”. In: *Nature Photonics* 12 (2018), pp. 516–527.

[25] E. Vetsch et al. “Optical Interface Created by Laser-Cooled Atoms Trapped in the Evanescent Field Surrounding an Optical Nanofiber”. In: *Phys. Rev. Lett.* 104 (20 2010), p. 203603.

[26] A. Goban et al. “Demonstration of a State-Insensitive, Compensated Nanofiber Trap”. In: *Phys. Rev. Lett.* 109 (3 2012), p. 033603.

[27] M. E. Kim et al. “Trapping single atoms on a nanophotonic circuit with configurable tweezer lattices”. In: *arXiv:1810.08769v1* (2018).

[28] J. M. McGuirk et al. “Alkali-metal adsorbate polarization on conducting and insulating surfaces probed with Bose-Einstein condensates”. In: *Phys. Rev. A* 69 (6 2004), p. 062905.

[29] David Hunger et al. “Resonant Coupling of a Bose-Einstein Condensate to a Micromechanical Oscillator”. In: *Phys. Rev. Lett.* 104 (14 Apr. 2010), p. 143002.

[30] J. M. Obrecht, R. J. Wild, and E. A. Cornell. “Measuring electric fields from surface contaminants with neutral atoms”. In: *Phys. Rev. A* 75 (6 2007), p. 062903.

[31] Mauro Antezza, Lev P. Pitaevskii, and Sandro Stringari. “Effect of the Casimir-Polder force on the collective oscillations of a trapped Bose-Einstein condensate”. In: *Phys. Rev. A* 70 (5 2004), p. 053619.

[32] Yu-ju Lin et al. “Impact of the Casimir-Polder Potential and Johnson Noise on Bose-Einstein Condensate Stability Near Surfaces”. In: *Phys. Rev. Lett.* 92 (5 2004), p. 050404.

[33] J. M. Obrecht et al. “Measurement of the Temperature Dependence of the Casimir-Polder Force”. In: *Phys. Rev. Lett.* 98 (6 2007), p. 063201.

[34] N. Schlosser et al. “Sub-poissonian loading of single atoms in a microscopic dipole trap”. In: *Nature* 551 (2017), pp. 485–488.

[35] A. M. Kaufman, B. J. Lester, and C. A. Regal. “Cooling a Single Atom in an Optical Tweezer to Its Quantum Ground State”. In: *Phys. Rev. X* 2 (4 2012), p. 041014.

[36] J. D. Thompson et al. “Coherence and Raman Sideband Cooling of a Single Atom in an Optical Tweezer”. In: *Phys. Rev. Lett.* 110 (13 2013), p. 133001.

[37] V. R. Almeida et al. “All-optical control of light on a silicon chip”. In: *Nature* 431 (2004), pp. 1081–1084.

[38] In: *https://www.imec-int.com/en/integrated-silicon-photonics, Leuven, Belgium* (https://www.imec-int.com/en/home).

[39] Steven A. Miller et al. “Low-loss silicon platform for broadband mid-infrared photonics”. In: *Optica* 4.7 (2017), pp. 707–712.

[40] Paul B. Dieterle et al. “Superconducting Cavity Electromechanics on a Silicon-on-Insulator Platform”. In: *Phys. Rev. Applied* 6 (1 2016), p. 014013.

[41] Alessandro Pitanti et al. “Strong opto-electro-mechanical coupling in a silicon photonic crystal cavity”. In: *Opt. Express* 23.3 (Feb. 2015), pp. 3196–3208.

[42] Taofiq K. Paraıso et al. “Position-Squared Coupling in a Tunable Photonic Crystal Optomechanical Cavity”. In: *Phys. Rev. X* 5 (4 2015), p. 041024.

[43] D. Navarro-Urrios et al. “Nanocrystalline silicon optomechanical cavities”. In: *Opt. Express* 26.8 (Apr. 2018), pp. 9829–9839.

[44] Daniel Barredo et al. “An atom-by-atom assembler of defect-free arbitrary 2D atomic arrays”. In: *Science* (2016).

[45] Manuel Endres et al. “Atom-by-atom assembly of defect-free one-dimensional cold atom arrays”. In: *Science* 354.6315 (2016), pp. 1024–1027.

[46] J. S. Douglas et al. “Quantum many-body models with cold atoms coupled to photonic crystals”. In: *Nature Photonics* 9 (2015), pp. 326–331.

[47] Jonathan D. Hood et al. “Atom–atom interactions around the band edge of a photonic crystal waveguide”. In: *Proceedings of the National Academy of Sciences* 113.38 (2016), pp. 10507–10512. DOI: 10.1073/pnas.1603788113.

[48] Stephan Welte et al. “Photon-Mediated Quantum Gate between Two Neutral Atoms in an Optical Cavity”. In: *Phys. Rev. X* 8 (1 2018), p. 011018.

[49] Andrew J. Daley et al. “Quantum Computing with Alkaline-Earth-Metal Atoms”. In: *Phys. Rev. Lett.* 101 (17 2008), p. 170504.

[50] A. J. Daley. “Quantum computing and quantum simulation with group-II atoms”. In: *Springer* Quantum Inf Process (2011).

[51] A. M. Kaufman et al. “Entangling two transportable neutral atoms via local spin exchange”. In: *Nature* 527 (2015), pp. 208–211.

[52] M. Saffman, T. G. Walker, and K. Mølmer. “Quantum information with Rydberg atoms”. In: *Rev. Mod. Phys.* 82 (3 2010), pp. 2313–2363.

[53] Andrew D. Ludlow et al. “Optical atomic clocks”. In: *Rev. Mod. Phys.* 87 (2 2015), pp. 637–701.

[54] K. Beloy et al. “Determination of the $5d6s\ ^3D_1$ state lifetime and blackbody-radiation clock shift in Yb”. In: *Phys. Rev. A* 86 (5 2012), p. 051404.

[55] D. A. Steck. “Quantum and Atom Optics”. In: *http://steck.us/teaching* ().

[56] Nicolas Sangouard et al. “Quantum repeaters based on atomic ensembles and linear optics”. In: *Rev. Mod. Phys.* 83 (1 2011), pp. 33–80.

[57] Sean D. Barrett and Pieter Kok. “Efficient high-fidelity quantum computation using matter qubits and linear optics”. In: *Phys. Rev. A* 71 (6 2005), p. 060310.

[58] H. Bernien et al. “Heralded entanglement between solid-state qubits separated by three metres”. In: *Nature* 497 (2013), pp. 86–90.

[59] D. S. Barker et al. “Three-photon process for producing a degenerate gas of metastable alkaline-earth-metal atoms”. In: *Phys. Rev. A* 93 (5 2016), p. 053417.

[60] Martin M. Boyd et al. “Nuclear spin effects in optical lattice clocks”. In: *Phys. Rev. A* 76 (2 2007), p. 022510.

[61] A. V. Gorshkov et al. “Alkaline-Earth-Metal Atoms as Few-Qubit Quantum Registers”. In: *Phys. Rev. Lett.* 102 (11 2009), p. 110503.

[62] Lucio Robledo et al. “High-fidelity projective read-out of a solid-state spin quantum register”. en. In: *Nature (London)* 477.7366 (Sept. 2011), pp. 574–578. ISSN: 0028-0836.

[63] J. Calsamiglia and N. Lütkenhaus. “Maximum efficiency of a linear-optical Bell-state analyzer”. In: *Applied Physics B* 72.1 (2001), pp. 67–71.

[64] A. Napoli and J. Pedro. “Getting the Most from Currently Deployed Optical Fiber Infrastructure”. In: *Fibre Systems, Viewpoint* (2017).

[65] Nicolas Sangouard, Romain Dubessy, and Christoph Simon. “Quantum repeaters based on single trapped ions”. In: *Physical Review A* 79.4 (2009), p. 042340.

[66] F. Marsili et al. “Detecting single infrared photons with 93% system efficiency”. In: *Nature Photonics* 7 (2013), pp. 210–214.

[67] T. Legero et al. “Time-resolved two-photon quantum interference”. In: *Applied Physics B* 77.8 (2003), pp. 797–802.

[68] Xu-Jie Wang et al. “Experimental Time-Resolved Interference with Multiple Photons of Different Colors”. In: *Phys. Rev. Lett.* 121 (8 2018), p. 080501.

[69] Thomas Böttger et al. “Spectroscopy and dynamics of Er^{3+} : Y_2SiO_5 at 1.5 μm”. In: *Phys. Rev. B* 74 (7 2006), p. 075107.

[70] Paul Seidler et al. “Slotted photonic crystal nanobeam cavity with an ultrahigh quality factor-to-mode volume ratio”. In: *Opt. Express* 21.26 (2013), pp. 32468–32483.

[71] Takashi Asano et al. “Photonic crystal nanocavity with a Q factor exceeding eleven million”. In: *Opt. Express* 25.3 (2017), pp. 1769–1777.

[72] P. C. Maurer et al. “Room-Temperature Quantum Bit Memory Exceeding One Second”. In: *Science* 336.6086 (2012), pp. 1283–1286.

[73] Andreas Reiserer et al. “Robust Quantum-Network Memory Using Decoherence-Protected Subspaces of Nuclear Spins”. In: *Phys. Rev. X* 6 (2 2016), p. 021040.

[74] S. Probst et al. “Microwave multimode memory with an erbium spin ensemble”. In: *Phys. Rev. B* 92 (1 2015), p. 014421.

[75] Stefano Pirandola et al. “Fundamental limits of repeaterless quantum communications”. In: *Nature communications* 8 (2017), p. 15043.

[76] S.-P. Yu et al. “Nanowire photonic crystal waveguides for single-atom trapping and strong light-matter interactions”. In: *Applied Physics Letters* 104.11 (2014), p. 111103.

[77] Kartik Srinivasan and Oskar Painter. “Momentum space design of high-Q photonic crystal optical cavities”. In: *Opt. Express* 10.15 (2002), pp. 670–684.

[78] Jasper Chan et al. “Optical and mechanical design of a “zipper” photonic crystal optomechanical cavity”. In: *Opt. Express* 17.5 (2009), pp. 3802–3817.

[79] Jasper Chan et al. “Optimized optomechanical crystal cavity with acoustic radiation shield”. In: *Applied Physics Letters* 101.8 (2012), p. 081115.

[80] Kejie Fang et al. “Generalized non-reciprocity in an optomechanical circuit via synthetic magnetism and reservoir engineering”. In: *Nature Physics* 13.5 (Jan. 2017), pp. 465–471.

[81] J. Gallego et al. “High-finesse fiber Fabry–Perot cavities: stabilization and mode matching analysis”. In: *Applied Physics B* 122.3 (2016), p. 47.

[82] J. Gallego et al. “Strong Purcell Effect on a Neutral Atom Trapped in an Open Fiber Cavity”. In: *Phys. Rev. Lett.* 121 (17 Oct. 2018), p. 173603.

[83] T. G. Tiecke et al. “Efficient fiber-optical interface for nanophotonic devices”. In: *Optica* 2.2 (2015), pp. 70–75.

[84] Ryuta Yamamoto et al. “An ytterbium quantum gas microscope with narrow-line laser cooling”. In: *New Journal of Physics* 18.2 (2016), p. 023016.

[85] S. Saskin et al. “Narrow-line cooling and imaging of Ytterbium atoms in optical tweezer array”. In: *arXiv:1810.10517v1* (2018).

[86] Alexandre Cooper et al. “Alkaline-Earth Atoms in Optical Tweezers”. In: *Phys. Rev. X* 8 (4 2018), p. 041055.

[87] M. A. Norcia, A. W. Young, and A. M. Kaufman. “Microscopic Control and Detection of Ultracold Strontium in Optical-Tweezer Arrays”. In: *Phys. Rev. X* 8 (4 2018), p. 041054.

[88] Y. Meng et al. “Near-Ground-State Cooling of Atoms Optically Trapped 300 nm Away from a Hot Surface”. In: *Phys. Rev. X* 8 (3 2018), p. 031054.

[89] Zhi-Ming Tang et al. “Magic wavelengths for the 6 s 2 1 S 0 - 6 s 6 p 3 P 1 transition in ytterbium atom”. In: *Journal of Physics: Conference Series* 875.3 (2017), p. 022050.

[90] F. Scazza. “Probing SU(N)-symmetric orbital interaction with ytterbium Fermi gases in optical lattices”. In: *PhD thesis, Ludwig-Maximilians-Universitat Munchen* (2015).

[91] H. Bernien et al. “Probing many-body dynamics on a 51-atom quantum simulator”. In: *Nature* 551 (2017), pp. 579–584.

[92] Ralf Ritter et al. “Atomic vapor spectroscopy in integrated photonic structures”. In: *Applied Physics Letters* 107.4 (2015), p. 041101.

[93] R Ritter et al. “Coupling thermal atomic vapor to an integrated ring resonator”. In: *New Journal of Physics* 18.10 (2016), p. 103031.

[94] Andrei Derevianko, Sergey G. Porsev, and James F. Babb. “Electric dipole polarizabilities at imaginary frequencies for hydrogen, the alkali–metal, alkaline–earth, and noble gas atoms”. In: *Atomic Data and Nuclear Data Tables* 96.3 (2010), pp. 323–331. ISSN: 0092-640X.

[95] Paul E. Barclay, Kartik Srinivasan, and Oskar Painter. “Nonlinear response of silicon photonic crystal microresonators excited via an integrated waveguide and fiber taper”. In: *Opt. Express* 13.3 (2005), pp. 801–820.

[96] Thomas J. Johnson, Matthew Borselli, and Oskar Painter. “Self-induced optical modulation of the transmission through a high-Q silicon microdisk resonator”. In: *Opt. Express* 14.2 (2006), pp. 817–831.

[97] K. Bücher, J. Bruns, and H. G. Wagemann. "Absorption coefficient of silicon: An assessment of measurements and the simulation of temperature variation". In: *Journal of Applied Physics* 75.2 (1994), pp. 1127–1132.

[98] Je-Hyung Kim et al. "Two-Photon Interference from the Far-Field Emission of Chip-Integrated Cavity-Coupled Emitters". In: *Nano Letters* 16.11 (2016), pp. 7061–7066.

[99] T. Steinmetz et al. "Stable fiber-based Fabry-Pérot cavity". In: *Applied Physics Letters* 89.11 (2006), p. 111110.

[100] Y. Colombe et al. "Strong atom-field coupling for Bose-Einstein condensates in an optical cavity on a chip". In: *Nature* 450 (2007), pp. 272–276.

[101] D Hunger et al. "A fiber Fabry–Perot cavity with high finesse". In: *New Journal of Physics* 12.6 (2010), p. 065038.

[102] U. I. Safronova and M. S. Safronova. "Third-order relativistic many-body calculations of energies, transition rates, hyperfine constants, and blackbody radiation shift in $^{171}Yb^{+}$". In: *Phys. Rev. A* 79 (2 2009), p. 022512.

[103] V. A. Dzuba and V. V. Flambaum. "Calculation of nuclear-spin-dependent parity nonconservation in *sd* transitions of Ba^{+}, Yb^{+}, and Ra^{+} ions". In: *Phys. Rev. A* 83 (5 2011), p. 052513.

[104] B. K. Sahoo and B. P. Das. "Parity nonconservation in ytterbium ion". In: *Phys. Rev. A* 84 (1 2011), p. 010502.

[105] S. G. Porsev, M. S. Safronova, and M. G. Kozlov. "Correlation effects in Yb^{+} and implications for parity violation". In: *Phys. Rev. A* 86 (2 2012), p. 022504.

[106] T. Feldker et al. "Spectroscopy of the $^2S_{1/2} \rightarrow ^2 P_{3/2}$ transition in Yb ii: Isotope shifts, hyperfine splitting, and branching ratios". In: *Phys. Rev. A* 97 (3 2018), p. 032511.

[107] T. Schneider, E. Peik, and Chr. Tamm. "Sub-Hertz Optical Frequency Comparisons between Two Trapped $^{171}Yb^{+}$ Ions". In: *Phys. Rev. Lett.* 94 (23 2005), p. 230801.

[108] Matthias Steiner et al. "Single Ion Coupled to an Optical Fiber Cavity". In: *Phys. Rev. Lett.* 110 (4 2013), p. 043003.

[109] M Zwerger et al. "Quantum repeaters based on trapped ions with decoherence-free subspace encoding". In: *Quantum Science and Technology* 2.4 (2017), p. 044001.

[110] P. Komar et al. "A quantum network of clocks". In: *Nature Physics* 10 (2014), pp. 582–587.

Chapter 9

CONCLUSION AND FUTURE DIRECTIONS

This thesis presented the work towards the implementation of optical and photonic systems for their use in quantum spectroscopic experiments. Specifically, two different experimental approaches have been developed, one of which relies on waveguide based narrowband entangled photon generation, while the other extends this process to specially designed free-space gratings capable of producing extremely broadband signals. Both setups are ideally suited for the subsequent exploration of entangled photon interactions in chemical and atomic systems with appropriate transitions. The theoretical and experimental design elements which are required for the successful implementation of these instruments have been described in detail, so as to enable the simple transition to alternative wavelengths that could prove to be more suitable for specific atomic or molecular species of interest. The spectral-temporal resolutions these entangled photon interferometers have been shown to be capable of make them highly important and useful instruments for a wide-variety of applications. While experimental spectroscopic measurements have been performed, these were deemed to be outside of the scope and breadth of this work, and as such are reserved for the theses of other group members. Finally, the demonstration of initial steps towards utilizing novel nonlinear ferroelectric materials for the generation of cw radiation, as well as entangled photon pairs at UV wavelengths has been presented. The novelty of extending the interferometric instruments presented in this work to this wavelength range is a crucial step in enabling the study of chemical reaction kinetics, reaction rate constants, or gas chemical compositions using low-flux sources.

Given that each individual chapter has highlighted and contrasted the advantages and drawbacks of the presented experiments, here, I would like to outline more general themes for what directions the near-term experimental pursuits could be and would be within reach.

Ce^{3+}-doped fibers

Within the scope of entangled two-photon absorption, which as of yet has been a challenging endeavour in the spectroscopy community due to lack of efficient absorbers with strong fluorescence, the move towards highly controlled solid-state systems

would be an ideal route to pursue. In order to demonstrate the real advantages of using entangled photon pairs for applications which rely on the near-simultaneous absorption of two photons which have some underlying quantum correlations between them, experimental setups that are extremely efficient in terms of interaction and signal collection are needed. To this end, following from the general theme of strong light confinement, I propose the use of rare-earth doped optical fibers as a particularly lucrative system. The strong confinement of light mitigates the need for precise focusing into liquid samples that are contained in a cuvette, thus alleviating the bottleneck associated with the strong scattering of individual photons from an entangled pair. Further, the precise knowledge of dopant concentrations would enable the accurate calculation of the number of interacting emitters in a given length of fiber. Correspondingly, the fact that optical fibers displaying low absorption can be multiple meters in length means that the effective interaction volume would be on the order of $\sim \pi * r^2 * L \sim 10^{-10} m^3$ in contrast to the small effective volume of a lens, which given realistic experimental conditions is on the order of 10^{-14} – $10^{-15} m^3$. This 4 orders of magnitude improvement would significantly increase the number of two-photon absorption events taking place and therefore a much larger ratio of the entangled photon pairs could participate in the generation of a measured fluorescence signal. In addition to this improvement in interaction strength, the fundamentally guided mode nature of optical fibers makes the collection of the fluorescence signal particularly simple and also serves to help with directing the signal into high-efficiency fiber-coupled detectors. Although the effective cone which can be collected from an emitter will be dictated by the numerical aperture of the fiber used, and further losses are expected given that the backwards-propagating direction is not (easily) experimentally accessible for measurement, the additional benefit of being able to completely decouple the sample (i.e. the fiber) from the rest of the experiment means that the detected signal is necessarily originating from two-photon absorption events. Therefore spectral measurements of the detected fluorescence would definitively point towards the existence and strength, or lack thereof, of entangled light matter interactions.

More concretely, cerium (Ce) doped optical fibers have gathered significant interest as a result of their uses as phosphors, scintillators, and in more general terms, detectors for ionizing radiation. This stems from their 5d-4f transition which is well suited for the generation of broadband fluorescence in the visible to near-infrared range. Recent work has shown that Ce-doped single mode optical fibers with core diameters of $\sim 13 \mu m$ have been fabricated and characterized for their absorption

and fluorescence properties [1]. Absorption has been shown to be very high in the near-UV region, with $> 100 dB/m$ values being measured near 400nm wavelength excitation. The subsequent characterization of the generated fluorescence spectrum shows large power densities in the 500nm-800nm range, which would make it ideal for the implementation into the entangled photon interferometers described in this body of work. Furthermore, the distinctive loss of fluorescence at longer fiber lengths attributed to re-absorption at Ce^{3+} ion sites means that spectral filtering is an inherent experimental advantage, thus reducing the likelihood of pump-dominated background noise.

Fiber-based broadband interferometer implementation

A second, near-term objective which could provide significant benefits for the interferometers utilizing broadband SPDC would be the transition to waveguided implementations of the source, and photonic-crystal optical fibers (PhC) for the downstream optics. As discussed, a major drawback to the free-space gratings used was the extremely high chromatic dispersion, and the aggressive opening angles of the SPDC cone as a function of wavelength. By constraining the modes of the three interacting fields to a waveguide structure, it would be possible to use the same chirped technique in the periodic poling as for the gratings, however limiting the emission to be immediately single-mode guided. While waveguide dispersion would obviously still need to be accounted for, this could be either remedied source-side, or further downstream through some dispersion compensating elements. The single-mode guided broadband signal would be ideally conditioned to be coupled into optical fibers, which now ideally should support single-mode propagation for a very wide range of wavelengths.

PhC fibers have emerged in recent years as prime candidates for precisely this purpose. The mode field diameters of these fibers are compatible with the standard sizes used in the more ubiquitous, commercially available telecom fibers. By the virtue of their design, the mode field sizes across the entire supported low-loss wavelength range (400nm-1700nm) are almost identical, meaning that achromatic optical elements responsible for collimation and focusing should be well suited. Furthermore, the polarization maintaining capability of the PM fibers would significantly help with discrimination between the SPDC signal and pump-induced fluorescence in the crystal.

Two-photon addressable 1D and 2D photonic circuits

A particularly unique extension that the on-chip integration of entangled photon interferometers offers is the implementation of one- and two-dimensional photonic crystal structures which could be interfaced with molecular qubits that are designed with two-photon resonant transitions. Such photonic crystals, as shown in Fig.9.1, would enable recent advances in waveguide-QED principles to be implemented, with the additional benefit of achieving true single molecule addressability through the use of two-photon absorption techniques utilizing entangled photon pairs. Specifically in the molecular qubit domain, the potential for building easily scalable super-lattices with essentially randomly accessible qubit-nodes would open the door to a number of new interacting many-body systems to be studied. Such a 'random-access' system consisting of either single or a crosshatch pattern of waveguides would allow for individual qubits to be interacted with and used for on-demand storage and retrieval. This higher-order selectivity of the qubits could also make it possible to entangle arbitrary molecules in the array. Furthermore, as it is possible to design photonic crystals which allow for circular polarization modes to be propagated, it is feasible to realize architectures with qubit addressability where $\Delta m = m_j$.

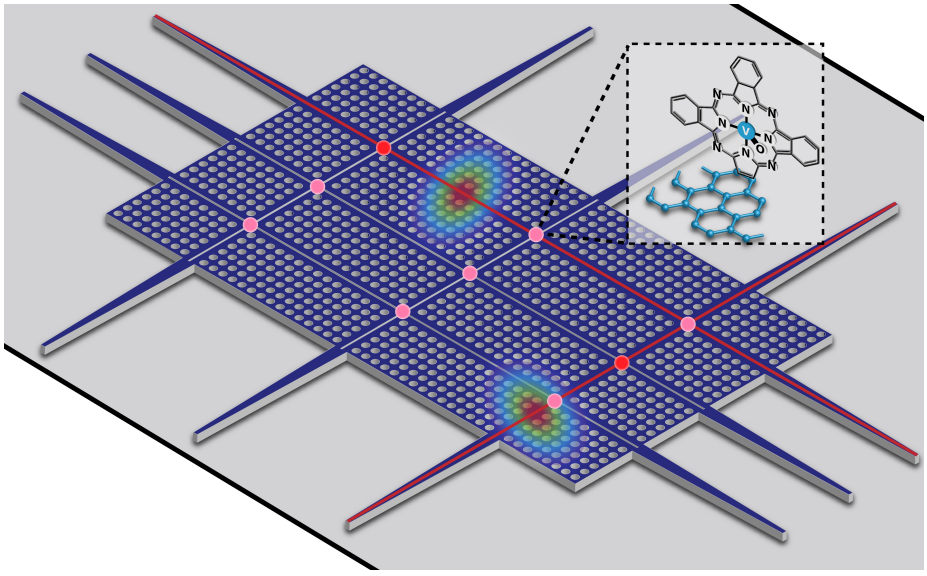

Figure 9.1: Two-dimensional photonic circuit utilizing slot waveguides as a means to achieve super-lattices with individually addressable molecular qubits located at specific nodes. The propagating modes supported by the slot waveguides are overlayed on top of the lattice.

In conjunction with the experimental manipulation of entangled photon pairs de-

scribed in this thesis, there is a real potential to further enhance the capabilities of such circuits. Specifically, through the adjustment of the relative time-delay between correlated photons and the designation of the input ports of the lattice used, it would be possible to have perfect selectivity over which qubits are two-photon excited. Alternatively, by incorporating the polarization degree-of-freedom of the photon pairs, it would be possible to tune the arrival time of the photons through waveguide dispersion. This would allow individual input ports to be used for both photons. Provided the coherence times of the entangled states are short enough, material and waveguide dispersive effects could aid in the overlap of the photon wavepackets at the location of the desired qubit and induce a two-photon absorption event.

An accompanying advantage of such a system would be the significantly enhanced decay rates into the guided modes of the waveguides which are coupled to the molecular qubits through the inherent Purcell enhancement of these structures. Therefore, any qubit relaxation that carries with it the emission of a photon could in principle be read-out through an associated input/output waveguide port. In addition to the traditional guided modes supported by simple waveguides, the introduced periodicity of the two-dimensional photonic crystal structure opens up a bandgap in the dispersion relation of the structure. Inside this bandgap, the photonic modes are forbidden to propagate and therefore end up decaying in an exponential form. Near the band-edge, the slope of the dispersion relation goes to zero and therefore leads to slow-light conditions ($v_g = \frac{d\omega}{dk}$). This increases the interaction time with the emitter, similar to that of a traditional light re-circulation in a cavity.

The main benefit provided by this added complexity is that tuning of the band edges to the transition frequencies of the proposed qubits allows for emitter-photon bound states to be induced. Here, by (for example electrically) tuning the qubit resonance to be inside the bandgap, the molecule could only emit a photon into an evanescently decaying photonic mode that has an exponential profile. As a result, instead of a guided mode of the form e^{ikx} being coupled into the photonic structure, a bound-state of the form $e^{-\kappa x}$ is formed in the near-field of the qubit. Therefore, novel complex systems are realizable where multiple qubits are coupled to a single photonic crystal waveguide, the resonant frequency of each of which could be individually (and dynamically) tuned to control the type of emission profile that it is to display. Furthermore, since the exponential decay length of the bound state depends on how deep inside the bandgap the emission frequency lies, the coupling strength J_{ij} between nearest (or next-nearest) neighbor qubits i and j could be controlled

with high precision, hence allowing for dynamic interaction Hamiltonians to be implemented.

References

[1] Amit Yadav et al. “Visible to near-infrared broadband fluorescence from Ce-doped silica fiber”. In: *Optical Materials Express* 11.8 (2021), pp. 2528–2538.

Appendix A

SPDC ANGULAR DISTRIBUTION

Birefringent Phase Matching

[n.b. It is important to remember that the pump-wavevector k_p is a function of not only wavelength, but also the angle it makes relative to the optic axis of the crystal (via the refractive index). Hence $k_p(\lambda, n(\lambda, \theta_\pi))$.]

More explicitly, $k_p(\lambda, n(\lambda, \theta_\pi)) = \frac{2\pi n(\lambda,\theta_\pi)}{\lambda}$, with $\frac{1}{n^2(\lambda,\theta_\pi)} = \frac{cos^2(\theta_\pi)}{n_o^2(\lambda)} + \frac{sin^2(\theta_\pi)}{n_e^2(\lambda)}$.

Longitudinal components:

$$k_p = k_s cos\theta_s + k_i cos\theta_i \tag{A.1}$$

Transverse components:

$$k_s sin\theta_s = -k_i sin\theta_i \tag{A.2}$$

Reformulating the transverse part by squaring both sides:

$$k_s^2 sin^2\theta_s = k_i^2 sin^2\theta_i \tag{A.3}$$

$$k_s^2 \left(1 - cos^2\theta_s\right) = k_i^2 \left(1 - cos^2\theta_i\right) \tag{A.4}$$

$$k_s^2 - k_s^2 cos^2\theta_s = k_i^2 \left(1 - cos^2\theta_i\right) \tag{A.5}$$

$$k_s^2 cos^2\theta_s - k_s^2 = k_i^2 \left(cos^2\theta_i - 1\right) \tag{A.6}$$

$$k_s^2 cos^2\theta_s = k_i^2 \left(cos^2\theta_i - 1\right) + k_s^2. \tag{A.7}$$

Rewriting the longitudinal part:

$$k_p - k_i cos\theta_i = k_s cos\theta_s \tag{A.8}$$

$$k_s^2 cos^2\theta_s = \left(k_p - k_i cos\theta_i\right)^2. \tag{A.9}$$

Substituting Eq. 7 into 9:

$$k_i^2\left(cos^2\theta_i - 1\right) + k_s^2 = \left(k_p - k_i cos\theta_i\right)^2 \tag{A.10}$$

$$k_i^2 cos^2\theta_i - k_i^2 + k_s^2 = k_p^2 + k_i^2 cos^2\theta_i - 2k_p k_i cos\theta_i \tag{A.11}$$

$$k_s^2 - k_i^2 = k_p^2 - 2k_p k_i cos\theta_i. \tag{A.12}$$

Rearranging:

$$-2k_p k_i cos\theta_i = k_s^2 - k_i^2 - k_p^2 \tag{A.13}$$

$$2k_p k_i cos\theta_i = k_p^2 - k_s^2 + k_i^2 \tag{A.14}$$

$$cos\theta_i = \frac{k_p^2 - k_s^2 + k_i^2}{2k_p k_i} \tag{A.15}$$

$$\theta_i = cos^{-1}\left(\frac{k_p^2 - k_s^2 + k_i^2}{2k_p k_i}\right). \tag{A.16}$$

Subsequently, convert to angles in the lab frame of reference via Snell's law to get the actual angle once the light exits the crystal.

$$\begin{aligned} sin\theta_s^{'} &= n_o(\omega_s) sin\theta_s \\ sin\theta_i^{'} &= n_o(\omega_s) sin\theta_i, \end{aligned} \tag{A.17}$$

therefore giving the final angles:

$$\begin{aligned} \theta_s^{'} &= sin^{-1}(n_o(\omega_s) sin\theta_s) \\ \theta_i^{'} &= sin^{-1}(n_o(\omega_s) sin\theta_i). \end{aligned} \tag{A.18}$$

Quasi Phase Matching

The situation here is slightly simpler, as one no longer needs to take into account the angle between the pump beam and the crystal axis.

Longitudinal components:

$$k_p = k_s cos\theta_s + k_i cos\theta_i + k_\Lambda \tag{A.19}$$

Transverse components:

$$k_s sin\theta_s = -k_i sin\theta_i \tag{A.20}$$

Reformulating the transverse part by squaring both sides:

$$k_s^2 sin^2\theta_s = k_i^2 sin^2\theta_i \tag{A.21}$$

$$k_s^2 \left(1 - cos^2\theta_s\right) = k_i^2 \left(1 - cos^2\theta_i\right) \tag{A.22}$$

$$k_s^2 - k_s^2 cos^2\theta_s = k_i^2 \left(1 - cos^2\theta_i\right) \tag{A.23}$$

$$k_s^2 cos^2\theta_s - k_s^2 = k_i^2 \left(cos^2\theta_i - 1\right) \tag{A.24}$$

$$k_s^2 cos^2\theta_s = k_i^2 \left(cos^2\theta_i - 1\right) + k_s^2. \tag{A.25}$$

Rewriting the longitudinal part:

$$k_p - k_i cos\theta_i - k_\Lambda = k_s cos\theta_s \tag{A.26}$$

$$k_s^2 cos^2\theta_s = \left(k_p - k_i cos\theta_i - k_\Lambda\right)^2. \tag{A.27}$$

Substituting Eq. 7 into 9:

$$k_i^2 \left(cos^2\theta_i - 1\right) + k_s^2 = \left(k_p - k_i cos\theta_i - k_\Lambda\right)^2 \tag{A.28}$$

$$k_i^2 cos^2\theta_i - k_i^2 + k_s^2 = k_p^2 + k_i^2 cos^2\theta_i + k_\Lambda^2 - 2k_p k_i cos\theta_i - 2k_p k_\Lambda + 2k_\Lambda k_i cos\theta_i \tag{A.29}$$

$$k_s^2 - k_i^2 = k_p^2 + k_\Lambda^2 - 2k_p k_i cos\theta_i - 2k_p k_\Lambda + 2k_\Lambda k_i cos\theta_i. \tag{A.30}$$

Rearranging:

$$2k_\Lambda k_i cos\theta_i - 2k_p k_i cos\theta_i = k_s^2 - k_i^2 - k_p^2 - k_\Lambda^2 + 2k_p k_\Lambda \tag{A.31}$$

$$2k_p k_i cos\theta_i - 2k_\Lambda k_i cos\theta_i = k_p^2 - k_s^2 + k_i^2 + k_\Lambda^2 - 2k_p k_\Lambda \tag{A.32}$$

$$cos\theta_i \left(2k_p k_i - 2k_\Lambda k_i\right) = k_p^2 - k_s^2 + k_i^2 + k_\Lambda^2 - 2k_p k_\Lambda \tag{A.33}$$

$$\theta_i = cos^{-1}\left(\frac{k_p^2 - k_s^2 + k_i^2 + k_\Lambda^2 - 2k_p k_\Lambda}{2k_p k_i - 2k_\Lambda k_i}\right). \tag{A.34}$$

Subsequently, convert to angles in the lab frame of reference via Snell's law to get the actual angle once the light exits the crystal:

$$\begin{aligned} sin\theta_s^{'} &= n_o(\omega_s) sin\theta_s \\ sin\theta_i^{'} &= n_o(\omega_s) sin\theta_i, \end{aligned} \tag{A.35}$$

therefore giving the final angles:

$$\begin{aligned} \theta_s^{'} &= sin^{-1}(n_o(\omega_s) sin\theta_s) \\ \theta_i^{'} &= sin^{-1}(n_o(\omega_s) sin\theta_i). \end{aligned} \tag{A.36}$$

Appendix B

TWO-PHOTON MICHELSON INTERFEROMETER

Taking a lossless beamsplitter with 50:50 split ratio, which has 4 ports. Ports 1 and 2 are designated as the inputs, while 3 and 4 are the outputs.

$$\hat{a}_1^\dagger \rightarrow \frac{1}{\sqrt{2}}\left(\hat{a}_3^\dagger + i\hat{a}_4^\dagger\right) \tag{B.1}$$

$$\hat{a}_2^\dagger \rightarrow \frac{1}{\sqrt{2}}\left(i\hat{a}_3^\dagger + \hat{a}_4^\dagger\right) \tag{B.2}$$

First, the following input state is considered, where 2 photons are directed into port 1 of the beamsplitter.

$$\psi_{in} = |2\rangle = \frac{1}{\sqrt{2}}\hat{a}_1^\dagger\hat{a}_1^\dagger|0\rangle \tag{B.3}$$

$$\frac{1}{\sqrt{2}}\hat{a}_1^\dagger\hat{a}_1^\dagger|0\rangle \rightarrow \psi_{out} = \frac{1}{\sqrt{2}}\frac{1}{\sqrt{2}}\frac{1}{\sqrt{2}}\left(\hat{a}_3^\dagger + i\hat{a}_4^\dagger\right)\left(\hat{a}_3^\dagger + i\hat{a}_4^\dagger\right) \tag{B.4}$$

$$= \frac{1}{2\sqrt{2}}\left(\hat{a}_3^\dagger\hat{a}_3^\dagger + i\hat{a}_4^\dagger\hat{a}_3^\dagger + i\hat{a}_3^\dagger\hat{a}_4^\dagger - \hat{a}_4^\dagger\hat{a}_4^\dagger\right) \tag{B.5}$$

$$= \frac{1}{2}\left(|2,0\rangle - |0,2\rangle\right) + \frac{i}{\sqrt{2}}\left(|1,1\rangle\right) \tag{B.6}$$

$$= \frac{1}{\sqrt{2}}\frac{\left(|2,0\rangle - |0,2\rangle\right)}{\sqrt{2}} + \frac{i}{\sqrt{2}}\left(|1,1\rangle\right) \tag{B.7}$$

$$\frac{1}{\sqrt{2}}\psi_{2002} + \frac{i}{\sqrt{2}}\psi_{11}. \tag{B.8}$$

Thus, we can define the output from a 2-photon input state in terms of the useful single photon per output mode, $|1,1\rangle$, part and the "parasitic" two photons per output mode, $|2,0\rangle$ *and* $|0,2\rangle$ part.

The significance of the parasitic term is that it is an unusable byproduct of the beamsplitter interaction that ultimately limits the visibility of an HOM interference effect.

Now the reflections from $M1$ and $M2$ in each arm of the interferometer result in the following input state (additionally dropping the phase factors).

$$\chi_{in} = \psi_{out} \tag{B.9}$$

Despite this state obviously being input into the same beamsplitter given the Michelson-type arrangement, for clarity let us model the problem as a separate step, whereby the input state χ_{in} is entering a beamsplitter with input ports 3 and 4 and output ports 5 and 6, respectively. The following transformations hold:

$$\hat{a}_3^\dagger \rightarrow \frac{1}{\sqrt{2}}\left(\hat{a}_5^\dagger + i\hat{a}_6^\dagger\right) \tag{B.10}$$

$$\hat{a}_4^\dagger \rightarrow \frac{1}{\sqrt{2}}\left(i\hat{a}_5^\dagger + \hat{a}_6^\dagger\right). \tag{B.11}$$

An immediate observation can be made regarding the state which is now found in the arms of the interferometer. Since the parasitic state ψ_{2002} is of no use and it furthermore will still undergo a transformation when it is reflected and made to pass through the beamsplitter (see below with $\hat{a}_3^\dagger\hat{a}_3^\dagger$ and $\hat{a}_4^\dagger\hat{a}_4^\dagger$), the output port which is being monitored will now also contain spurious single photon states in addition to the bunched two-photon states which are a result of the desired HOM interference. Let us highlight the useful (green) and unwanted (red) parts of the state which is found in the arms of the interferometer.

$$\chi_{in} = \psi_{out} = \frac{1}{2\sqrt{2}}\left(\hat{a}_3^\dagger\hat{a}_3^\dagger + \hat{a}_4^\dagger\hat{a}_3^\dagger + \hat{a}_3^\dagger\hat{a}_4^\dagger + \hat{a}_4^\dagger\hat{a}_4^\dagger\right) \tag{B.12}$$

Obviously this limits the maximum attainable visibility of the HOM interference to 50%.

Taking this composite input state and solving each part separately, we get:

$$\hat{a}_3^\dagger\hat{a}_3^\dagger \rightarrow \frac{1}{\sqrt{2}}\frac{1}{\sqrt{2}}\left(\hat{a}_5^\dagger + i\hat{a}_6^\dagger\right)\left(\hat{a}_5^\dagger + i\hat{a}_6^\dagger\right) \tag{B.13}$$

$$= \frac{1}{2}\left(\hat{a}_5^\dagger\hat{a}_5^\dagger + i\hat{a}_6^\dagger\hat{a}_5^\dagger + i\hat{a}_5^\dagger\hat{a}_6^\dagger - \hat{a}_6^\dagger\hat{a}_6^\dagger\right) \tag{B.14}$$

$$\hat{a}_4^\dagger\hat{a}_3^\dagger \rightarrow \frac{1}{\sqrt{2}}\frac{1}{\sqrt{2}}\left(i\hat{a}_5^\dagger + \hat{a}_6^\dagger\right)\left(\hat{a}_5^\dagger + i\hat{a}_6^\dagger\right) \tag{B.15}$$

$$= \frac{1}{2}\left(i\hat{a}_5^\dagger\hat{a}_5^\dagger + \hat{a}_6^\dagger\hat{a}_5^\dagger - \hat{a}_5^\dagger\hat{a}_6^\dagger + i\hat{a}_6^\dagger\hat{a}_6^\dagger\right) \tag{B.16}$$

$$\hat{a}_3^\dagger\hat{a}_4^\dagger \rightarrow \frac{1}{\sqrt{2}}\frac{1}{\sqrt{2}}\left(\hat{a}_5^\dagger + i\hat{a}_6^\dagger\right)\left(i\hat{a}_5^\dagger + \hat{a}_6^\dagger\right) \tag{B.17}$$

$$= \frac{1}{2}\left(i\hat{a}_5^\dagger\hat{a}_5^\dagger - \hat{a}_6^\dagger\hat{a}_5^\dagger + \hat{a}_5^\dagger\hat{a}_6^\dagger + i\hat{a}_6^\dagger\hat{a}_6^\dagger\right) \tag{B.18}$$

$$\hat{a}_4^\dagger\hat{a}_4^\dagger \rightarrow \frac{1}{\sqrt{2}}\frac{1}{\sqrt{2}}\left(i\hat{a}_5^\dagger + \hat{a}_6^\dagger\right)\left(i\hat{a}_5^\dagger + \hat{a}_6^\dagger\right) \tag{B.19}$$

$$= \frac{1}{2}\left(\hat{a}_6^\dagger\hat{a}_6^\dagger + i\hat{a}_6^\dagger\hat{a}_5^\dagger + i\hat{a}_5^\dagger\hat{a}_6^\dagger - \hat{a}_5^\dagger\hat{a}_5^\dagger\right). \tag{B.20}$$

Therefore we have a situation where if the assumption is made that the ψ_{11} state is made to consist of two indistinguishable photons, an expected HOM interference should occur (blue), with the caveat that half of the bunched photons are lost via the output port of the beamsplitter which is unobserved (orange).
Thus giving a final output state of the form.

$$\chi_{out} = \frac{1}{2\sqrt{2}}\frac{1}{2}\left(2i\hat{a}_6^\dagger\hat{a}_5^\dagger + 2i\hat{a}_5^\dagger\hat{a}_6^\dagger + 2i\hat{a}_5^\dagger\hat{a}_5^\dagger + 2i\hat{a}_6^\dagger\hat{a}_6^\dagger\right) \tag{B.21}$$

$$= \frac{1}{4\sqrt{2}}\left(2i\hat{a}_6^\dagger\hat{a}_5^\dagger + 2i\hat{a}_5^\dagger\hat{a}_6^\dagger + 2i\hat{a}_5^\dagger\hat{a}_5^\dagger + 2i\hat{a}_6^\dagger\hat{a}_6^\dagger\right) \tag{B.22}$$

What can be deduced from the final output state χ_{out} is that, in addition to a half of the useful bunched 2-photon signal being lost (orange), we also observe single photon states with a probability of $1/2$ (naturally only the creation operator $\hat{a}_6^\dagger$ would contribute to this from the terms $2i\hat{a}_6^\dagger\hat{a}_5^\dagger$ and $2i\hat{a}_5^\dagger\hat{a}_6^\dagger$), stemming from the original un-split 2-photon states $\hat{a}_3^\dagger\hat{a}_3^\dagger$ and $\hat{a}_4^\dagger\hat{a}_4^\dagger$.

In terms of what we would observe at the final coincidence detection, when the interferometer path lengths are equalized such that the single photon states in each arm can subsequently undergo interference, we get a maximum in the production of the useful 2-photon state (useful meaning that it is emitted from the port that directs this bunched state towards the final beamsplitter and the two detectors). When this is the case, the 2-photon state again undergoes a transformation that looks exactly the same as that in Eq. 4, thus generating a coincidence signal half the time.

When the interferometer arms are made to be unequal, the generation of the useful 2-photon state via HOM interference seizes to exist. This then corresponds to the blue terms above no longer cancelling and now contributing to the output state χ_{out} as terms in lieu of the original single photon states which stem from the unwanted un-split 2-photon states $\hat{a}_3^\dagger\hat{a}_3^\dagger$ and $\hat{a}_4^\dagger\hat{a}_4^\dagger$.